

TA7  
W34m  
no.CERC-87-7  
c.3

US Army Corps  
of Engineers

MISCELLANEOUS PAPER CERC-87-7

# SHORT-TERM IMPOUNDMENT OF LONGSHORE SEDIMENT TRANSPORT

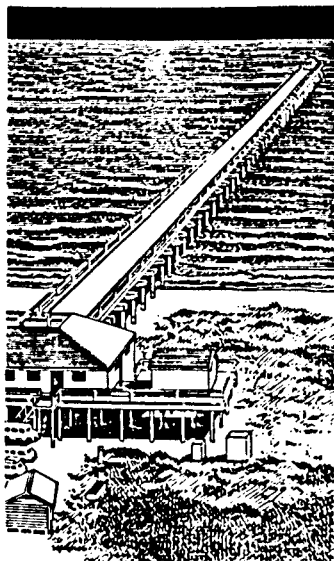
by

Kevin R. Bodge, Robert G. Dean

Development of Coastal and Oceanographic Engineering  
University of Florida  
Gainesville, Florida 32611

and

Field Research Facility  
Coastal Engineering Research Center  
US Army Engineer Waterways Experiment Station  
SR Box 271, Kitty Hawk, North Carolina 27949



March 1987

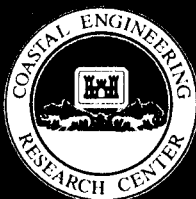
Final Report

Approved For Public Release; Distribution Unlimited

Prepared for DEPARTMENT OF THE ARMY  
US Army Corps of Engineers  
Washington, DC 20314-1000

Under Contract No. DACW39-85-C-0062

Monitored by Coastal Engineering Research Center  
US Army Engineer Waterways Experiment Station  
PO Box 631, Vicksburg, Mississippi 39180-0631



1612015

US-CE-C Property of  
United States Government

TA7  
W34m  
no. CERC-87-7  
C.3

Unclassified

SECURITY CLASSIFICATION OF THIS PAGE

REPORT DOCUMENTATION PAGE				Form Approved OMB No 0704-0188 Exp. Date: Jun 30, 1986	
1a. REPORT SECURITY CLASSIFICATION Unclassified		1b. RESTRICTIVE MARKINGS			
2a. SECURITY CLASSIFICATION AUTHORITY		3. DISTRIBUTION/AVAILABILITY OF REPORT Approved for public release; distribution unlimited,			
2b. DECLASSIFICATION/DOWNGRADING SCHEDULE					
4. PERFORMING ORGANIZATION REPORT NUMBER(S) Miscellaneous Paper CERC-87-7		5. MONITORING ORGANIZATION REPORT NUMBER(S)			
6a. NAME OF PERFORMING ORGANIZATION See reverse.	6b. OFFICE SYMBOL (If applicable)	7a. NAME OF MONITORING ORGANIZATION USAEWES, Coastal Engineering Research Center			
6c. ADDRESS (City, State, and ZIP Code) See reverse.		7b. ADDRESS (City, State, and ZIP Code) PO Box 631 Vicksburg, MS 39180-0631			
8a. NAME OF FUNDING/SPONSORING ORGANIZATION US Army Corps of Engineers	8b. OFFICE SYMBOL (If applicable)	9. PROCUREMENT INSTRUMENT IDENTIFICATION NUMBER Contract No. DACW-39-85-0062			
8c. ADDRESS (City, State, and ZIP Code) Washington, DC 20314-1000		10. SOURCE OF FUNDING NUMBERS			
		PROGRAM ELEMENT NO.	PROJECT NO.	TASK NO.	WORK UNIT ACCESSION NO.
11. TITLE (Include Security Classification) Short-Term Impoundment of Longshore Sediment Transport					
12. PERSONAL AUTHOR(S) Bodge, Kevin R., Dean, Robert G.					
13a. TYPE OF REPORT Final report	13b. TIME COVERED FROM _____ TO _____	14. DATE OF REPORT (Year, Month, Day) March 1987	15. PAGE COUNT 364		
16. SUPPLEMENTARY NOTATION Available from National Technical Information Service, 5285 Port Royal Road, Springfield, VA 22161.					
17. COSATI CODES			18. SUBJECT TERMS (Continue on reverse if necessary and identify by block number)		
FIELD	GROUP	SUB-GROUP	Beach Erosion (LC) Shore protection (LC)		
			Groins (Shore protection) (LC) (LC)		
			Sediment transport (LC)		
19. ABSTRACT (Continue on reverse if necessary and identify by block number) The cross-shore distribution of longshore sediment transport is investigated through the distribution of sediment impounded against a shore-perpendicular barrier over short-term intervals in field and laboratory environments. For each field experiment, a low-profile groyne was deployed across a natural beach in less than 8 hr, and profiles near the groyne were repeatedly surveyed for 8 to 20 hr thereafter. For each laboratory experiment, a low-profile barrier was installed across a pre-equilibrated fine sand model beach, and profile changes near the barrier were measured after 5 to 40 minutes of regular, obliquely incident, unidirectional wave action. Breaking wave angle and longshore current and wave height across the surf zone were also measured. The effects of cross-shore transport and tidal fluctuation were addressed in the survey data, and the effectiveness of the barriers as impoundment agents is discussed. Local downdrift profile changes were found to be poor indicators of the local updrift impoundment. In general, (Continued)					
20. DISTRIBUTION/AVAILABILITY OF ABSTRACT <input checked="" type="checkbox"/> UNCLASSIFIED/UNLIMITED <input type="checkbox"/> SAME AS RPT. <input type="checkbox"/> DTIC USERS			21. ABSTRACT SECURITY CLASSIFICATION Unclassified		
22a. NAME OF RESPONSIBLE INDIVIDUAL			22b. TELEPHONE (Include Area Code)	22c. OFFICE SYMBOL	

DD FORM 1473, 84 MAR

83 APR edition may be used until exhausted.  
All other editions are obsolete.

SECURITY CLASSIFICATION OF THIS PAGE  
Unclassified

Research Library  
USACE ERDC  
Vicksburg, MS

Unclassified

SECURITY CLASSIFICATION OF THIS PAGE

6a. NAME OF PERFORMING ORGANIZATION (Continued).

Department of Coastal and Oceanographic Engineering  
University of Florida  
and  
Field Research Facility  
Coastal Engineering Research Center  
US Army Engineer Waterways Experiment Station

6c. ADDRESS (City, State, and ZIP Code) (Continued).

Gainesville, FL 32611  
and  
SR Box 471  
Kitty Hawk, NC 27949

19. ABSTRACT (Continued).

the longshore transport profiles were found to be bimodal with peaks just landward of the breakpoint and near the shoreline. The relative significance of the longshore transport shifted from the near-breakpoint peak to the near-shoreline peak as the wave condition varied from spilling to collapsing breakers.

Alternately stated, the longshore transport distribution appeared strongly beach profile dependent, as transport was most pronounced over local regions of high bed steepness. Between 10 and 30 percent of the total longshore transport was observed seaward of the breakpoint for all cases. Longshore transport in the swash zone represented at least 5 to 60 percent of the total transport where the largest swash contributions were associated with plunging/collapsing and collapsing surf conditions. A simple model is proposed to describe the normalized longshore transport distribution across the swash and surf zone as a function of the local longshore current, beach slope, and dissipation of wave energy per unit surf volume. The setup, longshore current, and longshore transport are described for an equilibrium beach profile which is finite-sloped at the shoreline. The shoreward convection of longshore current by wave mass transport is also discussed in relation to the longshore transport distribution.

Unclassified

SECURITY CLASSIFICATION OF THIS PAGE

## PREFACE

The study herein was sponsored by the Office, Chief of Engineers, US Army Corps of Engineers, at the Coastal Engineering Research Center (CERC) of the US Army Engineer Waterways Experiment Station (WES) under Contract No. DACW-39-85-C-0062. Additional support was provided by the Department of Coastal and Oceanographic Engineering, Gainesville, Florida. Field work for the study was executed at the CERC Field Research Facility (FRF), Duck, North Carolina, with the cooperation of Mr. Curtis Mason, Chief, FRF. The laboratory investigation of the study was conducted at the University of Florida Coastal and Oceanographic Engineering Laboratory. The support of Mr. Marc Perlin, Laboratory Director, and the entire laboratory staff was instrumental in the successful completion of the field and laboratory efforts of the study.

This report was prepared by Dr. Robert Dean, Graduate Research Professor, and Mr. Kevin Bodge, Research Associate, Department of Coastal and Oceanographic Engineering, University of Florida. Initial trials executed on Florida's beaches to determine the potential practicability of the field studies included the assistance of LT Dave Mesa and Messrs. William Buckingham and Danny Brown, as well as many members of Mr. Bodge's introductory coastal engineering classes. The intensive field work of the study at the FRF was made possible through the participation of LT Paul Rodriguez (formerly of CERC) and the dedicated efforts of Ms. Diana Cronin and Mr. Brack Stovall. Ms. Cronin and Messrs. Stovall and Bodge endured 3 months of exhausting, unique, and often dangerous work while living together in a 17-ft travel trailer in the FRF parking lot for the duration of the study. Mr. Bolin competently assisted with the laboratory experiments of the study, often from dawn until past dusk. The greater portions of the manuscript and the figures were prepared by Meses. Gail Terry and Lillean Pieter, respectively, of the Coastal Engineering Department, University of Florida.

Technical Monitor of the study herein was Dr. Lee L. Weishar, Coastal Processes Branch (CR-P), CERC, under direct supervision of Dr. Steven A. Hughes, Chief, CR-P, and Mr. H. Lee Butler, Chief, Research Division; and under general supervision of Dr. James R. Houston and Mr. Charles C. Calhoun, Jr., Chief and Assistant Chief, CERC, respectively.

COL Dwayne G. Lee, CE, was Commander and Director of WES during publication of this report. Dr. Robert W. Whalin was Technical Director.

TABLE OF CONTENTS

	<u>Page</u>
PREFACE . . . . .	i
LIST OF TABLES . . . . .	vi
LIST OF FIGURES . . . . .	vii
1. INTRODUCTION . . . . .	1
2. REVIEW OF LONGSHORE SEDIMENT TRANSPORT RELATIONSHIPS AND CROSS-SHORE DISTRIBUTION DATA . . . . .	6
2.1 Fundamental Expressions for Total Longshore Sediment Transport . . . . .	6
2.2 Existing Distributed Longshore Sediment Transport Models .	19
2.3 Existing Field and Laboratory Data for the Distribution of Longshore Sediment Transport Across the Surf Zone . . .	32
2.4 Chapter Summary . . . . .	51
3. FIELD INVESTIGATION: EXPERIMENTAL METHOD AND DATA PRESENTATION	53
3.1 Introduction . . . . .	53
3.2 Experimental Method . . . . .	53
3.2.1 Overview . . . . .	53
3.2.2 Groyne Construction and Removal . . . . .	54
3.2.3 Profiling Techniques . . . . .	57
3.2.4 Groyne Deployment and Profiling Procedure . . . . .	60
3.2.5 Additional Measurements . . . . .	61
3.3 Description of the Experimental Conditions . . . . .	62
3.3.1 Overview . . . . .	62
3.3.2 Groyne #1 . . . . .	68
3.3.3 Groyne #2 . . . . .	68
3.3.4 Groyne #3 . . . . .	73
3.3.5 Groyne #4 . . . . .	78
3.3.6 Sediment Characteristics . . . . .	88
4. TIDAL DECONVOLUTION AND REMOVAL OF CROSS-SHORE TRANSPORT EFFECTS . . . . .	90
4.1 Introduction . . . . .	90
4.2 General Description of Approach . . . . .	90

4.3	Tidal Deconvolution Techniques . . . . .	93
4.3.1	"Simple" Tidal Deconvolution . . . . .	93
4.3.2	Matrix Tidal Deconvolution . . . . .	95
4.3.3	Illustrative Evaluation of Tidal Deconvolution through Numerical Simulation . . . . .	100
4.3.4	Tidal Deconvolution and Field Data . . . . .	108
4.4	Removal of Cross-Shore Transport Signals . . . . .	113
4.5	Calculation of Longshore Transport Rate at a Depth Contour	117
4.6	Limiting Depth Contours of Barrier Effectiveness . . . . .	122
4.7	Total Longshore Transport Rate . . . . .	125
4.8	Expressing the Longshore Transport Distribution across the Surf Zone Width . . . . .	125
5.	RESULTS FROM THE FIELD INVESTIGATION . . . . .	127
5.1	Introduction . . . . .	127
5.2	Distribution of Longshore Sediment Transport . . . . .	127
5.2.1	Groyne #2 . . . . .	127
5.2.2	Groyne #3 . . . . .	133
5.2.3	Groyne #4 . . . . .	144
5.3	Total Longshore Sediment Transport . . . . .	152
5.4	Limiting Effectiveness of the Groynes . . . . .	156
5.5	Offshore Distribution of Longshore Transport for the Two "Best" Data Sets . . . . .	156
6.	LABORATORY INVESTIGATION: MODEL APPARATUS AND EXPERIMENTAL METHOD . . . . .	159
6.1	Introduction . . . . .	159
6.2	The Physical Model . . . . .	160
6.3	Profiling Apparatus . . . . .	164
6.4	Wave Measurement . . . . .	167
6.5	Longshore Current and Wave Angle Measurement . . . . .	168
6.6	Fluorescent Sand Tracer . . . . .	169
6.7	Experimental Procedure . . . . .	170
6.8	Laboratory Data Analysis . . . . .	172
7.	LABORATORY INVESTIGATION: RESULTS . . . . .	173
7.1	Introduction . . . . .	173
7.2	Plunging/Spilling Series--Field Experiment Conditions Without Tide . . . . .	175
7.2.1	Description of Experiment . . . . .	175
7.2.2	Appropriate Groyne Profile . . . . .	177
7.2.3	First Impoundment Interval . . . . .	178
7.2.4	Second Impoundment Interval . . . . .	189
7.3	Plunging Series . . . . .	191
7.3.1	Description of Experiment . . . . .	191
7.3.2	No Groyne "Control" Interval . . . . .	192
7.3.3	Impoundment Data Analysis Methodology . . . . .	193
7.3.4	First Impoundment Interval ("B to C") . . . . .	195
7.3.5	Second Impoundment Interval ("C to D") and Smearing . . . . .	197
7.3.6	Bed and Streamer Traps . . . . .	199

7.4	Plunging/Collapsing Series and Tests with Simulated Tidal Fluctuations . . . . .	201
7.4.1	Description of Experiment . . . . .	201
7.4.2	Tests with Tidal Fluctuation . . . . .	204
7.4.3	Non-Tidal Tests . . . . .	210
7.4.4	Effectiveness of the Tidal Deconvolution . . . . .	217
7.5	Collapsing Series . . . . .	220
7.5.1	Description of Experiment . . . . .	220
7.5.2	Impoundment Results . . . . .	221
7.6	Spilling Series . . . . .	224
7.6.1	Description of Experiment . . . . .	224
7.6.2	Impoundment Results . . . . .	227
7.7	Total Transport . . . . .	231
7.8	Characteristic Features of the Longshore Transport Distribution . . . . .	232
8.	MODELING THE LONGSHORE SEDIMENT TRANSPORT DISTRIBUTION . . . . .	236
8.1	Introduction . . . . .	236
8.2	Bagnold Model . . . . .	236
8.3	Stress Model . . . . .	242
8.4	Alternate Model #1 . . . . .	245
8.5	Alternate Model #2 . . . . .	248
8.6	Alternate Model #3 . . . . .	251
8.7	Alternate Model #4 . . . . .	254
8.8	Alternate Model #5 . . . . .	257
8.9	The Proportionality Constants . . . . .	259
8.10	Comparison to Field Data . . . . .	260
8.11	The Preferred Model . . . . .	264
8.12	Some Considerations of Non-Linear Effects . . . . .	265
8.12.1	Preliminary Remarks . . . . .	265
8.12.2	Total Transport . . . . .	265
8.12.3	Shoreward Convection of Longshore Current by Wave Mass Transport . . . . .	271
8.12.4	Net Longshore Bottom Stress Induced by Non-Linear Wave Orbital Motion . . . . .	277
9.	LONGSHORE CURRENT AND SEDIMENT TRANSPORT ACROSS A SET-UP NON-SINGULAR CONCAVE-UP BEACH . . . . .	280
9.1	Introduction . . . . .	280
9.2	Non-Singular Equilibrium Profile . . . . .	280
9.3	Wave Induced Set-Up and Set-Down . . . . .	284
9.4	Longshore Current . . . . .	287
9.5	Comparison of the Predicted Longshore Current with the Laboratory Observations . . . . .	293
9.6	Swash on a Planar Beach . . . . .	298
9.7	Longshore Sediment Transport . . . . .	299
10.	SUMMARY AND CONCLUSIONS . . . . .	307

APPENDIX A:	CONSTRUCTION OF PYRAMID-STYLE SAND BAG UNITS . . . . .	320
APPENDIX B:	EVALUATION OF ELEMENTS IN THE TIDAL DECONVOLUTION MATRIX, A . . . . .	323
APPENDIX C:	LEAST-SQUARES SOLUTION OF THE OVER-CONSTRAINED TIDAL DECONVOLUTION TECHNIQUE . . . . .	325
APPENDIX D:	LEAST-SQUARES FIT TO THE TOTAL TRANSPORT FUNCTION ALONG A DEPTH CONTOUR . . . . .	327
APPENDIX E:	ESTABLISHING BED COORDINATES FROM LABORATORY PROFILER DEVICE . . . . .	329
APPENDIX F:	SWASH ON A PLANAR BEACH . . . . .	333
REFERENCES	. . . . .	338

LIST OF TABLES

<u>Table</u>	<u>Page</u>
3-1: Summary of Field Experiments . . . . .	62
3-2: Representative Surf Conditions for Field Experiments . . . . .	65
3-3: Sediment Grain Size Distribution--Field Data . . . . .	89
5-1: Total Longshore Transport--Field Data . . . . .	153
6-1: Physical Model Design Parameters . . . . .	164
7-1: Representative Surf Conditions for Laboratory Test Series . . . . .	174
7-2: Total Longshore Transport Estimates from the Laboratory Impoundment Data Sets . . . . .	232

LIST OF FIGURES

<u>Figure</u>	<u>Page</u>
2-1: Comparison of total longshore sediment transport field data with the CERC Formula . . . . .	8
2-2: Comparison of total longshore sediment transport field data with the "energetics" model . . . . .	11
2-3: Variation of the CERC Formula proportionality constant K with wave steepness as found from laboratory investigations . . .	12
2-4: Comparison between median sediment diameter and the CERC Formula proportionality constant K from field data and laboratory data . . . . .	14
2-5: Variation of the CERC Formula proportionality constant K with similarity parameter for selected laboratory and field data .	17
2-6: Variation of the proportionality constant $K^*/g$ (from $I_{\ell} = K^* S_{xy}$ ) with surf similarity parameter . . . . .	18
2-7: Normalized distribution of longshore transport across a planar beach from the Bagnold, Svasek, and Thornton models . . . . .	22
2-8: Normalized distribution of longshore transport for a planar beach calculated for the Komar and Madsen models . . . . .	25
2-9: Example of Bailard's distributed longshore transport model. .	31
2-10: Prototype measurement of suspended sediment concentration, longshore current, and tracer advection speed (from Zenkovitch, 1960) . . . . .	34
2-11: Laboratory measurement of distributed longshore transport using downdrift traps (from Bijker, 1971) . . . . .	36
2-12: Field measurement of distributed longshore and cross-shore transport by Sawaragi and Deguchi (1978) using circular traps in the bed at Isonoura Beach . . . . .	38
2-13: Field measurement of distributed longshore and cross-shore transport by Sawaragi and Deguchi (1978) using circular traps in the bed at Matshuho Beach . . . . .	39

2-14: Normalized distributed longshore transport from laboratory measurements of Sawaragi and Deguchi (1978) . . . . .	41
2-15: Average normalized longshore current and wave height across the surf zone from laboratory measurements of Sawaragi and Deguchi (1978) . . . . .	41
2-16: Normalized longshore transport distribution as measured by Tsuchiya (1982) . . . . .	42
2-17: Normalized longshore transport distribution developed from relative rotation of depth contours at a pocket beach after a change in wave direction (from Berek and Dean, 1982) . . .	44
2-18: Normalized longshore distribution developed from sediment impoundment updrift of a barrier on a laboratory beach (from Fulford, 1982) . . . . .	46
2-19: Distribution of longshore transport calculated from field measurements of longshore current and suspended sediment concentration (from Downing, 1984) . . . . .	48
2-20: Distribution of immersed weight longshore sediment transport calculated from field measurements of longshore current and suspended sediment concentration (from Sternberg et al. 1984)	49
3-1: The pyramid-shaped sand bag unit . . . . .	56
3-2: An individual sand bag showing the fill-flap design . . . . .	56
3-3: Groyne #3 at low tide . . . . .	58
3-4: Groyne #4, looking landward from updrift side at mid-tide . .	58
3-5: Typical survey plan for the field impoundment experiments . .	59
3-6: Typical nearshore bathymetry at the field investigation site during the impoundment experiments . . . . .	64
3-7: Approximate modal wave period and significant (unrefracted) deep water wave height during the four field experiments . .	66
3-8: Breaking wave angle estimated from HF radar imagery during the fourth field experiment (Groyne #4) . . . . .	66
3-9: Beach profiles 2 hours and 15 hours after deployment of Groyne #1 . . . . .	69
3-10: Tidal fluctuation, beach profiling "loop" intervals, and groyne deployment sequence for Groyne #2 . . . . .	70
3-11: Beach profiles 3 m up- and downdrift of the groyne for Groyne #2 during groyne construction and approximately 16 hours after groyne completion . . . . .	71

3-12: Beach profiles updrift and immediately downdrift of the barrier for Groyne #2 during groyne construction and approximately 16 hours after groyne completion . . . . .	72
3-13: Tidal fluctuation, beach profiling "loop" intervals, and groyne deployment sequence for Groyne #3 . . . . .	74
3-14: Time history of surf zone location and mean longshore currents during Groyne #3 . . . . .	75
3-15: Beach profiles 3 m up- and downdrift of the groyne for Groyne #3 before, 2 hours after, and 7 hours after groyne deployment	76
3-16: Representative beach profiles measured far updrift of the barrier for Groyne #3 before, 2 hours after, and 7 hours after groyne deployment . . . . .	77
3-17: Visual observation of wave height and types, and Eulerian measurement of longshore current across the surf zone during the post-groyne deployment interval of Groyne #3 . . . . .	79
3-18: Tidal fluctuation, beach profiling "loop" intervals, and groyne deployment sequence for Groyne #4 . . . . .	80
3-19: Time history of surf zone location and mean longshore current during Groyne #4, first post-groyne deployment survey interval . . . . .	81
3-20: Time history of surf zone location and mean longshore current during Groyne #4, second post-groyne deployment survey interval . . . . .	82
3-21: Beach profiles 3 m up- and downdrift of the barrier for Groyne #4 approximately 6 hours and 20 hours after groyne construction . . . . .	83
3-22: Beach profiles 3 m downdrift prior to and after construction of the barrier for Groyne #4 . . . . .	84
3-23: Beach profiles 3 m updrift prior to and after construction of the barrier for Groyne #4 . . . . .	85
3-24: Beach profiles 91.4 m updrift prior to and after construction of the barrier for Groyne #4 . . . . .	86
3-25: Visual observation of wave height and type, and Eulerian measurement of longshore current across the surf zone during the first post-groyne deployment impoundment interval of Groyne #4 . . . . .	87
3-26: Visual observation of wave height and type, and Eulerian measurement of longshore current across the surf zone during the second post-groyne deployment impoundment interval of Groyne #4 . . . . .	88

4-1:	The coordinate system adopted for a 3-dimensional beach with shore-perpendicular barrier and fluctuating tidal water level	91
4-2:	"Simple" tidal deconvolution . . . . .	95
4-3:	"Matrix" tidal deconvolution . . . . .	97
4-4:	Simulated profile changes over time for a beach of given initial profile subjected to a prescribed total transport function and fluctuating tidal water level . . . . .	102
4-5:	Comparison of the tidally deconvolved transport functions and the actual prescribed transport function for simple, N=M matrix, and least-squares matrix tidal deconvolution schemes. (Numerical simulation.) . . . . .	104
4-6:	The transport functions deconvolved from "noisy" profile-change data compared to the actual prescribed functions. (Numerical simulation.) . . . . .	105
4-7:	The running filter used to smooth the transport functions developed through the matrix tidal deconvolution schemes . .	106
4-8:	The smoothed transport functions compared to the actual prescribed transport functions developed from N=M matrix and least-squares matrix tidal deconvolution of "noisy" profile-change data. (Numerical simulation.) . . . . .	107
4-9:	Tidally deconvolved total transport functions $\Lambda(z)$ developed for profile change data from survey loops 4 and 5 of Groyne #4, 9 m updrift of the barrier . . . . .	109
4-10:	Comparison of the tidally deconvolved total transport functions $\Lambda(z)$ developed using the simple, smoothed (N=M) matrix, and smoothed least-squares matrix techniques. (Field data.) . .	110
4-11:	Tidally deconvolved total transport functions $\Lambda(z)$ developed for profile change data from survey loops 1 and 2 of Groyne #3, 9 m updrift of the barrier . . . . .	112
4-12:	Comparison of the measured profiles at survey time $t_2$ and the profiles calculated from the tidally deconvolved total transport function at time $t_2$ using the least-squares matrix technique. (Field data.) . . . . .	114
4-13:	Fit of the total transport function along a depth contour using non-cumulative and cumulative values . . . . .	118
4-14:	Fit of the total transport function along a depth contour using non-cumulative and cumulative values . . . . .	119
4-15:	Integration of the longshore component of the total transport function $\Lambda_y(z)$ updrift of the barrier in order to evaluate the volumetric rate of impoundment along the contour . . . .	120

4-16:	An example illustrating the calculation of the longshore trapping time $\Delta t_q(z)$ for which contour $z$ was "blocked" by the presence of the barrier during the survey interval $\Delta t$ . . .	123
5-1:	Distribution of longshore sediment transport rate for still-water depth contours. Groyne #2, loops 1-3 . . . . .	128
5-2:	Effective relative trapping time and time-weighted barrier relief for each depth contour. Groyne #3, loops 1-3 . . . . .	129
5-3:	Distribution of longshore sediment transport rate for still-water depth contours. Groyne #2, loops 1-2 . . . . .	131
5-4:	The total transport function $\Lambda(z)$ calculated for each of 11 profiles, and illustrated along various depth contours. Groyne #3, loops 2-3 . . . . .	134
5-5:	Effective relative trapping time and time-weighted barrier relief for each depth contour. Groyne #3, loops 2-3 . . . . .	136
5-6:	Distribution of longshore sediment transport rate for still-water depth contours. Groyne #3, loops 2-3 . . . . .	137
5-7:	Effective relative trapping time and time-weighted barrier relief for each depth contour. Groyne #3, loops 1-2 . . . . .	139
5-8:	Distribution of longshore sediment transport rate for still-water depth contours. Groyne #3, loops 1-2 . . . . .	140
5-9:	Effective relative trapping time and time-weighted barrier relief for each depth contour. Groyne #3, loops 1-3 . . . . .	142
5-10:	Distribution of longshore sediment transport rate for still-water depth contours. Groyne #3, loops 1-3 . . . . .	143
5-11:	Total transport function $\Lambda(z)$ calculated for each of 10 profiles, and illustrated along various depth contours. Groyne #4, loops 4-5 . . . . .	146
5-12:	Effective relative trapping time and time-weighted barrier relief for each depth contour. Groyne #4, loops 4-5 . . . . .	147
5-13:	Distribution of longshore sediment transport rate for still-water depth contours. Groyne #4, loops 4-5 . . . . .	148
5-14:	Effective relative trapping time and time-weighted barrier relief for each depth contour. Groyne #3, loops 1-3 . . . . .	149
5-15:	Distribution of longshore sediment transport rate for still-water depth contours. Groyne #4, loops 1-3 . . . . .	151
5-16:	Distribution of longshore sediment transport rate for still-water depth contours. Groyne #4, loops 1-5 . . . . .	152

5-17:	The longshore transport distribution, longshore current, wave height, and average beach profile across the surf zone for Groyne #4, loops 4-5 . . . . .	157
5-18:	The longshore transport distribution, longshore current, wave height, and average beach profile across the surf zone for Groyne #3, loops 2-3 . . . . .	158
6-1:	Plan view of the laboratory model . . . . .	160
6-2:	Oblique sketch of the support walls, rail system, cart, and profiler used in the laboratory model . . . . .	165
7-1:	Profile of groyne, adjacent beach profiles, and beach profile changes immediately downdrift and updrift of the groyne. Plunging/spilling test series . . . . .	176
7-2:	The total transport function determined for the first impoundment interval of the plunging/spilling test series . . . . .	179
7-3:	Illustrative sketch of wave and current pattern around the impoundment barrier in the laboratory model . . . . .	180
7-4:	Graphical description of variables used to calculate the horizontal displacement $\Delta x$ , between two beach profiles for the general case of a non-uniquely defined contour . . . . .	184
7-5:	Idealized total transport function $\Lambda(y)$ and associated transport $q(y)$ along a given depth contour (or offshore location) updrift of the barrier on the laboratory beach . . . . .	185
7-6:	The longshore transport distribution, longshore current, wave height, and average beach profile across the surf zone for the first impoundment interval of the plunging/spilling test series . . . . .	188
7-7:	Comparison of the longshore transport distribution found from the first and second impoundment intervals of the plunging/spilling test series . . . . .	190
7-8:	Beach profile change before groyne deployment at the site of the groyne for the plunging test series . . . . .	192
7-9:	Beach profile changes at 5 m updrift and downdrift of the groyne for the first and second impoundment intervals of the plunging test series . . . . .	195
7-10:	The longshore transport distribution, longshore current, wave height, and average beach profile across the surf zone for the first impoundment interval of the plunging test series . . . . .	196
7-11:	Comparison of the longshore transport distribution found from the first and second impoundment intervals of the plunging test series . . . . .	198

7-12: Comparison of combined bed and streamer trap sediment accumulation rate, suspended sediment contribution, and longshore sediment transport rate (from impoundment data) across shore. Plunging test series . . . . .	200
7-13: Time history of the mean water level fluctuation and survey loops for the laboratory investigation involving simulated tide effects . . . . .	203
7-14: Beach profiles measured immediately updrift and downdrift of the groyne during the pre-, intermediate, and post-impoundment surveys for the laboratory test involving simulated tidal fluctuations . . . . .	205
7-15: Distribution of longshore transport rate for still water depth contours derived from the rising, falling, and entire tide impoundment intervals . . . . .	207
7-16: Beach profiles measured immediately updrift of the groyne site for the non-tidal plunging/collapsing test series . . .	212
7-17: The longshore transport distribution, longshore current, wave height, and average beach profile across the surf zone for the plunging/collapsing (non-tidal) test series . . . . .	213
7-18: Comparison of the longshore transport distribution across the surf zone for the short-term and longer-term impoundment intervals, and fluorescent tracer field after 18 minutes of wave action. Plunging/collapsing (non-tidal) test series . .	215
7-19: Comparison of the longshore transport distributions across shore developed using tidal deconvolution. Plunging/collapsing test series . . . . .	218
7-20: Comparison of typical beach profiles updrift of the groyne for the field studies and the laboratory studies . . . . .	220
7-21: Beach profiles at the groyne deployment site before impoundment, and immediately updrift and downdrift of the groyne after the impoundment interval for the collapsing test series	221
7-22: The longshore transport distribution, longshore current, wave height, and average beach profile across the surf zone for the collapsing test series . . . . .	223
7-23: Beach profiles measured before and after impoundment for the spilling wave test series . . . . .	226
7-24: The longshore transport distribution, longshore current, wave height, and average beach profile across the surf zone for the spilling test series . . . . .	228

7-25:	Longshore transport distribution developed from impoundment data and fluorescent tracer field after 36 minutes of wave action for the spilling test series . . . . .	230
7-26:	Normalized longshore transport distribution across the surf zone developed from the best impoundment data sets of the laboratory and field experiments . . . . .	233
8-1:	Comparison of normalized measured longshore transport distributions from laboratory data with the Bagnold model (no set-up, shoreline-discontinuous evaluation) . . . . .	238
8-2:	Comparison of normalized measured longshore transport distributions from laboratory data with the Bagnold model (set-up, shoreline-continuous evaluation) . . . . .	241
8-3:	Comparison of normalized measured longshore transport distributions from laboratory data with the stress model . . . . .	244
8-4:	Comparison of normalized measured longshore transport distributions from laboratory data with alternate model #1 . . . . .	247
8-5:	Comparison of normalized measured longshore transport distributions from laboratory data with alternate model #2 . . . . .	249
8-6:	Comparison of normalized measured longshore transport distributions from laboratory data with alternate model #3 . . . . .	252
8-7:	Comparison of normalized measured longshore transport distributions from laboratory data with alternate model #4 . . . . .	255
8-8:	Comparison of normalized measured longshore transport distributions from the two best field data sets with alternate model #2 . . . . .	261
8-9:	Comparison of normalized measured longshore transport distributions from the two best field data sets with alternate model #3 . . . . .	262
8-10:	Comparison of normalized measured longshore transport distributions from the two best field data sets with the Bagnold model . . . . .	263
8-11:	Ratio of the stream function and linear theory values of the longshore wave energy flux $P_{\ell}$ and the longshore radiation stress $S_{xy}$ for several cases evaluated at breaking . . . . .	267
8-12:	The uprush angle $\alpha_{sw}$ , for water particles entering the swash zone with velocity $u_s$ associated with a bore arriving at the shoreline with angle $\alpha_s$ and in the presence of a near-shoreline longshore current $V_{\ell s}$ . . . . .	275
9-1:	The "non-singular concave-up equilibrium beach profile" . . . . .	282

9-2:	Comparison of average beach profiles from three of the laboratory test series with a non-singular equilibrium profile . . .	283
9-3:	The calculated total water depth across the surf zone for an $h=Ax^{2/3}$ -type beach profile compared with the approximation $d=ABx^{2/3}$ . . . . .	286
9-4:	Coefficients $A_1$ and $B_1$ of the longshore current expression for the planar foreshore portion of the non-singular equilibrium beach profile . . . . .	291
9-5:	Normalized (Lagrangian) measured longshore current across the surf zone from the laboratory test series compared to the calculated longshore current for a non-singular equilibrium beach profile for various values of the mixing parameter, $P$ . . . .	295
9-6:	Normalized (Eulerian) measured longshore current across the surf zone from the two "best" field impoundment experiments compared to the calculated longshore current for a non-singular equilibrium beach profile . . . . .	297
9-7:	Dimensionless longshore transport across the surf zone for a non-singular equilibrium beach profile evaluated without inclusion of swash . . . . .	301
9-8:	Dimensionless longshore transport across the surf zone for a non-singular equilibrium beach profile evaluated for shoreward-shifted longshore current profile, and linear decay of wave height from the profile match point to the shoreward limit of runup . . . . .	304
9-9:	Dimensionless longshore transport across the surf zone for a planar beach assuming linear wave decay from the breakpoint to the still water line . . . . .	305
A-1:	Construction detail for an individual sand bag unit for use in the pyramid-style groyne . . . . .	321
E-1:	Illustrative sketch of profiler apparatus geometry . . . . .	330
E-2:	Circuit diagram of profiler . . . . .	332
F-1:	Geometry of swash upon an inclined plane . . . . .	334

SHORT-TERM IMPOUNDMENT OF LONGSHORE  
SEDIMENT TRANSPORT

CHAPTER 1

INTRODUCTION

Even the most casual beach observer will note that sediments do not move only on and off the beach, but along it as well. The movement of sand or other beach material along the shore is termed "longshore sediment transport," or "littoral drift." Considerable effort has been directed towards qualitative and quantitative descriptions of longshore sediment transport because it plays a significant role in the process of shoreline response to waves and currents. Although some progress has been made in the determination and prediction of total longshore sediment transport, the question of where the transport takes place on the beach remains essentially unanswered. Knowledge of the distribution of longshore sediment transport across the surf zone is central to the effective design of groynes, jetties, and especially weirs, and to the appropriate planning of pipeline landfalls and trenching across the surf zone. In addition, insight to the distribution of longshore transport aids in understanding spit development, the migration of prominent natural or artificially placed shoreline features, and perhaps the mechanism of the longshore transport process as a whole. Finally, a parameterized description of the distributed longshore transport is an integral part of any complete three-dimensional model of littoral processes which the coastal geology and engineering communities strive to develop.

From existing predictive models, it is generally thought that the maximum longshore transport occurs in the seaward-half of the surf zone and that transport vanishes towards the shoreline (see next chapter). None of the models effectively treat longshore transport above the shoreline (i.e., in the swash zone). Some of the models are discontinuous at the breaker line, while some predict small contributions to the transport outside of the breaker line. Available data indicate that maximum longshore transport occurs in the landward-half of the surf zone at least as often or more often than in the seaward-half, and that significant levels of transport occur at or above the shoreline. Generally less than a third of the total transport is observed to occur outside of the breaker line. Few of the transport models explicitly or effectively describe the effect of the dynamic nature of the beach or breaking wave characteristics upon the longshore transport--whereas the data suggest that these two parameters may be of importance to longshore transport processes.

The present study represents an attempt to gain additional insight to the cross-shore distribution of longshore sediment transport. The study relies upon a "short-term sediment impoundment" experimental technique which was developed and applied by the author in both field and laboratory environments. The technique involves the rapid deployment of a shore-perpendicular barrier on an initially undisturbed beach. Beach profile changes in the vicinity of the barrier are repeatedly surveyed as longshore sediment transport is impounded against the barrier. Surf zone wave heights and currents are simultaneously monitored. The measured beach profile changes are evaluated for cross-shore and longshore components of sediment transport along particular depth

contours (where an adjustment for tidal fluctuation is made when necessary). Ideally, after removal of the cross-shore transport signals, the average longshore transport rate between surveys along each particular depth contour of interest can then be established. If bypassing of the barrier occurs, then at least the significance of the longshore transport along any particular depth contour can be established relative to the other depth contours. In either case, the shape of the longshore transport distribution across shore can be achieved. The experimental technique is termed "short-term" because the impoundment-related beach profile changes are surveyed with the same time scale as the directional wave event associated with the longshore transport impoundment. Such an event may be thought of as a condition of quasi-steady "longshore wave energy flux" or longshore radiation stress, for example. Alternately, the beach profile changes are surveyed with the same time scale of local beach geomorphologic changes. That is, profile changes are surveyed only over the time for which the undisturbed beach profiles are quasi-steady and/or for which the sediment impoundment is not so large that severe bypassing and cross-shore smearing of the impoundment occurs. Thus, the "short-term" impoundment approach allows one to correlate specific directional wave events and beach morphologies to the related longshore transport distribution.

Previous impoundment (or deposition) techniques have been generally "long-term" in character (Johnson, 1952; Bruno and Gable, 1976; Bruno et al., 1980; Dean et al., 1982). In these studies, weekly or monthly surveys of the impoundment (or deposition) of sediment against a barrier or in a basin were compared to integrated hourly or daily wave data such that estimates of the longshore transport rate could not be correlated

to specific wave or beach conditions. Furthermore, the action of many varied tidal and cross-shore processes smeared the distribution of the impoundment (or deposition) of sediment and therefore obscured the distribution of the longshore transport.

In the present study, four separate short-term impoundment experiments were executed on the sandy Atlantic-coast beach of Duck, North Carolina, during the summer of 1984. For each experiment, a shore-perpendicular sand bag groyne was rapidly constructed over an eight hour period and the subsequent sediment impoundment against the groyne was surveyed over an eight to twenty hour period thereafter. Each experiment was conducted during a quasi-steady, relatively low-energy directional wave event. Short-term impoundment experiments were then executed on a fine sand beach with regular waves in the laboratory in order to gain better understanding of the field results and the variation of the distributed longshore sediment transport profile with varying surf conditions.

Owing to the unknown trapping integrity of the barriers constructed in the field and the poorly understood scaling relationships between models and the prototype, the intent of this investigation is not to present absolute magnitudes of total or distributed longshore transport. Instead, this investigation emphasizes the relative contribution of local longshore transport to the total transport; that is, its intent is to present a normalized description of the distribution of longshore transport across the surf zone as a function of beach and surf conditions. In so doing, insight is gained to the mechanisms and significance of various beach and surf conditions on the total longshore sediment transport.

The following chapter of this paper highlights the existing total longshore sediment transport literature and presents a state of the art review of the predictive models and data base for the distribution of longshore transport across the surf zone. Chapter 3 describes the field impoundment experiments. Chapter 4 details the tidal and cross-shore deconvolution techniques which were developed to analyze the field data (and to some extent, the laboratory data). Chapter 5 presents the longshore sediment transport distributions developed from the field data using the deconvolution methodologies described in Chapter 4. Additionally, a preliminary discussion of the quality of the field data is offered in Chapter 5. Chapter 6 describes the model and experimental procedure utilized for the laboratory study. Chapter 7 presents the longshore transport distributions developed from the laboratory experiments for five different types of breaking wave conditions (collapsing through spilling), including the scaled field conditions. The effects of tidal fluctuation, groyne profile, and the impoundment duration--as determined from the laboratory experiments--are also discussed in this chapter. In Chapter 8, several existing and alternate models are tested for agreement with the experimentally determined (normalized) longshore transport distribution profiles. Some considerations of non-linear effects are also discussed. A simple relation (employing linear theory) is proposed as the best engineering model to describe the normalized longshore transport distribution across the surf zone. In Chapter 9 is presented the normalized longshore current and longshore transport distribution profiles for a non-singular equilibrium beach profile (that is, a profile composed of a planar foreshore matched to a concave-up profile). Summary and conclusions are presented in Chapter 10.

## CHAPTER 2

### REVIEW OF LONGSHORE SEDIMENT TRANSPORT RELATIONSHIPS AND CROSS-SHORE DISTRIBUTION DATA

#### 2.1 Fundamental Expressions for Total Longshore Sediment Transport

Reviews of the total longshore sediment transport field and laboratory data base may be found in Savage (1962), Das (1971), King (1972), Greer and Madsen (1978), Walton and Chiu (1979), Bruno, Dean, and Gable (1980), and Hallermeier (1982). Sayao and Kamphuis (1983) offer a review of total longshore transport relationships, several of which are intercompared in Bakker (1970), van de Graaf and van Overeem (1979), and Swart and Fleming (1980). The intent of the following pages is to highlight several existing total longshore transport equations so as to identify surf and beach parameters which may be of importance to the investigation of the distributed longshore transport.

The early laboratory work of Krumbein (1944), and field work of Watts (1953) and Caldwell (1956) suggested the following relationship between the total longshore sediment volumetric transport rate  $Q_\ell$ , and the so-called longshore wave energy flux factor  $P_\ell$ ,

$$Q_\ell = K_q P_\ell \quad (2.1)$$

where  $K_q$  is a dimensional "constant," and

$$P_\ell = E C_g \sin\alpha \cos\alpha \quad (2.2)$$

In Eq. (2.2),  $\alpha$  is the angle between the wave crest and the shoreline, and  $E$  is the wave energy density,

$$E = \frac{1}{8} \rho g H^2 \quad (2.3)$$

where  $\rho$  is the density of the fluid,  $g$  is the acceleration due to gravity, and  $H$  is the root mean square (rms) wave height. The wave group celerity  $C_g$  is related to the wave (phase) celerity  $C$ , by

$$\frac{C_g}{C} = n = \frac{1}{2} \left( 1 + \frac{2kh}{\sinh 2kh} \right) \quad (2.4)$$

In Eq. (2.1), the value of  $P_\ell$  is typically evaluated at the breakpoint such that  $P_\ell$  is more completely written as  $P_{\ell b}$ . Throughout this paper, the subscript  $b$  denotes quantities evaluated at the wave breakpoint.

Inman and Bagnold (1963) expressed Eq. (2.1) in terms of an immersed weight longshore sediment transport rate  $I_\ell$ , where

$$I_\ell = (\rho_s - \rho) g a' Q_\ell \quad (2.5)$$

and where  $\rho_s$  is the density of the sediment, and  $a'$  is the ratio of sand grain volume without voids to total volume with voids. Equation (2.1) is then written

$$I_\ell = K P_{\ell b} \quad (2.6)$$

where  $K$  is a dimensionless constant. Equation (2.6), in various forms, is referred to as the "CERC Formula." This equation is widely accepted

and applied (primarily because of its simplicity) despite its empirical nature and the uncertainty associated with the value of the constant of proportionality,  $K$ . Since the introduction of this expression, the recommended value of  $K$  has varied by a factor of four (Inman, 1978). Based upon the range of values found for  $K$  from field studies, Dean (1978) estimates that total longshore drift can be predicted to within -67% to +200% error. At present, the recommended value of  $K$  is 0.78 (CERC, 1984). Figure 2-1 illustrates most of the total longshore transport field data base compared with the recommended relationship. Laboratory results (not shown) suggest  $K$  values much less than 0.78.

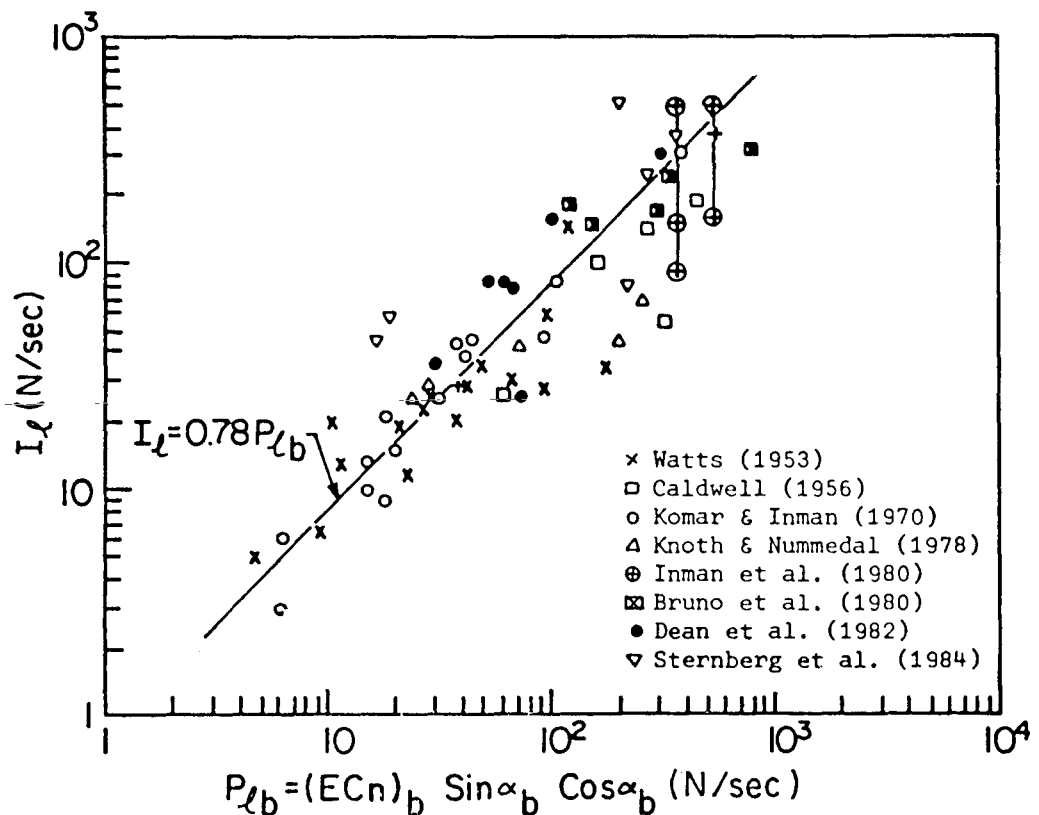


Figure 2-1: Comparison of total longshore sediment transport field data with the CERC Formula.

Longuet-Higgins (1972) pointed out that the parameter  $P_{\ell}$  described above is not the longshore component of energy flux, and, in fact, has no obvious physical meaning. He re-expressed  $P_{\ell}$  as the product of two "physically meaningful" quantities,

$$P_{\ell} = \left( E \frac{C}{C} \cos \alpha \sin \alpha \right) C = S_{xy} C \quad (2.7)$$

where  $S_{xy}$  is the depth- and time-averaged alongshore momentum flux in the onshore direction per unit longshore distance, or longshore radiation stress, for short. At the breaker point,

$$P_{\ell b} = S_{xy} C_b \quad (2.8)$$

where  $S_{xy}$  can be calculated anywhere outside the breaker line for a coastline with straight and parallel depth contours if there is no wave energy dissipation outside the breaker line. From Eq. (2.8) above, the CERC Formula (Eq. 2.6) may be expressed

$$I_{\ell} = K S_{xy} C_b \quad (2.9)$$

or, alternately,

$$I_{\ell} = K^* S_{xy} \quad (2.10)$$

where  $K^*$  is a constant with dimensions of length per time. Vitale (1981) indicates that Eqs. (2.6) and (2.10) are equally good (or equally poor) indicators of total longshore sediment transport. The field data of Bruno et al. (1980) indicate that Eq. (2.10) is a slightly better predictor of total longshore transport than Eq. (2.6).

Inman and Bagnold (1963) and Komar and Inman (1970) presented an alternative to the empirical CERC Formula based upon the "energetics" approach of Bagnold (1963):

$$I_{\ell} = K' (E C_g)_b \left( \frac{\cos \alpha}{u_o} \right)_b \bar{V}_{\ell} \quad (2.11)$$

where  $K'$  is a dimensionless constant of proportionality,  $u_o$  is the maximum near-bottom horizontal orbital velocity, and  $\bar{V}_{\ell}$  is the average longshore current. The subscript  $b$  refers to the breaking position, as usual. The terms in parentheses represent the mean wave force applied to the bed which mobilizes sediment for longshore transport by the current  $\bar{V}_{\ell}$ . An advantage of this model is that the source of  $\bar{V}_{\ell}$  is unspecified. Komar and Inman (1970) found  $K'=0.28$  based upon field measurements of longshore transport and current. In the absence of measured longshore current,  $\bar{V}_{\ell}$  is often approximated by the planar beach expression:

$$\bar{V}_{\ell} = \frac{5\pi}{16} (u_o \frac{m}{C_f}) \sin 2\alpha_b \quad (2.12)$$

after Longuet-Higgins (1970), where  $C_f$  is a bed friction factor, and  $m$  is the beach slope (rise over run). Substitution of Eq. (2.12) into (2.11) yields

$$I_{\ell} = K'' (E C_n)_b \cos \alpha_b \frac{m}{C_f} \sin 2\alpha_b \quad (2.13)$$

Komar (1971) suggests that  $m \cos \alpha_b / C_f$  is a constant. If so, then Eq. (2.13) reduces to the CERC Formula, where

$$K = K' \frac{5\pi}{16} \frac{m \cos \alpha_b}{C_f} \quad (2.14)$$

Comparison of field data with Eq. (2.11) is shown in Figure 2-2.

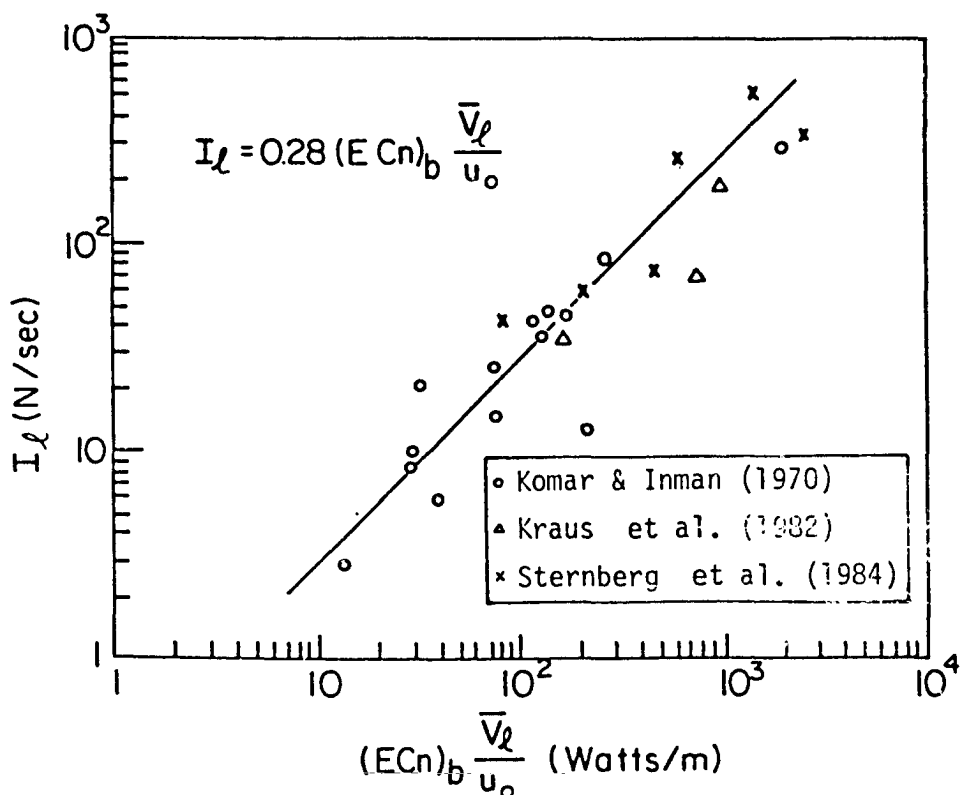


Figure 2-2: Comparison of total longshore sediment transport field data with the "energetics" model.

Several investigators have suggested that the constants of proportionality,  $K$  and  $K^*$  in Eqs. (2.6) and (2.10), respectively, are not constants after all. Instead,  $K$  and  $K^*$  may be dependent upon some wave and/or sediment characteristics. From laboratory results, Saville (1950), Shay and Johnson (1951), and Vicente (as cited in Sayao and Kamphuis, 1983) suggested that the total longshore sediment transport,

and therefore the proportionality constant  $K$  in the CERC Formula, increases with increasing deepwater wave steepness up to  $H_o/L_o \approx 0.01$  to  $0.025$ , and decreases thereafter. Overall, for waves of identical energy levels, Saville suggested that lower steepness waves result in greater total drift than higher steepness waves. The approximate relationship between wave steepness and the proportionality constant  $K$  is illustrated in Figure 2-3 for six different laboratory investigations.

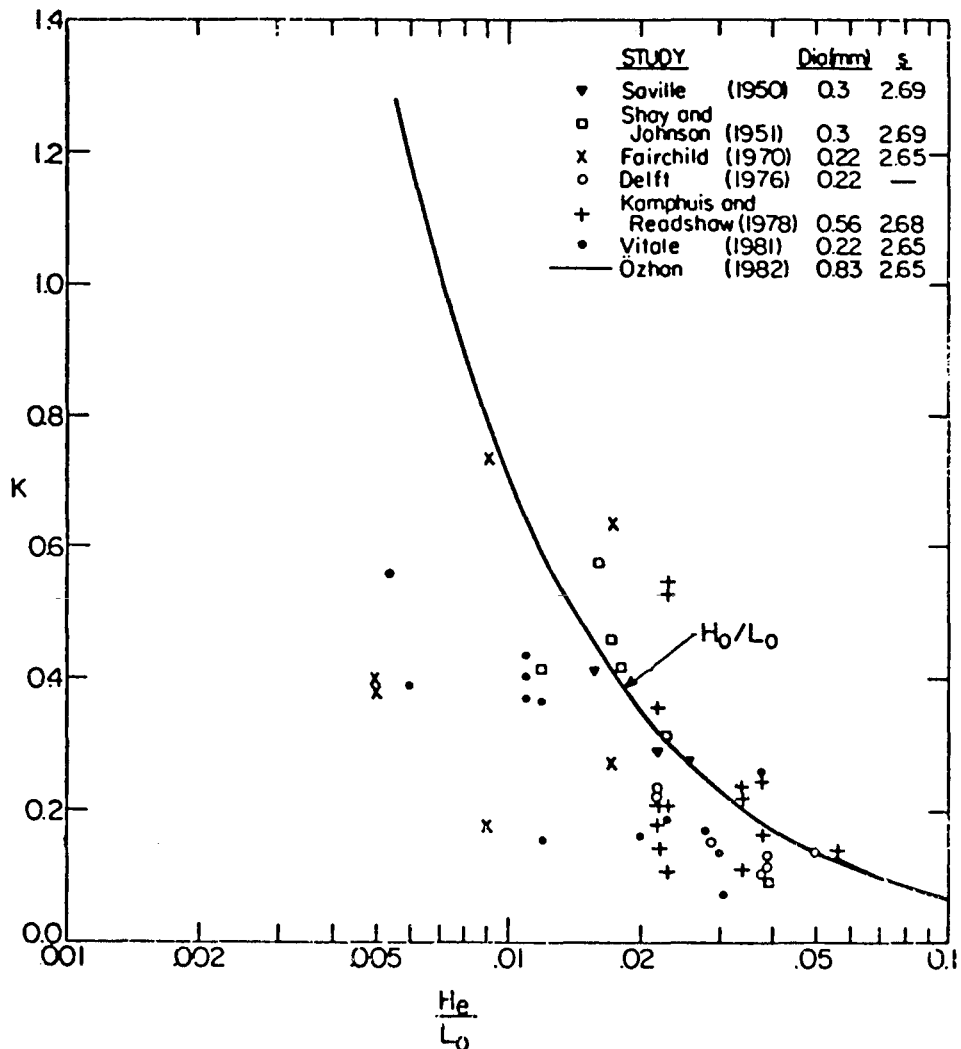


Figure 2-3: Variation of the CERC Formula proportionality constant  $K$ , with wave steepness as found from laboratory investigations.

The steepness  $H_e/L_o$  refers to the calculated wave height  $H_e$  at the theoretical limiting water depth for appreciable longshore bedload transport  $d_e$ , where

$$d_e = \frac{U_e^2}{0.03 (s-1) g} \quad (2.15)$$

from Hallermeier (1978). The term  $U_e$  is the maximum near-bed linear-theory wave orbital velocity, and  $s$  is the specific gravity of the sediment. The values of  $K$  were obtained through

$$K = \frac{I_{\ell}}{P_{\ell b}} \approx \frac{I_{\ell}(\text{measured})}{P_{\ell e}} = \frac{I_{\ell}(\text{measured})}{\frac{1}{16} \rho g (H^2 C_g)_e \sin 2\alpha_e} \quad (2.16)$$

Accordingly,  $K$  in Eq. (2.16) is not exactly identical to  $K$  in Eq. (2.6) since  $P_{\ell e}$  is only an approximation of  $P_{\ell b}$ . Figure 2-3 was developed from the compilation of laboratory data presented by Hallermeier (1982). Although there is considerable scatter, a general decrease in  $K$  is noted for an increase in wave steepness (and therefore decreasing immersed weight longshore sediment transport with increasing wave steepness for a given level of longshore wave energy flux). This observation is substantiated by Ozhan (1982) who found from separate laboratory investigation that

$$K \approx 0.007 \left( \frac{H_o'}{L_o} \right)^{-1} \quad (2.17)$$

where  $H_o'$  is the unrefracted deepwater wave height, and  $K$  is identical to that expressed in Eq. (2.6). Ozhan's relationship is shown by the solid line in Figure 2-3.

Castanho (1970), Bajournas (1970), van Hijum (1976), Swart (1976), and Dean (1978) have suggested somewhat conflicting relationships between longshore sediment transport and sediment size. In Figure 2-4 the mean values of the CERC Formula proportionality constant  $K$  ( $\pm$  one standard deviation) found from several laboratory and field longshore sediment present in each study. It is noted that the laboratory data

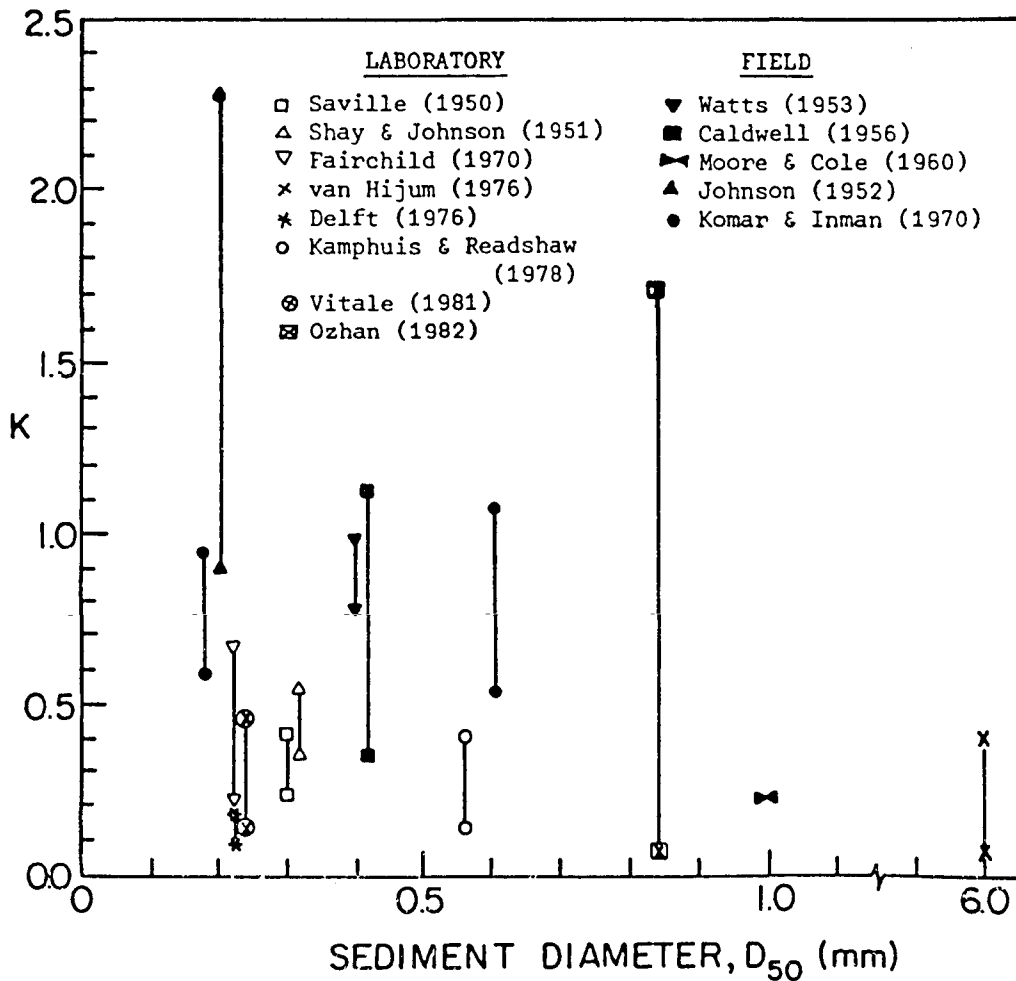


Figure 2-4: Comparison between median sediment diameter and the CERC Formula proportionality constant  $K$  from field data and laboratory data. The bars indicate one standard deviation of  $K$  above and below the mean value of  $K$ .

points have not been scaled up to the prototype and that the laboratory values of  $K$  are approximate (see Eq. (2.16)). An obvious relationship between sediment size and  $K$  is not apparent from the figure.

Dean (1973) suggested that longshore transport may be described by considering the portion of wave energy flux dissipated by settling sand grains. His suspension-dominant model indicates

$$K \propto \frac{\sqrt{g H_b} m \cos \alpha_b}{C_f w_s} \quad (2.18)$$

where  $m$  is the beach bed slope, and  $w_s$  is the sediment fall velocity. Komar (1977) found no readily apparent relationship between  $K$  and  $w_s$  after examination of available longshore transport data.

Much of the debate on the relationship between longshore transport and sediment size depends upon whether the dominant mode of transport is suspension or bedload. In general, however, one would expect intuitively that larger sediments would be transported less readily than smaller sediments. However, since larger sediments are associated with steeper beaches, a given wave train will break closer to shore for beaches of larger sediment and therefore the breaking wave energy or radiation stresses will be concentrated over a smaller surf zone. Hence, greater transport may be realized on beaches composed of materials of larger diameter. These two opposing intuitive arguments have yet to be reconciled.

Recently, from laboratory experiments on sand beaches, Kamphuis and Readshaw (1978), Vitale (1981), Kamphuis and Sayao (1982), and Ozhan (1982) each observed a relationship between total longshore transport proportionality constants ( $K$  and/or  $K^*$  or a similar constant) and the surf similarity parameter  $\xi_b$ , where

$$\xi_b = \frac{m}{\sqrt{H_b/L_o}} \quad (2.19)$$

and  $H_b$  is the breaking wave height and  $L_o$  is the deepwater wavelength. Since it is generally recognized that the (equilibrium) beach slope,  $m$ , is related to the sediment size, the surf similarity parameter somewhat combines the effect of both sediment size and wave steepness. (Choice of the appropriate beach slope,  $m$ , is controversial; some recommendations are made by Sayao and Kamphuis (1983). In the present study,  $m$  is taken as the average bed slope about the breakpoint--unless otherwise noted.)

Figure 2-5 compares the surf similarity parameter and  $K$  for several laboratory investigations and selected field data. Figure 2-6 compares the surf similarity parameter and  $K^*$  for the laboratory data of Kamphuis and Readshaw (1978). In Figure 2-5, the values of  $K$  for the Kamphuis and Readshaw (1978) and Komar and Inman (1970) data represent the actual proportionality constant of the CERC Formula, while the values of  $K$  for the remaining laboratory data are approximated by Eq. (2.16). The laboratory data of Kamphuis and Readshaw and the field data of Komar and Inman are represented by the surf similarity parameter  $\xi_b$ , where  $m$  is taken as an average surf zone bottom slope and local breaking bottom slope, respectively, and significant wave height is utilized for the field data. The remaining laboratory data are represented by a similarity parameter:

$$\xi_e = \frac{m}{\sqrt{H_e/L_o}} \quad (2.20)$$

where  $H_e$  is the wave height at the effective limiting depth for appreciable longshore transport (Eq. (2.15)). The values of  $H_e$  and  $m$  are taken from Hallermeier (1982) for these data. Figures 2-5 and 2-6 indicate a logarithmic increase of  $K$  and  $K^*$  with  $\xi_b$ . In general, examination of relationships using the similarity parameter is more appropriately done with a logarithmic scale since the similarity parameter is logarithmic in character.

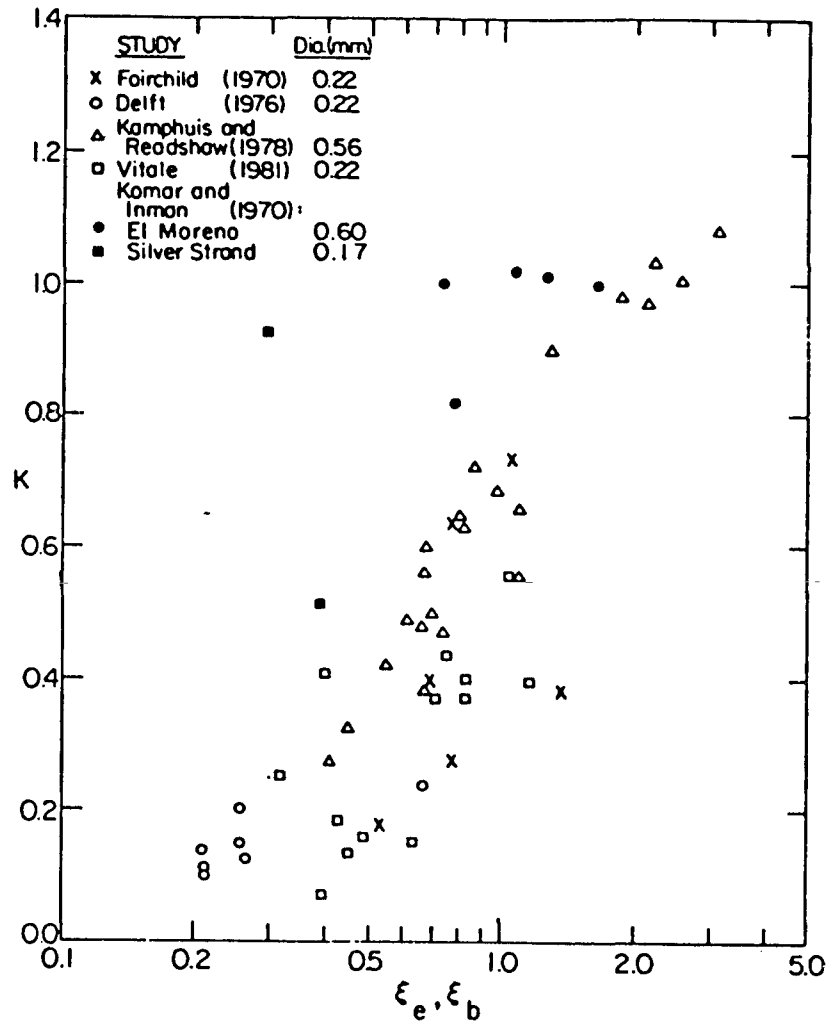


Figure 2-5: Variation of the CERC Formula proportionality constant  $K$  with similarity parameter for selected laboratory and field data.

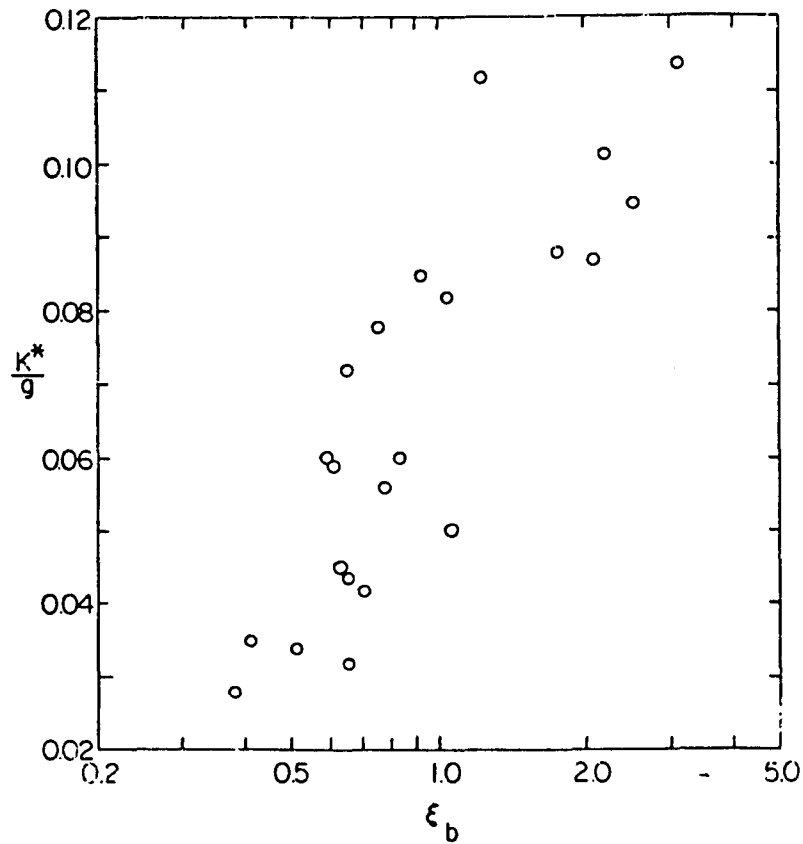


Figure 2-6: Variation of the proportionality constant  $K^*/g$  (from  $I_\ell = K^*S_{xy}$ ) with surf similarity parameter as observed by Kamphuis and Readshaw (1978).

Galvin (1968) and Battjes (1974) reported that the surf similarity parameter may be used to describe breaker type. According to Battjes

$$\begin{array}{ll}
 \epsilon_b > 2.0 & \text{Surging (Collapsing)} \\
 0.4 < \epsilon_b < 2.0 & \text{Plunging} \\
 \epsilon_b < 0.4 & \text{Spilling}
 \end{array} \tag{2.21}$$

From these limits and the trends shown by Figures 2-5 and 2-6, one may conclude that plunging and collapsing breakers lead to greater longshore transport than spilling breakers for a given level of longshore wave energy flux or radiation stress.

The tendency of  $K$  and  $K^*$  to increase with the similarity parameter means that for a given wave steepness, larger sediment sizes exhibit greater longshore transport rates (since larger sediment is associated with steeper slopes and therefore larger values of  $m$ ). This lends credibility to the argument that longshore transport increases on steeper beaches for a given level of longshore wave energy flux or radiation stress.

In brief summary of this section, the proportionality "constants"  $K$  and  $K^*$  in Eqs. (2.6) and (2.10) are probably not constant at all, but generally (i) increase with decreasing wave steepness; (ii) exhibit a disputed trend with sediment size, density, and fall velocity; and (iii) increase with the surf similarity parameter which combines beach slope (and so partly sediment type) and wave steepness. Since the surf similarity parameter is related to the wave breaker type, and the character or structure of the surf zone varies for different wave breaker types, one may expect that the total longshore sediment transport (and so perhaps the distribution of longshore sediment transport across the surf zone) should somehow depend upon the breaker type.

## 2.2 Existing Distributed Longshore Sediment Transport Models

Bagnold (1963) proposed that wave orbital motion mobilizes beach sands and wave power is expended maintaining the sand in motion so that any mean local longshore current  $V_L$  transports the sand. Bagnold

suggested a suspended and bedload model in accordance with this "energetics" approach which may be written

$$i_l = k_B \frac{d}{dx} (E C_g) \frac{V_l}{u_o} \quad (2.22)$$

for small angles of wave approach, where  $i_l$  is the local immersed weight longshore sediment transport rate per unit offshore distance, and where the x-axis is directed offshore with origin at the shoreline. The proportionality constant  $k_B$  is dimensionless. The term  $u_o$  represents the near-bottom wave orbital velocity.

Assuming linear theory, shallow water conditions, constant proportion  $\kappa$  between water depth  $h$  and wave height  $H$ , and further assuming that the longshore current is given by Longuet-Higgins (1970) for a non-mixing planar beach case (Eq. (2.12)), the Bagnold expression becomes

$$i_l = \frac{25\pi}{128} k_B \rho g^{3/2} \kappa^2 \frac{m^2 \sin \alpha_b}{C_f} \sqrt{h_b} h \quad (2.23)$$

A simple distributed model based upon the concept of the CERC Formula was proposed by Svasek in 1969 (see Bakker, 1970). Svasek assumed that the longshore component of sediment transport is proportional to the loss of energy flux between the beach contours; i.e.,

$$i_l(z) \propto \frac{d}{dh} (E C_g \sin \alpha \cos \alpha) \quad (2.24)$$

where  $i_l(z)$  is the local immersed weight longshore sediment transport rate per unit depth. For the same assumptions as described above, (i.e., linear theory, shallow water,  $H=\kappa h$ ), the Svasek model may be written

$$i_{\ell} = \frac{3}{8} K \rho g^{3/2} \kappa^2 \frac{m \sin \alpha_b}{\sqrt{h_b}} h^2 \quad (2.25)$$

where  $K$  is the constant of proportionality from the CERC Formula, and use has been made of the relationship

$$i_{\ell} = i_{\ell}(x) = m i_{\ell}(z) \quad (2.26)$$

Throughout this paper, the notation  $i_{\ell}$  refers to the local immersed weight longshore transport rate per unit offshore distance, whereas  $i_{\ell}(z)$  refers to the transport rate per unit depth.

Thornton (1972) proposed a distributed longshore transport model based upon the energetics approach of Bagnold. Specifically,

$$i_{\ell} = - \frac{B_s}{1-1/s} \frac{\partial}{\partial x} (E \bar{C}_g) \left[ \frac{V_{\ell}}{u_o} \right]^{1/2} \quad (2.27)$$

where  $B_s$  is a dimensionless constant. For the same assumptions as described above, the Thornton model becomes

$$i_{\ell} = B'_s \rho g^{3/2} m^{5/4} \sqrt{\sin \alpha_b} h_b^{1/4} h^{5/4} \quad (2.28)$$

for a planar beach with no-mixing longshore current given by Longuet-Higgins (1970). The proportionality constant  $B'_s$  is dimensionless.

Figure 2-7 illustrates the normalized longshore transport distributions for the Bagnold, Svasek, and Thornton models for a planar beach. As described above, a no-mixing Longuet-Higgins longshore current profile has been assumed for the Bagnold and Thornton models. The normalization  $i_{\ell} x_b / I_{\ell}$ , where  $I_{\ell}$  is the total transport and  $x_b$  is the

surf zone width, may be thought of as the local longshore transport  $i_l$  compared to a uniformly distributed transport across the surf zone,  $I_l/x_b$ . It is noted that none of the models represent transport landward of the shoreline. Each model exhibits a sharp discontinuity in transport at the breaker line since no transport is predicted seaward of the breakpoint (assuming no energy losses outside of the surf zone).

Abdelrahman (1983) further developed Thornton's model by describing the gradient in energy flux as a function of energy dissipation due to breaking (modelled after a periodic bore) and due to bottom friction

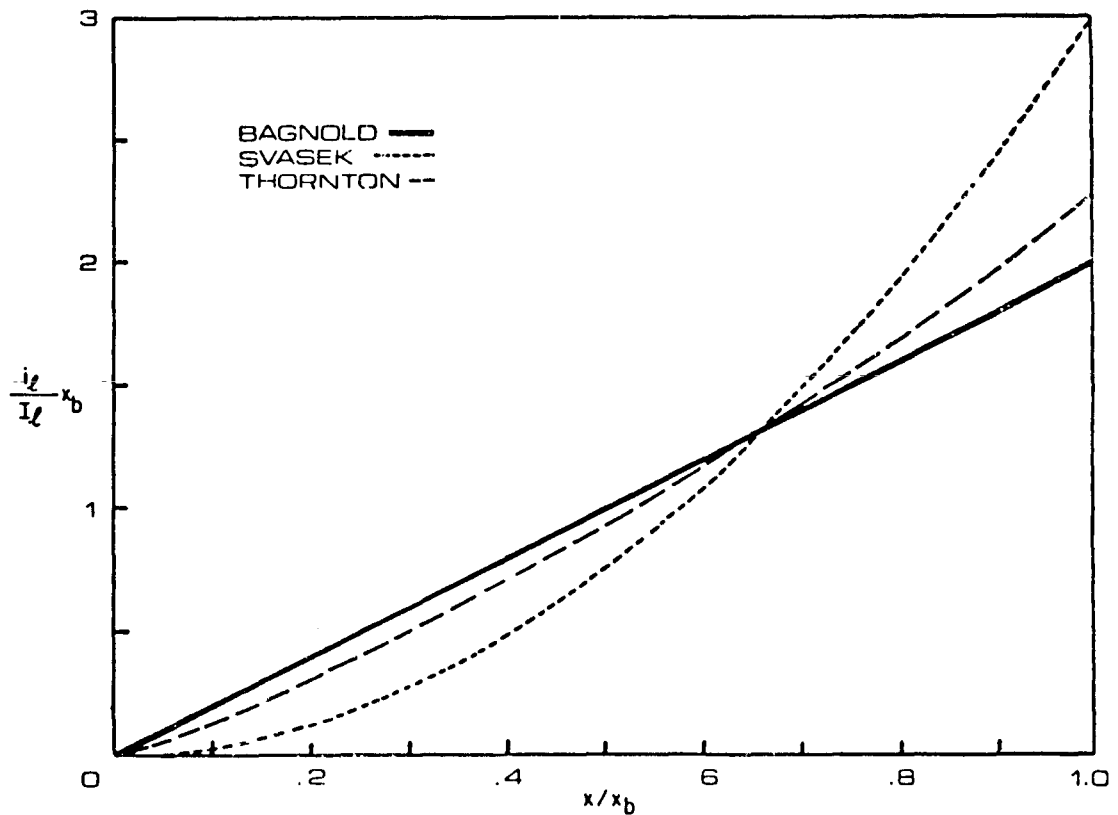


Figure 2-7: Normalized distribution of longshore transport across a planar beach from the Bagnold, Svasek, and Thornton models. A no-mixing Longuet-Higgins (1970) longshore current profile is assumed for the Bagnold and Thornton models.

(eventually neglected). The local longshore current  $V_\ell(x)$  was also expressed through energy dissipation due to breaking after Liu and Dalrymple (1978). Abdelrahman's final expression (which appears dimensionally incorrect) predicts the peak longshore transport at about eight-tenths of the distance from the shoreline to the breaker line for the cases tested, and predicts transport which decreases to zero at the shoreline. The model was developed and utilized for random waves.

Komar (1971, 1975, and 1977) also extended Bagnold's (1963) model, likewise envisioning that breaking wave-induced stress at the bed mobilizes sediment making it available for advection by a longshore current. Therefore, Komar reasoned that the local longshore sediment transport is related to the product of breaking wave-related stress and longshore current. The wave-related stress is taken as a function of the maximum horizontal component of wave orbital motion,  $u_o$ , which Komar suggested is greatest at the break point and decreases to zero at the shoreline. His general expression for the local immersed weight longshore sediment transport per unit distance is

$$i_\ell = \frac{\pi k_1 f_w}{8} \rho g \kappa^2 h V_\ell \quad (2.29)$$

where  $f_w$  is a bed drag coefficient for wave motions and  $k_1$  is a proportionality constant.

If the stress exerted on the bed by longshore current is also included as a sediment "mobilizing" factor, Komar suggested the following expression for distributed longshore transport

$$i_\ell = k_2 V_\ell \left[ C_f V_\ell^2 + \frac{\rho g f_w}{8} \kappa^2 h \right] \quad (2.30)$$

where  $k_2$  is another proportionality constant and  $C_f$  is a frictional drag coefficient for the longshore current velocity. Since Komar assumed that stress due to wave motion is greatest at the breaker line, inclusion of the longshore current related stress suggests that the distribution of longshore transport will shift seaward for small angles of wave incidence since the contribution of stress due to waves will dominate that due to longshore current. Large angles of incidence will create stronger longshore current and a longshore transport distribution profile which more closely follows that of the longshore current. Breaking wave height should not affect the distribution of longshore transport since changes in wave height will more or less equally affect the longshore current and wave orbital velocities.

Figure 2-8 illustrates the normalized (by maxima) longshore transport distributions from the Komar models for a planar beach and for wave and longshore current conditions shown in the figure. Some transport is predicted seaward of the breakpoint when lateral mixing is considered, but neither model predicts transport above the shoreline in the swash. Komar (1971) argues on a theoretical basis that the swash zone can be modelled identically as the surf zone, but swash zone application of any of the existing models is not obvious.

Bijker (1971) was among the first investigators to develop a longshore transport model based upon river-borne sediment transport studies. Bijker's expression for the bedload component of longshore transport, taken after Frijlink, is of the form

$$q_{l-bed} = \text{transport parameter} * e^{\text{stirring parameter}} \quad (2.31)$$

In classical fashion, Bijker's suspended load contribution, taken after

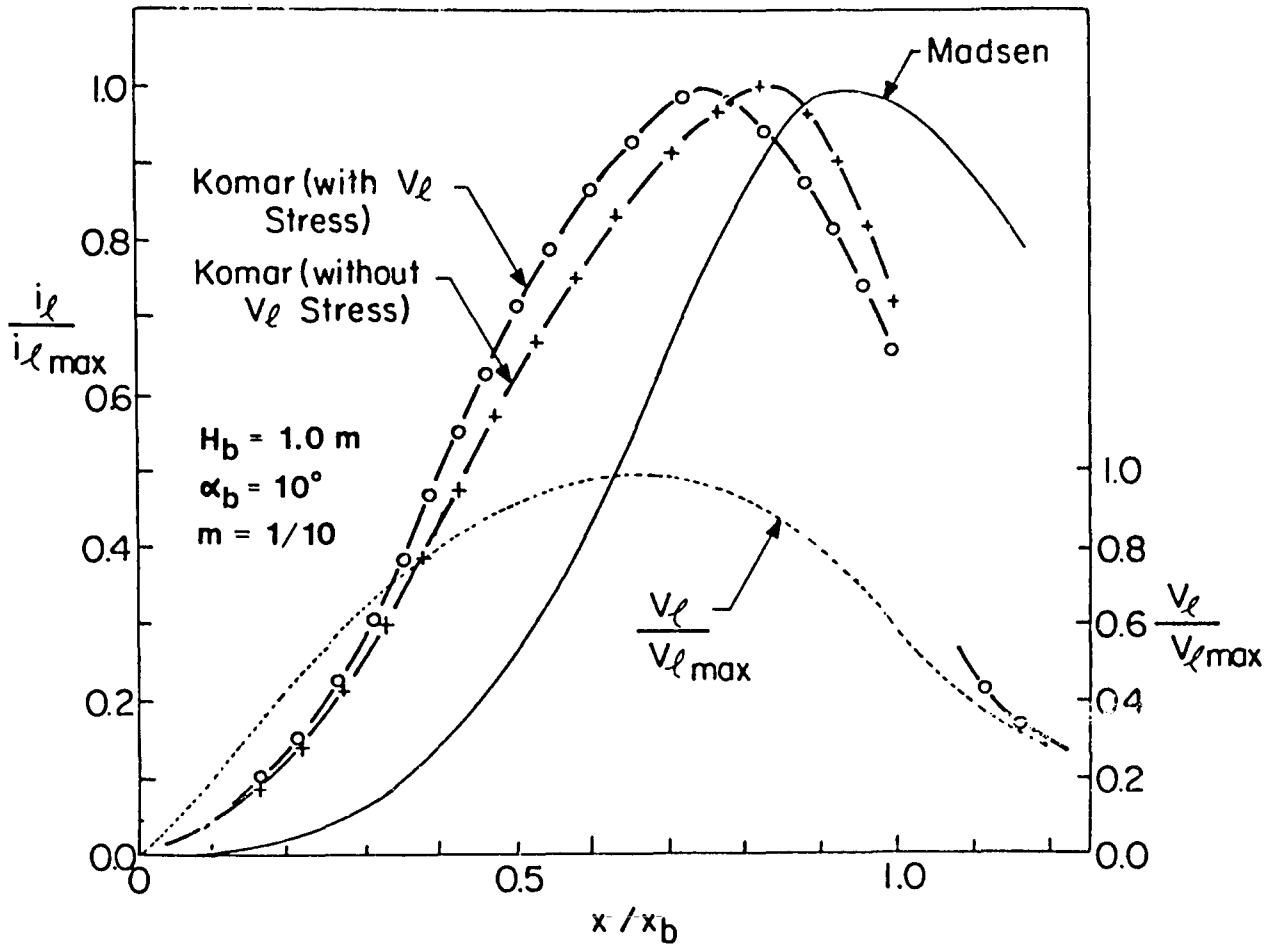


Figure 2-8: Normalized distribution of longshore transport for a planar beach calculated for the Komar and Madsen models using the wave conditions and longshore current profile shown.

Einstein's work, is expressed in terms of the bedload component through somewhat complicated integrals which depend upon the bed roughness or ripple height, fall velocity, and bed shear velocity. Bijker's method is cumbersome to apply, and it is also sensitive to the value of the assumed thickness of the bedload transport. An example from Bijker's

model is shown in the next section (Fig. 2-11). Swart (1976) discussed the Bijker model and suggested that a total load (i.e., bedload + suspended load) model is more appropriate. Swart used a modified Ackers-White (1973) approach and found a lengthy expression for the local longshore transport which is not detailed herein.

Madsen (1978) suggested a distributed longshore transport model which is based upon an experimentally verified expression for sediment transport under oscillatory flow:

$$\vec{\phi}(t) = 40 \vec{\psi}^3(t) \quad (2.32)$$

after Brown (1950), Einstein (1972), and Madsen and Grant (1976), where  $\phi(t)$  and  $\psi(t)$  are instantaneous values of the non-dimensional transport function and Shields parameter, respectively. Specifically,

$$\vec{\phi}(t) = \frac{\vec{q}(t)}{w_s D} \quad (2.33)$$

$$\vec{\psi}(t) = \frac{\vec{\tau}_b(t)}{\rho g (s-1) D} \quad (2.34)$$

Here,  $\vec{q}(t)$  is the instantaneous volumetric sediment transport rate per unit width, and  $w_s$  and  $D$  are the sediment fall velocity and grain size, respectively. The instantaneous bottom shear stress  $\tau_b(t)$  is given by

$$\vec{\tau}_b(t) = \frac{1}{2} \rho f_{cw} | \vec{u}_w(t) + \vec{V} | ( \vec{u}_w(t) + \vec{V} ) \quad (2.35)$$

where  $\vec{u}_w$  and  $\vec{V}$  are unsteady (wave) and steady (current) velocities, respectively, and  $f_{cw}$  is a bed friction factor due to combined waves and

currents. Time-averaging in the longshore direction and employing linear (shallow water) wave theory, Madsen found

$$q_l = 1.7 \frac{w_s}{D^2} \left( \frac{f_{cw}}{g(s-1)} \right)^3 u_o^5 V_l \quad (2.36)$$

The normalized (by maxima) longshore transport distribution across a planar beach (for the same conditions shown for the Komar models) is illustrated for the Madsen model in Figure 2-8. Evaluation of transport landward of the shoreline is not straight-forward from Madsen's model. However, the model does not exhibit a discontinuity in transport at the breaker line if a lateral-mixing model for  $V_l(x)$  is assumed. It is also noted that the model's dependence upon  $w_s/D^2$  implies that the longshore transport decreases with increasing sediment size for the case of spherical sand grains.

The laboratory data of Sawaragi and Deguchi (1978), discussed in the next section, suggests the following empirical description of distributed longshore sediment transport

$$q_l \approx 9.1 V_l D_{50} F_*^{3.9} \quad (2.37)$$

where

$$F_* = \frac{u_*^2 - u_{*c}}{g(s-1) D_{50}} \quad (2.38)$$

The friction velocity  $u_*^2 = \tau_b/\rho$ , where the bottom shear stress,  $\tau_b$ , is due to the combined peak wave orbital velocity and longshore current, and the critical friction velocity,  $u_{*c}$ , is defined for various diameter sands after Iwagaki's investigations of sediment transport threshold velocities for open channel flow (see Sawaragi and Deguchi, 1978).

Walton and Chiu (1979) suggested a distributed longshore sediment transport model of the form:

$$i_l = K_w P_{lb} \chi(x) \quad (2.39)$$

which is similar in form to the CERC Formula as  $K_w$  is a dimensionless constant of proportionality, but where  $\chi(x)$  is a local modifying function which details the bedload and suspended load components of transport independently as functions of the local longshore current and water depth. Besides basic uncertainty of the value  $K_w$  as in the CERC formula, there is difficulty in selecting the separate bedload and suspended load transport coefficients in the modifying term  $\chi(x)$ . Using a Longuet-Higgins type longshore current profile, the model typically predicts maximum longshore transport in the seaward half of the surf zone for a planar beach. A discontinuity is present at the breaker line and transport decreases to zero at the shoreline.

A series of simple expressions which individually reflect some of the concepts described in the preceding pages was tested by Fulford (1982) using laboratory data from Savage (1959) and Bijker (1971). These models included

$$1: i_l = K_1 V_l u_o \quad (2.40a)$$

$$2: i_l = K_2 V_l u_o \frac{1}{h(x)} \quad (2.40b)$$

$$3: i_l = V_l [K_3 u_o + K_3' \frac{1}{h(x)} \frac{d}{dx}(E C_g \cos \alpha)] \quad (2.40c)$$

$$4: i_l = K_4 V_l [u_o + \frac{d}{dx}(E C_g \cos \alpha)] \quad (2.40d)$$

$$5: i_l = K_5 V_l \tau_b \quad (2.40e)$$

where the K's are proportionality constants, and  $\tau_b$  is the local bottom shear stress induced by the longshore component of wave orbital motion (Dean, 1977) or by maximum wave orbital/longshore current velocities (Longuet-Higgins, 1970). Fulford evaluated each model using the expression for longshore current across a planar beach after Longuet-Higgins (1970). Although Fulford concluded that Model 3 (Eq. (2.41c)) agreed best with the laboratory data he tested against, none of the models compared well with the laboratory results.

Hallermeier (1982) derived an expression for the local bedload component of the longshore sediment transport based upon a laboratory expression for bedload transport under oscillatory motion. His model functionally appears as

$$q_l \approx \frac{\sigma u_o^3 \sqrt{D}}{(g(s-1))^{3/2}} \tan \alpha \quad (2.41)$$

where  $\sigma$  is the wave frequency. Hallermeier directly integrated this expression across the surf zone to yield the total bedload longshore transport and did not discuss the distribution of transport outright.

Tsuchiya (1982) considered the local longshore sediment transport in the form

$$q_l = \bar{c} h V_l \quad (2.42)$$

where  $\bar{c}$  is the average local concentration of sediment expressed as a function of the local applied and critical shear stress. Tsuchiya's model generally predicts the maximum longshore drift at about three-quarters of the distance from the shoreline to the breaker line with significant amounts of transport seaward of the breaker line for

decreasing critical shear stress values. This is not too surprising since Tsuchiya's model is suspension-dominant in character.

Finally, Bailard and Inman (1981) and Bailard (1984) proposed an (initially complicated) energetics-based expression for the distribution of longshore sediment transport which independently describes the bed-load and suspended load components of transport as functions of the local longshore current and water depth. Accordingly, the model is similar in structure to that of Walton and Chiu (1979) and therefore involves the same difficulty of selecting separate bedload and suspended load transport coefficients. Typical normalized distributed longshore transport curves obtained from the model for a planar beach are shown in Figure 2-9. The maximum transport is predicted to occur at about nine-tenths of the distance from the shoreline to the breaker line. Transport is described seaward of the breaker line with a slight gradient discontinuity, but is not described above the shoreline.

Briefly summarizing this section, roughly a dozen expressions have been suggested for the distribution of longshore sediment transport. In general, most of the models assume that sediment is locally mobilized (i) as a function of energy dissipation from the breaking waves, or (ii) by the bed shear stress induced by the peak horizontal wave orbital velocities alone or by the combined peak orbital velocities and longshore current. The mobilized sediment is then advected downdrift by the local longshore current. Accordingly, knowledge of the distribution of longshore current across the surf zone is important in most of the existing distributed longshore transport models. Many investigators have relied upon the planar beach longshore current model suggested by Longuet-Higgins (1970).

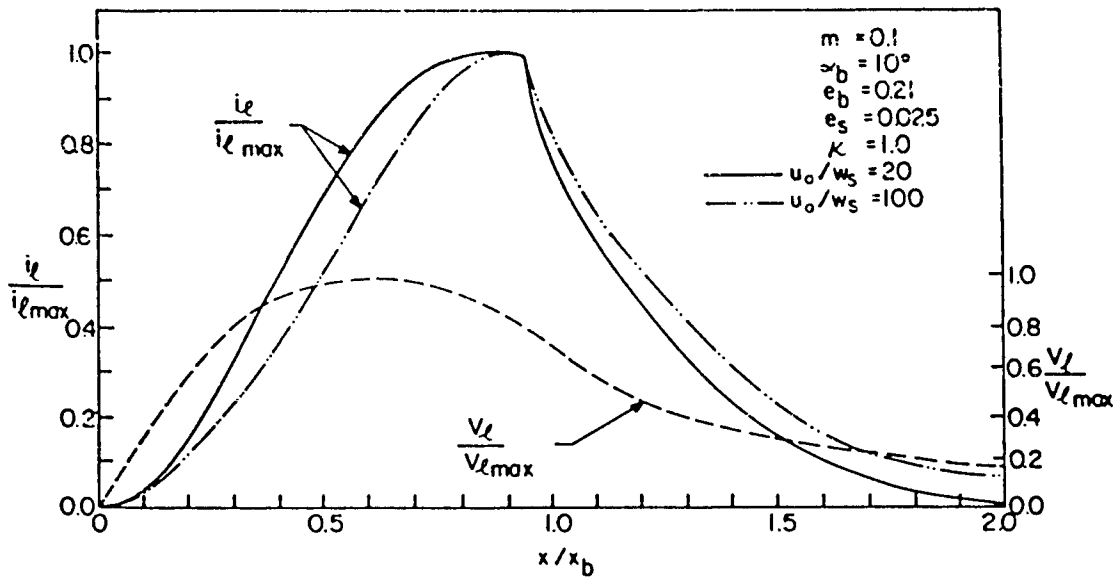


Figure 2-9: Example of Bailard's distributed longshore transport model. A Longuet-Higgins type longshore current profile is used (as shown) with mixing parameter  $P = 0.2$ . Adapted from Bailard (1984).

Most all of the existing models suggest that the longshore sediment transport is greatest between the mid-surf zone and the breaker line for a planar beach, and that the longshore transport tends to zero at the shoreline and outside the breaker line. Models which do not include bottom stress due to longshore current or non-breaking wave orbital motion exhibit discontinuities in transport at the breaker line with zero transport seaward of the breaker line. None of the models explicitly describe nor are well conditioned to treat longshore transport in the swash zone.

### 2.3 Existing Field and Laboratory Data for the Cross-Shore Distribution of Longshore Sediment Transport

The data base which describes the cross-shore distribution of longshore sediment transport is relatively limited. With few exceptions, relevant studies are fairly recent. Aside from the significant level of longshore transport observed in the swash zone, the most notable feature of the data base is a substantial and thus far unexplained variation in the distribution profiles of the transport.

The earliest published prototype observations of the distribution of longshore transport were by the Beach Erosion Board (1933). Measured sediment concentrations from collected water samples beneath a pier were used to indicate the relative magnitude of the suspended component of longshore drift across the surf zone. The results suggested longshore transport maxima at the breaker line and in the swash zone. Transport decreased with increasing depth seaward of the breaker line. Wave conditions during the tests were not well documented.

From a moveable-bed investigation in the laboratory, Saville (1950) did not quantify the distribution of longshore transport across shore, but noted the importance of the beach profile and wave conditions upon the magnitude and mechanism of longshore transport. Most generally, he observed that the bulk of the longshore transport occurred within the surf zone and on the foreshore, while the significant levels of sediment motion observed outside the surf zone were primarily on/offshore in character. Saville emphasized that locations of concentrated longshore transport might correspond to those of concentrated cross-shore processes; that is, when a beach is in disequilibrium with the wave conditions, greater amounts of sediment are mobilized for transport as the profile adjusts to the wave climate. Saville suggested that this

not only increases the total longshore transport (substantiated by laboratory measurements of Kamphuis and Readshaw, 1978) but may affect where the transport occurs. Saville observed that on equilibrium storm beach profiles, the longshore transport was primarily due to advection of sediment by the longshore current within the surf zone. On equilibrium summer beach profiles, the transport was almost entirely due to beach "drifting" along the foreshore (caused directly by the waves). The transition between these two cases occurred abruptly at a wave steepness value  $H_o/L_o = 0.03$  (which corresponds to the transition between spilling and plunging waves for Saville's laboratory beach slope of 1:10). Most significantly, the total transport along summer beaches was much greater than that along storm beaches for the same wave energy levels. This suggests that foreshore "drifting," or longshore transport in the swash zone, is associated with plunging waves and is at least as significant as longshore transport associated with longshore currents seaward of the shoreline.

Zenkovitch (1960) evaluated fluorescent tracer movements as an indicator of longshore drift across beaches in the Soviet Union. A typical result from his study is shown in Figure 2-10 which details the measured distribution profiles of longshore current, longshore sediment advection velocity, and suspended sediment concentration. Like the early Beach Erosion Board results, peak longshore drift was observed at the breaker location(s) and the shoreline/swash location. Generally, longshore transport increased in areas of observed high turbulence levels (bar breaks and shoreline) and decreased in lesser turbulence areas (troughs). Relatively large spilling breakers prevailed during the collection of the data shown in Figure 2-10.

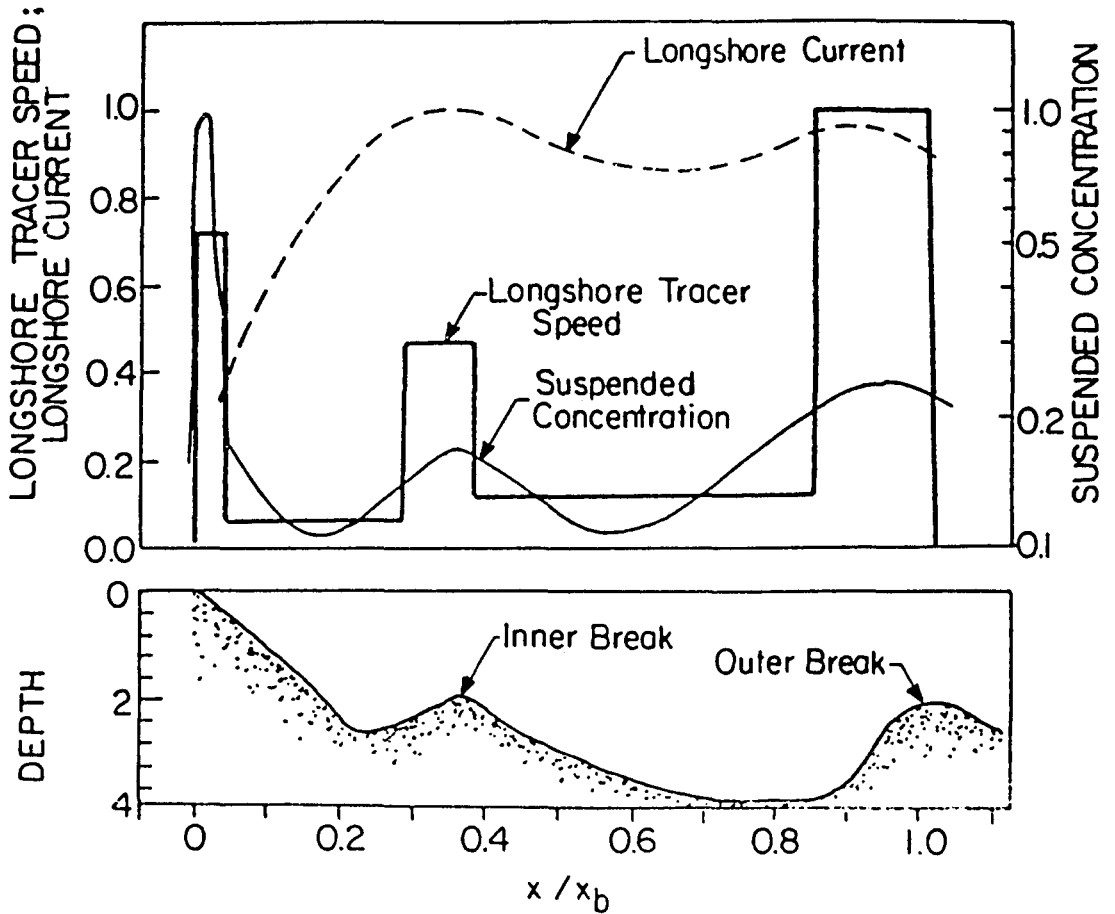


Figure 2-10: Prototype measurement of suspended sediment concentration, longshore current, and tracer advection speed (from Zenkovitch, 1960). Each distribution is normalized by its observed maximum value. Adapted from Walton and Chiu (1979).

Ingle (1966) described a number of fluorescent tracer experiments on prototype beaches which yielded longshore transport distribution profiles similar to those of Zenkovitch, described above.

Thornton (1968) used several 20-cm high traps operated from atop a pier at Fernandina Beach, Florida, to collect the longshore component of sand transport. In general, he found that longshore transport increased

shoreward; and like the previous investigators, he found that greater longshore transport was associated with bars rather than troughs. Thornton rationalized (and substantiated through measurements) that kinetic energy increases shoreward and therefore bed shear and associated mobilization of sediments increases shoreward. Thornton's measurements were limited to the outer portion of the surf zone and excluded mean water depths of less than about half a meter.

Bruun (1969) utilized the same technique as Thornton, but caught fluorescent sand tracer in the traps. Bruun found several dissimilar distributions of longshore transport and, unlike Thornton, observed greater longshore transport in the beach troughs than over the bars. Bruun suggested that this was likely due to an absence of wave breaking over the bars and/or strong tidally-driven longshore currents which were present in the troughs.

Bijker (1971) conducted laboratory experiments where sand transported along a model beach spilled into a cross-shore series of deposition bins located at the extreme downdrift end of the beach. Figure 2-11 illustrates the cross-shore profile of longshore transport derived from the distribution of material deposited in the bins after about 10 hours of testing ( $H_b \approx 16-17$  cm,  $h_b \approx 18-21$  cm,  $T = 1.55$  sec). Bijker indicates that the distribution may be suspect because of transport disturbances caused by the downdrift-end weir over which the sand flowed in order to enter the bins. The longshore current, wave height, and beach profiles 2 m updrift of the bins are shown in Fig. 2-11 and the longshore transport computed from Bijker's model for these conditions is also shown. Bijker reported that the distribution of sand caught in the bins changed with time as the beach profiles slowly evolved: the peak

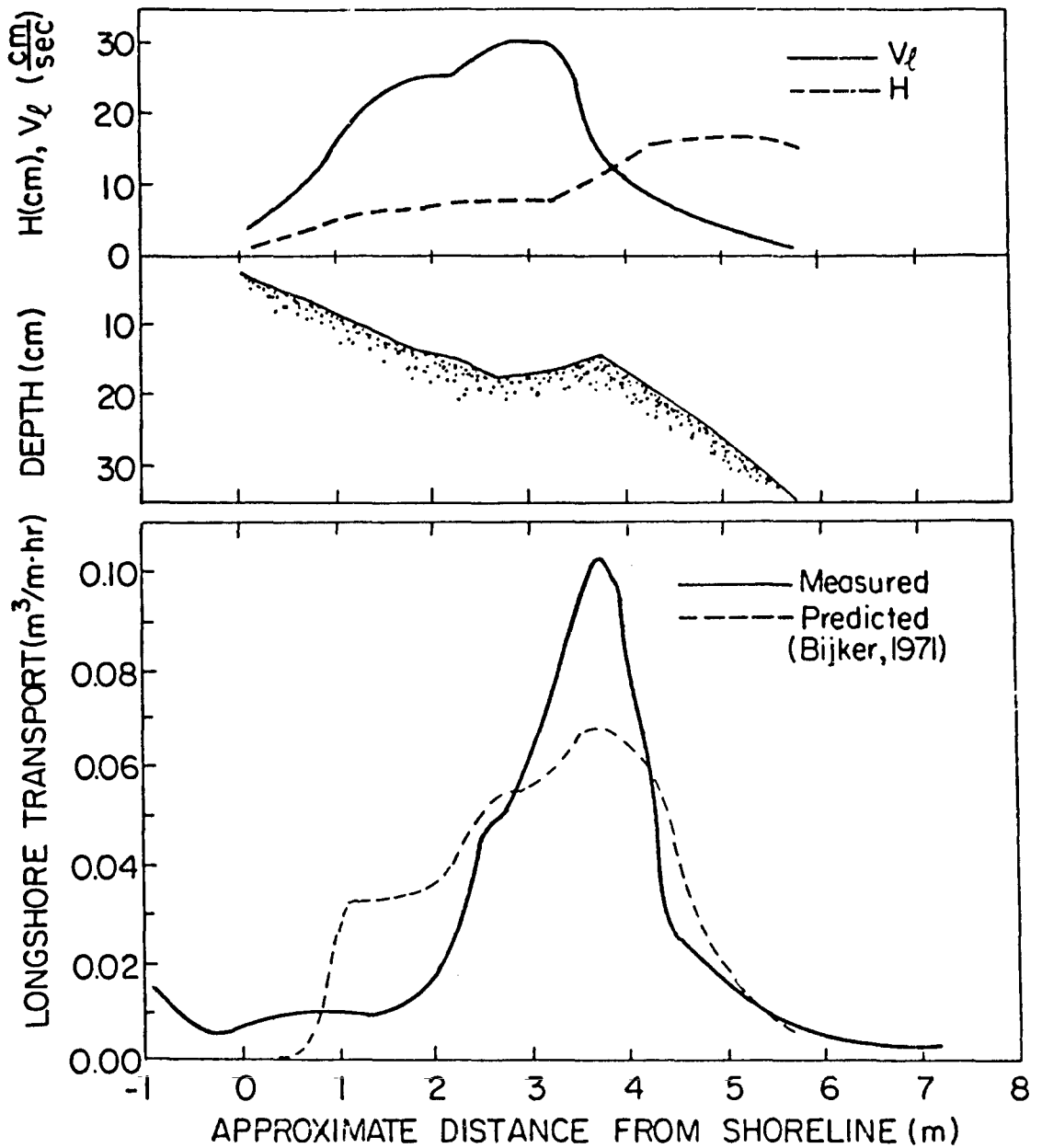


Figure 2-11: Laboratory measurement of distributed longshore transport using downdrift traps. Beach, wave height, longshore current, and predicted longshore transport profiles are shown at 2 meters updrift of traps. Adapted from Bijker (1971).

longshore transport initially occurred seaward of the bar position and gradually moved inside the bar position as the bar became more pronounced. Bijker suggests that this may be attributed to a greater concentration of the longshore current between the shoreline and the bar as the bar grew in relief.

Sawaragi and Deguchi (1978) placed round traps divided into pie-shaped sections into the bed in order to collect sediment transport from several established directions simultaneously. Their findings of the longshore transport and cross-shore transport distributions from two field efforts each at Isonoura and Matsuho Beaches are shown in Figures 2-12 and 2-13, respectively. The approximate values of deepwater wave steepness  $H_o/L_o$  and surf similarity parameter  $\xi_b$ , as calculated by this author, are listed for each experiment. Most notably, the measurements indicate four different longshore sediment transport distribution profiles: (1) maximum in the swash zone (Matsuho-a), (2) maximum towards the shoreline (Isonoura-a), (3) maximum at the breaker line (Matsuho-b), and (4) bimodal with maxima at the shoreline and at the breaker line, (Isonoura-b). In each case, there is significant longshore transport observed above the shoreline, and about 10% to 30% of the total transport is observed seaward of the breaker line. There also appears to be some correlation between the cross-shore and longshore distribution of transport.

From inspection of the beach profile, breaker location, and surf similarity parameter, it is noted that there was a slight terrace landward of the breaker point at Isonoura Beach (b) for conditions of relatively large, spilling waves. Under similar conditions, earlier investigators such as Zenkovitch (1960) found bimodal longshore transport

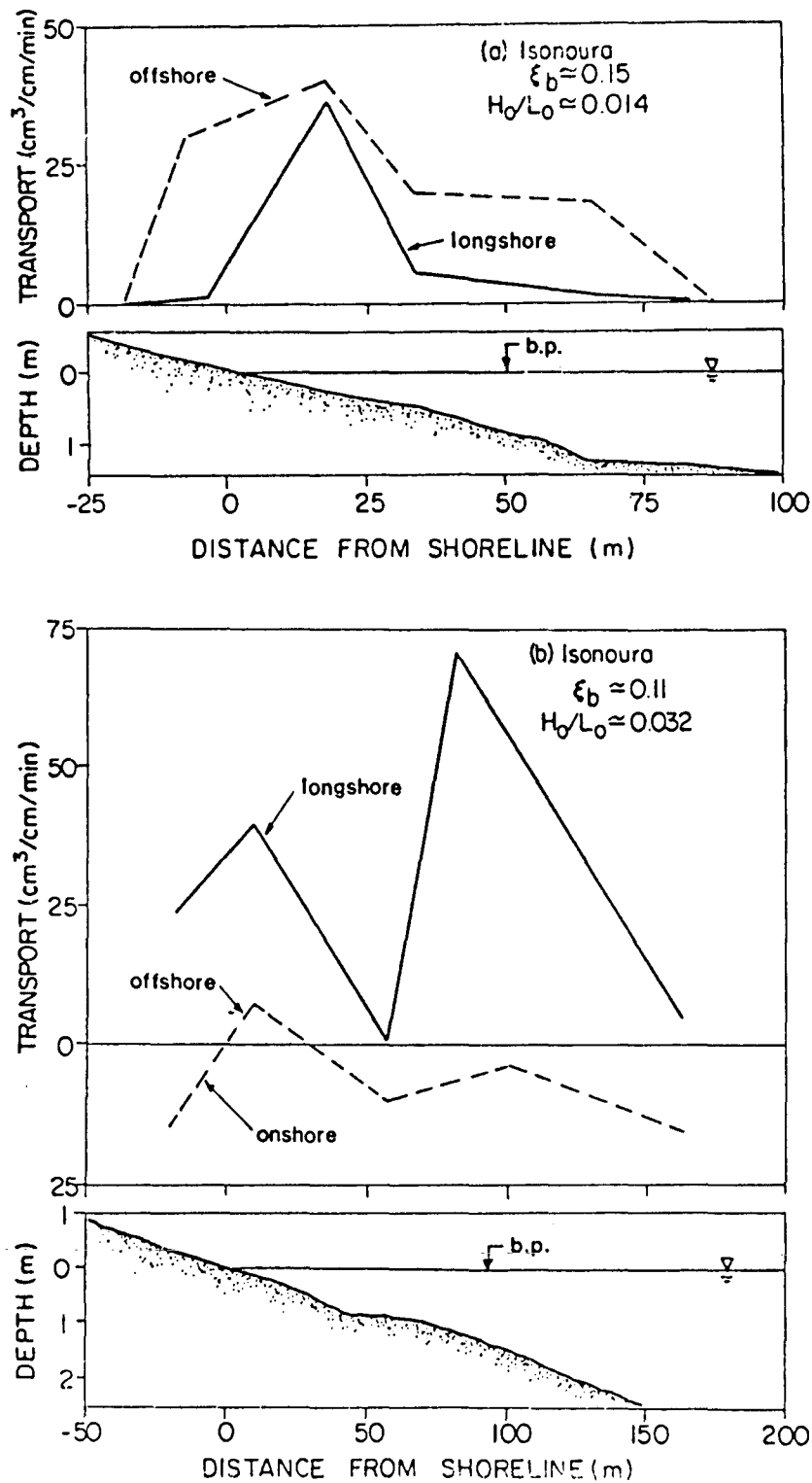


Figure 2-12: Field measurement of distributed longshore and cross-shore transport by Sawaragi and Deguchi (1978) using circular traps in the bed at Isonoura Beach. Adapted from Sawaragi and Deguchi (1978).

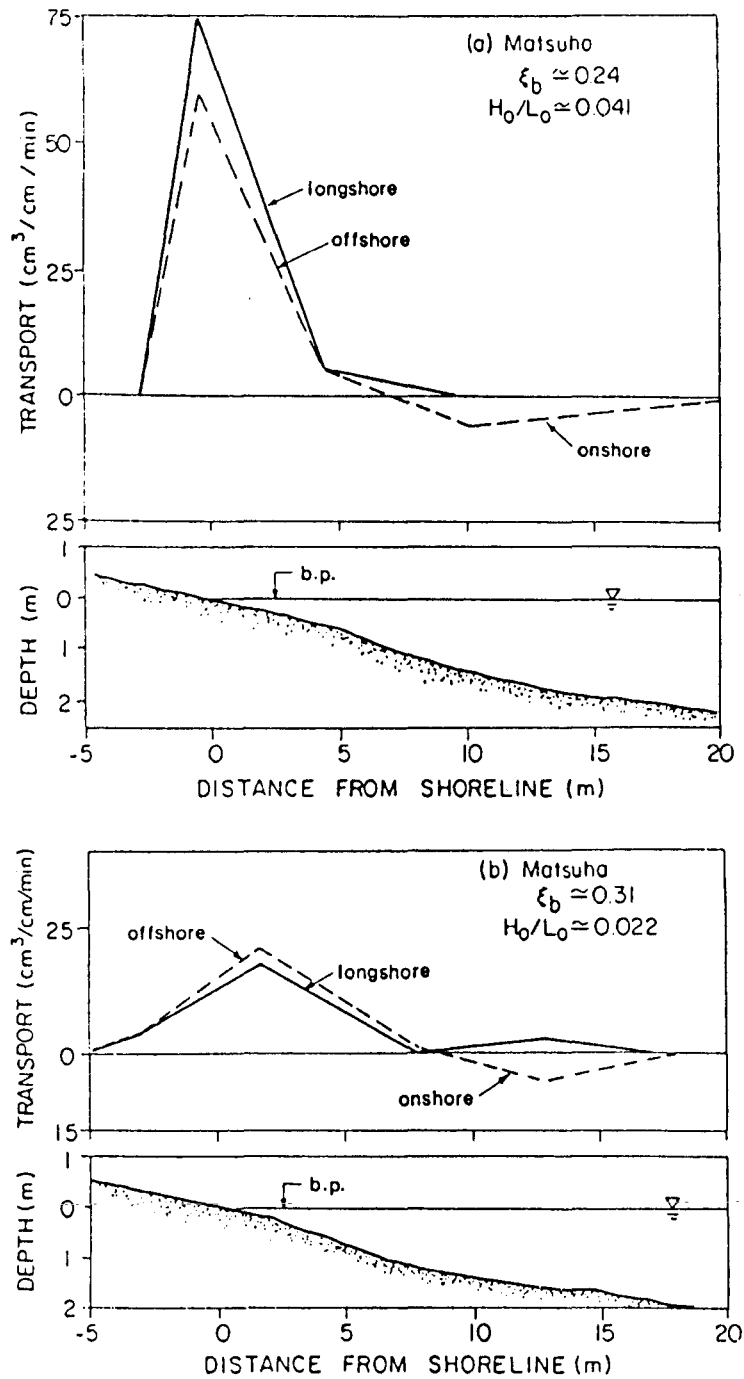


Figure 2-13: Field measurement of distributed longshore and cross-shore transport by Sawaragi and Deguchi (1978) using circular traps in the bed at Matsuho Beach. Adapted from Sawaragi and Deguchi (1978).

distribution profiles similar to Sawaragi and Deguchi's. For Isonoura Beach (a), waves were breaking landward of the terrace and were probably also of a spilling type; the bimodal transport distribution of Isonoura (b) is replaced by a single peak in the inner surf zone. Perhaps this is because the smaller waves of Isonoura (a) broke closer to the shoreline compared to the large waves of Isonoura (b). The surf zone at Matsuho Beach was relatively small and so it is difficult to discuss the distribution of transport. However, it is noted that the waves were likely plunging/spilling almost directly onto the foreshore and, for these cases, the reported swash zone contribution to the longshore transport is significant.

Sawaragi and Deguchi (1978) subsequently used their trapping technique on a movable bed laboratory beach and also measured the cross-shore and longshore components of the bed shear stress on a similar fixed bed laboratory beach. Their findings of the longshore transport distribution profile for two different sediment sizes are shown in Figure 2-14. For each sediment size tested, the normalized distribution profiles,  $q_l/q_{lmax}$ , appear to be essentially independent of the deepwater wave steepness. However, the average location of the peak longshore transport is shifted shorewards within the surf zone for the larger sediment tests relative to the finer sediment tests. Sawaragi and Deguchi similarly found that the distributions of normalized wave height,  $H/H_{max}$ , and longshore current,  $V_l/V_{lmax}$ , were fairly independent of the deepwater wave steepness values tested. The average distribution profiles of these two parameters are shown in Figure 2-15 for comparison to the longshore transport distributions. The laboratory data generally indicate a peak in longshore transport at six-tenths to eight-tenths of

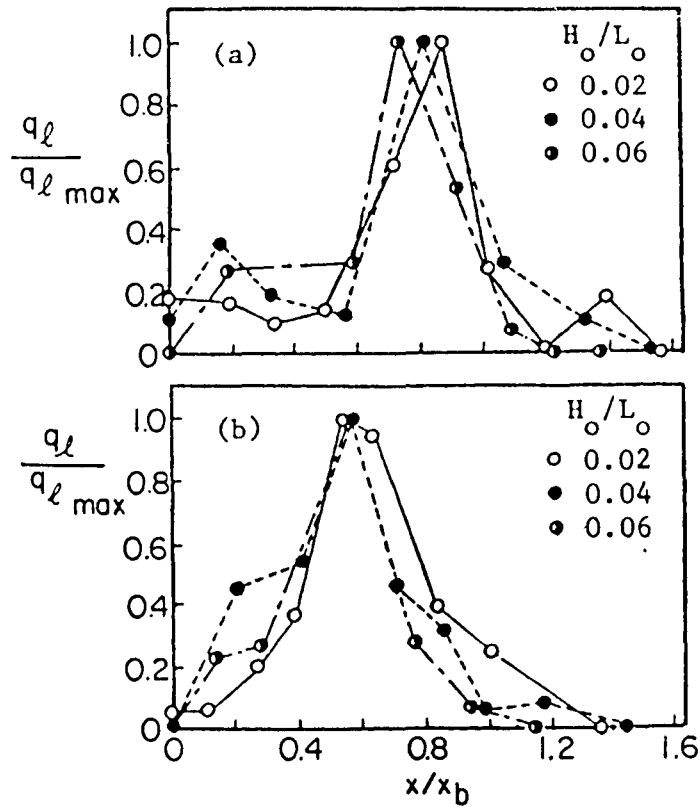


Figure 2-14: Normalized distributed longshore transport from laboratory measurements of Sawaragi and Deguchi (1978); median sand diameter of (a) 0.34 mm, (b) 0.68 mm. Adapted from Sawaragi and Deguchi (1978).

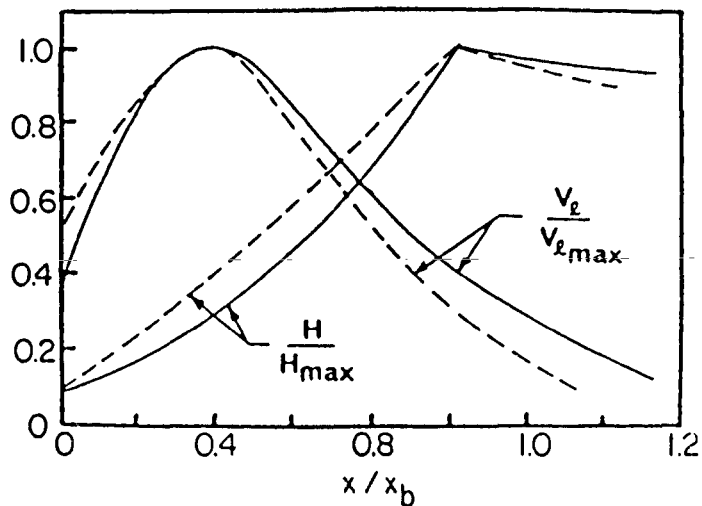


Figure 2-15: Average normalized longshore current and wave height across the surf zone from laboratory measurements of Sawaragi and Deguchi (1978). Solid (broken) curves represent median sand diameter of 0.34 mm (0.68 mm). Adapted from Sawaragi and Deguchi (1978).

the distance from the shoreline to the breaker line with 10% to 20% of the total transport occurring seaward of the breaker line and some unknown (but apparently non-zero) amount of longshore transport above the shoreline. For the finer sediment, the longshore transport at the shoreline,  $x/x_b=0$ , increased with decreasing wave steepness (or increasing surf similarity parameter). The measured laboratory distribution of longshore transport across the surf zone was similar to the measured distribution of cross-shore transport (not shown). This agrees with the field observations.

Tsuchiya (1982) presents one case of distributed longshore sediment transport data from an experimental investigation. His data are shown in normalized form in Figure 2-16, where  $x/x_b=0$  is the mean shoreline location. A primary peak is noted about eight-tenths of the distance from the shoreline to the breaker line. Secondary peaks are noted in the swash zone, inner surf zone, and just outside the breaker line. Details of Tsuchiya's experiment are not known by this author.

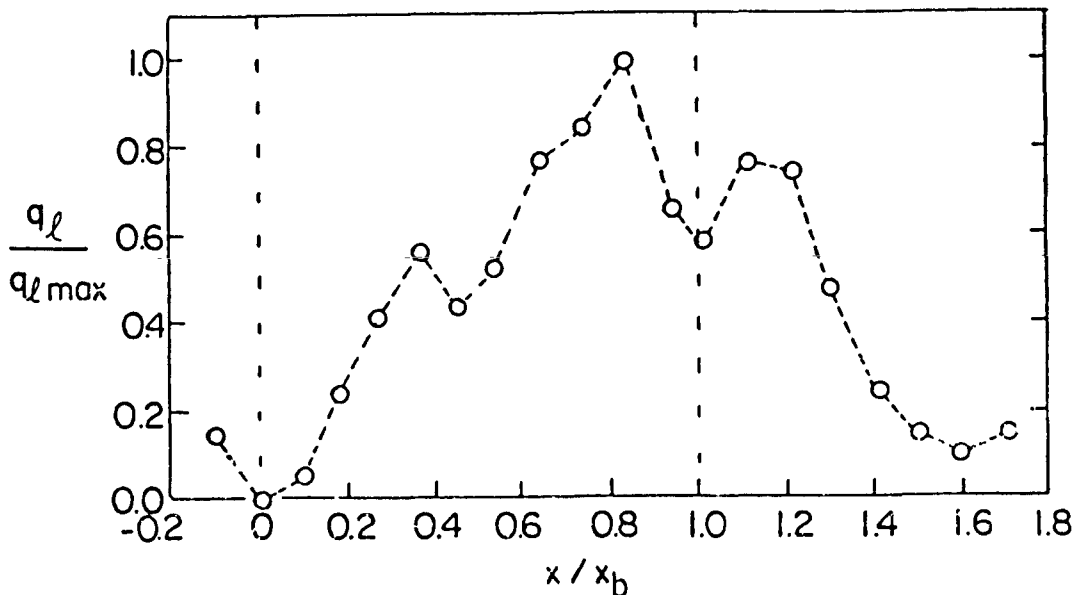


Figure 2-16: Normalized longshore transport distribution as measured by Tsuchiya (1982). Adapted from Tsuchiya (1982).

Berek and Dean (1982) analyzed the rotation of depth contours in a pocket beach (Leadbetter Beach, Sta. Barbara, California) after a change in wave direction. The authors hypothesize that the relative amount of contour rotation can be interpreted as the cross-shore distribution of longshore sediment transport so long as cross-shore transport does not appreciably contribute to the contour changes. The local longshore transport at particular depth contours of interest was calculated over the two-month intervals between surveys through consideration of hourly fluctuations in tide and longshore wave energy flux and, of course, the measured contour changes along the pocket beach between surveys. Berek and Dean's results are shown in Figure 2-17. The local longshore transport has been normalized by the value at the mean shoreline. The authors indicate less confidence in the October to December evaluation because of presumed "leaks" in the pocket beach. Distribution models of three other investigators discussed in the previous section are shown for comparison. These three other predictive models were evaluated over the temporally fluctuating tide and longshore wave energy flux in a manner similar to the evaluation of the original field data. Accordingly, these models' predicted distribution,  $q_l(x)$ , moved across the mean water depths,  $h(x)$ , so that the local longshore transport at the mean shoreline,  $q_l(h=0)$ , for these models was non-zero. Berek and Dean's investigation indicates that longshore transport increases towards the mean shoreline, or at least is greatest in the inner surf zone. The results also indicate significant levels of transport seaward of the presumed mean breaking depth. Swash zone transport is implicitly included in the calculated longshore drift because of the tidal fluctuations; however, it is not explicitly described in Berek and Dean's graphical results.

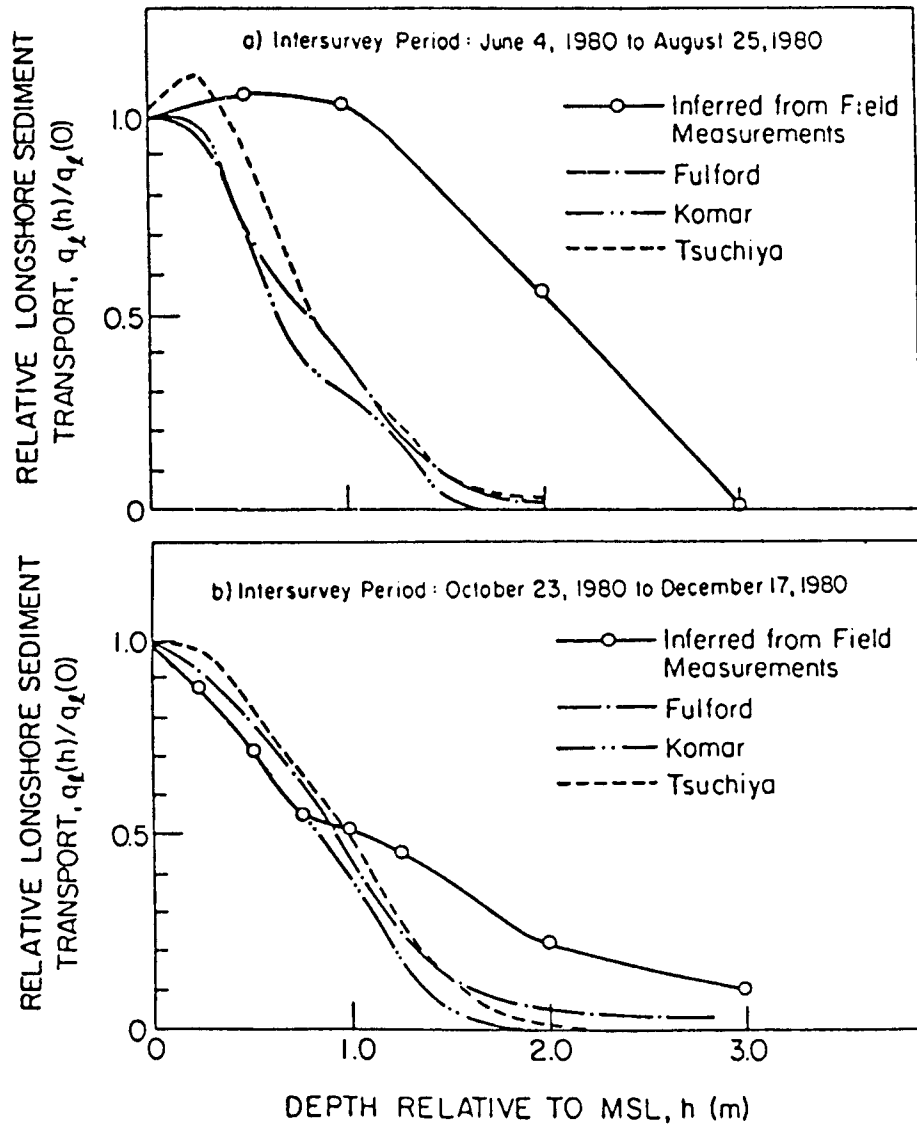


Figure 2-17: Normalized longshore transport distribution developed from relative rotation of depth contours at a pocket beach after a change in wave direction. Dashed lines indicate various predictive model results for the measured prototype surf and tide fluctuations. From Berek and Dean (1982).

From the results of a major field effort using fluorescent tracers, Kraus et al. (1982) identified four basically different longshore transport distributions across the surf zone: (1) generally uniform, (2) bimodal with peaks in the swash and breaker locations, (3) maximum

towards the breaker line, and (4) maximum towards the shoreline. These four different distribution profiles are similar in type to the field results of Sawaragi and Deguchi (1978). The surf similarity parameter,  $\xi_b$ , was approximated by this author for each of the six experiments from which these distribution classifications were derived: type (1),  $\xi_b \approx 0.12$ ; type (2),  $\xi_b \approx 0.11$  to 0.15; type (3),  $\xi_b \approx 0.11$  to 0.23; and type (4),  $\xi_b \approx 0.18$  to 0.35. From these data, a description of the longshore transport distribution based upon surf similarity parameter seems unlikely. However, it is noted that the highest value of  $\xi_b$  (which indicates a greater tendency for wave plunging) is associated with maximum longshore transport near the shoreline (type 4). The reported wave conditions for each of the six experiments considered were mixed spilling and plunging (Sunamura and Kraus, 1985). Kraus et al. suggests that there is no reason to expect a "standard" distribution profile for longshore sediment transport in the prototype given the variability of longshore current distribution across real beaches and given the variability of the dominant mode of sediment transport (i.e., suspended load vs. bedload).

Fulford (1982) examined contour changes updrift of a high-relief groyne after 10 hours of oblique wave attack on a laboratory beach (Savage, 1959). The beach was in only approximate equilibrium with the wave conditions before the test was begun. Fulford's work represents an "impoundment technique" analysis, similar to that used in the present study, where the local longshore sediment transport is calculated through integration of measured profile changes updrift of a shore-perpendicular barrier. From Savage's data, Fulford presented a longshore transport distribution profile as shown in Figure 2-18. The

cross-shore coordinate  $x/x_b=0$  corresponds to the zero-hour still-water shoreline location. The distribution indicates peak longshore transport at  $x/x_b=0.35$  and that 18% of the total transport occurs landward of the setup shoreline location and another 18% occurs seaward of the average breaker location. The updrift limit of barrier effect,  $y^*$ , was found to be about one groyne length (measured from the top of the berm to the toe of the groyne). The surf similarity parameter for Savage's tests was approximately  $\xi_b=0.23$  to 0.28 (using rms wave parameters calculated by Fulford). The nearshore peak in longshore transport agrees roughly with

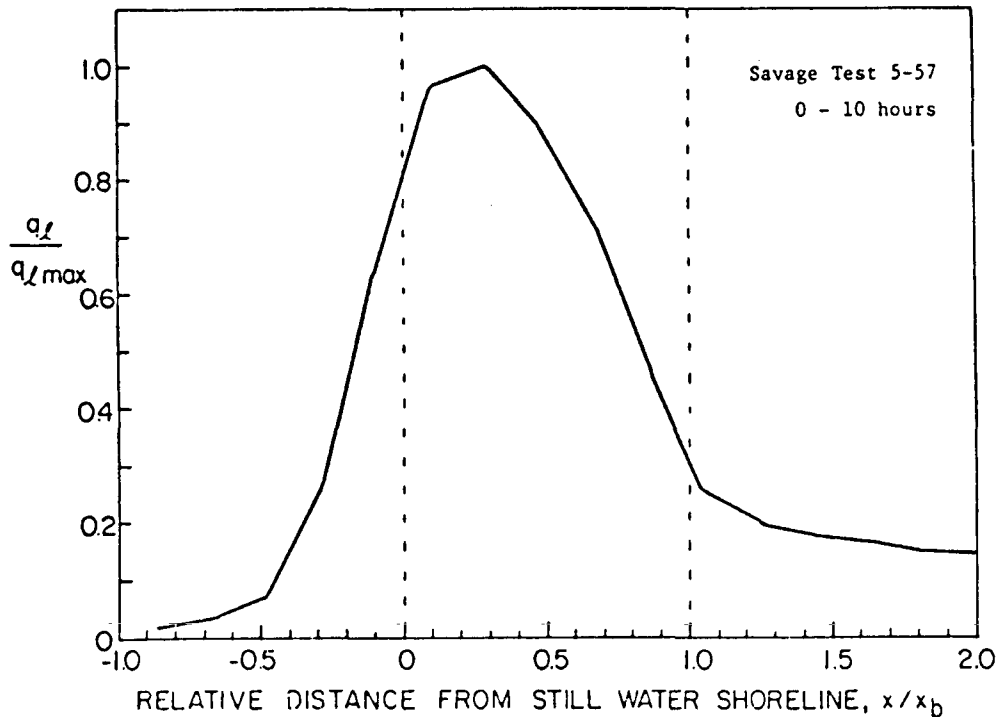


Figure 2-18: Normalized longshore transport distribution developed from sediment impoundment updrift of a barrier on a laboratory beach (Savage, 1959). Approximate breaking position immediately updrift of groyne after impoundment was  $x/x_b=1.3$ . Adapted from Fulford (1982).

with the Sawaragi and Deguchi (1978) and Kraus et al. (1982) field data for this range of the surf similarity parameter.

It is noted that Fulford's distribution does not close to zero seaward of the breaker line. This is partly because the groyne did not extend significantly beyond the breaker line and partly because Fulford did not account for cross-shore transport effects. Specifically, the contours outside of the breaker line shifted considerably seaward during the ten-hour test (out to a depth  $h \approx 2.5h_b$ ). This shift, interpreted by Fulford as a longshore transport signal, was relatively constant across the entire length of the beach and was therefore mostly unrelated to the impoundment of longshore transport by the barrier.

Abdelrahman (1983) evaluated beach profile changes out to wading depths over several stormy days along Leadbetter Beach, Sta. Barbara, California, in order to approximate the distribution of longshore sediment transport. Abdelrahman assumed that cross-shore transport was negligible during the survey period because of the absence of pronounced berms or bars in the profiles. His data analysis technique was based upon that of an impoundment approach; however, this requires that a gradient of longshore transport exists along the beach. It appears that Abdelrahman calculated the mean alongshore gradient in longshore transport and assumed that its distribution was similar to that of the longshore transport. His results, not shown here, indicate considerable shoreline/swash zone longshore transport--or more correctly, considerable longshore gradient in shoreline/swash zone transport.

Downing (1984) and Sternberg et al. (1984) measured vertical sediment concentration profiles simultaneously with the longshore current across the surf zone on natural beaches, and developed local longshore

suspended sediment transport values through

$$\overline{q}_\ell(x) = \overline{V}_\ell(x;t) \int_{-h}^0 c(x,z;t) dz \quad (2.43)$$

where  $c(x,z,t)$  is the local instantaneous sediment concentration profile, and the over-bar indicates time averaging. Figure 2-19 illustrates Downing's findings for a wide, spilling, relatively planar-bed surf zone at Twin Harbor Beach, Washington. The figure depicts the normalized discrete distribution of suspended sediment concentration,

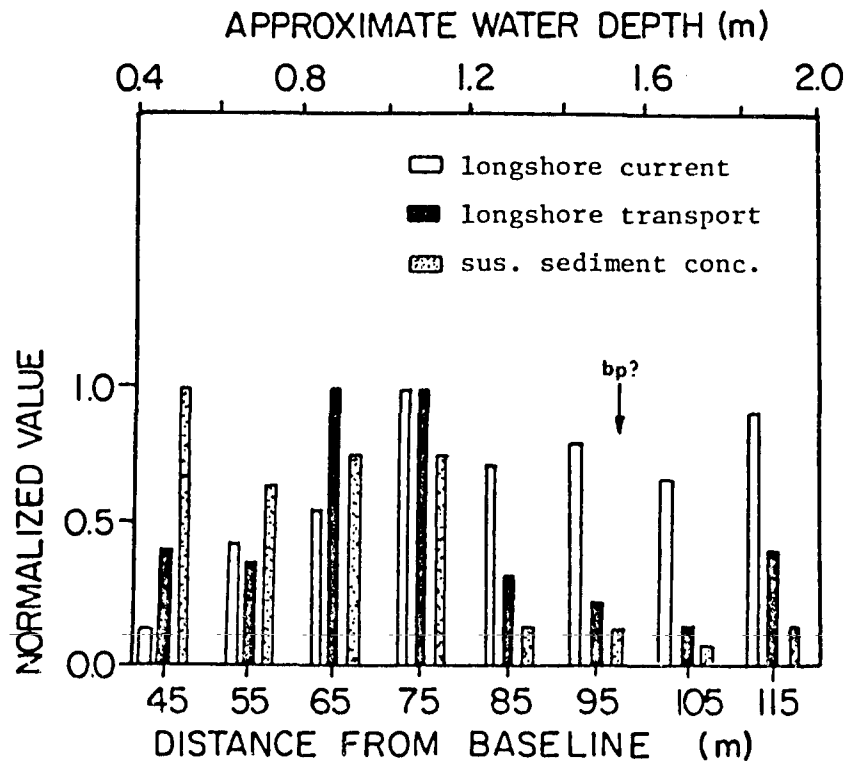


Figure 2-19: Distribution of longshore sediment transport calculated from field measurements of longshore current and suspended sediment concentration. Each quantity is normalized by its maximum value. Adapted from Downing (1984).

longshore current, and calculated longshore transport. Use of Eq. (2.43) with the sediment concentration and longshore current data indicates maximum longshore transport in the mid-surf zone which corresponds to the maximum longshore current. However, the maximum suspended sediment concentrations were found nearshore. Note that the measurements do not include water depths less than about half a meter.

The results of Sternberg et al. (1984), using Eq. (2.43) with field data from Leadbetter Beach, Sta. Barbara, California, are shown in Figure 2-20. The value  $x/x_b=0$  indicates the mean shoreline position.

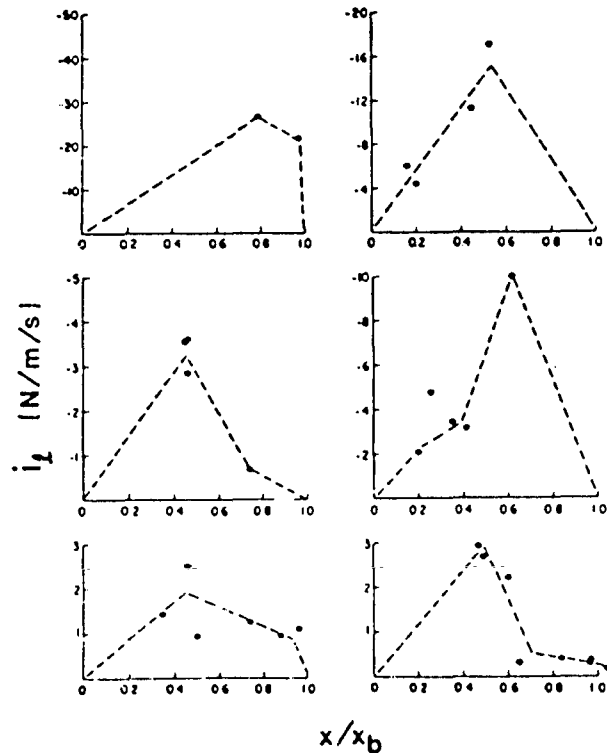


Figure 2-20: Distribution of immersed weight longshore sediment transport calculated from field measurements of longshore current and suspended sediment concentration. From Sternberg, Shi, and Downing (1984).

Cross-shore resolution of the longshore transport distribution is relatively poor and few data points are available near the shoreline. Based upon the investigators' extrapolations for each data set, the maximum longshore transport is located at about the mid-surf position. The authors report that considerable longshore transport was observed in the swash zone but measurements could not be taken in this area.

Equation (2.43) implies that longshore current is uniform through the water column. A more appropriate expression would be

$$q_{\ell}(x) = \overline{\int_{-h}^0 v_{\ell}(x, z; t) c(x, z; t) dz} \quad (2.44)$$

However, neither Downing nor Sternberg et al. measured vertical distribution of the longshore current. Since both investigators found a logarithmic decrease of sediment concentration above the bed, use of Eq. (2.43) could appreciably alter the calculated longshore transport distribution--if the longshore current is not uniform over depth as originally assumed. It is also noted that the work of Downing and Sternberg et al. neglects bedload transport.

Most recently, as part of "DUCK-85," the Coastal Engineering Research Center (CERC) sampled the longshore suspended component of sediment transport using a series of "streamer traps" positioned through the water column and across the surf zone (N. Kraus, personal communication; see also Mason, Kraus, and Holman, 1985). Final results of the data analysis were not available at the time of this writing; however, preliminary results indicate that the greatest transport occurs near the bed and decreases upwards through the water column. Transport was measured above the mean water level as well. Longshore transport was

maximum near the breaker line, very small outside the surf zone, and decreased towards shore despite the presence of a bar close to the shoreline. No measurements were reported for water depths less than about half a meter.

Briefly summarizing this section, distributed longshore transport field and laboratory investigations indicate that (1) significant levels of longshore transport occur above the shoreline (i.e., in the swash zone), (2) contribution of the swash zone transport to the total littoral drift increases as waves break near or upon the foreshore and possibly increases with the surf similarity parameter, (3) about 10% to 30% of the total longshore transport is observed seaward of the breaker line, (4) maximum longshore sediment transport is at least as likely to occur within the shoreward half of the surf zone as within the seaward half of the surf zone, (5) greater longshore drift is often associated with shallower depths (i.e., break-point bars and the shoreline), and (6) field measurements demonstrate great variability in the shape of the longshore sediment transport distribution profile.

#### 2.4 Chapter Summary

Several generalizations can be made regarding longshore sediment transport based upon the literature review presented in this chapter. First, total longshore sediment transport predictive models typically lack sensitivity to the dynamic state of the beach geometry and to the location and/or type of wave breaking. Second, existing distributed longshore transport models predict the maximum transport in the seaward-half of the surf zone for a planar beach. These models neglect swash zone contributions and indicate that transport vanishes at or near the

mean shoreline. Formulation of the transport distribution is most typically taken as the product of the wave orbital motion/longshore current induced bed shear stress (mobilizing parameter) and the longshore current (advection parameter). Third, field (and some laboratory) data often indicate maximum longshore transport in the landward-half of the surf zone and significant levels of transport at and above the mean shoreline. Since the position of the longshore transport maxima predicted by the models for a planar beach often conflicts with the field and laboratory data, one might conclude that the existing models are poor predictors of the longshore transport distribution, and/or that evaluation of the existing models for a planar beach yield poor representations of the actual longshore transport distribution which exists in nature. Fourth, the total longshore transport has been shown to increase with increasing value of the surf similarity parameter (for a given longshore energy flux or radiation stress), and increasing surf similarity parameter values indicate a tendency for plunging or surging (collapsing) wave breaking. Some of the available observations and data suggest that near-shoreline and/or swash longshore transport dominates for plunging and surging (collapsing) conditions. Since plunging and collapsing breakers are associated with both greater total longshore transport and near-shoreline/swash transport, near-shoreline and/or swash transport must be quite significant. In any case, from the data, the longshore transport distribution profiles appear to be related to the beach profile geometry and possibly to the type and/or location of wave breaking.

## CHAPTER 3

### FIELD INVESTIGATION: EXPERIMENTAL METHOD AND DATA PRESENTATION

#### 3.1 Introduction

An intensive field measurement effort was undertaken at the Coastal Engineering Research Center (CERC) Field Research Facility (FRF) at Duck, North Carolina, over the period July 16 through October 2, 1984, to collect data which describes the impoundment of longshore sediment transport against a shore-perpendicular barrier rapidly deployed across an initially undisturbed beach, as well as relevant nearshore surf and sediment data. The following pages describe the techniques utilized to impound and measure the littoral drift. Beach profile, surf, and sediment data collected during the impoundment experiments are also described. A detailed description of the FRF experiment site is offered in Birkemeier et al. (1981).

#### 3.2 Experimental Method

##### 3.2.1 Overview

For each impoundment experiment, a shore-perpendicular sand-bag groyne was constructed approximately 150 meters south of the FRF pier. Visual inspection indicated that the beach and surf south of this location were relatively free of pier effects for wave events from the south. Although execution of the experiment much further from the pier

may have reduced further pier effects upon the investigation site, field operation within 150 to 300 meters of the pier greatly facilitated effective data collection. Beach profiles in the vicinity of the groyne were usually surveyed before and after groyne deployment (over one or two tide cycles). It was intended that these beach profiles over time and space would indicate the total volume of sediment impounded against the barrier as well as its distribution across the surf zone. Coincident with the post-groyne-construction beach profiling, measurements were made of the local longshore current and wave height at three locations across the surf zone, sediment samples were taken updrift and downdrift of the groyne, and tidal water level changes and breaking wave angle were recorded.

### 3.2.2 Groyne Construction and Removal

The site whereupon each groyne was constructed was marked by two ropes, separated by about 2.5 meters, which stretched from the top of the berm to well past the low-tide breaker line. The groynes were built using a series of sand-bag units laid end to end. Each sand-bag unit was tied between the two shore-perpendicular ropes in order to hold it in place while it was filled. The bags were filled by pumping slurry from approximately 8 m downdrift of the groyne using a 600 gallon-per-minute pump with 10-cm hard-rubber suction hose and 10-cm flexible PVC discharge hose. During filling, small slits were cut about the bags to relieve the back-pressure caused by the great volume of slurry water which was pumped into the bags. Filter cloth (Filter-X material) was placed underneath the sand-bags on the foreshore in order to prevent these bags from "jetting" and sinking into the soft, dry berm sediment

during pumping. Repetitive surveys of the groyne over a several day period indicated that the groynes did not appreciably sink into the bed after construction.

It was discovered that pyramid-shaped sand bag units were best suited for an optimally high and quickly built groyne. Three long cylindrical bags were sewn together in a triad to form a pyramid (Figure 3-1). Each bag was 3.7-meters long and 30 to 50 cm in diameter. (Larger diameter bags did not fill well and slumped to the same height as the 50 cm diameter bags.) The top bag in the pyramid overhung the bottom two bags by 1.2 meters. In this way, the groyne could be built in a brick-laying fashion: the bottom bags were placed end-to-end to their upshore neighboring bags while the top bag overlaid the seaward 1.2 meters of the neighboring upshore bags. Each bag was filled from its landward end so that the landward ends were always well-filled compared to the seaward ends. The "brick-laying" style of construction ensured a more consistent groyne height because the landward (well-filled) ends of the top bags compensated for the poorly-filled seaward ends of the neighboring upshore bottom bags.

Each individual bag in a pyramid unit was constructed from a sheet of Filter-X material sewn into a tube shape. Circular pieces of Filter-X were sewn onto the ends of the tube shape. A 30-cm overlap was sewn into the tube shape and was termed the "flap" (Figure 3-2). The flap served as a secondary or false ceiling to the inside of the bag. A slit was cut across the top of the tube above the flap and another slit was cut across the flap just below and slightly seaward of the top slit. These two slits allowed entry of the discharge hose through which the slurry was pumped. When the bag filled, the flap and the top surface of

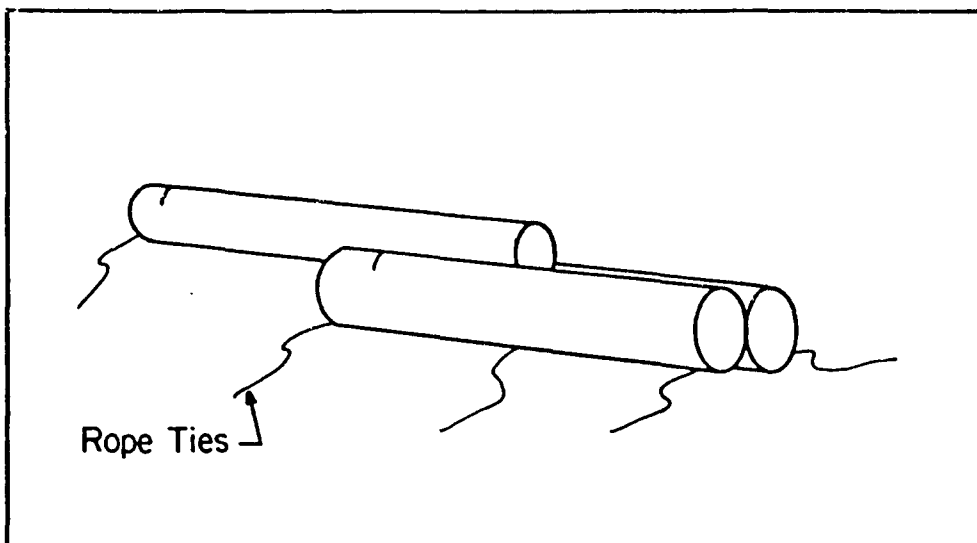


Figure 3-1: The pyramid-shaped sand bag unit (not to scale).

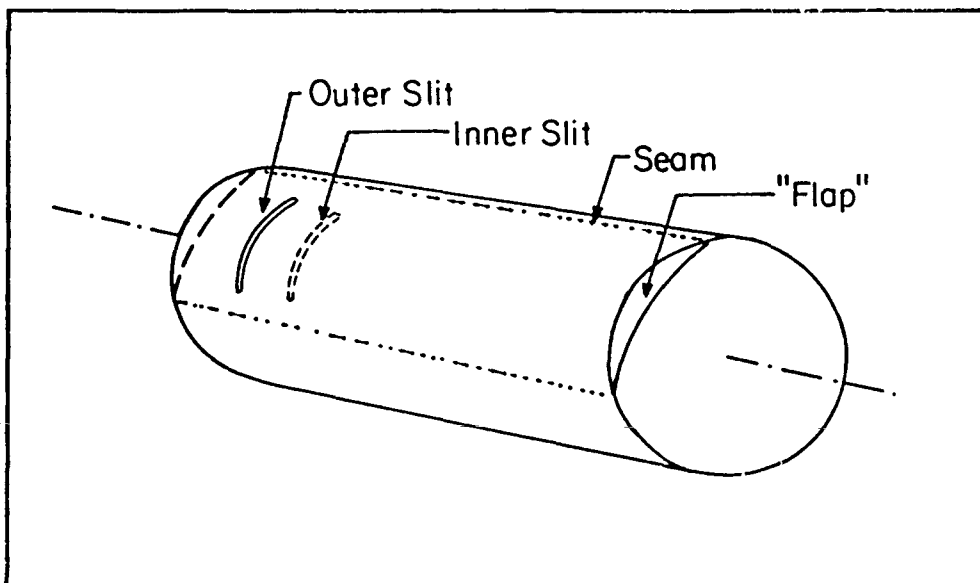


Figure 3-2: An individual sand bag showing the fill-flap design. (End pieces not shown).

the tube tightened together due to the weight of the sand pushing out on the side walls of the tube. This served to close the bag and prevented sand from leaking out of the slits. (It was important to almost completely remove the discharge hose from the slits before the flap tightened or else risk locking the hose inside the bag.) One-meter long rope ties were sewn into the seams of the bags in order to secure the bags while filling them on the beach face. The bags were stitched with an industrial hand-held sewing machine using nylon-cotton thread. Photographs of two groynes constructed with the pyramid-style units are shown in Figures 3-3 and 3-4. Appendix A further details the construction of the sand bags.

The removal of the barrier after each experiment must be seriously considered during the planning phase of the field effort. The updrift impoundment as well as the relatively low wave activity required for the execution of the experiments almost completely buried the groyne several days after each experiment. This made immediate groyne removal all but impossible. For this investigation, the top of the bags were slit open and/or removed. Attempts at jetting the sediment out of the opened bags proved fruitless. Instead, the remains of the bags were left to await the action of erosive waves which quickly and effectively freed the bags and swept the groyne site clear. The floating remains of the bags were then retrieved by hand when possible.

### 3.2.3 Profiling Techniques

A survey baseline was laid at the base of the primary dune parallel to and 71.65 m seaward of the FRF baseline. Stations were established along the baseline at 9.15 m spacing, (Figure 3-5). Standard level,



Figure 3-3: Groyne #3 at low tide.  
Photo by D. Cronin.



Figure 3-4: Groyne #4--looking landward from updrift side at mid-tide. Photo by K. Bodge.

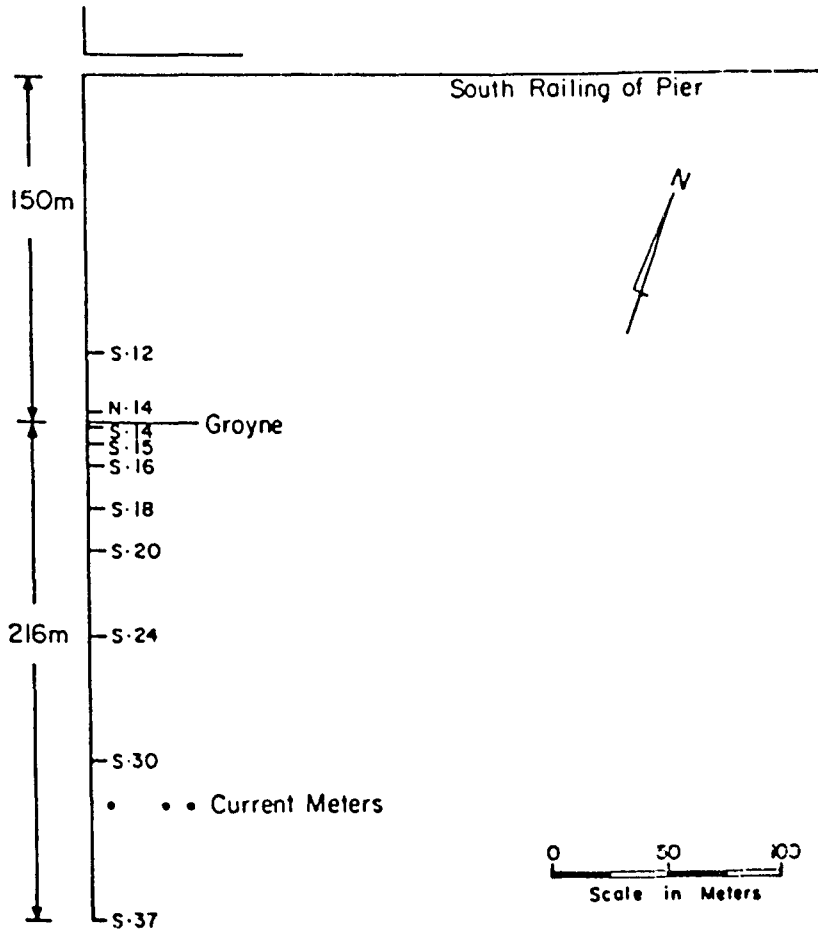


Figure 3-5: Typical survey plan for the field impoundment experiments.

chain, and rod-man survey techniques were generally used for the pre-groyne construction surveys. An OMNI Total Station Transit was used for the night surveys. After dark, chemical light sticks were attached around the OMNI prism to aid the transit operator in locating the rod-man in the surf. Light sticks were also used as range markers for the rod-man and to highlight hand-signal communication between the OMNI operator and the surf and beachface workers. The bullet site on the OMNI was back-lit by a 12-V lamp in order to aid OMNI targeting. Most of the surveys were executed to 1.5 meter water depths. During the last impoundment experiment, the FRF's Coastal Research Amphibious Buggy

(CRAB) extended the profiles by making two shore-parallel transects seaward of the rod-man's maximum offshore location.

Several surveys were made to test the repeatability and accuracy of the OMNI survey system. Average vertical profile error was 1.5 cm and the maximum error was approximately 4 cm.

#### 3.2.4 Groyne Deployment and Profiling Procedure

It was found that the most effective impoundment measurements could be made when the groyne construction began at the berm, just above the swash zone at high tide, and followed the falling swash zone through low tide. Then, after a one to two hour lapse (while the pumping equipment was secured and the survey gear deployed), beach profiling commenced as the tide rose such that the waves were breaking within the end of the groyne and the groyne extended completely across the surf zone. Beach profiling continued until the wave break migrated back outside (seaward) of the end of the groyne on the subsequent falling tide. In general, one loop of profiles was taken on the rising tide (just after the break moved inside the end of the groyne) and another loop was taken on the falling tide and completed just as the break moved back outside the end of the groyne. This resulted in two sets, or loops, of profiles which described the sediment impoundment across the entire surf zone during the high water portion of the tidal curve. Each loop of profiles typically consisted of ten survey lines--2 downdrift, 6 within the trap, and 2 "control" lines well updrift of the groyne. Spacing along the beach between profile lines typically increased from about 9 m near the groyne to about 60 m far updrift of the groyne. Usually, a complete loop of profiles was also taken in the early morning or afternoon just

before or during each groyne deployment. The elevation along the top of each groyne was surveyed immediately after each experiment.

### 3.2.5 Additional Measurements

Longshore current. Eulerian measurements of longshore current were made at three locations across the surf zone approximately 185 meters updrift of the groyne. Impellor-type current meters (aligned shore-parallel) were mounted close to the bed on 5-cm diameter jettied steel pipes. The data from each of the three current meters were recorded by strip chart for 5 minutes once or twice an hour during the post-groyne-construction profiling. Each current meter was calibrated in the laboratory under steady flow conditions prior to the summer's field work. The current meter amplifiers were typically set with a 10-second response time in order to dampen short period gravity wave fluctuations.

Waves. Estimates of wave height and one-dimensional spectra were available for the entire period of each experiment from Baylor gauges located underneath the FRF pier. Directional spectra data were available from the FRF P-U-V directional wave gauge located south of the end of the pier for the duration of each experiment. Observations of wave type and height within the surf zone were made by visual reference to red-and-white 15-cm graduated marks on the steel pipes which supported the current meters. High-frequency (HF) radar imagery was utilized to identify the breaker angle near the shoreline.

Sediment. Hand-grab surface sediment samples were collected near the end of each experiment. Typically, samples were taken at three to five cross-shore locations updrift and downdrift of the groyne.

### 3.3 Description of the Experimental Conditions

#### 3.3.1 Overview

Four groynes, comprising four separate experiments, were established during the period July 16 through August 30, 1984. (An attempted groyne deployment on September 26 was aborted due to dangerous surf conditions and the sudden appearance of an unexpected northeasterly storm.) The individual experiments will be referred to as Groyne #1, #2, #3, and #4. A summary of each of the four experiments is presented in Table 3-1.

Of the four experiments conducted, the last two were by far the most successful. The pyramid-style "brick-laying" bag deployment system was developed for these experiments which enabled the rapid construction

Table 3-1: Summary of Field Experiments

EXPERIMENT NO.	#1	#2	#3	#4
TOTAL # PROFILE LOOPS	3 1 POST-DEPLOYMENT 1 MIDNIGHT-(PARTIAL) 1 NEXT MORNING	4 1 POST-DEPLOYMENT 2 MIDNIGHT (PARTIAL) 1 NEXT MORNING	3 1 PRE-DEPLOYMENT 1 RISING TIDE 1 FALLING TIDE	5 1 PRE-DEPLOYMENT 1 RISING TIDE 1 FALLING TIDE 1 RISING TIDE 1 FALLING TIDE
SURF ZONE WAVE HEIGHT AND POSITION OBSERV.			✓	✓
CURRENT DATA	1 DYE STUDY		2 1/2 CURRENT METERS	3 CURRENT METERS
SED. SAMPLES		✓	✓	✓
TRACER STUDY			✓	
HF RADAR DATA	✓	✓	✓	HIGH-QUALITY ✓
COMMENTS	Low groyne. Longshore features. Profiling loops not tied to tidal cycle.	Low groyne. Deployed on rising tide. Profiling loops not tied to tidal cycle.	High-quality.	High-quality.

of a high-relief groyne with negligible gaps. Additionally, these two experiments represent the most complete set of data consisting of all supplementary measurements listed above. The first two impoundment experiments were of relatively poor quality since field procedures were still under development. These experiments did not employ the pyramid-style groyne system, nor was the groyne deployment and survey sequence coordinated with the tide. Accordingly, the groynes were of smaller relief and considerable impoundment occurred during construction.

Each experiment was executed when the beach site was fairly regular and surf conditions were acceptably small and steady. In the summer months along North Carolina's Outer Banks the most consistent wave events are small (less than about one meter breaking height), of moderate period (7-9 seconds), and arrive at a relatively steady and significant angle from the south (breaking angles between  $5^{\circ}$  and  $15^{\circ}$  to the shoreline). These conditions--most favorable for the experimental procedures described herein--result from a high pressure system over the north Caribbean which dominates the southeastern U.S. coastal weather pattern during the summer. Tropical storm activity (including Hurricanes Gloria and Isadora), as well as unexpected squalls from the northeast, interrupted the ideal southerly wave climate for days or weeks at a time. In general, however, the summer beach contours at the FRF experiment site adjust to the dominant southerly wave climate; the shoreline builds south of the FRF pier and recedes north of the pier. Figure 3-6 illustrates typical nearshore bathymetry at the FRF during the impoundment experiments. During the intensive beach profiling intervals after groyne deployment, no longshore features (such as beach cusps) were observed in the study area with the exception of Groyne #1.

Of possible interest, however, was a cusp field (18 to 26 m wavelengths) which typically appeared about 24 hours after each groyne deployment and extended updrift from a location beginning about five groyne-lengths from the groyne. It was not clear whether the appearance of these cusp fields was related to the presence of the groyne.

All of the experiments reported herein were executed during the "ideal" southerly wave events described above. The approximate surf conditions for each experiment are listed in Table 3-2. The values in the table represent a synthesis of visual observation, Baylor gauge wave

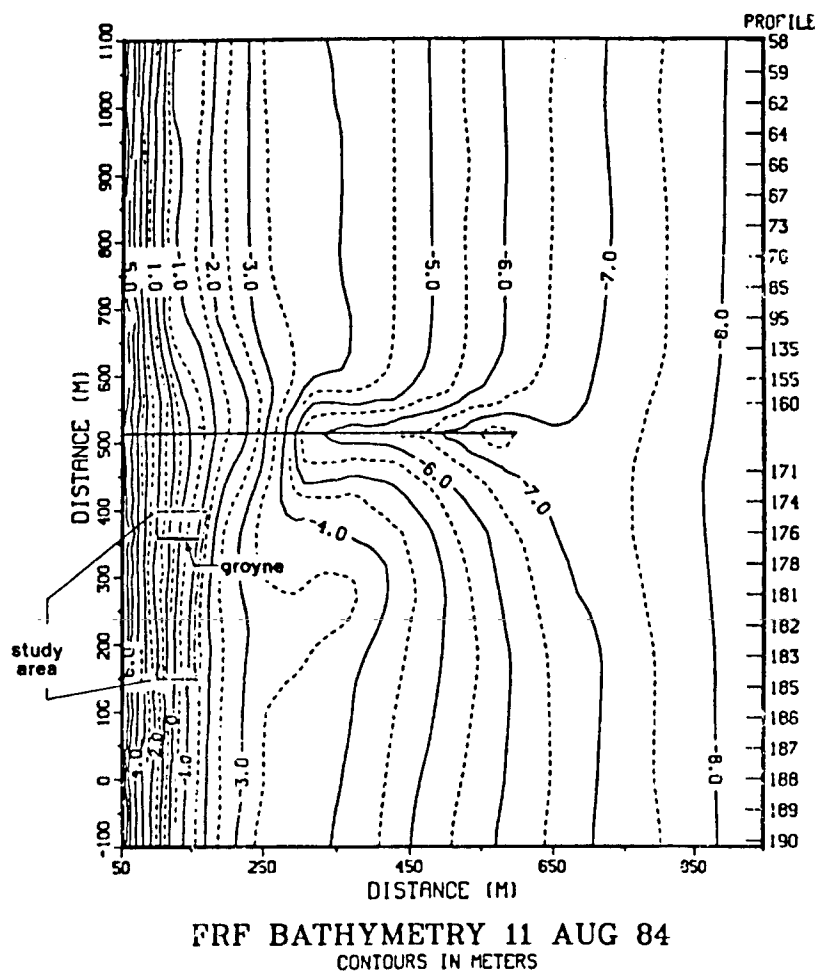


Figure 3-6: Typical nearshore bathymetry at the field investigation site during the impoundment experiments. Courtesy of CERC Field Research Facility, Duck, N.C.

data from the FRF pier, HF radar imagery, tidal data, and beach profile data. The surf parameters listed most closely correspond to significant values typical for each experiment. Figure 3-7 illustrates the time series of (unrefracted) significant deep water wave height and modal wave period for each of the experiments, as determined from Baylor gauges along the pier. Hourly estimates of breaking wave angle (taken from HF radar imagery) were available only for Groyne #4, and are illustrated in Figure 3-8. Figures 3-7 and 3-8 indicate that the directional wave events were quasi-steady for each impoundment experiment (with the

Table 3-2: Representative Surf Conditions  
for Field Experiments (1984)

Exp't. & Date	$H_b$ (m)	$h_b$ (m)	$\alpha_b$ (deg)	T (s)	$H_o'$ (m)	$m_f^1$	$m_b^2$	$R^3$ (m)	$\xi_b$	brkr type
Groyne#1 7/27-28	0.65	0.82	5	8.1	0.37	0.075	0.035	0.8	0.44	PL
Groyne#2 8/03-04	0.52	0.64	6-7	9.0	0.27	0.072	0.038	1.0	0.59	PL/SP
Groyne#3 8/19-20	0.60	0.78	5-6	9.0	0.37	0.085	0.042	1.0	0.61	PL
Groyne#4 8/29-30 0900-0500	0.60	0.95	7-8	8.1	0.36	0.077	0.029	.85	0.38	SP/PL
Groyne#4 8/29-30 0900-1500	0.45	0.70	5-6	8.2	0.24	0.077	0.030	.85	0.46	~ PL

- 
- 1 foreshore bed slope
  - 2 typical breakpoint bed slope
  - 3 average maximum vertical runup
  - 4 PL=plunging, SP=spilling

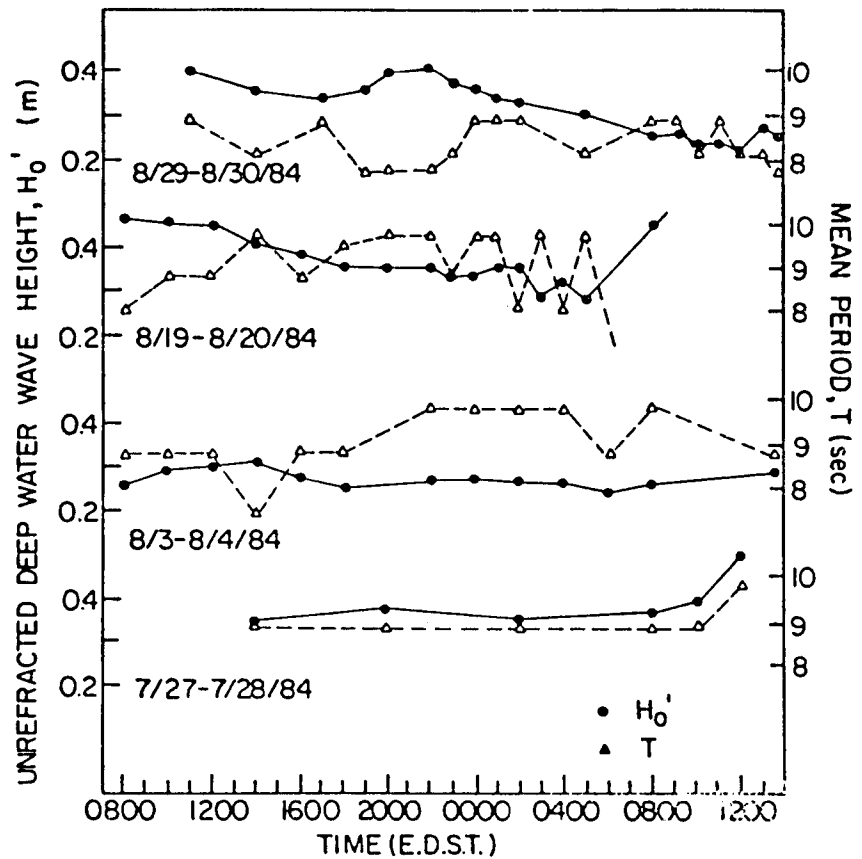


Figure 3-7: Approximate modal wave period and significant (unrefracted) deep water wave height during the four field experiments.

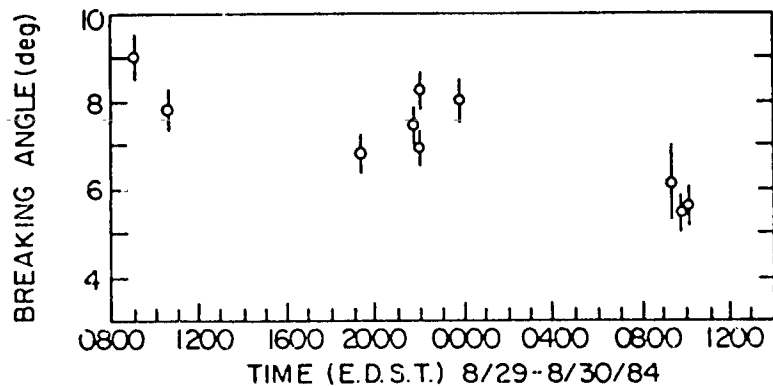


Figure 3-8: Breaking wave angle estimated from HF radar imagery during the fourth field experiment (Groyne #4). Values represent the angle between the breaking wave and the shoreline (incidence from the south).

possible exception of Groyne #4--for which the directional energy was somewhat less during the second impoundment interval than during the first). The portions of the beach over which the groyne deployment and surveying were executed were relatively monotonic for each experiment and were characterized by a planar foreshore and a slightly concave-up shape seaward of the low-water line. The raw beach profile data collected during the last three experiments are tabulated in Bodge and Dean (1985).

Meteorological data were collected routinely by the FRF during each experiment. Wind and precipitation were light to negligible, and no drastic changes in atmospheric pressure or temperature occurred during any of the deployment or impoundment stages of the experiments.

Each of the groynes extended from the maximum extent of high tide run-up to about 5 meters seaward of the low tide still water shoreline (i.e., about one bag-diameter below the low tide mean water level). The groynes were between 30 and 47 meters in length. The average relief above the bed of the pyramid-style barriers (Groynes #3 and #4) was about 40 cm. The average relief of the first two barriers (Groynes #1 and #2) was about 25 cm. Construction of each groyne required the pumping of 70 to 120 tons of sediment and was usually completed in an 8-hour period between 0900 and 1700 E.D.S.T. by this author and three to four other field hands. This same field crew also executed the round-the-clock beach profiling and wave/current measurement tasks subsequent to each groyne deployment. The work was extremely intense, exhaustive, and often dangerous. The success of these experiments is directly attributable to the competent and dedicated efforts of the seemingly tireless field hands who assisted this author.

### 3.3.2 Groyne #1

The first impoundment experiment, Groyne #1, was viewed as a qualitative success inasmuch as a reasonable barrier was deployed in a short period of time and updrift impoundment was observed. Beach profiles updrift of the groyne taken just after and approximately 15 hours after groyne deployment are shown in Figure 3-9. The integrity of the barrier and the quality of the surveys associated with Groyne #1 are suspect, and the presence of a cusp field beginning about 60 meters updrift of the groyne precluded the use of far-updrift profiles as a cross-shore control signal. Accordingly, the data collected from this experiment will not be discussed quantitatively. It is noted, however, that accretion immediately updrift of the barrier was centered about the upper foreshore.

### 3.3.3 Groyne #2

Construction of the second groyne utilized single, large diameter sand bags laid end to end, and was initiated below the low-water shoreline on a rising (lunar apogean) spring tide. The tide rose more swiftly than the sand bags could be deployed, and so a gap in the groyne construction resulted when pumping activity was forced to move upshore. The upper portion of the groyne was then deployed along and above the rising water level and completed as the tide crested. Bags at and above the upper swash zone which were not placed upon a filter cloth sheet settled into the bed from the jet-like action of the slurry pumped into the bags. While waiting for the tide to fall so that the gap in the groyne could be closed, impoundment rapidly occurred against the portion of the groyne which was already constructed. The impoundment

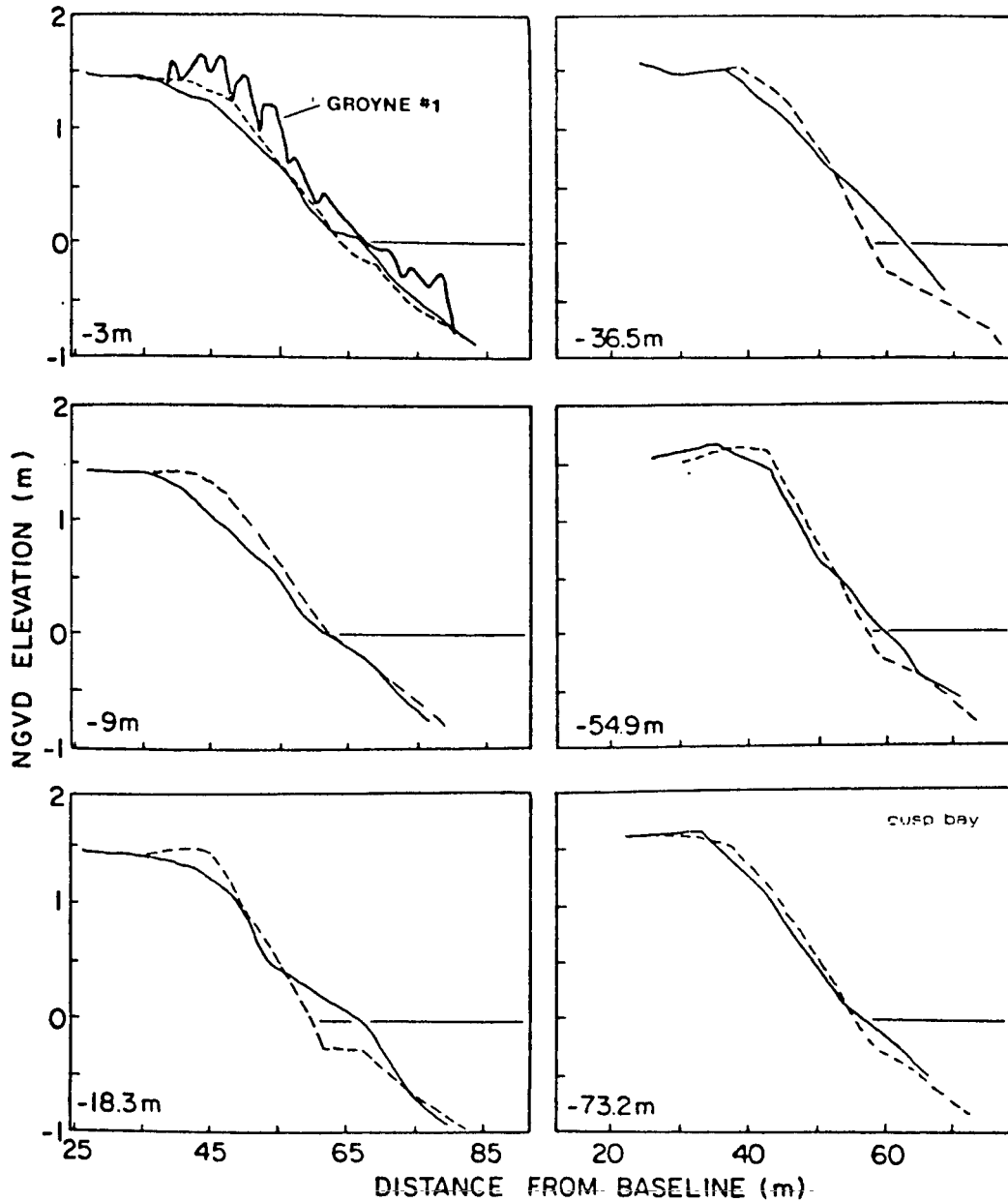


Figure 3-9: Beach profiles 2 hours (solid lines) and 15 hours (broken lines) after deployment of Groyne #1. Relative location updrift of groyne is indicated for each pair of profiles.

was most prominent in the upper swash zone where sediment was observed to accrete against the groyne at a vertical rate of about 2 mm/minute. Single beach profiles were executed up- and downdrift of the groyne during this period. As the tide fell, the gap in the groyne was closed

and additional bags were laid atop the remainder of the groyne, where possible, to make up for the barrier relief which was lost due to impoundment during high tide. Figure 3-10 illustrates the groyne deployment sequence and tidal fluctuation for Groyne #2. It became obvious that the groynes must be deployed starting at the berm and following the tide falling down the beach.

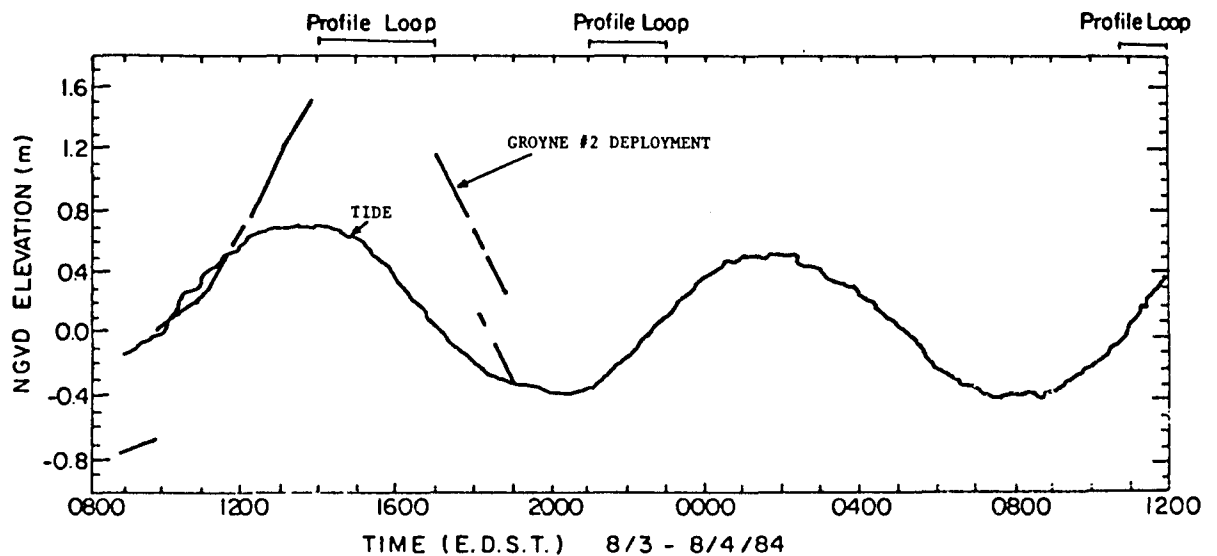


Figure 3-10: Tidal fluctuation, beach profiling "loop" intervals, and groyne deployment sequence for Groyne #2.

The profile of the completed groyne is shown in Figure 3-11 relative to the beach profiles immediately updrift and downdrift of the groyne during construction and sixteen hours after completion of the groyne. Several beach profiles measured updrift and immediately downdrift of the groyne during these two times are shown in Figure 3-12 a and b. In the figure, each profile has been horizontally displaced such that the profiles just above maximum uprush (i.e., at and behind the berm) are aligned. This is necessary for direct profile comparison along

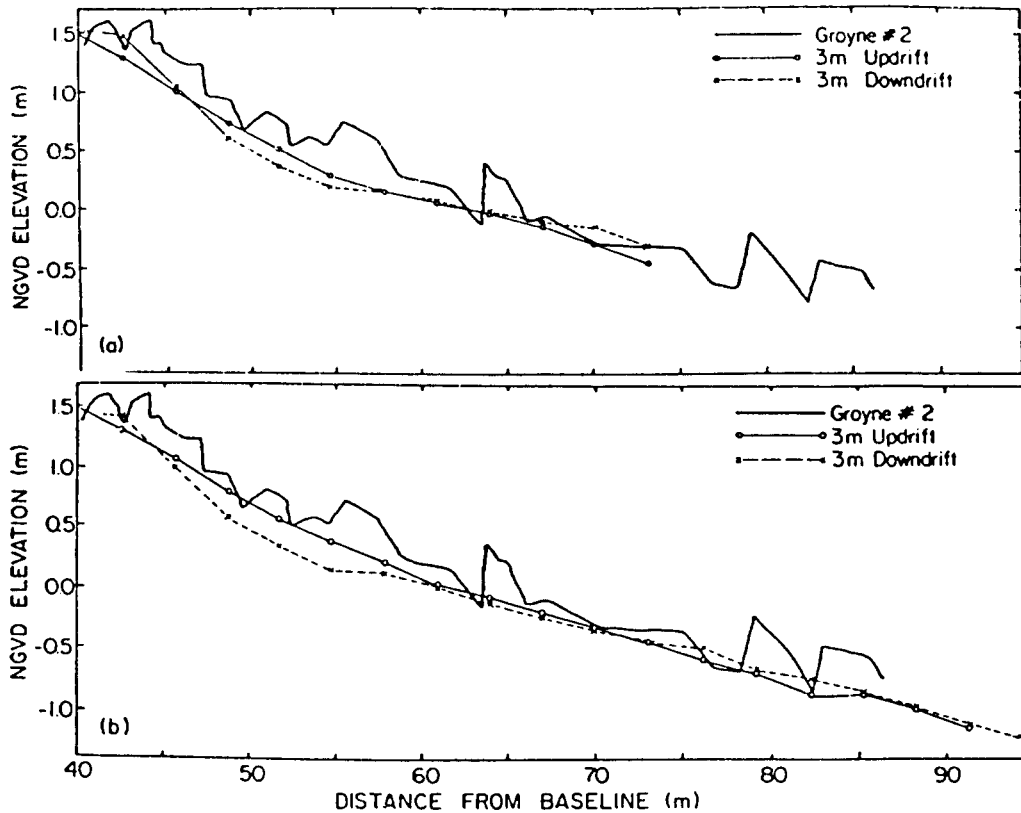


Figure 3-11: Beach profiles three meters up- and downdrift of the groyne (bold line) for Groyne #2: (a) during groyne construction, and (b) approximately 16 hours after groyne completion.

the beach because the survey baseline was not exactly parallel to the shoreline. The horizontal shift for a given profile is the same in both Figures 3-12 a and b. Considering that the beach profiles were fairly uniform before groyne deployment commenced, it is observed from Figure 3-12a that the profile immediately updrift of the groyne (-3m), and to some extent the profile just further updrift (-9m), accreted considerably during the first stage of groyne construction--as described earlier. The profiles further updrift and immediately downdrift are recessed relative to these two profiles. After groyne completion (Figure 3-12b) the foreshore continued to accrete on the updrift side, but eroded on

the downdrift side. The profiles below NGVD remained relatively steady during the experiment, although some accretion apparently occurred just downdrift of the groyne. The mean tidal level during the interval between the two loops of profiles was 5 cm below NGVD.

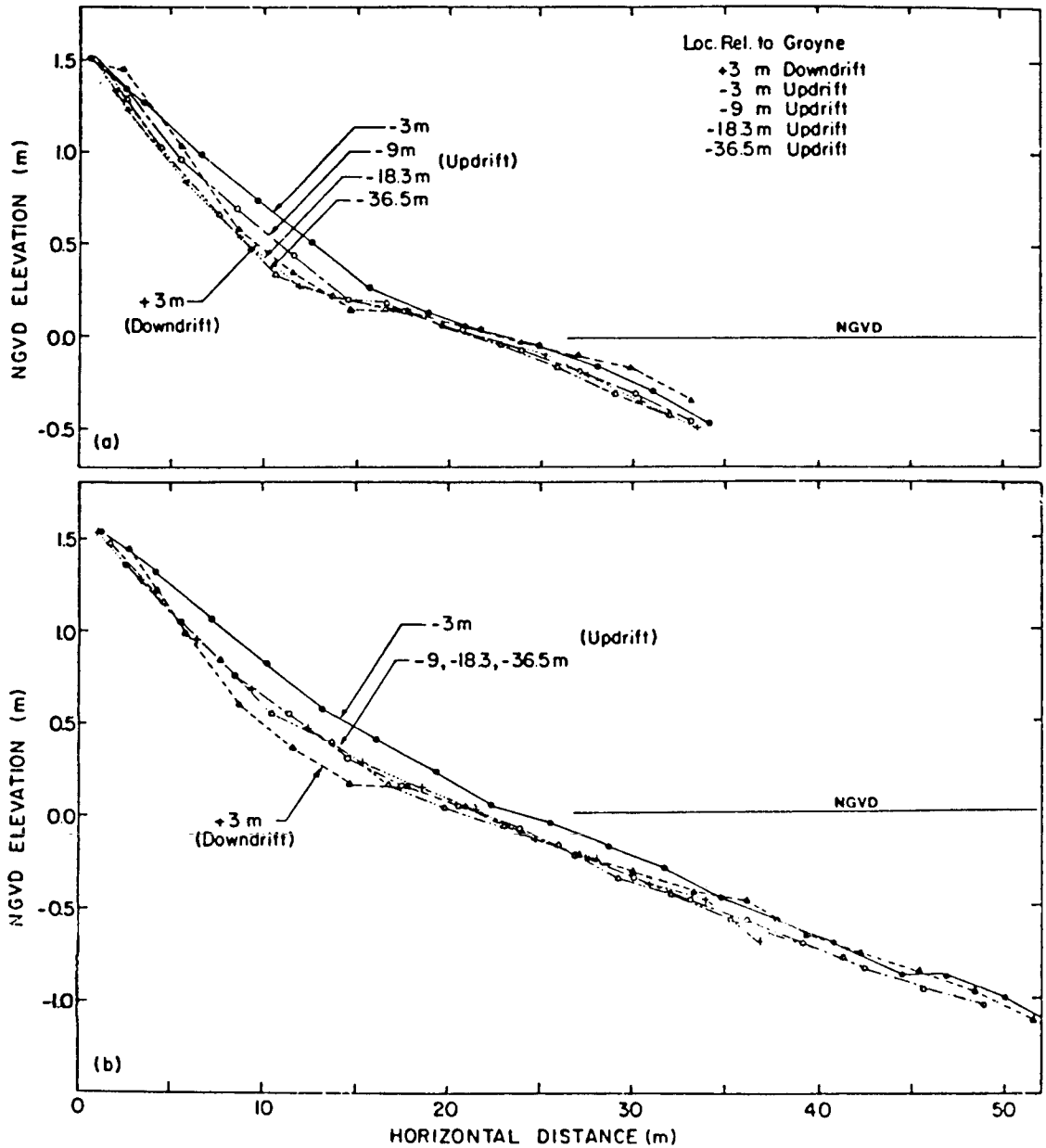


Figure 3-12: Beach profiles updrift and immediately downdrift of the barrier for Groyne #2: (a) during groyne construction, (b) approximately 16 hours after groyne completion. Profiles are horizontally shifted for approximate berm alignment.

### 3.3.4 Groyne #3

The third experiment was the first to use the pyramid-style groyne deployed during a falling tide. Construction began at the berm just before high tide and rapidly reached the still water shoreline as the water level crested. Unfortunately, the neap high tide lingered much longer than was expected relative to the groyne-deployment time. Sediment impoundment began in the swash zone as the field crew awaited the fall of the tide so that further deployment could proceed. (Bag-filling in still water depths greater than about one bag diameter had earlier proven ineffective.) The groyne was finally completed to a depth of about 20 cm below the low tide water level as darkness fell. The difficulty experienced during Groyne #3 was that deployment proceeded much more quickly than expected. Indeed, the pyramid-style construction rapidly created a substantial and comely barrier of high integrity. Figure 3-13 illustrates the tidal fluctuation and groyne deployment sequence for Groyne #3.

In addition to a pre-deployment loop, two survey loops were taken after groyne deployment: one each on the rising, then falling, tide while the surf zone was bounded by the barrier. The movement of the surf zone across the beach relative to the groyne and during the interval between surveys is depicted in Figure 3-14. The Eulerian measure of mean longshore current over time at each of three locations is also shown in the figure. The distance offshore (extreme left vertical axis) is referenced to the survey baseline. The approximate corresponding location of the groyne is shown on the extreme right of the figure. Since the baseline was not precisely shore-parallel, the surveyed location of the groyne is not directly transferrable to other

profile stations. Accordingly, the groyne location shown in the figure was determined by transferring the depth contours which the groyne occupied to the contours measured at the station where the current and visual surf-observation data were recorded.

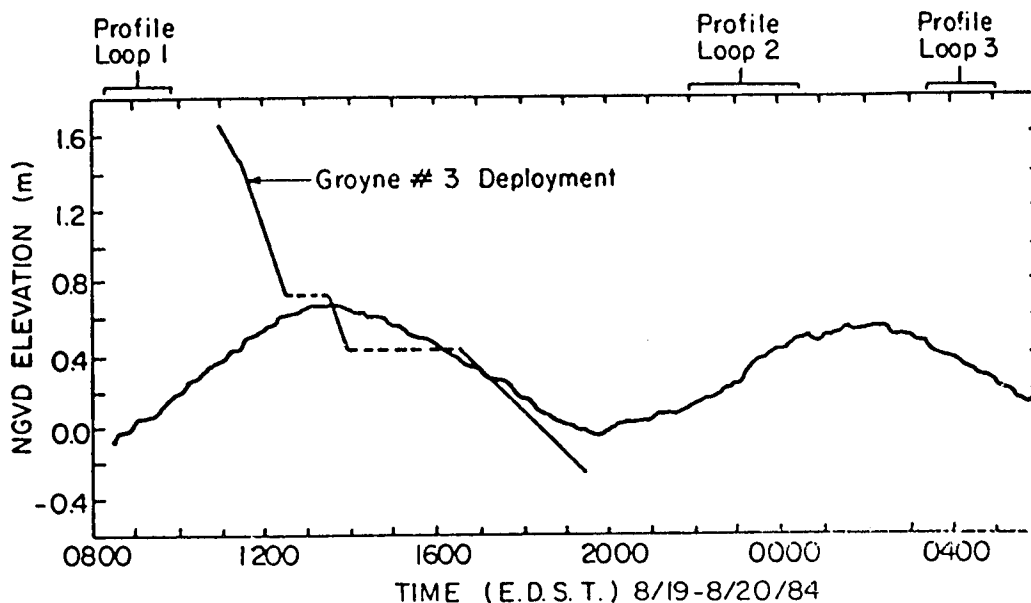


Figure 3-13: Tidal fluctuation, beach profiling "loop" intervals, and groyne deployment sequence for Groyne #3.

Figure 3-15 comparatively illustrates the beach profiles immediately up- and downdrift of the barrier (a) before, (b) two hours after, and (c) seven hours after deployment. From Figure 3-15a, it is readily seen that the barrier was constructed on an initially undisturbed beach, as desired. Considerable downdrift recession--immediately adjacent to the groyne--occurred about the mean water level. Elsewhere along the groyne, the downdrift side showed little net change except for some accretion near the seaward end. Accretionary features are observed updrift of the groyne well above the mean water level and towards the

end of the groyne. A localized loss is observed just below the mean water level immediately updrift of the groyne. The initially perplexing appearance of a small loss on the updrift side--and some accretion on the downdrift side--was later observed during the laboratory impoundment experiments and is discussed in Chapter 7.

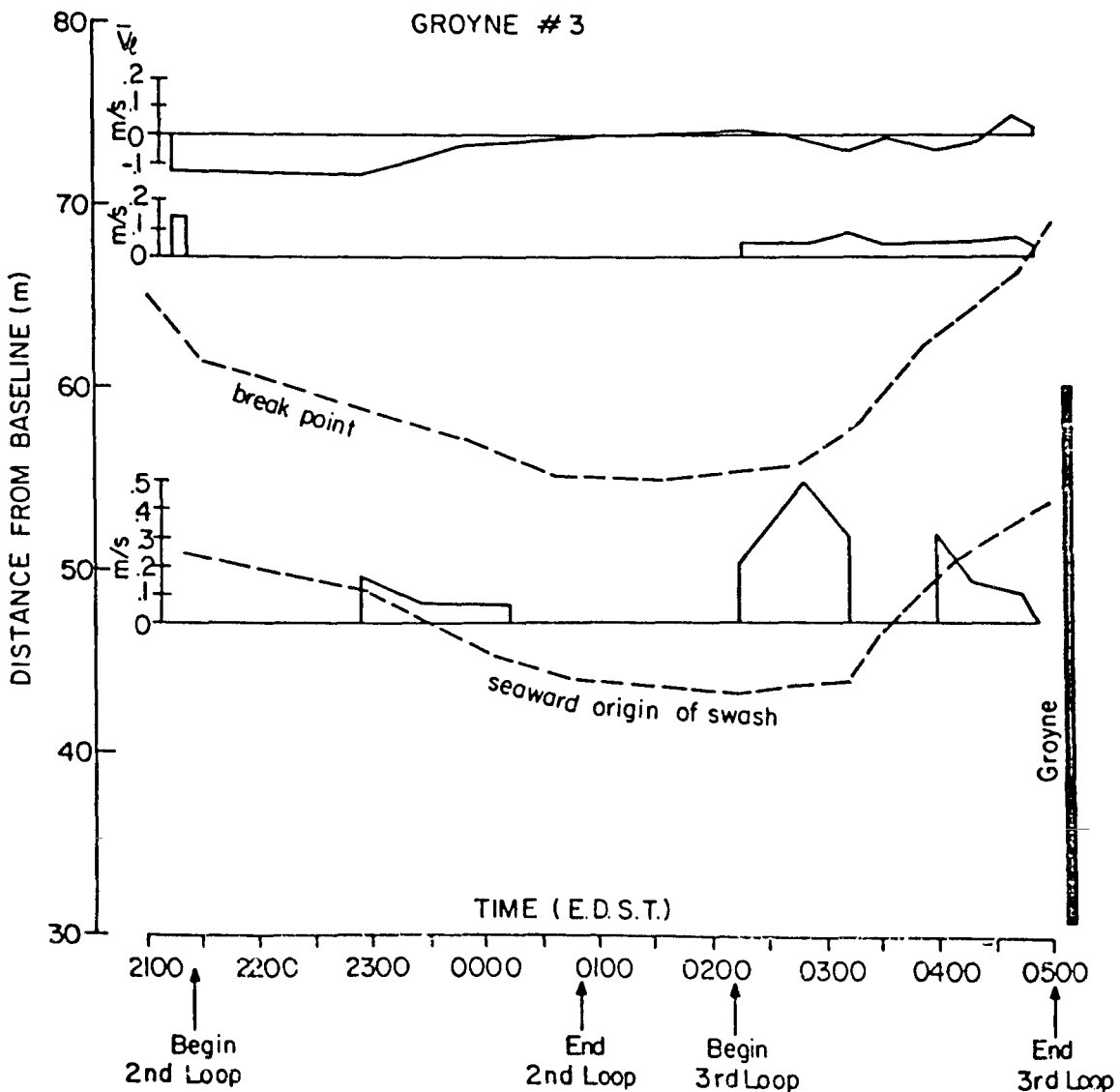


Figure 3-14: Time history of surf zone location and mean longshore currents during Groyne #3; 8/19-20/84. Positive-valued longshore current indicates flow towards the north.

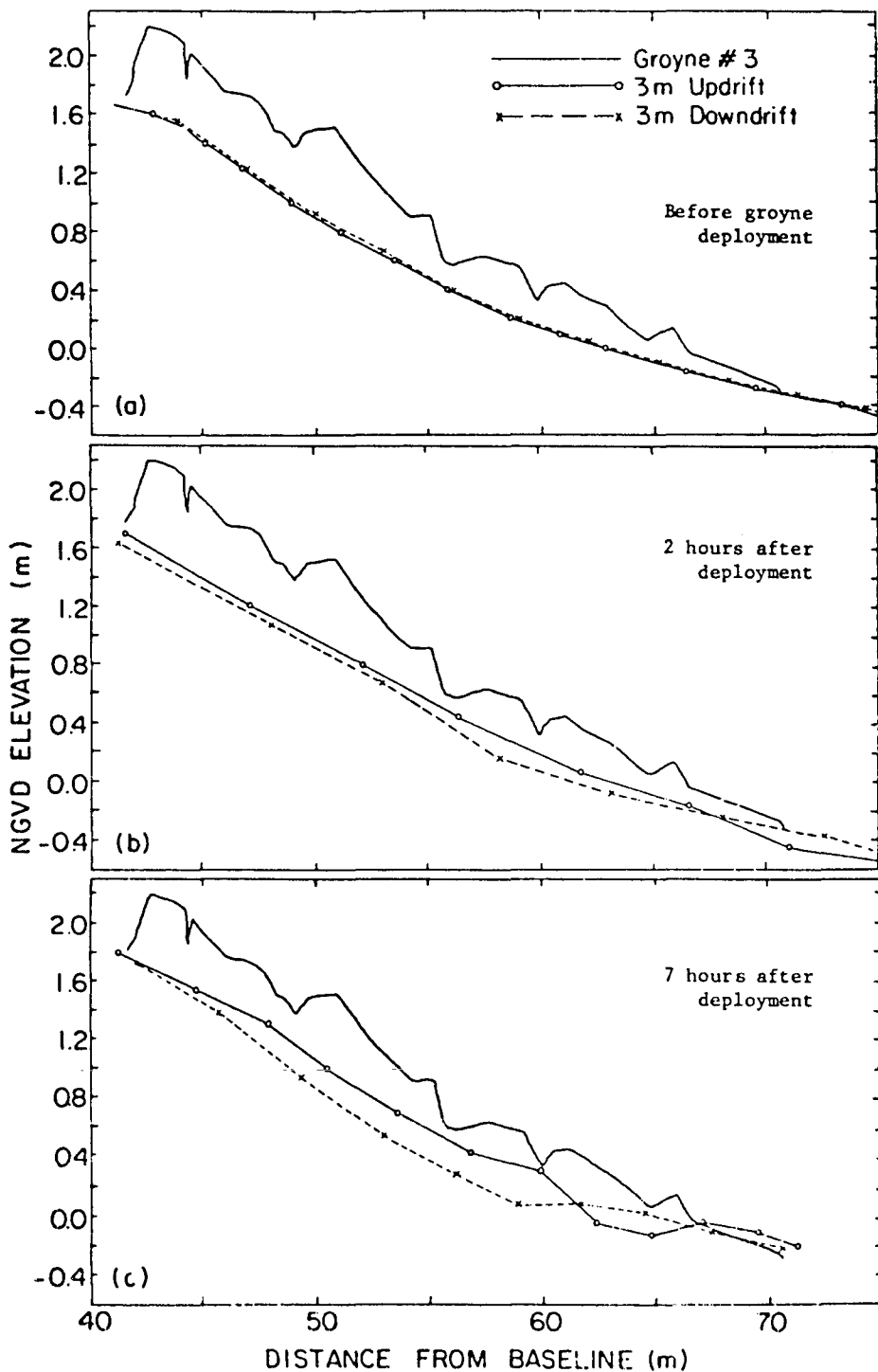


Figure 3-15: Beach profiles three meters up- and downdrift of the groyne (bold line) for Groyne #3: (a) before, (b) two hours after and (c) seven hours after groyne deployment.

Two sets of profile changes relatively far updrift of the groyne (two or three groyne lengths away) are illustrated in Figure 3-16. Assuming that the presence of the barrier did not affect these

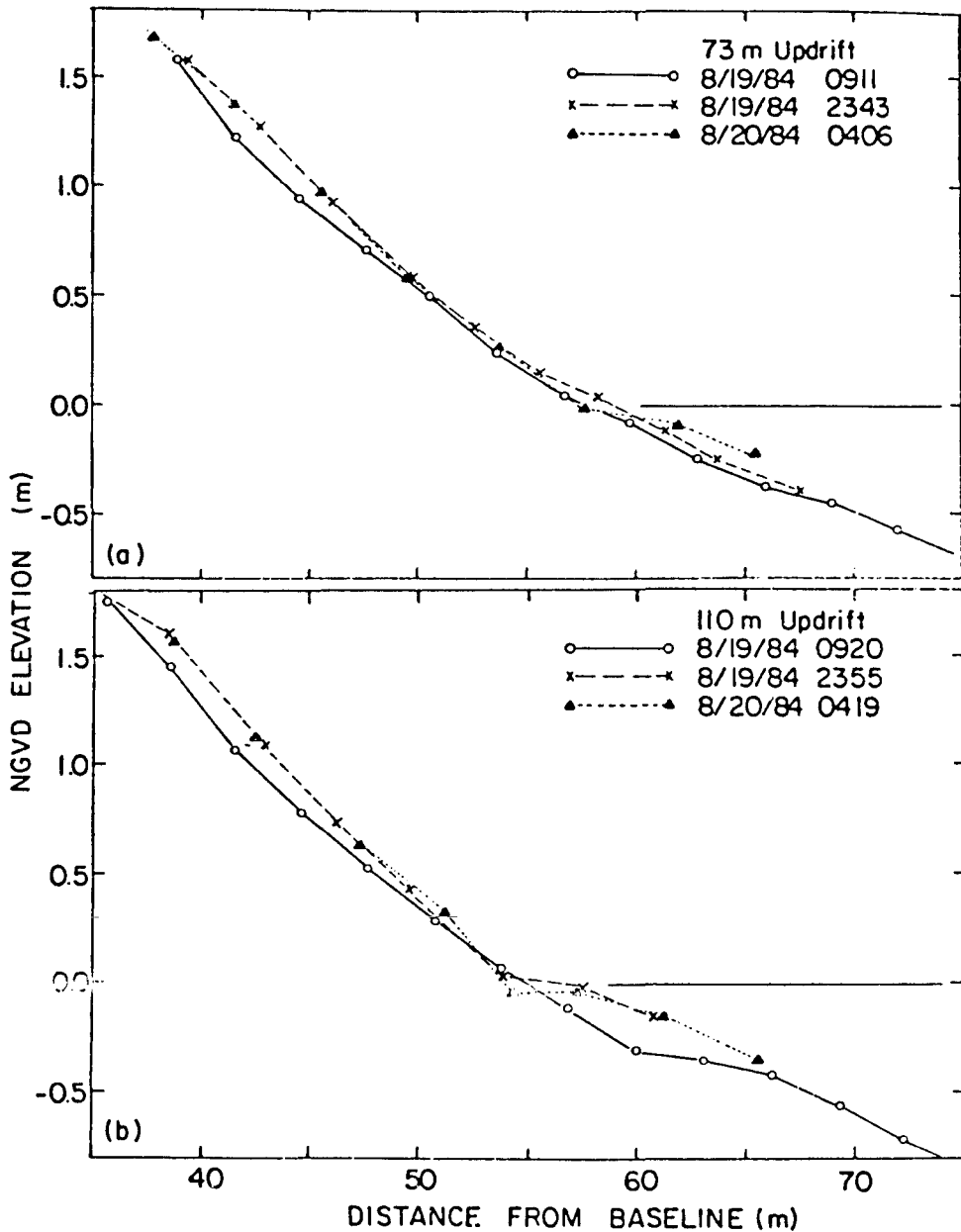


Figure 3-16: Representative beach profiles measured far updrift of the barrier for Groyne #3: before, two hours after, and seven hours after groyne deployment. Location of profiles relative to groyne is indicated for each set of profiles.

locations (a reasonable assumption based upon laboratory results), the updrift profile changes indicate that the beach was undergoing accretion along the foreshore and just below NGVD by cross-shore processes during groyne deployment, (0900 to 1930 hours). The far updrift profiles were relatively stable after groyne deployment except for some profile adjustments about NGVD. The mean water levels between the first and second survey loops and the second and third survey loops were 0.30 m and 0.42 m above NGVD, respectively.

Half-hourly wave observations of wave height and type were made at selected offshore locations during the post-deployment survey interval and are presented in graphical form in Figure 3-17a. The average (Eulerian record) longshore current measured at these same offshore locations is presented in Figure 3-17b. The longshore current was previously illustrated as a function of offshore location in Figure 3-14. In Figure 3-17, the longshore current and wave data are shown as a function of the still water depth. This presentation was accomplished by noting the NGVD-referenced elevation of each offshore observation point,  $z_o$ , and the NGVD-referenced tidal water level,  $\bar{\eta}$ , during each wave or current measurement. The still water depth corresponding to each measurement was then calculated as  $z_o - \bar{\eta}$ .

#### 3.3.5 Groyne #4

Groyne #4 was the most successful experiment of the four attempted. A pyramid-style groyne was constructed atop the remains of Groynes #2 and #3, which surfaced the evening before the fourth experiment began. The pre-deployment beach survey indicated that the groyne remnants had not seriously altered the site bathymetry except for immediately updrift

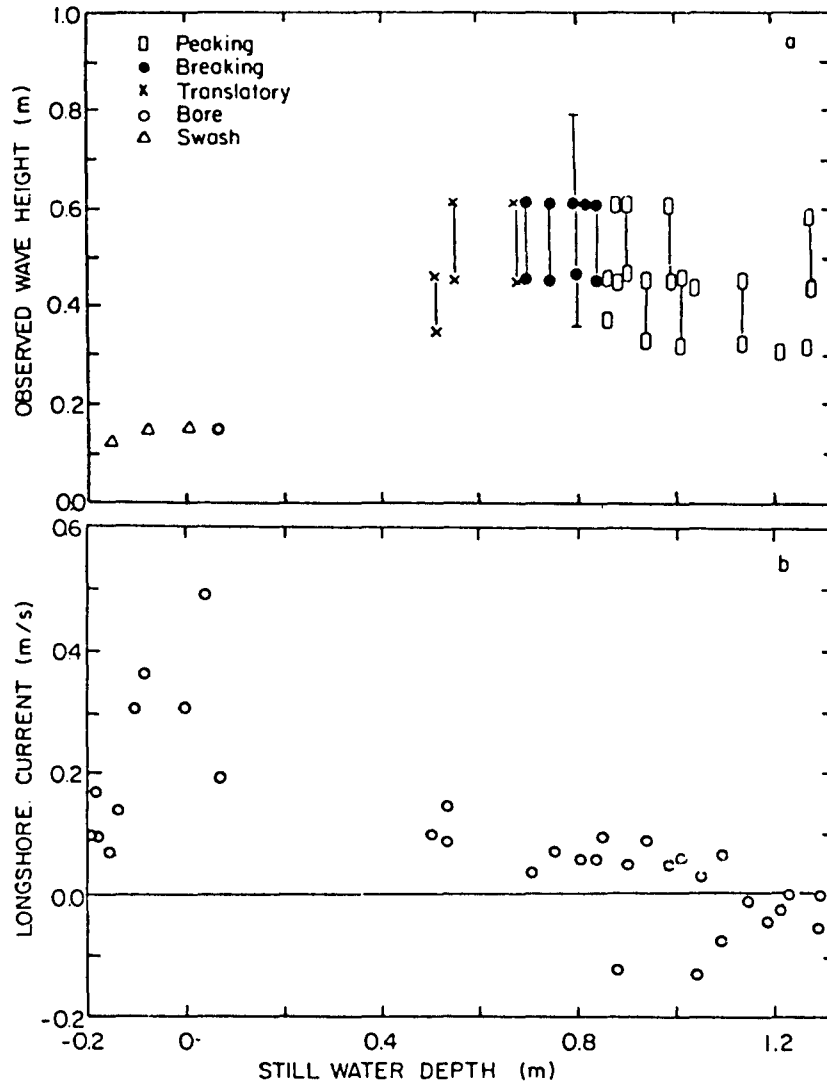


Figure 3-17: (a) Visual observation of wave height and types, and (b) Eulerian measurement of longshore current across the surf zone during the post-groyne deployment interval of Groyne #3; (8/19/84-1840 through 8/20/84-0500 EDST). Positive-valued current indicates flow towards the north.

of the old sand bags (mostly irregular scour holes). The groyne was deployed from the berm to below the low water line on a falling (lunar perigeon) spring tide. Figure 3-18 illustrates the tidal fluctuation and groyne construction sequence for Groyne #4.

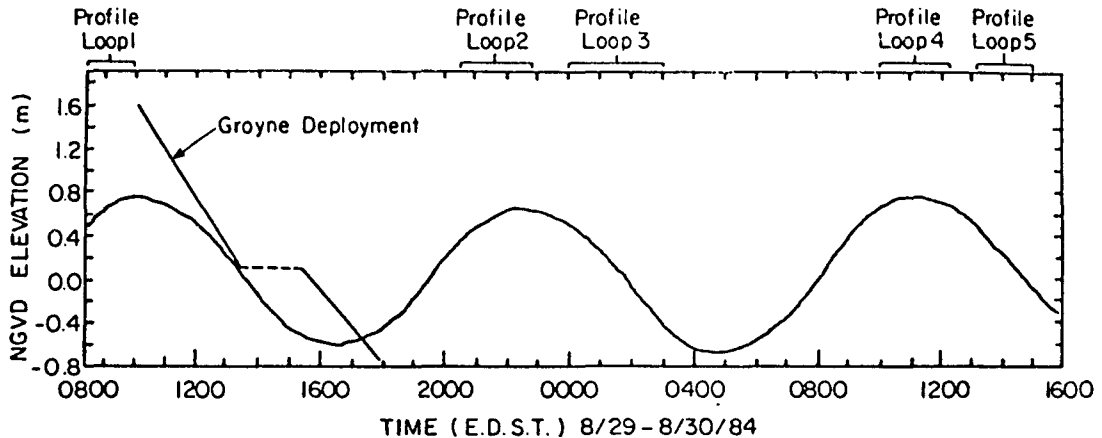


Figure 3-18: Tidal fluctuation, beach profiling "loop" intervals, and groyne deployment sequence for Groyne #4.

In addition to the pre-deployment survey loops, profile loops were taken after groyne deployment on the rising, then falling, tide when the surf zone was bounded by the barrier. Another two loops were taken during the subsequent rising, then falling, tide several hours later. Inspection of the barrier before execution of the last two survey loops indicated that the impoundment area was not yet filled to capacity. Figures 3-19 and 3-20 illustrate the movement of the surf zone relative to Groyne #4 during the two survey loop impoundment intervals after groyne deployment.

Figure 3-21 illustrates the groyne profile compared to the beach profiles immediately up- and downdrift during the third and fifth survey loops. (These loops may be each thought of as the termination of an ideal surveyed-impoundment interval.) It is seen that the updrift side generally accreted all along the profile--relative to the downdrift side--during the survey period.

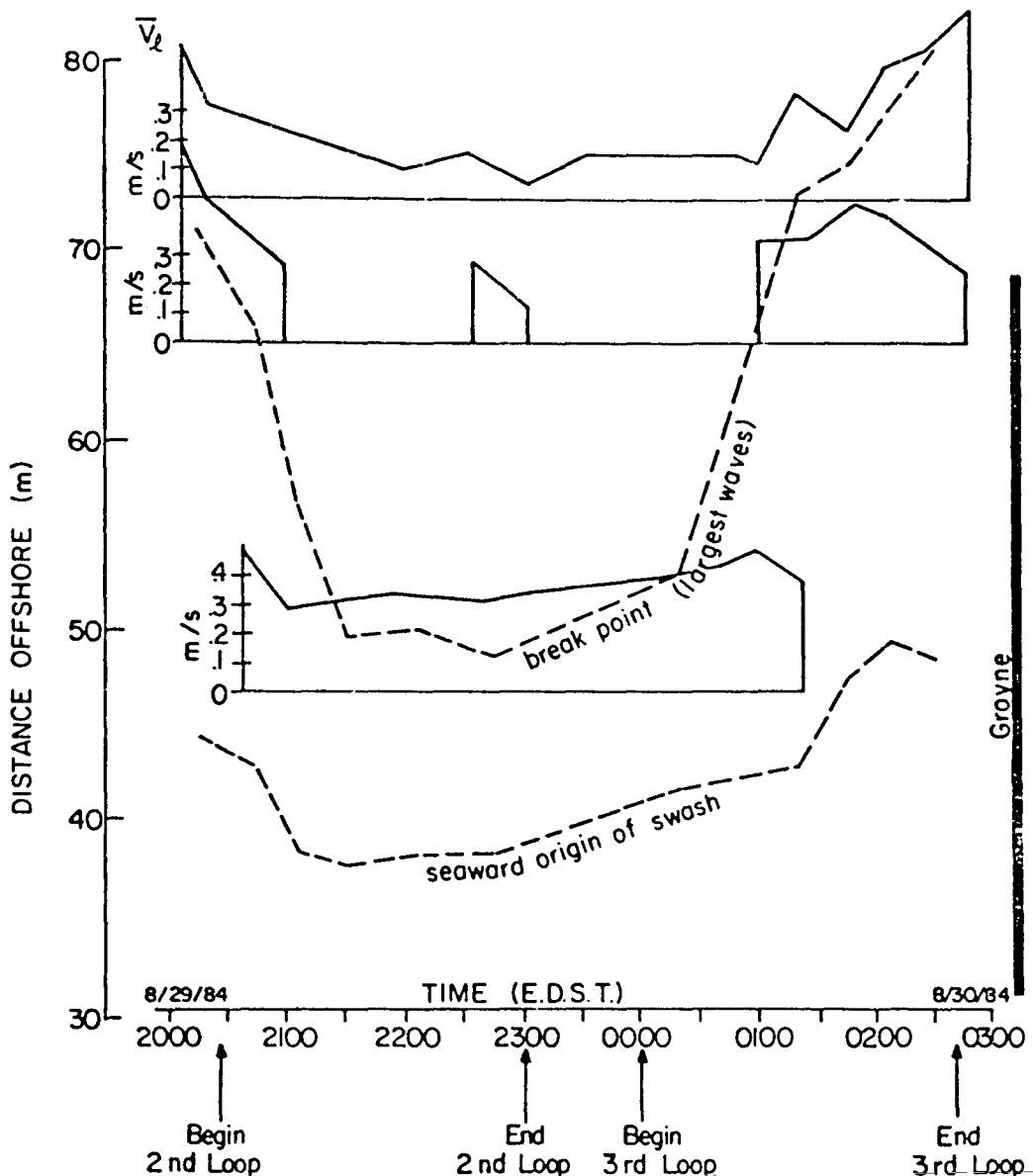


Figure 3-19: Time history of surf zone location and mean longshore currents during Groyne #4, first post-groyne deployment survey interval (8/29-30/84). Positive-valued longshore current indicates flow towards the north.

Figures 3-22 and 3-23 illustrate the beach profile changes over time immediately down- and updrift of the barrier, respectively, for the impoundment intervals of profile loops 1-2-3 and 4-5. The scour observed on the updrift side before groyne deployment rapidly filled in

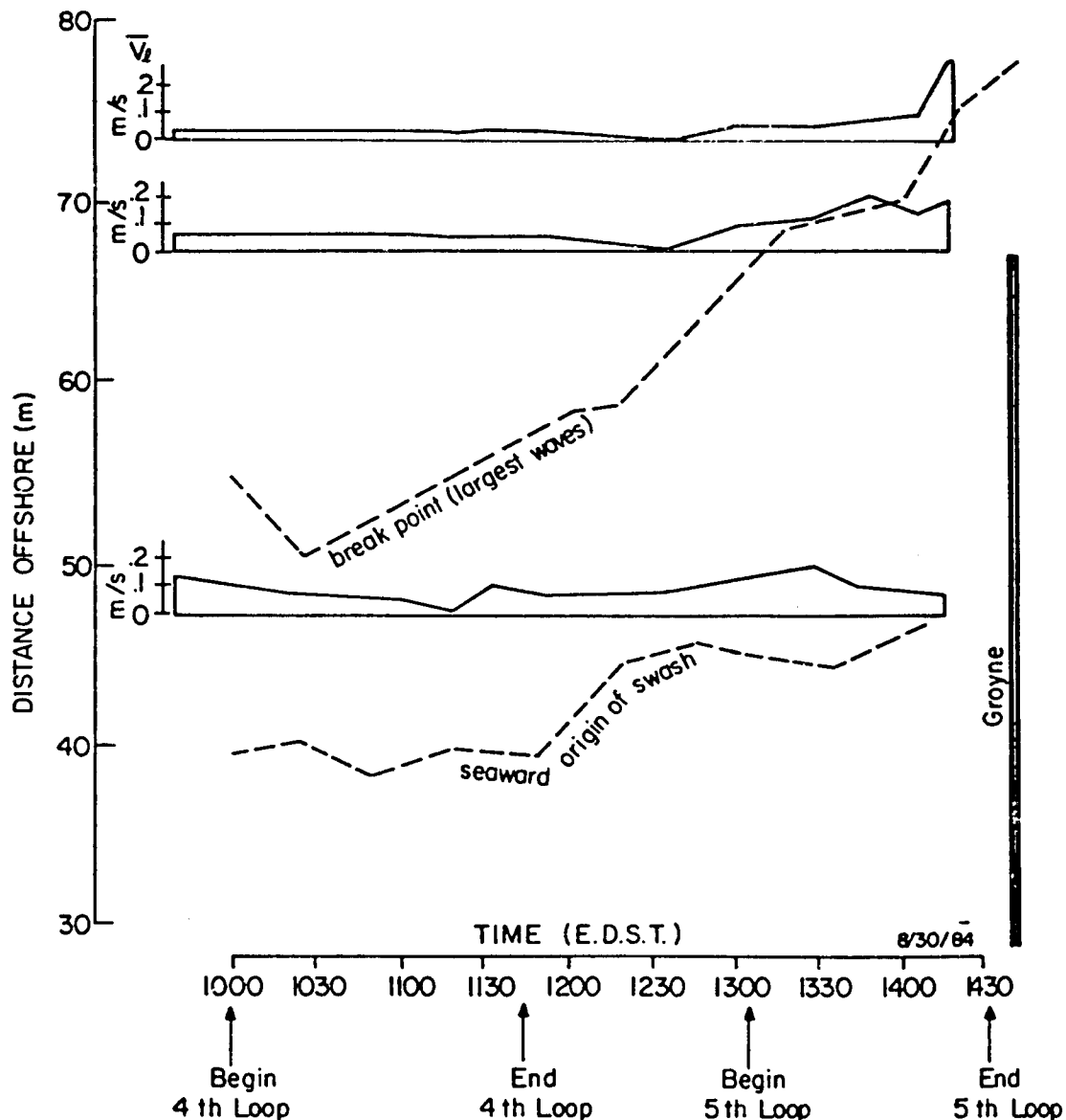


Figure 3-20: Time history of surf zone location and mean longshore current during Groyne #4, second post-groyne deployment survey interval (8/30/84). Positive-valued longshore current indicates flow towards the north.

during barrier construction. (It is noted that the barrier was wetted by swash as it was constructed.) The downdrift side receded slightly during barrier construction; but like Groyne #3, the downdrift and up-drift sides showed both localized accretion and recession after barrier

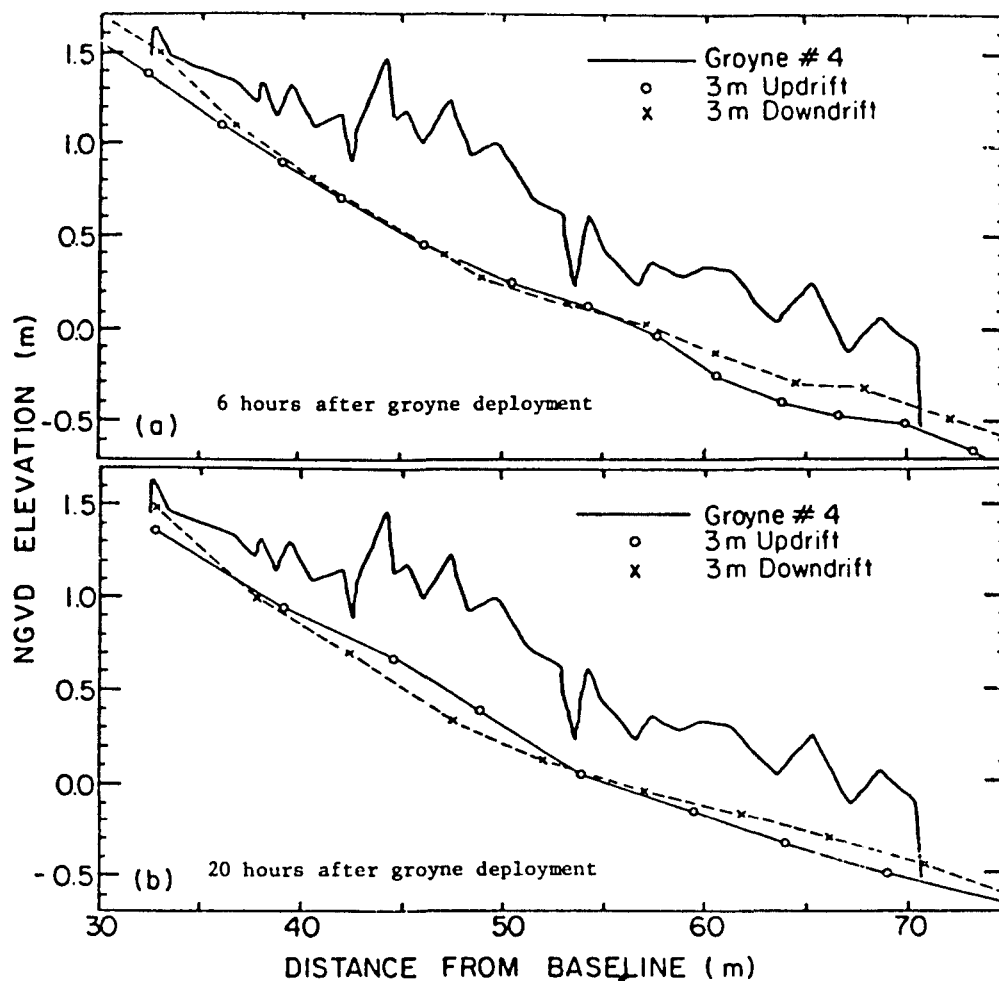


Figure 3-21: Beach profiles 3 m up- and downdrift of the barrier (bold line) for Groyne #4: (a) approximately 6 hours after groyne construction (profile loop 3) and (b) approximately 20 hours after groyne construction (loop 5).

construction. Profile changes two groyne-lengths updrift of the barrier are shown in Figure 3-24. These changes are typical for the profiles far updrift of the barrier for Groyne #4. It is seen that the beach was generally accretive during the barrier construction and first impoundment periods, with slight foreshore accretion during the last impoundment period. In general, however, the far-updrift (undisturbed) beach profiles were relatively steady.

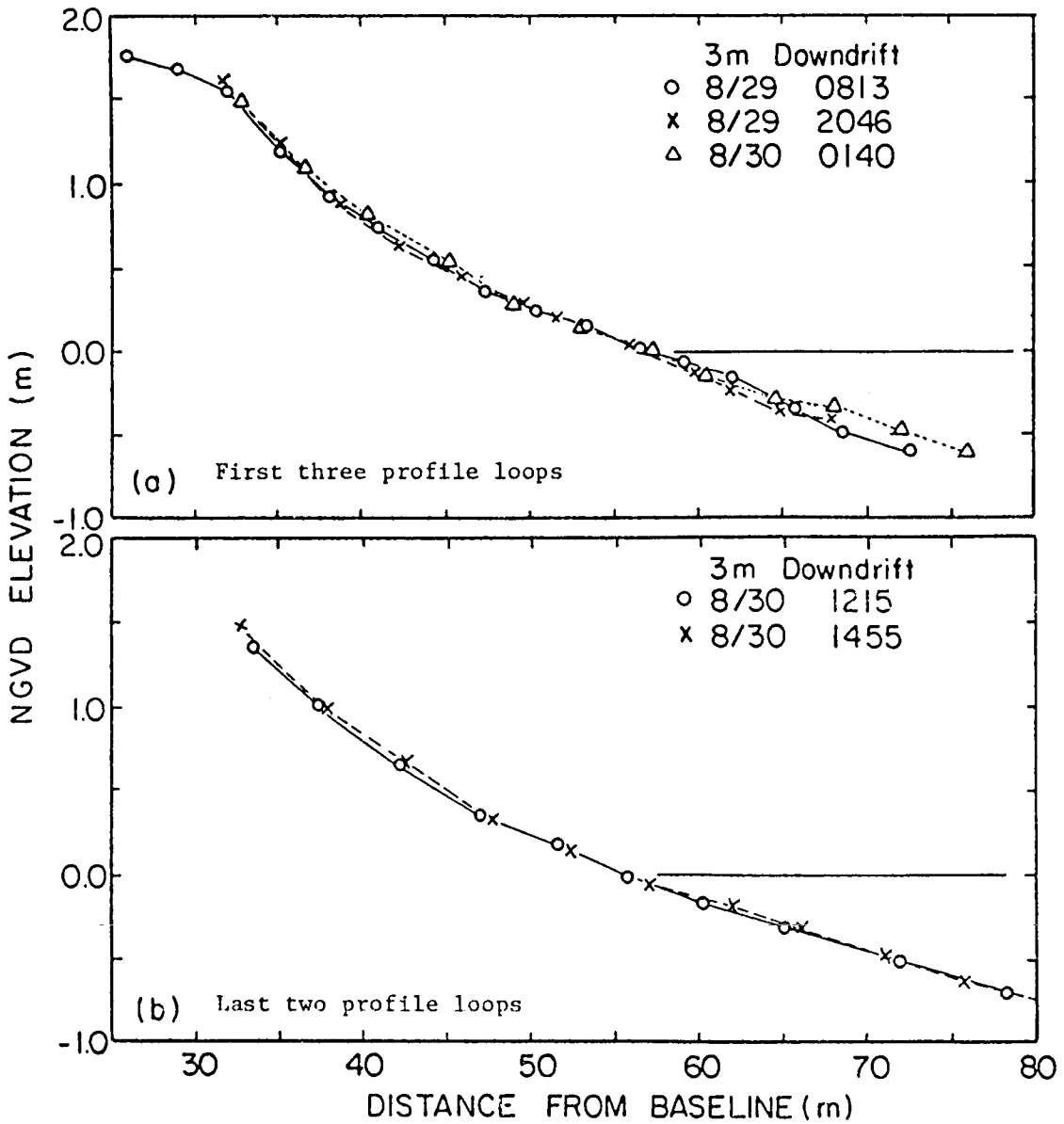


Figure 3-22: Beach profiles 3 m downdrift prior to and after construction of the barrier for Groyne #4.

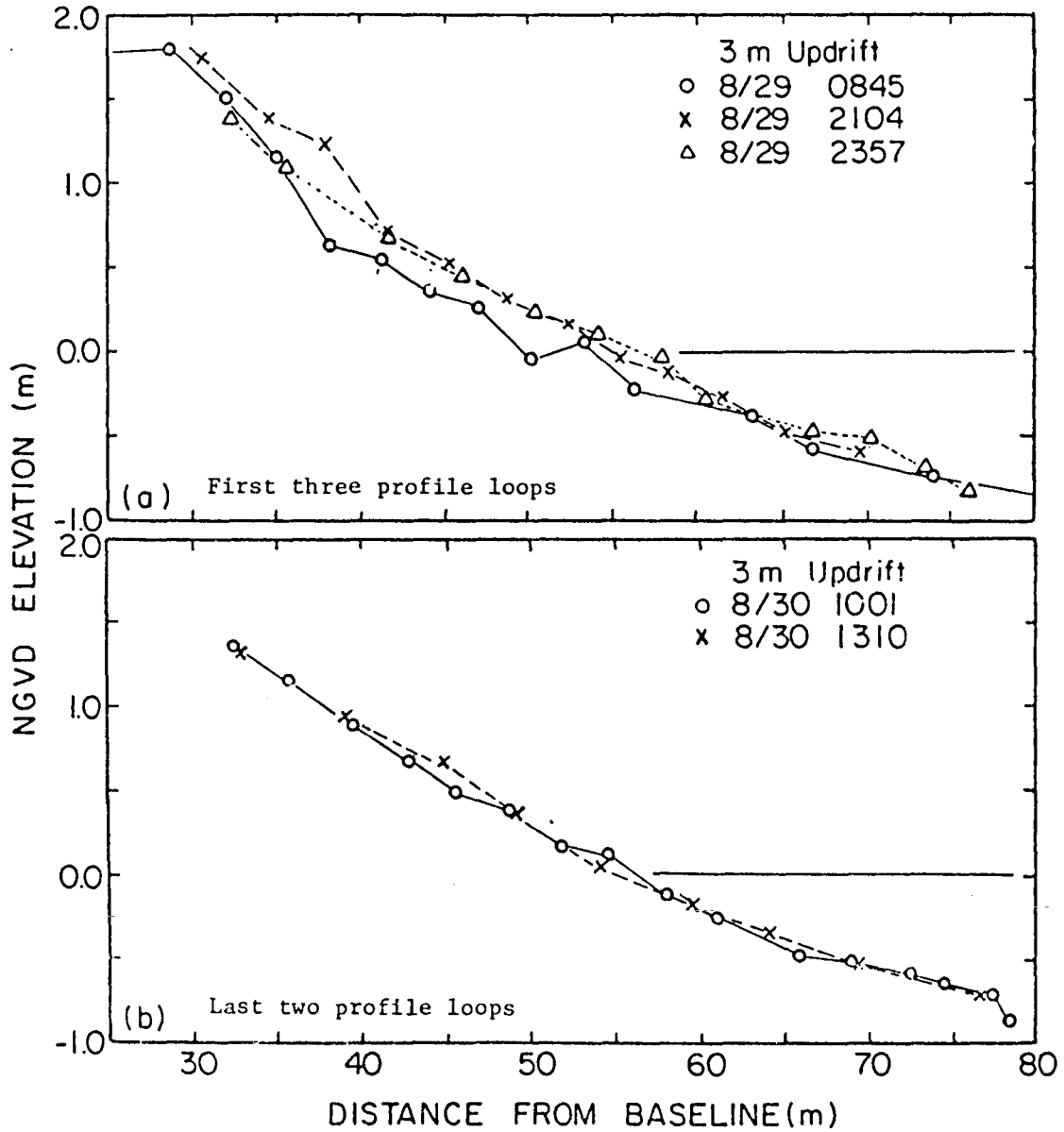


Figure 3-23: Beach profiles 3 m updrift prior to and after construction of the barrier for Groyne #4.

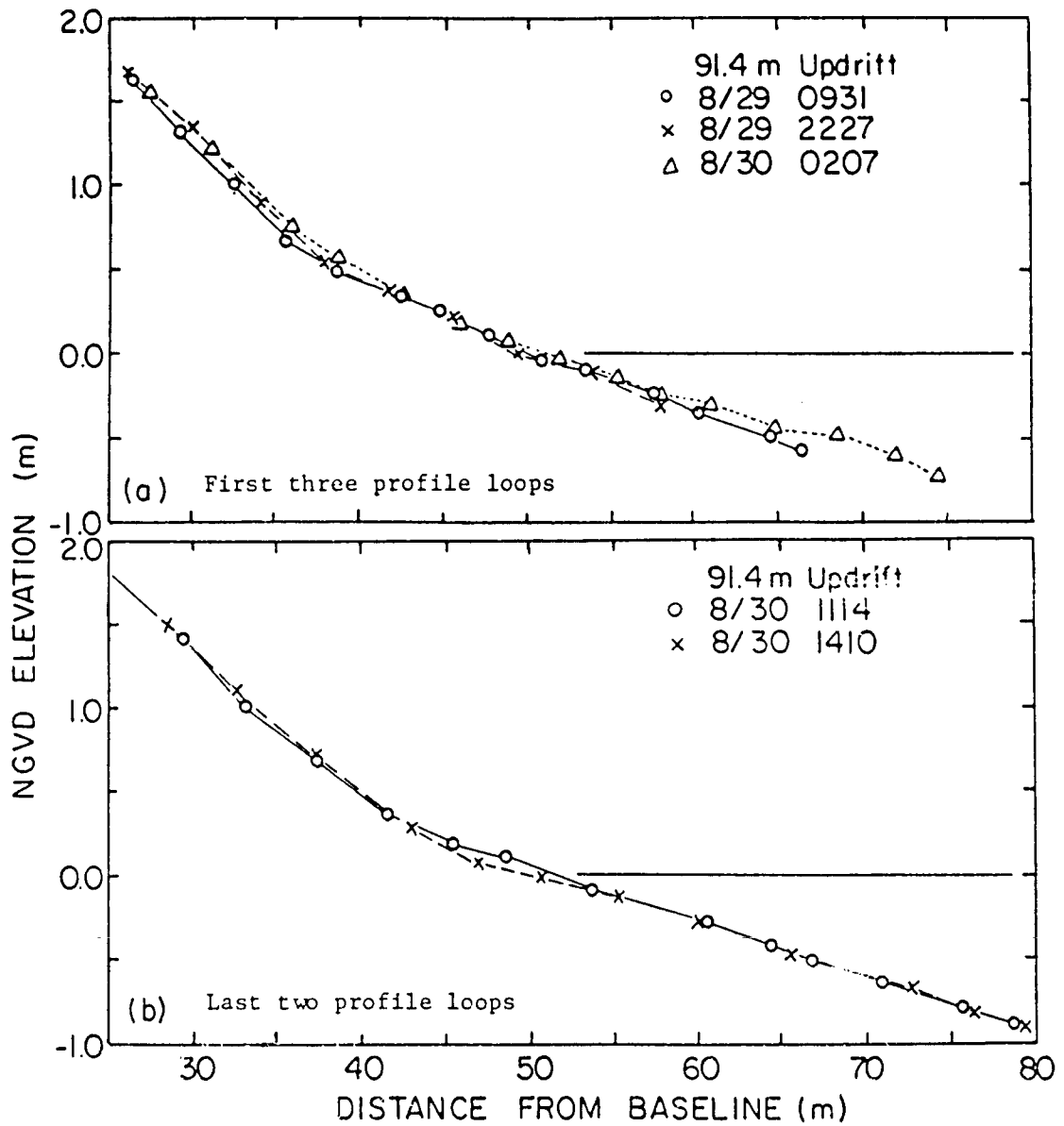


Figure 3-24: Beach profiles 91.4 m updrift prior to and after construction of the barrier for Groyne #4.

Visual observations of wave height and type and longshore current data are presented in Figures 3-25 and 3-26 a and b, respectively, for the post-deployment survey intervals. Presentation of the data in these two figures was accomplished in the same manner as described earlier for Figure 3-17.

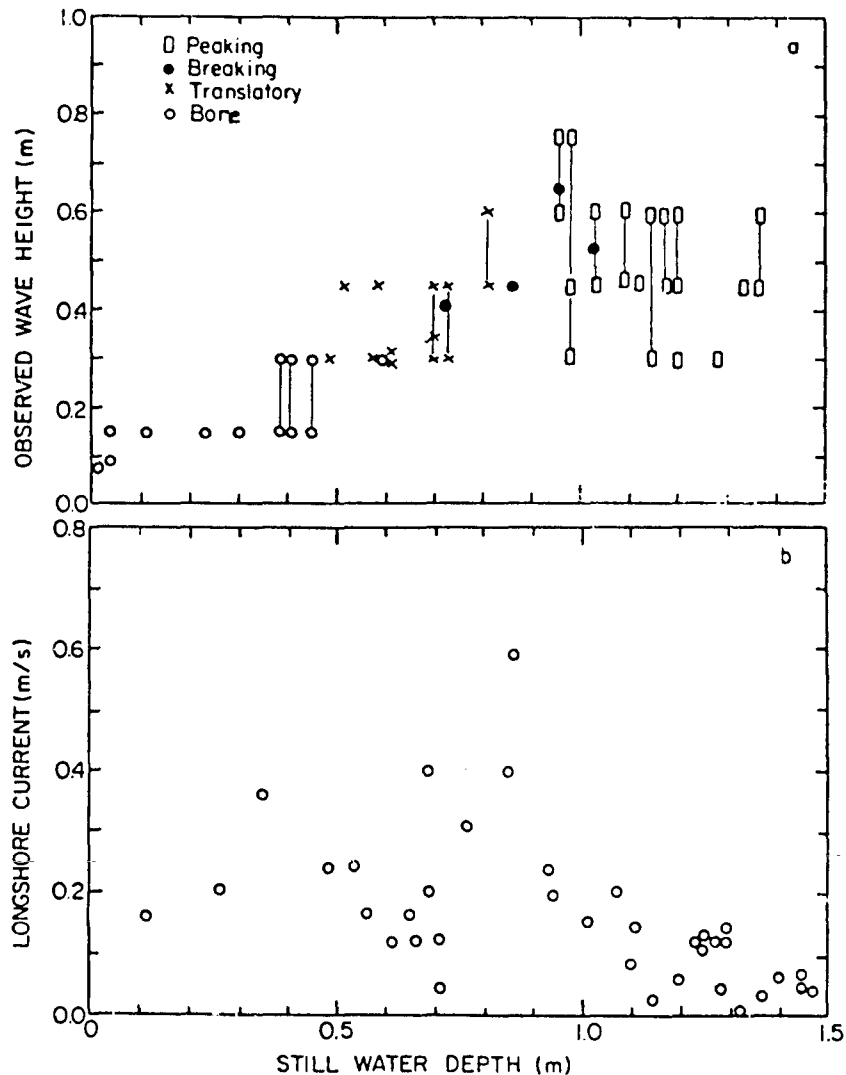


Figure 3-25: (a) Visual observation of wave height and type, and (b) Eulerian measurement of longshore current across the surf zone during the first post-groyne deployment impoundment interval of Groyne #4 (8/29/84-2016 through 8/30/84-0230 EDST). Longshore current was towards the north.

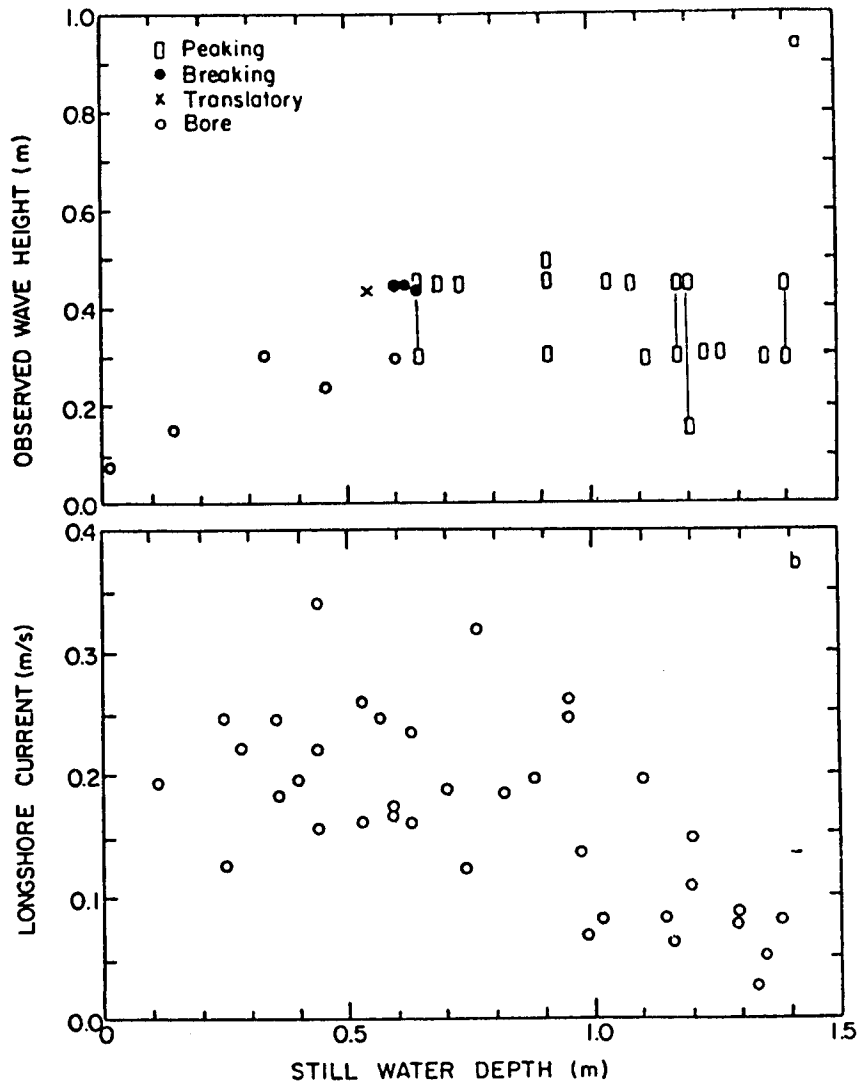


Figure 3-26: (a) Visual observation of wave height and type, and (b) Eulerian measurement of longshore current across the surf zone during the second post-groyne deployment interval of Groyne #4 (8/30/84 1000 through 1410 EDST). Longshore current was towards the north.

### 3.3.6 Sediment Characteristics

The size distribution of sediment samples collected during and/or immediately after each experiment is listed in Table 3-3. It is noted that Groyne #4 was executed in the presence of relatively coarse upshore sediment, and the sediment on the downdrift side of Groyne #4 was considerably finer than on the updrift side due to selective by-passing.

Table 3-3: Sediment Grain Size Distribution--Field Data

LOCATION (distance from groyne/ distance from baseline (m))*	d <sub>50</sub> (mm)	% FINER THAN: (mm)					
		2.00	0.84	0.42	0.246	0.149	0.105
Groyne #4							
+5/43	.29	98.4	80.9	65.1	38.8	3.0	1.0
-2/41	.83	93.0	51.7	28.9	14.9	1.6	0.1
+5/52	.41	94.4	66.9	51.9	27.8	2.0	0.1
-2/52	.84	81.9	49.0	39.3	27.4	3.2	0.4
+5/71	.25	96.9	86.2	78.8	51.0	4.7	1.3
-2/72	.23	98.7	95.2	93.1	57.1	6.6	2.0
-37/37	1.15	99.3	30.6	11.8	6.4	0.9	1.1
-37/41	.89	76.1	47.9	30.5	16.6	1.7	0.9
-37/48	1.10	83.7	45.1	49.2	30.1	3.2	1.1
-37/61	.25	94.9	80.8	72.7	46.5	3.1	0.4
-37/72	.25	96.7	88.9	82.9	46.7	6.6	3.4
Groyne #3							
+3/58	.22	98.8	89.1	81.3	59.3	4.1	2.4
+3/67	.20	98.1	91.3	84.1	69.5	5.9	1.4
+3/43	.16	--	97.2	93.7	80.5	6.6	2.0
Groyne #2							
+3/43	.24	--	--	98.5	62.2	3.7	0.8
-3/43	.23	--	--	99.1	69.6	4.1	0.8
+3/51	.23	--	99.0	95.0	66.4	7.0	3.0
-3/51	.22	99.6	97.6	88.8	58.4	4.6	1.7
+3/65	.42	88.8	62.0	52.4	40.8	7.4	3.6
-3/65	.17	93.1	83.8	81.3	73.6	11.8	2.2
+3/79	.15	98.0	95.5	94.2	88.4	22.0	3.6
-3/79	.17	97.6	96.5	95.2	88.7	23.6	4.3

\* (+) = downdrift, (-) = updrift

## CHAPTER 4

### TIDAL DECONVOLUTION AND REMOVAL OF CROSS-SHORE TRANSPORT EFFECTS

#### 4.1 Introduction

This chapter describes the methodologies developed to remove tidal and cross-shore effects from the impoundment (survey) data in order to isolate the longshore sediment transport signal along a series of depth contours for each experiment. Additionally described are methodologies developed to assess the effectiveness of each groyne as a longshore transport impoundment agent across the surf zone.

#### 4.2 General Description of Approach

Consider a beach with a shore-perpendicular barrier (Figure 2-1) with  $x$ -,  $y$ -, and  $z_0$ -axes directed offshore from a baseline, alongshore from the barrier, and positive-upwards from the National Geodetic Vertical Datum (NGVD) or other fixed reference, respectively. An alternate vertical axis,  $z$ , is defined positive-upwards from the still water level (SWL). Any particular water depth contour  $h$  (defined as positive below SWL) can be expressed by  $h = -z$ . At time  $t$ , the elevation of the still water level relative to NGVD is  $\bar{\eta}(t)$  and is referred to here as "tide." The vertical coordinates  $z_0$  and  $z$  are therefore related by

$$z(t) = z_0 - \bar{\eta}(t) \quad (4.1)$$

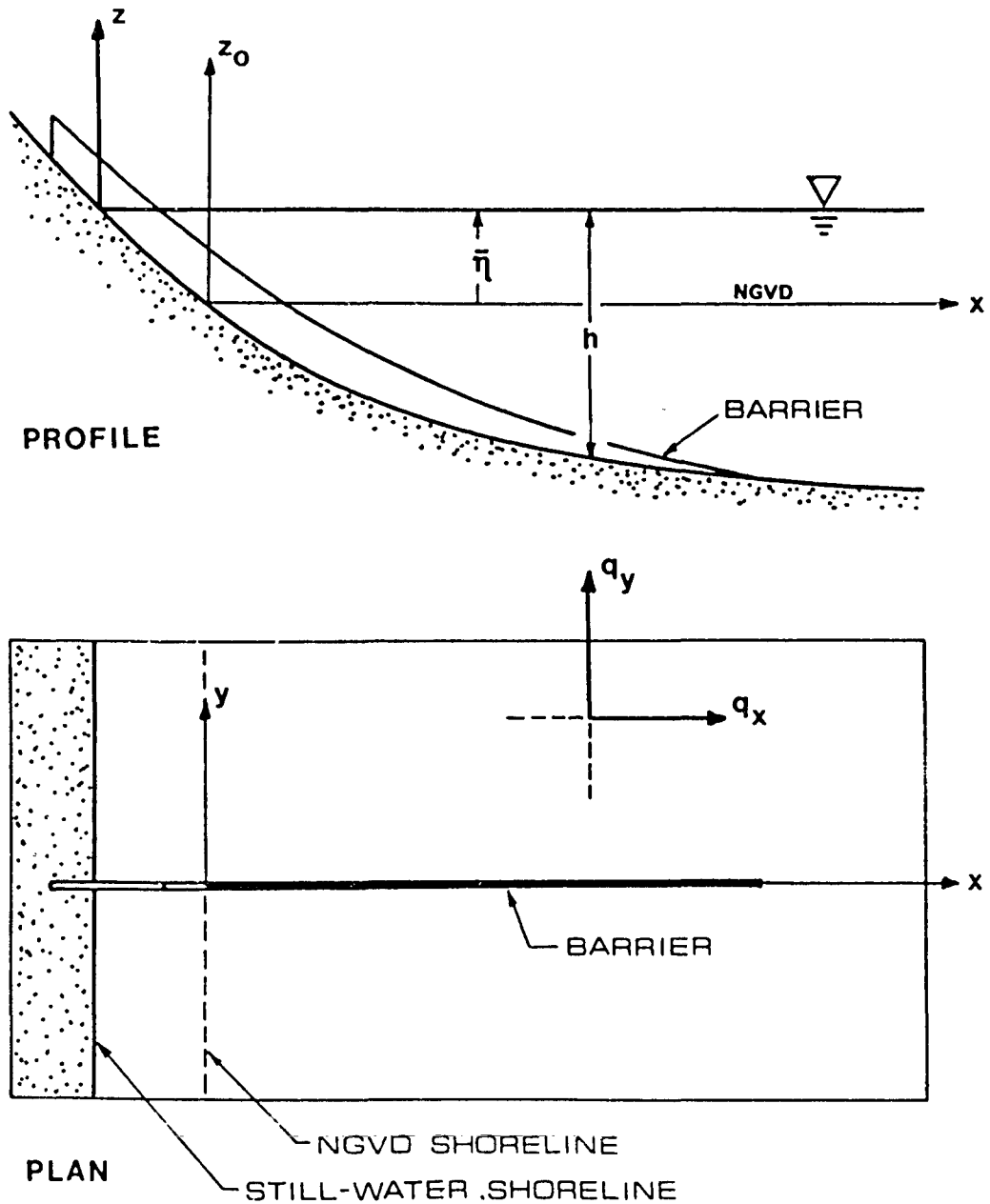


Figure 4-1: The coordinate system adopted for a three-dimensional beach with a shore-perpendicular barrier and fluctuating tidal water level.

The "conservation of sand" equation describes the vertical rate of change of bed elevation at a fixed point  $(x, y, z_0)$ , as

$$\left. \frac{\partial z}{\partial t} \right|_{z_0} = - \left( \frac{\partial q_x(y)}{\partial x} + \frac{\partial q_y(x)}{\partial y} \right) \quad (4.2)$$

where  $q_x(y)$  and  $q_y(x)$  represent the local cross-shore and longshore sediment transport rates per unit width, respectively. The local bed slope  $m$  at this point is defined by the traditional convention:

$$m = - \left. \frac{\partial z}{\partial x} \right|_{z_0} \quad (4.3)$$

The cross-shore and longshore components of the sediment transport rate may then be expressed as

$$\begin{aligned} q_x(z) &= \frac{1}{m} q_x(y) \\ q_y(z) &= \frac{1}{m} q_y(x) \end{aligned} \quad (4.4)$$

where  $q_x(z)$  and  $q_y(z)$  represent the local cross-shore and longshore sediment transport rates per unit depth, respectively, and where  $z$  is given by Eq. (4.1). Equation (4.2) can therefore be written as

$$\left. \frac{\partial x}{\partial t} \right|_{z_0} = - \left( \frac{\partial q_x(z)}{\partial x} + \frac{\partial q_y(z)}{\partial y} \right) \Big|_{z=z_0 - \bar{\eta}(t)} \quad (4.5)$$

The left hand side of Eq. (4.5) describes the horizontal rate of growth (or recession) of the beach at reference elevation  $z_0$  which corresponds to the instantaneous depth contour or elevation  $z = z_0 - \bar{\eta}(t)$ . The right hand side is the horizontal divergence of the total transport rate along the contour  $z$ . For brevity of notation, Eq. (4.5) is re-written as follows,

$$\left. \frac{\partial x}{\partial t} \right|_{z_0} = - \vec{v} \cdot \vec{q} \quad (4.6)$$

$$= \Lambda_x(z) + \Lambda_y(z) = \Lambda(z)$$

where  $\Lambda(z)$  is hereafter referred to as the "total transport function", and  $\Lambda_x(z)$  and  $\Lambda_y(z)$  are the contributions to the so-called total transport function due to cross-shore and longshore transport.

In practice, the total transport function  $\Lambda(z)$  was developed along a series of contours  $z$  through tidal deconvolution from the measured horizontal profile change  $\partial x \sim \Delta x$  (or average rate thereof,  $\partial x / \partial t \sim \Delta x / \Delta t$ ) at a series of reference elevations  $z_0$  for which the relationship between  $z$  and  $z_0$  was known through Eq. (4.1) and the measured tide data. The cross-shore component  $\Lambda_x(z)$  of the total transport function was then identified along each contour  $z$  and was subtracted from the total transport function to yield the longshore component  $\Lambda_y(z)$ . The local longshore transport rate along each contour  $z$  was then developed through

$$q_y(z) = \int_0^{y^*} \Lambda_y(z) \partial y \quad (4.7)$$

where  $y^*$  is defined as the updrift limit of perturbation, (i.e., impoundment), caused by the presence of the barrier.

### 4.3 Tidal Deconvolution

#### 4.3.1 "Simple" Tidal Deconvolution

In the first tidal deconvolution scheme developed, the average rate of horizontal profile change between surveys was calculated from the profile data for a series of reference elevations,  $z_0$ . Specifically,

for a given profile along the beach,

$$\left. \frac{\partial x}{\partial t} \right|_{z_0} = \frac{x(z_0, t_2) - x(z_0, t_1)}{t_2 - t_1} \quad (4.8)$$

where the coordinate  $x(z_0, t_1)$  refers to the baseline-referenced distance  $x$  corresponding to the reference elevation  $z_0$  for a survey taken at time  $t_1$ . In practice, the values of  $x$  for each profile were determined by linear interpolation of each profile's survey data for a series of NGVD elevations  $z_0$  vertically separated by  $\Delta z_0 = 0.1$  m spacing. Physically, Eq. (4.8) represents the average rate of volumetric accretion or recession at reference elevation  $z_0$  per unit beach width per unit beach height.

The average rate of horizontal profile change determined at each reference elevation, as described above, was assumed to correspond to the time- or tidally-averaged water depth calculated at each reference elevation over the interval for which each reference elevation was wetted. Specifically, the contour or elevation  $z$  (relative to the still water level) for each reference elevation  $z_0$  was approximated by

$$z = z_0 - \bar{\eta}(t_1, t_2) \quad (4.9)$$

where  $\bar{\eta}(t_1, t_2)$  is the mean value of the tide between times  $t_1$  and  $t_2$ . In general,  $t_1$  and  $t_2$  represent the first and last times, respectively, for which the reference elevation  $z_0$  was submerged by the swash or the mean water level; that is,  $z_0 < \bar{\eta}(t) + \bar{R}(t)$ , where  $\bar{R}$  is the average maximum vertical wave runup. Of course,  $t_1$  and  $t_2$  are bounded by the times at which the surveys of the given profile line were taken. This first tidal deconvolution technique, which relies on tidal-averaging, was termed "simple" tidal deconvolution.

Figure 4-2 illustrates the simple deconvolution approach for the case where the first survey of a profile line was taken on a rising tide and the second was taken on the falling tide. In Figure 4-2, the rate of profile change occurring at  $z_{01}$  is  $\Delta x_1/\Delta t_1$  which represents the transport process corresponding to a depth contour  $z = z_{01} - \bar{\eta}(\tilde{t}_1, \tilde{t}_2)$ . At reference elevation  $z_{02}$  the rate of profile change  $\Delta x_2/\Delta t_2$  corresponds to a depth contour  $z = z_{02} - \bar{\eta}(t_1, t_2)$ .

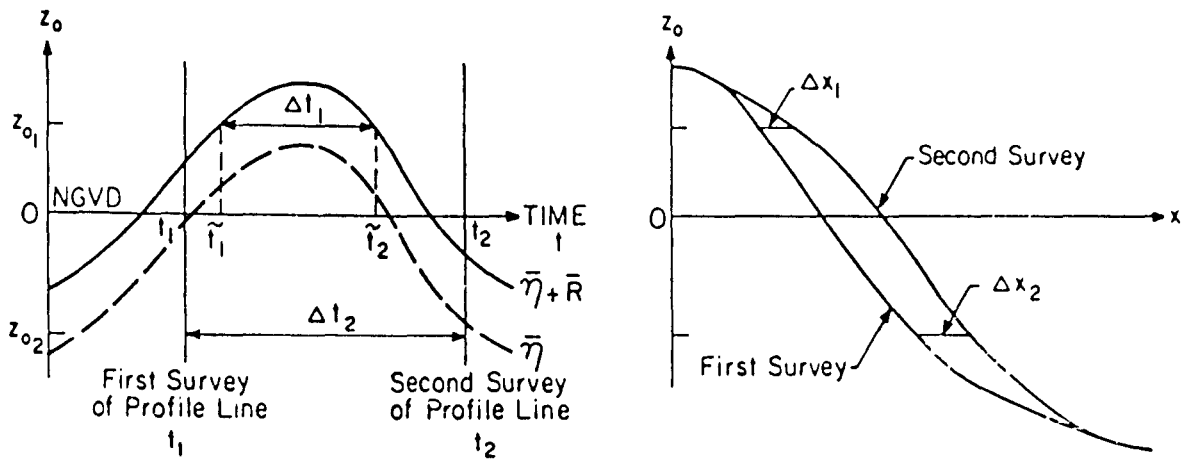


Figure 4-2: "Simple" tidal deconvolution: the rate of profile change,  $\Delta x/\Delta t$ , and an average value of the depth contour,  $z$ , is calculated for a given reference (NGVD) elevation  $z_0$ .

#### 4.3.2 Matrix Tidal Deconvolution

The second tidal deconvolution scheme, termed "matrix" tidal deconvolution, was based upon the assumption that the rate of horizontal profile change is uniquely determined for each water depth (for a given surf condition). Therefore, the measured (or interpolated) beach profile change at a given reference elevation is determined by the local rate of horizontal profile change associated with those depth contours which move with the tide across the given elevation. Specifically, with

reference to Eq. (4.1), the total transport function (or rate of profile change) defined at depth contour  $z$  will affect the NGVD elevation  $z_0$  during those times  $t$  when  $z$  is equal to  $z_0 - \bar{\eta}(t)$ . That is,

$$\Delta x(z_0) = \int_{t_1}^{t_2} \Lambda(z_0 - \bar{\eta}(t)) dt \quad (4.10)$$

Figure 4-3 illustrates the concept of this tidal deconvolution approach.

A discrete form of Eq. (4.10) was utilized for practical application to the data; i.e.,

$$\Delta x_n(z_{o_n}) = \sum_m^M a_{n,m} \Lambda_m(z_m) \quad (4.11)$$

The term  $a_{n,m}$  is the elapsed time over which NGVD elevation  $z_{o_n}$  was wetted to a depth  $z_m$ . During the time intervals  $a_{n,m}$ , a horizontal profile change  $\Delta x_n$  at  $z_{o_n}$  resulted due to the action of the transport function  $\Lambda_m = (dx/dt)_m$  associated with the contour  $z_m$ .

In Eq. (4.11), profile changes  $\Delta x_n$  between surveys were readily developed from the data base and archived for  $N$  values of  $z_{o_n}$  in  $\Delta z_0$  increments of 0.1 m, as described in the previous section. The values  $a_{n,m}$  were obtained for any given set of surveys through the use of Eq. (4.1) and tidal records,  $\bar{\eta}(t)$ . The discrete total transport function  $\Lambda_m(z_m)$  was evaluated, then, from the linear set of equations

$$\begin{array}{rcl} \Delta x_1(z_{o_1}) & a_{11} & a_{12} \quad \cdots \quad a_{1M} & \Lambda_1(z_1) \\ \Delta x_2(z_{o_2}) & = & a_{21} & a_{22} \quad \cdots \quad a_{2M} & \Lambda_2(z_2) \\ \vdots & & \vdots & & \vdots \\ \Delta x_N(z_{o_N}) & & a_{N1} & a_{N2} \quad \cdots \quad a_{NM} & \Lambda_M(z_M) \end{array} \quad (4.12)$$

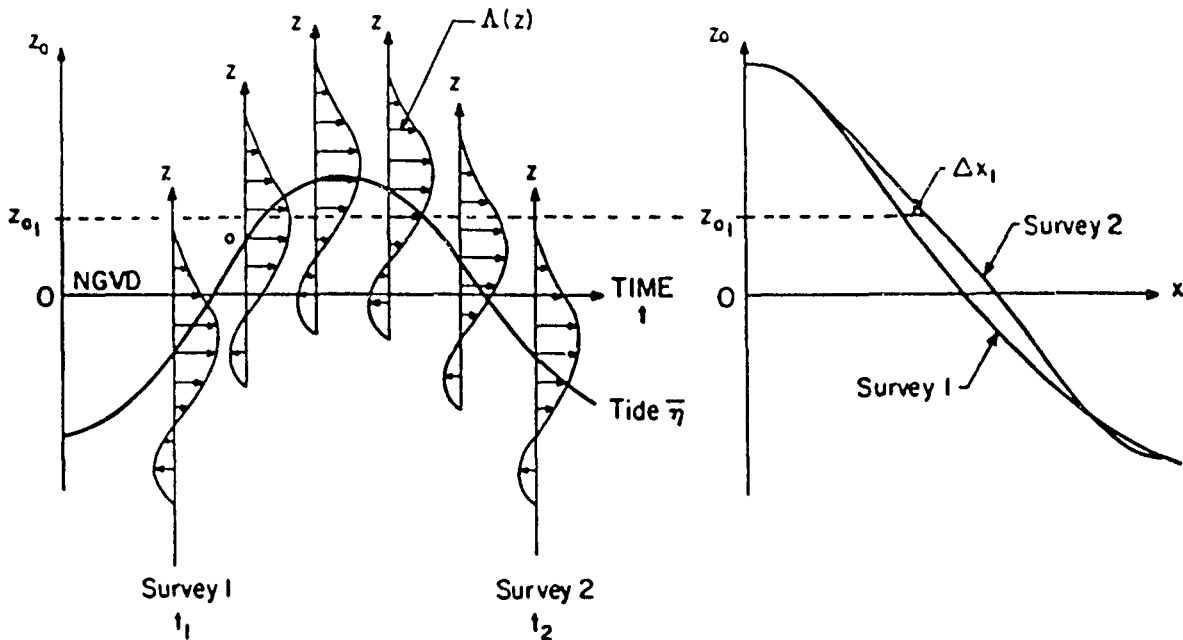


Figure 4-3: "Matrix" tidal deconvolution: the profile change,  $\Delta x$ , at a reference (NGVD) beach elevation,  $z_0$ , is assumed to be the result of a transport function,  $\Lambda(z)$ , which moves vertically across the profile with the tide.

Or, solving for  $\overline{\Lambda(z)}$ :

$$\overline{\Lambda(z)} = A^{-1} \cdot \overline{\Delta x(z_0)} \quad (4.13)$$

Calculation of the elements of matrix A is described in Appendix B.

In the discrete approach suggested by Eq. (4.12), the beach is essentially divided into N horizontal layers of vertical dimension  $\Delta z_0$ . Each layer grows or recedes horizontally by the amount  $\Delta x_n$  over the survey period of interest. The highest layer on the beach for which  $\Delta x_n$  data is available is denoted  $n=1$ ; the deepest layer is  $n=N$ . Similarly, the total transport function is divided into M discrete values which are defined at the center,  $z_m$ , of M depth contour layers. Each depth contour layer has a thickness  $\Delta z$ . The top surface of the

upper-most contour layer,  $z_1 + \frac{1}{2} \Delta z$ , is the maximum average vertical run-up  $\bar{R}$ . The bottom surface of the deepest layer, ( $z = z_M - \frac{1}{2} \Delta z$ ), must correspond to the greatest water depth which covered any part of the surveyed beach for which  $\Delta x_n$  data are available; that is,

$$z_M - \frac{1}{2} \Delta z = z_{o_N} - \bar{\eta}_{\max}(t_1, t_2) \quad (4.14)$$

where  $t_1$  and  $t_2$  are the time limits over which  $\Delta x_N$  was measured. It can be shown that the appropriate spacing of the depth contours is selected as

$$\Delta z = \frac{N-1}{M} \Delta z_o \quad (4.15)$$

For  $N=M$ , and reasonably large values of  $N$  (or correspondingly small values of  $\Delta z_o$  relative to the tidal range),  $\Delta z$  is approximately equal to  $\Delta z_o$ . For the limiting case,  $\Delta z = \Delta z_o$ , the highest layer on the beach,  $z_{o_1}$ , is wetted only by the upper-most depth contour  $z_1$  (which corresponds to the top of the swash zone). The second-highest layer on the beach,  $z_{o_2}$ , is wetted by the upper two depth contours: contour  $z_1$  during the interval just before and after peak high tide, and contour  $z_2$  during the peak high tide (while  $z_{o_1}$  is wetted by  $z_1$ ). One can extend this reasoning down the beach through layer  $z_{o_N}$  and will find that  $A$  is a lower triangular matrix. The solution  $\bar{\Lambda}(z)$  for such a matrix is very simple. From Eq. (4.13),

$$\begin{aligned} \Lambda_1(z_1) &= \frac{1}{a_{11}} \Delta x_1 \\ \Lambda_2(z_2) &= \frac{1}{a_{22}} [\Delta x_2 - a_{21} \Lambda_1] \\ &\vdots \\ \Lambda_m(z_m) &= \frac{1}{a_{mm}} [\Delta x_m - \sum_n^{m-1} a_{mn} \Lambda_n] \end{aligned} \quad (4.16)$$

The solution for  $\Lambda_m(z_m)$  "ripples" from the top of the swash zone down through the greatest depth contour  $z_M$ . Unfortunately, survey errors reflected by the values  $\Delta x_n$  will propagate through such a solution scheme and create oscillatory instabilities. For example, an underestimate of  $\Delta x_1$  will generate a too-low value of  $\Lambda_1$ . This will lead to an overestimate of  $\Lambda_2$  in order to satisfy the value  $\Delta x_2$ . This, in turn, will lead to a compensating underestimate of  $\Lambda_3$ , and so on.

If  $N$  is large and  $N=M$  such that  $\Delta z_o \approx \Delta z$  and no linear apportionment is done in the creation of the elements  $a_{n,m}$  (see Appendix B), then it can be shown that  $A$  is a lower triangular banded matrix for which each row in the band is identical. The bandwidth  $K_b$  is equal to the number of  $z_o$  contours which the tide  $\bar{\eta}$  passed through during the period over which the  $\Delta x$  values were obtained. For such a case, the "ripple" solution of  $\overline{\Lambda(z)}$  described by Eq. (4.16) comes about because the first  $K_b-1$  beach layers,  $z_{o1}, z_{o2}, \dots, z_{o_{K_b-1}}$ , were wetted by only 1, 2, ...  $K_b-1$  separate depth contours, respectively. The "ripple" solution is avoided if the set of equations (Eqs. (4.12) or (4.13)) is over-constrained; that is, if  $N > M$ . It appears appropriate that a reasonable over-constraint is to let

$$M = N - (K_b - 1) \quad (4.17)$$

Accordingly, from Eq. (4.15),

$$\frac{\Delta z}{\Delta z_o} = \frac{N-1}{N-K_b+1} \quad (4.18)$$

The over-constrained set of equations (that is, Eqs. (4.12) or (4.13), where  $N > M$ ) are solved for  $\overline{\Lambda(z)}$  by a least-squares technique described in Appendix C.

Valid application of the matrix tidal deconvolution requires that both cross-shore and longshore processes are quasi-steady during the time interval between successive surveys and that neither process is affected by the gradual accretion (or erosion) caused by longshore accumulation in the trap or background cross-shore processes. In its simplest form, the technique also requires that the measured beach profiles are monotonic; that is, that the locations of each reference elevation across the profiles are uniquely defined. Additionally, matrix tidal deconvolution assumes that the transport processes are dependent only upon local depth and not, among other parameters, local bed slope. Dean (1977) suggests that profile change is dependent upon both parameters; however, it is noted that for the data collected in the field experiments, the slope was relatively uniform along most of the measured profiles, and so the effect of a non-uniform beach slope in the tidal deconvolution may be small for the field data.

#### 4.3.3 Illustrative Evaluation of Tidal Deconvolution through Numerical Simulation

A numerical simulation was conducted to evaluate each of the three tidal deconvolution techniques described above: (a) simple deconvolution, (b) matrix deconvolution where  $N=M$ , and (c) least-squares matrix deconvolution where  $N > M$ . For the simulation studies, arbitrary but reasonable initial beach profiles,  $x(z_0, t_0)$ , tidal fluctuation,  $\bar{\eta}(t)$ , and total transport functions,  $\hat{\Lambda}(z)$ , were specified. The simulation proceeded in a manner similar to that graphically illustrated in Figure 4-3. The initial beach profile changed in response to the prescribed transport function and tidal water level according to the numerical scheme

$$\hat{x}_n(z_{o_n}, t_i) = \hat{x}_n(z_{o_n}, t_{i-1}) + \hat{\Lambda}(z) \cdot (t_i - t_{i-1}) \quad (4.19)$$

That is, the profile change at fixed elevation  $z_{o_n}$  was determined by the prescribed transport function  $\hat{\Lambda}(z)$  (where depth contour  $z$  corresponds to the still water depth at fixed elevation  $z_{o_n}$  during the time step  $t_{i-1}$  to  $t_i$ ).

Each of the three tidal deconvolution algorithms was utilized individually in an attempt to recover the prescribed total transport function  $\hat{\Lambda}(z)$  from the numerically-simulated profile changes  $\Delta\hat{x}_n$  and the simulated tidal data  $\bar{\eta}(t)$  for arbitrary times  $t_1$  to  $t_2$ . The tidally-deconvolved transport functions  $\Lambda(z)$  were then compared to the prescribed transport functions  $\hat{\Lambda}(z)$ . The total rms error between the profile changes generated by the deconvolved transport functions  $\Delta x$  and the prescribed transport functions  $\Delta\hat{x}$  was calculated as

$$\epsilon_{tot} = \sqrt{\frac{\sum_n^N (\Delta x - \Delta\hat{x})_n^2}{\sum_n^N (\Delta\hat{x})_n^2}} \quad (4.20)$$

Since each of the tidal deconvolution techniques originally rely on the measured profile changes to calculate the transport function  $\Lambda(z)$ , a "perfect" deconvolution would result in a tidally-deconvolved estimate of  $\Lambda(z)$  which would exactly retrieve the measured profile changes  $\Delta\hat{x}$ . Hence,  $\epsilon_{tot}$  would be identically zero.

Several simulation cases were studied for various initial profiles and prescribed total transport functions  $\hat{\Lambda}(z)$ . Some results of one representative simulation case are described below for an initial profile of the form

$$\hat{x}(z_o, t=0) = \begin{cases} -15 z_o & \text{for } z_o > 0 \\ 31.6 |z_o|^{3/2} & \text{for } z_o < 0 \end{cases} \quad (4.21)$$

Profile changes were numerically simulated for the arbitrarily prescribed total transport function

$$\hat{\Lambda}(z) = 1.2 (z+0.8)^3 \quad (4.22)$$

during a simulated tidal record

$$\bar{\eta}(t) = 1.0 \sin \left( \frac{\pi}{6} t - \frac{\pi}{6} \right) \quad (4.23)$$

A time step  $\Delta t=0.25$  was utilized in the simulation. Figure 4-4 illustrates the original beach profile at time  $t=0$  and subsequent profiles at times  $t=1.0, 3.25,$  and  $7.5$ . The tidal fluctuation,  $\bar{\eta}(t)$ , is also shown.

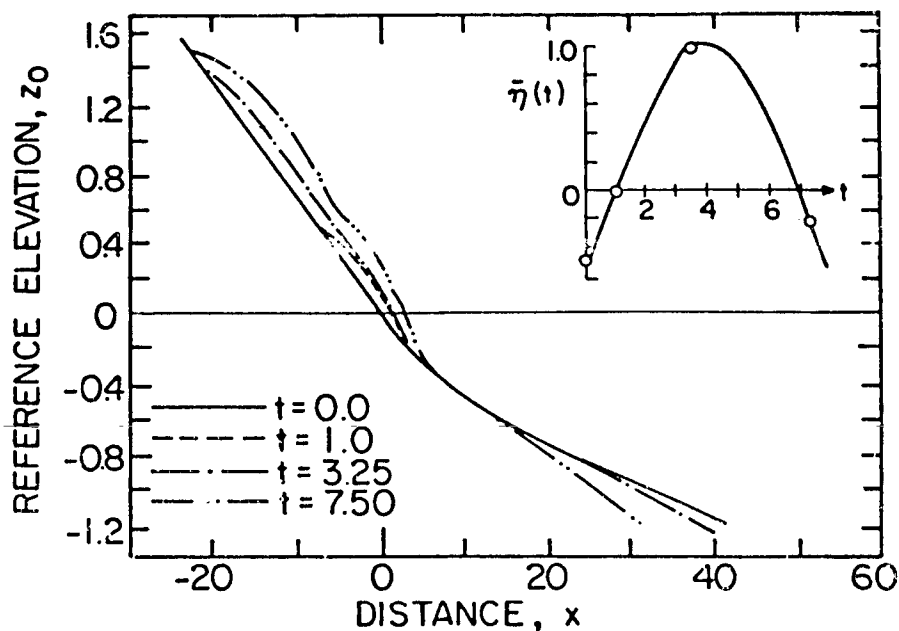


Figure 4-4: Simulated profile changes over time for a beach of given initial profile subjected to a prescribed total transport function and fluctuating tidal water level.

Figure 4-5 illustrates estimates of the transport function developed using each of the three tidal deconvolution algorithms from numerically-simulated profile change data between times  $t_1=3.25$  and  $t_2=7.5$ . The prescribed transport function  $\hat{\Lambda}(z)$ , Eq. (4.22), is shown by the dashed line. It is noted that the simple deconvolution technique (Fig. 4-5a) does not yield  $\Lambda(z)$  information for the deeper contours as contrasted to the matrix techniques. This limiting feature of the simple technique is typical and expected since the simple technique averages depth contours over time for a given fixed elevation  $z_0$ . Figure 4-5b illustrates the oscillatory instabilities associated with the  $N=M$  matrix technique, described earlier. In this case, the instabilities are triggered by slight numerical (discretization) error rather than survey error. The least-squares (over-constrained) matrix technique (Fig. 4-5c) yields the best estimate of the prescribed (simulated) transport function. Total rms errors in profile-change calculation using the tidally deconvolved transport functions are 29%, 2%, and 3%, respectively, for the simple,  $N=M$  matrix, and least-squares (over-constrained) matrix techniques.

In an effort to address the effect of survey error upon the tidal deconvolution techniques, random noise was introduced into the simulated profile change data. The noise represented no more than  $\pm 15\%$  of the actual simulated profile change at any elevation  $z_0$ . Figure 4-6 illustrates estimates of the prescribed transport function  $\hat{\Lambda}(z)$  Eq. 4.22, using each of the three tidal deconvolution algorithms from the "noisy" profile change data simulated between times  $t_1=1.0$  and  $t_2=3.25$ . It is evident that the simple technique (Fig. 4-6a) is far less sensitive to the random "error" than the matrix techniques. This

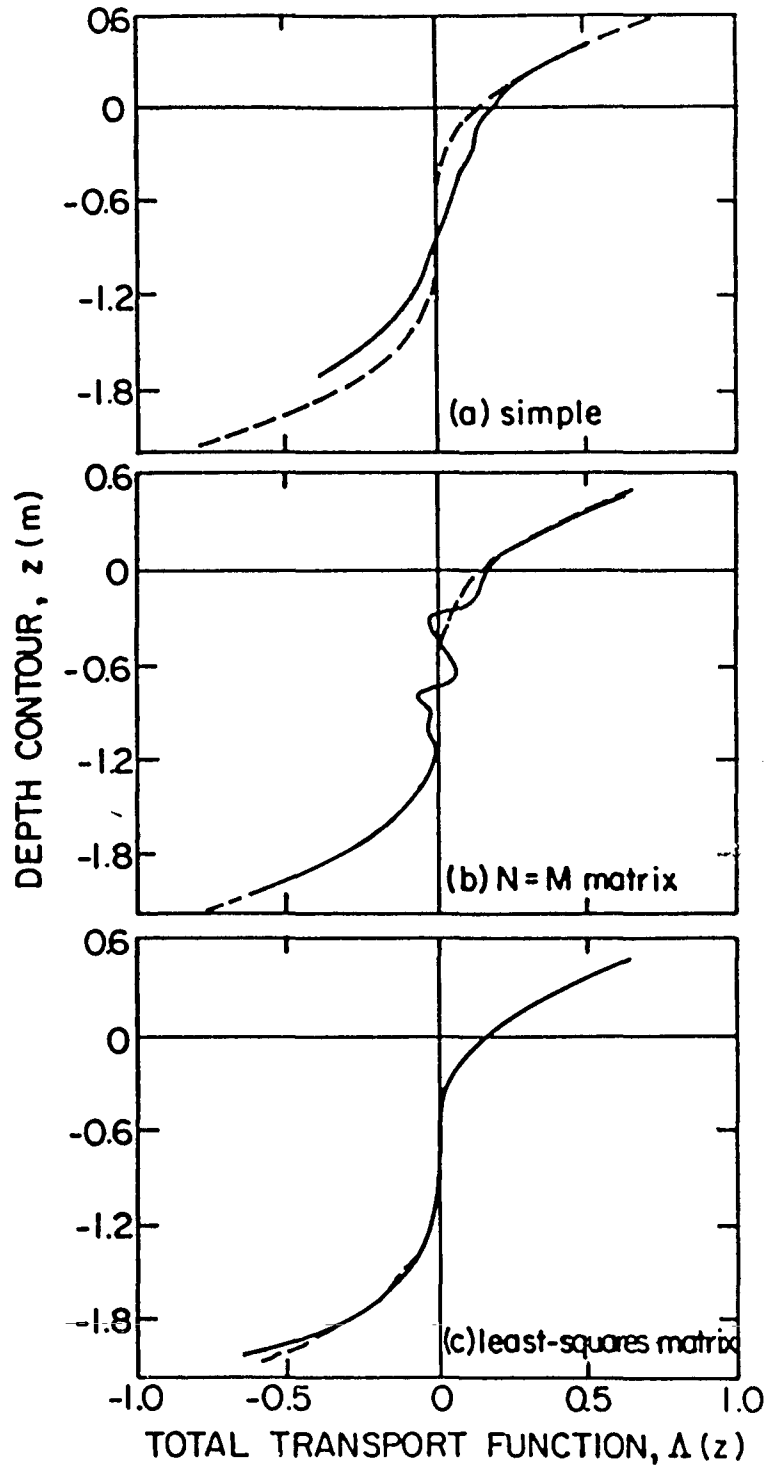


Figure 4-5: Comparison of the tidally deconvolved transport functions (solid lines) and the actual prescribed transport function (broken lines) for the (a) simple, (b)  $N=M$  matrix, and (c) least-squares matrix tidal deconvolution schemes. Numerical simulation.

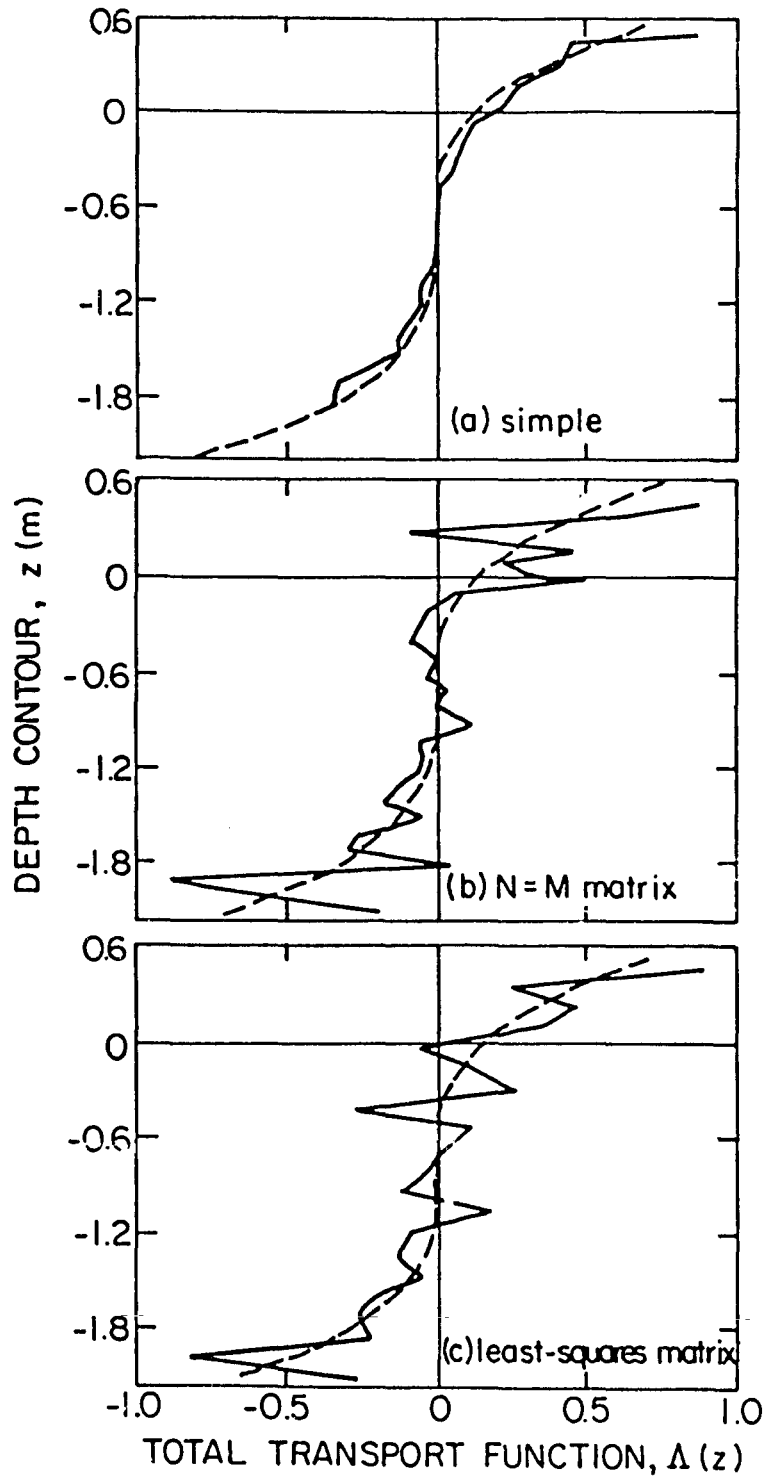


Figure 4-6: The transport functions deconvolved from "noisy" profile-change data (solid lines) compared to the actual prescribed functions (broken lines). Numerical simulation.

is not surprising, since the simple technique is effectively an "averaging" technique and therefore inherently smooths out random noise. The matrix techniques exhibit oscillatory instability about the prescribed function  $\hat{\Lambda}(z)$ . Total rms errors in recovery of the simulated "profile change" data using the simple,  $N=M$  matrix, and least-squares (over-constrained) matrix tidal deconvolution techniques are 23%, 8%, and 6%, respectively. Similarly, it is not surprising that the least-squares technique is slightly better than the  $N=M$  technique here since the former is also an inherently smoothing technique.

Although the erratic-looking transport functions developed by the matrix techniques yield profile changes which agree reasonably well with the given simulated data, it is reasonable to state that these deconvolved functions poorly represent the actual transport function. Accordingly, each of the deconvolved transport functions was smoothed by a running filter over depth  $z$ . The structure of the filter is illustrated in Figure 4-7. The smoothed transport functions from the

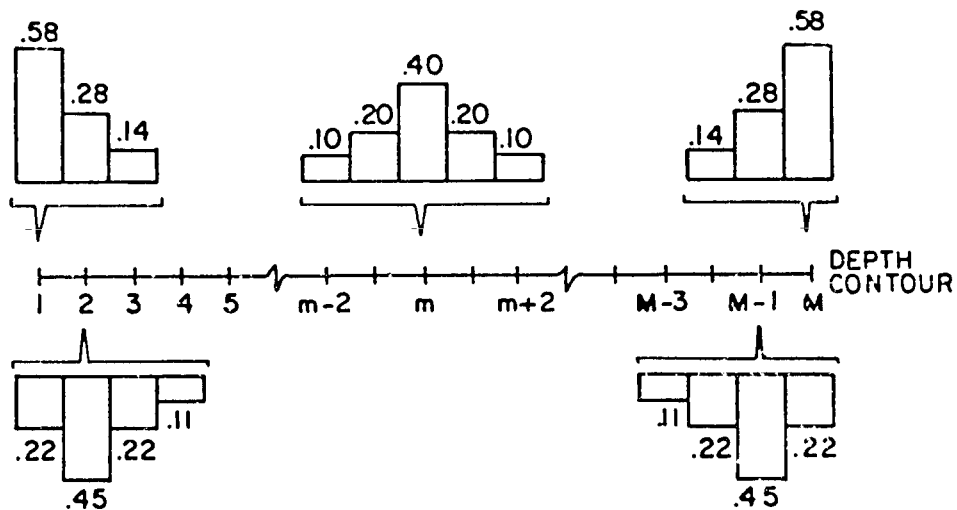


Figure 4-7: The running filter used to smooth the transport functions developed through the matrix tidal deconvolution schemes.

$N=M$  matrix technique and the least-squares matrix technique are shown in Figure 4-8 a and b, respectively, for the "noisy" simulation case of Figure 4-6. Smoothing the matrix techniques' results increases the error between the "retrieved" profile-changes and the simulated "noisy" profile changes (by about 5% for each technique in this case).

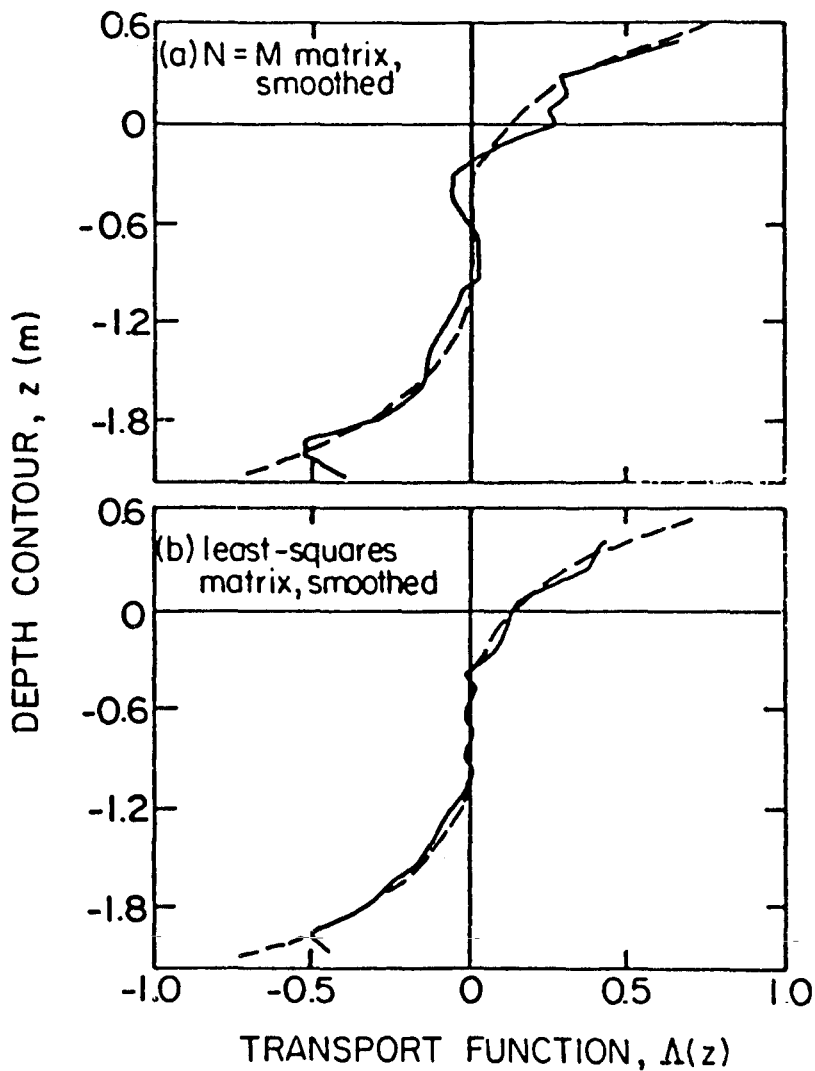


Figure 4-8: The smoothed transport functions (solid lines) compared to the actual prescribed transport functions (broken lines) developed from (a)  $N=M$  matrix and (b) least-squares matrix tidal deconvolution of "noisy" profile-change data. Numerical simulation.

Physically, this usually means that the magnitudes of the profile changes calculated from the smoothed deconvolved transport functions are not as great as those calculated from the un-smoothed functions. This, however, may be a desirable feature of the smoothing process for transport functions which are deconvolved from survey data contaminated by random error.

It is noted that several different smoothing filters were applied to the deconvolved transport functions generated from a number of survey-error simulation studies. The filter illustrated in Figure 4-7 generally gave the most satisfactory results; that is, relatively smooth functions,  $\Lambda(z)$ , with minimum increase in total rms error.

For the least-squares matrix technique, the degree of over-constraint,  $N > M$ , was also investigated. In general, it was found that the relation  $M = N - (K_b - 1)$ , expressed by Eq. (4.18), was satisfactory. Tighter constraint,  $M < N - (K_b - 1)$ , resulted in poorly-defined, severely discontinuous transport functions. Less constraint,  $N - (K_b - 1) < M < N$ , resulted in oscillatory, unstable transport functions which, of course, tended to the  $N=M$  matrix results as  $M \rightarrow N$ . Henceforth, all references to the least-squares matrix tidal deconvolution technique are assumed to be for the case  $M = N - (K_b - 1)$ .

#### 4.3.4 Tidal Deconvolution and Field Data

As part of a further investigation of tidal deconvolution, profile loops 4 and 5, taken 9 meters updrift of Groyne #4, were selected for tidal deconvolution using the (a) simple, (b)  $N=M$  matrix, and (c) least-squares (over-constrained) matrix techniques. The deconvolved transport functions  $\Lambda(z)$  obtained from each technique are shown in Figure 4-9.

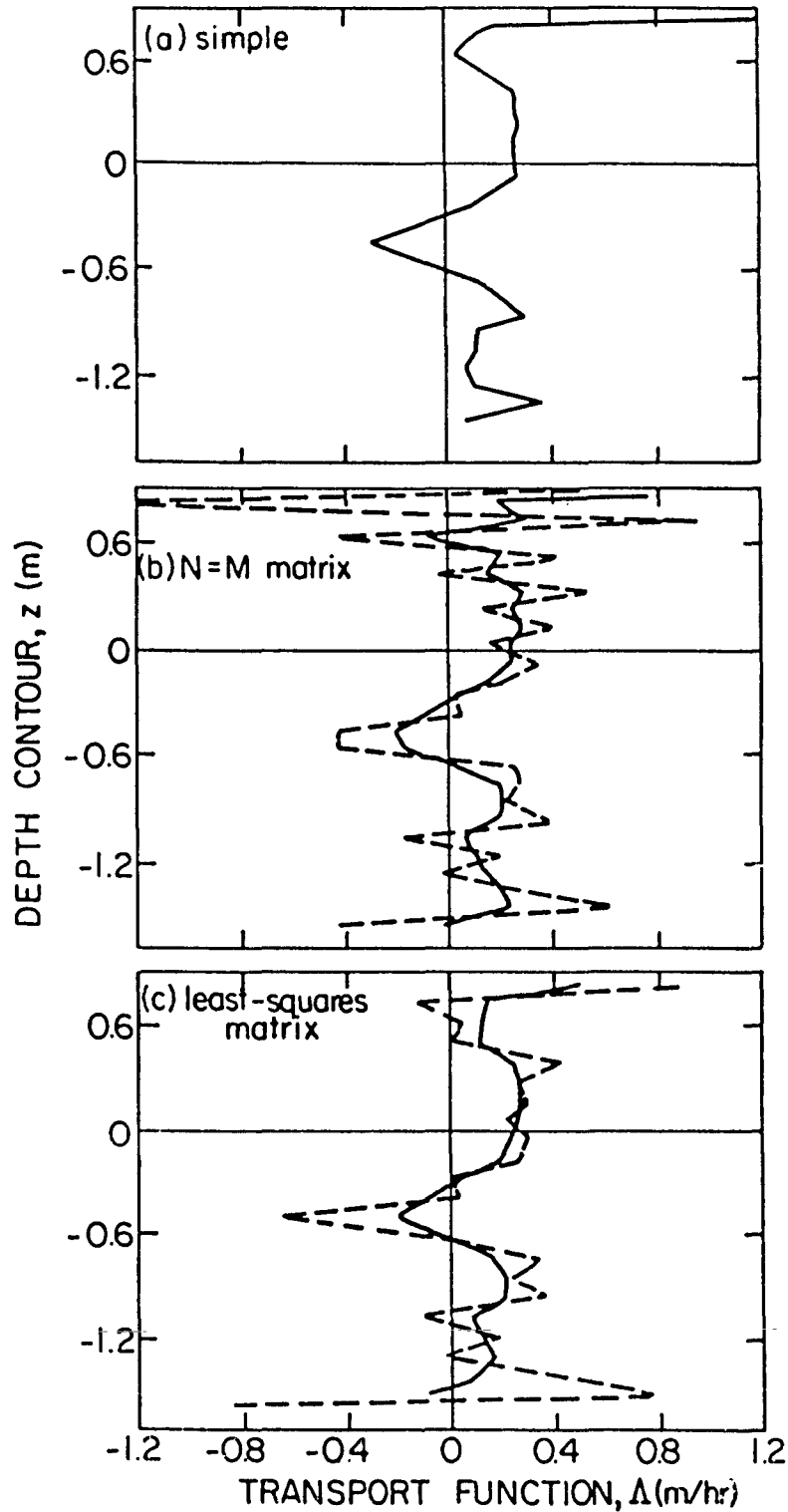


Figure 4-9: Tidally deconvolved total transport functions,  $\Delta(z)$ , developed for profile change data from survey loops 4 and 5 of Groyne #4, 9 meters updrift of the barrier. The solid (broken) curves in (b) and (c) represent the smoothed (unsmoothed) results of the matrix techniques.

Oscillatory instabilities appear in the results of the matrix solutions--similar to those observed for the case of simulated survey error (shown in Figure 4-6). Accordingly, these matrix results were smoothed by the running filter shown in Figure 4-7; the results are illustrated by solid lines in Figure 4-9 b and c. The total rms errors in retrieval of the measured profile changes using the deconvolved transport function are (a) 40% for the simple technique, (b) 2% for the un-smoothed N=M matrix technique and 36% for the smoothed result, and (c) 10% for the un-smoothed least-squares matrix technique and 49% for the smoothed result. Figure 4-10 compares the smoothed transport functions deconvolved using the matrix techniques and the un-smoothed transport function deconvolved from the simple technique (shown separately in Figure 4-9 a, b, and c). All three agree reasonably well and the simple

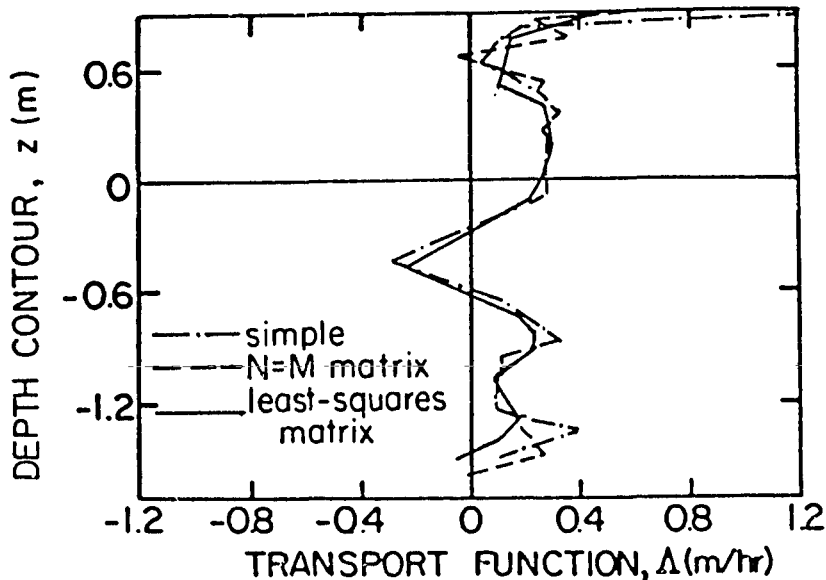


Figure 4-10: Comparison of the tidally deconvolved total transport functions,  $\Delta(z)$ , developed using the simple, smoothed (N=M) matrix, and smoothed least-squares matrix techniques. Field data from Groyne #4, 9 m updrift, profile loops 4 and 5.

technique develops the transport function  $\Lambda(z)$  over depth contours which are nearly as deep as for the matrix results. This is because the profile loops used for this test were taken over a fairly steady high tide such that the effect of the tidal fluctuation was relatively small.

Figure 4-11 illustrates the transport functions,  $\Lambda(z)$ , developed using each of the three tidal deconvolution techniques for the data of profile loops 1 and 2 taken 9 m updrift of Groyne #3. Once again, the matrix techniques generated erratic functions which were then smoothed by the running filter shown in Figure 4-7. The total rms errors associated with each result are (a) 40% for the simple technique, (b) 2% for the un-smoothed N=M matrix technique and 129% for the smoothed result, and (c) 9% for the un-smoothed least-squares technique and 17% for the smoothed result. As seen in the figure, smoothing the erratic results of the N=M matrix technique yields an almost uniform, zero-valued transport function, so that the profile changes predicted by the smoothed function are very small. This explains the large increase in rms error for the smoothed result of the N=M matrix technique as compared to the un-smoothed result. Profile loops 1 and 2 were taken over the greater portion of a high-low-high tidal fluctuation, hence the simple technique's results are seen to be a smoothed version of the least-squares matrix technique's results since the former technique smears the effect of the tide whereas the latter technique distinguishes the effect of the tide.

In general, for a dozen pairs of field profiles which were randomly selected for evaluation by all three tidal deconvolution algorithms, a total transport function,  $\Lambda(z)$ , was most reasonably and reliably estimated by the smoothed result of the least-squares matrix technique.

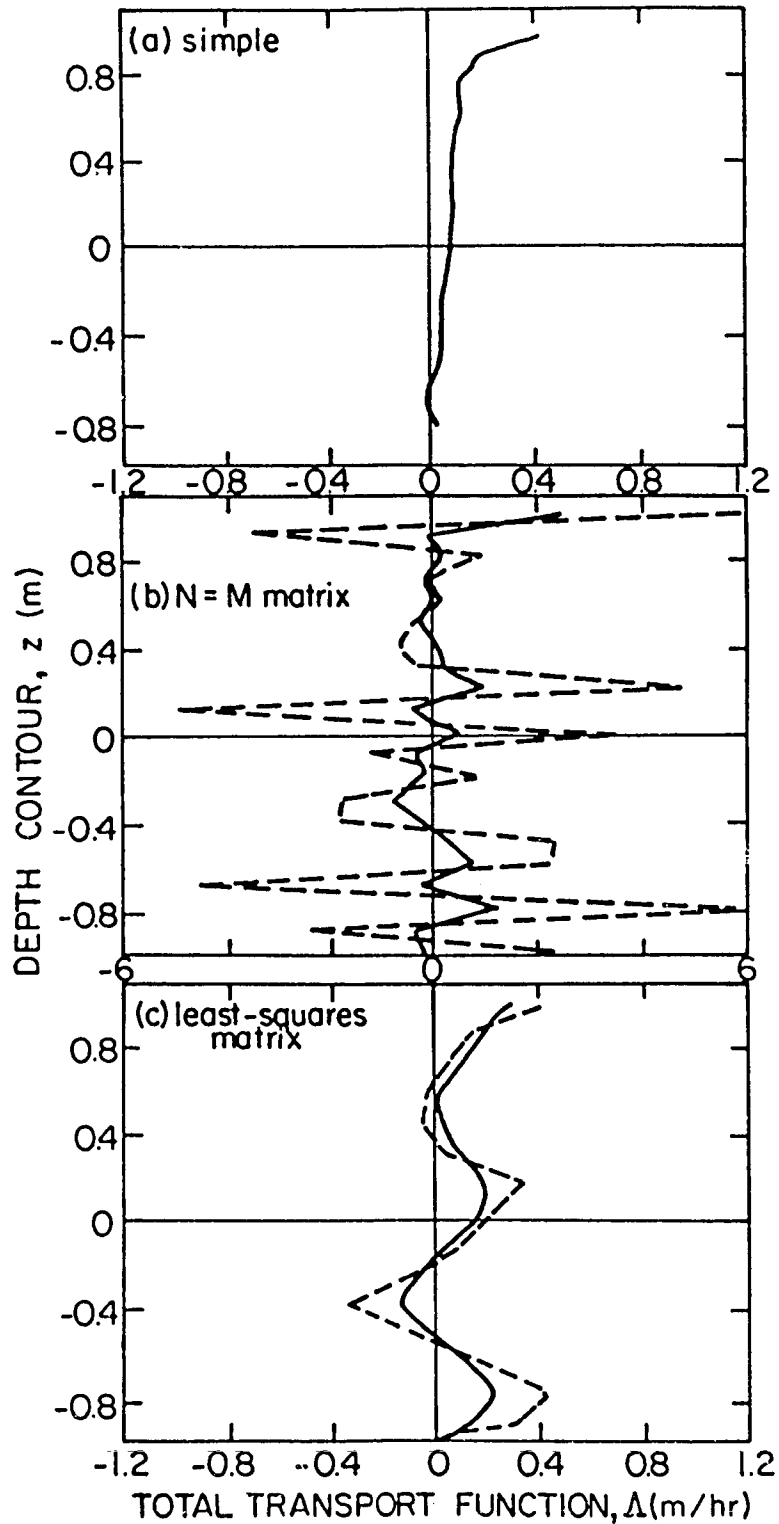


Figure 4-11: Tidally deconvolved total transport functions,  $\Delta(z)$ , developed for profile change data from survey loops 1 and 2 of Groyne #3, 9 meters updrift of the barrier. The solid (broken) curves in (b) and (c) represent the smoothed (unsmoothed) results of the matrix techniques.

Figure 4-12 illustrates the profile changes generated by smoothed transport functions  $\Lambda(z)$  developed using the least-squares matrix technique for three different profile pairs from the field data of Groyne #4. It is seen that lesser-quality deconvolved transport functions (i.e., those associated with higher rms error values), generally retrieve the correct trend of the profile-changes, but tend to underestimate (and occasionally overestimate) the erosion, or accretion at given reference elevations. Transport functions associated with total rms error values of less than about 30% generally reproduce the measured profile changes very well; that is, within the range of probable survey error. (It is noted that the average vertical survey error found with the OMNI system, 1.5 cm, is about 30% of the average vertical profile change measured between surveys near the groyne.) Of course, the unsmoothed transport functions from the matrix techniques can generate the measured profile changes fairly accurately in all cases, but the erratic appearance of the un-smoothed functions is unsatisfactory for the purposes for which the transport function values are intended--as will become more clear in the following sections.

#### 4.4 Removal of Cross-Shore Transport Signals

The tidally-deconvolved total transport functions,  $\Lambda(z)$ , contain both cross-shore and longshore components and possibly anomalous along-shore variation components. Assuming that the cross-shore transport component is constant along the beach at a given depth contour  $z=-h$ , and assuming that the longshore component is represented by an exponential function which vanishes some distance updrift of the groyne, it is reasonable to approximate the total transport function as

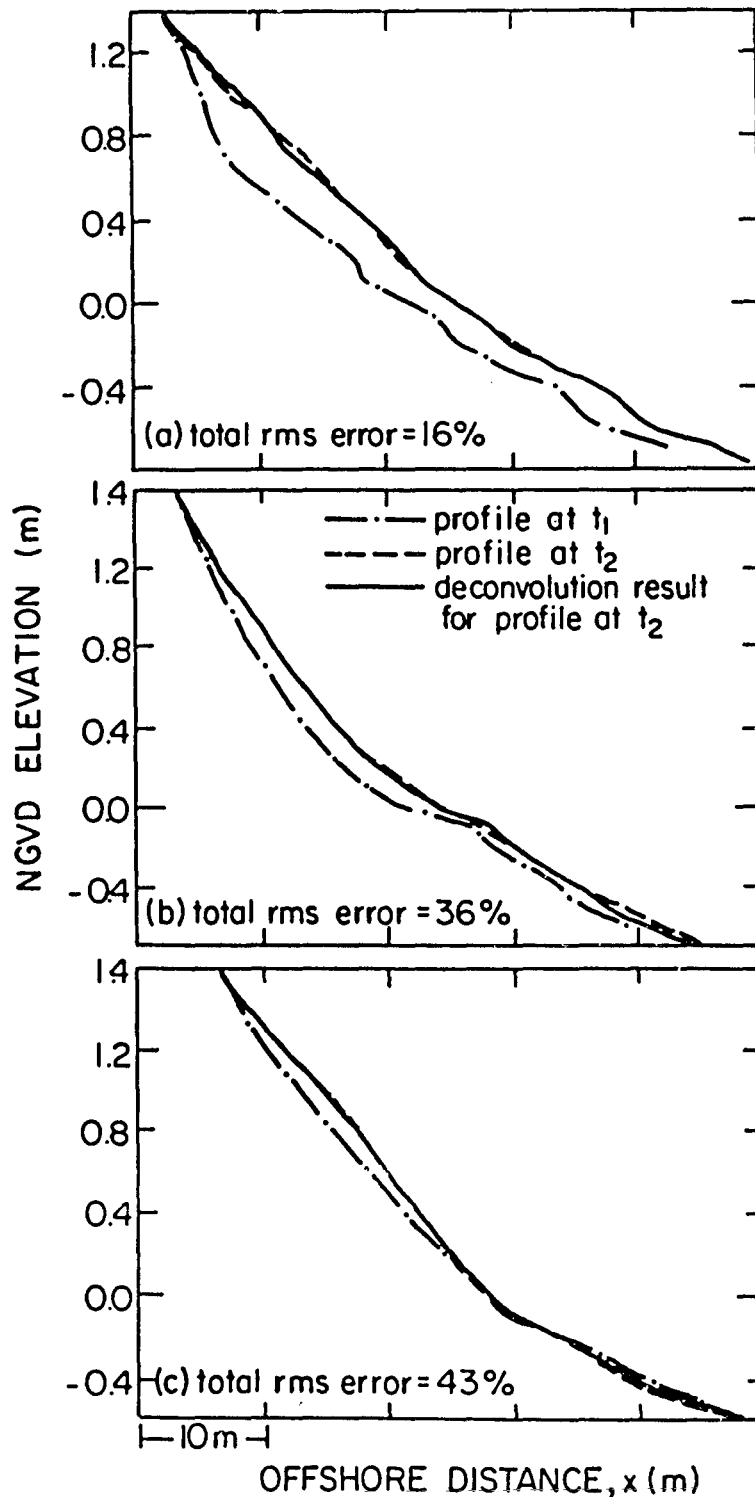


Figure 4-12: Comparison of the measured profiles at survey time  $t_2$  and the profiles calculated from the tidally deconvolved total transport function at time  $t_2$  using the least-squares (over-constrained) matrix technique. Field data from profile loops 1 and 5, Groyne #4, (a) 3 m, (b) 18.3 m, and (c) 216 m, updrift of the barrier.

$$\Lambda(z) = \Lambda_y(z) + \Lambda_x(z) = A(z) e^{-B(z)|y|} + C(z) \quad (4.24)$$

on the updrift side of the barrier. In Eq. (4.24), for given contour  $z$ , the exponential function (which is maximum near the barrier and decays in the updrift direction) represents the impoundment against the barrier caused by longshore transport. The constant  $C$  represents the cross-shore component of transport which is assumed to be uniform along the beach for the given contour  $z$ . The longshore component coefficients  $A(z)$  and  $B(z)$  and the cross-shore component coefficient  $C(z)$  may be evaluated for each depth contour by fitting Eq. (4.24) to the deconvolved total transport values,  $\Lambda(z)$ , using a least-squares technique (see Appendix D). The estimate of the cross-shore component  $C(z)$  should also correspond approximately to the average value of the total transport function determined from profile changes far updrift of the barrier (say, at least farther than one groyne length or one surf zone width updrift).

Poorly conditioned total transport values,  $\Lambda(z)$ , can be fit better by integrating Eq. (4.24) along a depth contour and fitting the result to the cumulative total transport function updrift of the barrier along this contour; i.e.,

$$\int_0^y \Lambda(z) dy = \frac{A(z)}{B(z)} (1 - e^{-B(z)|y|}) + C(z)y \quad (4.25)$$

However, use of Eq. (4.25) with the field data was not preferred since the deconvolved values of  $\Lambda(z)$  far updrift of the barrier were heavily weighted relative to the values closer to the barrier. (This was

because the spacing between profiles along the beach (i.e.,  $\Delta y$ ) increased with distance from the barrier.)

If anomalous longshore features (such as cusps) contributed to the total transport function, then fitting Eqs. (4.24) or (4.25) to the deconvolved  $\Lambda(z)$  values will generally "smooth" these anomalous contributions (assuming that the profile spacing is at least less than half the wavelength of the anomalous features). If "single point" anomalies were present along the beach (such as scour holes or rips), then the fit-quality of Eqs. (4.24) or (4.25) to the data will be poor.

Fitting deconvolved transport data with polynomial expressions and Fourier-series type expressions generally produces unsatisfactory results (unless one is dealing with dense profile data on beaches rich in longshore features). For the field data, the profiles--and therefore the deconvolved total transport data along a contour--were not sufficiently spatially intense to define anomalous longshore features without aliasing. However, few longshore features besides the impoundment fillet were observed in the survey area for Groynes #2, #3, and #4.

The quality of fit of the non-cumulative transport expression, Eq. (4.24), was defined for each depth contour as

$$\epsilon_{nc} = \sqrt{\frac{\sum_1^I [(Ae^{-B|y_i|} + C - \Lambda_i)]^2}{\sum_1^I \Lambda_i^2}} \quad (4.26)$$

and for the cumulative transport expression, Eq. (4.25), as

$$\epsilon_c = \sqrt{\frac{\sum_1^I [(\frac{A}{B}(1-e^{-B|y_i|}) + Cy_i - \int_0^y \Lambda_i dy)]^2}{\sum_1^I (\int_0^y \Lambda_i dy)^2}} \quad (4.27)$$

where  $I$  is the number of deconvolved total transport values determined along the depth contour. Values of  $\epsilon_{nc}$  or  $\epsilon_c = 0$  represent a perfect fit to the data. In Eqs. (4.26) and (4.27), it is implied that  $A$ ,  $B$ ,  $C$ ,  $\Lambda$ ,  $I$ ,  $\epsilon_{nc}$ , and  $\epsilon_c$  correspond to a depth contour  $z=-h$  of interest.

In practice, identification of a value (or range of values) of the cross-shore component  $C(z)$  of the total transport function  $\Lambda(z)$  was not always a rigid data interpretive process. As a general guideline, for a given contour, a single value of  $C(z)$  was identified using Eq. (4.24) if the quality of fit,  $\epsilon_{nc}$ , was less than about 0.25. For  $0.25 < \epsilon_{nc} < 0.5$ , the average value of  $C(z)$  determined through Eqs. (4.45) and (4.25) was used or, more often, a range of values of  $C(z)$  was selected--bounded by the values determined through Eqs. (4.24), (4.25), and/or the average value of the total transport function far updrift of the barrier. For  $\epsilon_{nc} > 0.5$ ,  $C(z)$  was taken as the far updrift average value of the total transport function plus or minus 30%. ("Far updrift of the barrier" refers here to at least one groyne length updrift of the barrier.) Figures 4-13 and 4-14 illustrate two examples from the field data of non-cumulative and cumulative "transport function fitting" along a depth contour. The quality of fit of each is indicated in the corner of each figure.

#### 4.5 Calculation of Longshore Transport Rate at a Depth Contour

Once a value or range of values of the cross-shore component  $C(z)$  of the total transport function was identified for a particular depth contour, the longshore component was obtained through

$$\Lambda_y(z) = \Lambda(z) - C(z) \quad (4.28)$$

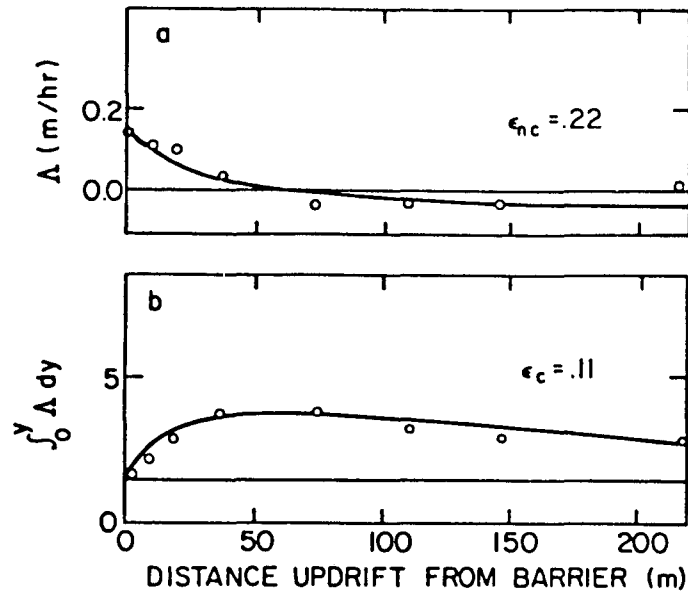


Figure 4-13: Fit of the total transport function along a depth contour using (a) non-cumulative values and (b) cumulative values. Field data from profile loops 1 and 2, Groyne #3, depth contour  $z = +0.3$  m.

The sediment impoundment rate along a depth contour due to longshore transport was then evaluated through:

$$\tilde{q}_y(z) = \int_0^{y_*} \Lambda_y(z) dy \quad (4.29)$$

where  $\tilde{q}_y(z)$  is a "non-adjusted" volumetric longshore sediment transport rate along depth contour  $z=-h$ , per unit depth. The meaning of "non-adjusted" is described below. The limit  $y_*$  refers to the updrift limit of perturbation (i.e., impoundment) caused by the presence of the barrier. In practice, the limit  $y_*$  was taken as the updrift location beyond which there was little or no contribution to the longshore

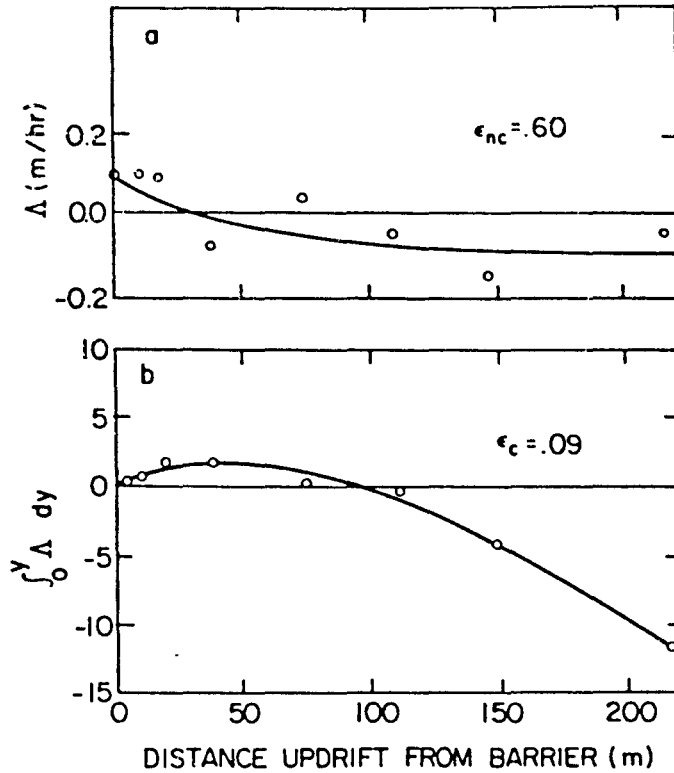


Figure 4-14: Fit of the total transport function along a depth contour using (a) non-cumulative values and (b) cumulative values. Field data from profile loops 1 and 3, Groyne #3, depth contour  $z = -0.2$  m.

sediment transport rate (or, the volumetric impoundment rate). Figure 4-15 illustrates the application of Eq. (4.29) for the two examples from the field data previously shown in Figures 4-13 and 4-14. Gross contributions to the impoundment rate (shown updrift of  $y_*$ ) are due to irregularities in the longshore component of the transport function  $\Lambda_y(z)$  which result from the approximate nature of the cross-shore component  $C(z)$  removed from the total transport function  $\Lambda(z)$ . It is noted that these irregularities "cancel out" far from the barrier. For many cases, a range of values of  $y_*$  were selected for each contour which reflected the author's best judgement of the updrift limit of impoundment (based

upon inspection of figures such as 4-13 and 4-14). The range of values identified for  $y_*$  and/or  $C(z)$  for each contour led to a range of values calculated for the ("non-adjusted") longshore transport rate  $\tilde{q}_y(z)$  for each contour. For plotting purposes, the average value of the range of  $\tilde{q}_y(z)$  along each contour was calculated, and the maximum and minimum extents of this range were taken as error bars for  $\tilde{q}_y(z)$ .

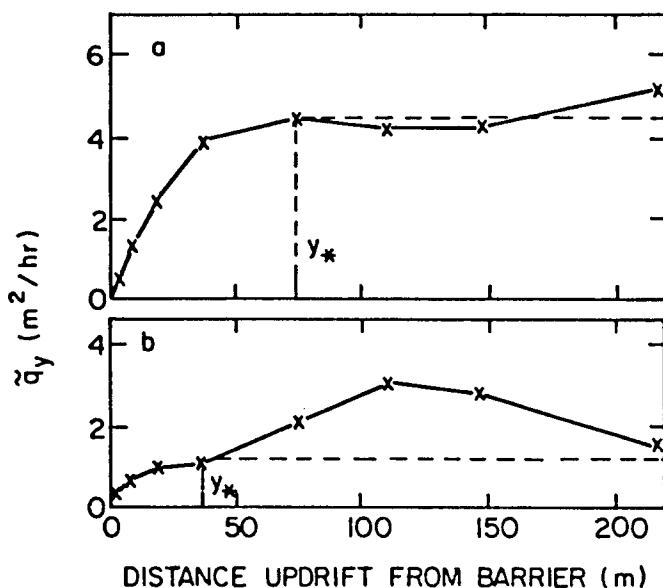


Figure 4-15: Integration of the longshore component of the total transport function,  $\Lambda_y(z)$ , updrift of the barrier in order to evaluate the volumetric rate of impoundment along the contour. Field data from Groyne #3, (a) profile loops 1 and 2,  $z = +0.3$  m, (b) profile loops 1 and 3,  $z = -0.2$  m.

Although the cross-shore component  $C(z)$ , was typically identified with reasonable confidence through the fitting of Eqs. (4.24) or (4.25), the longshore component,  $A(z) \exp[-B(z)|y|]$ , was not typically satisfactorily described. (This was because the impoundment fillet was not typically pure-exponential in character). Accordingly, it was not preferred to calculate the total longshore impoundment rate by

integrating the "fitted" longshore component of transport updrift of the barrier; that is, through the expression

$$\tilde{q}_y = \int_0^{\infty} A e^{-B|y|} dy = \frac{A}{B} \quad (4.30)$$

Instead,  $\tilde{q}_y$  was found through Eqs (4.28) and (4.29) as described above.

It is instructive to rewrite Eq. (4.29) for some particular depth contour  $z=-h$  as

$$\tilde{q}_y = \int_0^{y_*} \frac{dq_y}{dy} dy = q_y(y_*) - q_y(0) \quad (4.31)$$

or

$$\tilde{q}_y = -\int_0^{y_*} \frac{\partial x_\ell}{\partial t} dy \quad (4.32)$$

where  $\partial x_\ell / \partial t$  refers to the horizontal rate of profile change due to the longshore component of transport only. Also, it is recalled here that  $\tilde{q}_y$  refers to the "non-adjusted" longshore transport rate per unit depth. In Eq. (4.31),  $q_y(0) = 0$  if there is no sediment transport through or over the barrier; accordingly,

$$\tilde{q}_y = q_y(y_*) \quad (4.33)$$

Since  $q_y(y_*)$  represents the longshore transport rate at a location unperturbed by the presence of the barrier, it is demonstrated that Eq. (4.29) yields the longshore transport rate for the depth contour  $z=-h$  as if the beach was undisturbed.

For Eq. (4.32), it will be recalled that  $\partial x_\ell / \partial t$  is evaluated as  $\Delta x_\ell / \Delta t$  in practice; that is,  $\Delta x / \Delta t$ , but where the cross-shore component has been effectively removed. The value  $\Delta t$  is taken as the

elapsed time between surveys. However, since some contours were not blocked by the barrier for all time between surveys (due to gaps or low tide), the value  $\Delta t$  must be adjusted to reflect only the elapsed time during which longshore transport was effectively impounded by the barrier between surveys. Accordingly, the actual or "adjusted" estimate of the longshore transport rate was determined from

$$q_{\ell}(z) \equiv q_y(z) = \tilde{q}_y(z) \cdot \frac{\Delta t}{\Delta t_{\ell}(z)} \quad (4.34)$$

where  $q_{\ell}(z)$  is the "adjusted" local longshore transport rate at depth contour  $z=-h$ , and  $\Delta t_{\ell}(z)$  is the elapsed time between surveys for which contour  $z=-h$  was effectively blocked by the barrier. An illustrative example of the method by which the effective trapping time  $\Delta t_{\ell}(z)$  can be calculated for an arbitrary depth contour  $z_1$  is depicted in Figure 4-16.

#### 4.6 Limiting Depth Contours of Barrier Effectiveness

Unlimited application of Eq. (4.34), above, implies that the "adjusted" local longshore transport rate becomes very large or approaches infinity for depth contours which were barely blocked or never blocked by the barrier (i.e.,  $\Delta t_{\ell} \rightarrow 0$ ). When the elapsed time for which a depth contour was blocked,  $\Delta t_{\ell}$ , is considerably smaller than the total time between surveys,  $\Delta t$ , it seems reasonable to assume that the impoundment-related component of the measured profile change along the contour is suspect. Inappropriate application of Eq. (4.34) for these ineffectively blocked depth contours results in amplification of the suspect (dubious) impoundment-related transport signals (because  $Wt/\Delta t_{\ell} \gg 1$  for  $\Delta t_{\ell} \ll \Delta t$ ). Accordingly, a practical limit must be set



An alternate method to assess the effectiveness of the barrier at a particular depth contour is presented as follows. The effective time-weighted relief of the barrier,  $\overline{\Delta g}$ , may be approximated at M depth contours by

$$\overline{\Delta g} = \frac{1}{\Delta t} T \overline{\Delta g_o} \quad (4.35)$$

where  $\Delta t$  is the total time between survey loops and elements in the array  $\overline{\Delta g_o}$  represent the average relief of the barrier (above the bed) at NGVD elevations  $z_{o_n}$ . The elements  $t_{nm}$  in the matrix T represent the total time for which NGVD elevation  $z_{o_n}$  was occupied by depth contour  $z_m$ . For a tideless beach where  $z=z_o$ , the matrix T is diagonal with non-zero elements equal to  $\Delta t$  such that the product of  $1/\Delta t$  and T is the identity matrix.) In general application, however, one will readily note that Eq. (4.35) is a time-averaging scheme which yields the effective relief of the barrier above the bed for any depth contour which moves across the beach (and the barrier) with the tide.

The barrier was assumed to be potentially ineffective at depth contours for which the effective time-weighted barrier relief fell below a certain critical value. Typically, impoundment signals from the field data appeared dubious for depth contours with effective barrier relief above the bed of less than about 15 to 20 cm, or about 30% of the breaking wave height; hence, this value became a general (potential) limit for discounting impoundment data along a contour.

In practice, impoundment data (i.e., estimates of the local longshore transport rate) were excluded for depth contours which fell below the relative longshore trapping time criterion and/or the effective

barrier relief criterion described above. Insight to the quantitative selection of these criteria is gained from the presentation of the reduced data offered in the next chapter.

#### 4.7 Total Longshore Transport Rate

The total volumetric longshore sediment transport rate,  $Q_\ell$ , was found through

$$Q_\ell = \int_{-h_*}^R q_y(z) dz \quad (4.36)$$

where  $R$  and  $h_*$  are the contours corresponding to the maximum run-up and the limiting depth of longshore transport, respectively. In practice,  $h_*$  was taken as the deepest contour for which local longshore transport values were both available and reasonable (as described in the previous section). Accordingly, estimates of the total longshore sediment transport from the field data are low since local transport values most probably did not extend to contours as deep as the actual limit of transport. In several cases, however, data were available to a depth at least as great as the breaking depth (see Chapter 5).

#### 4.8 Expressing the Longshore Transport Distribution across the Surf Zone Width

The data analysis described up to this point has centered upon determination of the local longshore sediment transport rate per unit depth,  $q_\ell(z)$ . The local transport rate per unit offshore distance,  $q_\ell$ , was developed through the transformation:

$$q_\ell(x) = m(z) \cdot q_\ell(z) \quad (4.37)$$

where  $m(z)$  is the local bottom slope. For the data taken in the presence of tidal fluctuations,  $m(z)$  was taken as the bottom slope at the reference elevation  $z_0$  which, on tidal-average, corresponded to the elevation  $z$  (or depth contour  $z=-h$ ).

The details of the transformation are described below. A representative beach profile (the calculated average profile between surveys at a location far updrift of the barrier) was described at selected uniformly-spaced locations,  $x_1$ , in the offshore (horizontal) direction. The depth  $z_1$  (tidally-averaged over the local wetted time between surveys) and the local bottom slope  $m_1$  were calculated at each offshore location  $x_1$ . The appropriate longshore transport rate at the calculated elevation  $z_1$  was then interpolated from the previously calculated values of  $q_\ell(z)$ . Equation (4.37) was then applied using the value of  $m_1$  and the interpolated value,  $q_\ell(z_1)$ , in order to develop the local longshore transport rate per unit offshore distance at the location  $x_1$ .

CHAPTER 5  
RESULTS FROM  
THE FIELD INVESTIGATION

5.1 Introduction

The beach profile data collected from the last three field impoundment experiments, Groynes #2, #3, and #4 described in Chapter 3, were analyzed using the methodologies described in the previous chapter. The resulting estimates of the distributed and total longshore transport and the effectiveness of the barriers are presented in this chapter.

5.2 Distribution of Longshore Sediment Transport

5.2.1 Groyne #2

As described earlier, the second impoundment experiment (Groyne #2) utilized a non-pyramid-style groyne deployed on the rising, then falling, tide. Several gaps were present in the groyne. The first survey loop was taken during groyne construction (loop 1) and another survey loop was taken about sixteen hours after the groyne was completed (loop 3). Interim profiles taken between these two loops are collectively referred to as loop 2.

Loops 1-3. Beach profile changes measured between the groyne-construction and 16-hours post-deployment surveys (loops 1-3) were analyzed at five alongshore locations: four within 36 m (updrift) of the barrier and one 3 m downdrift. A smoothed estimate of the total transport function,  $\Lambda(z)$ , was obtained for each profile using least

squares matrix tidal deconvolution. The cross-shore contribution to the total transport function was identified and removed along each depth contour. The "non-adjusted" longshore transport rate was subsequently calculated and is illustrated in Figure 5-1a. The error bars reflect

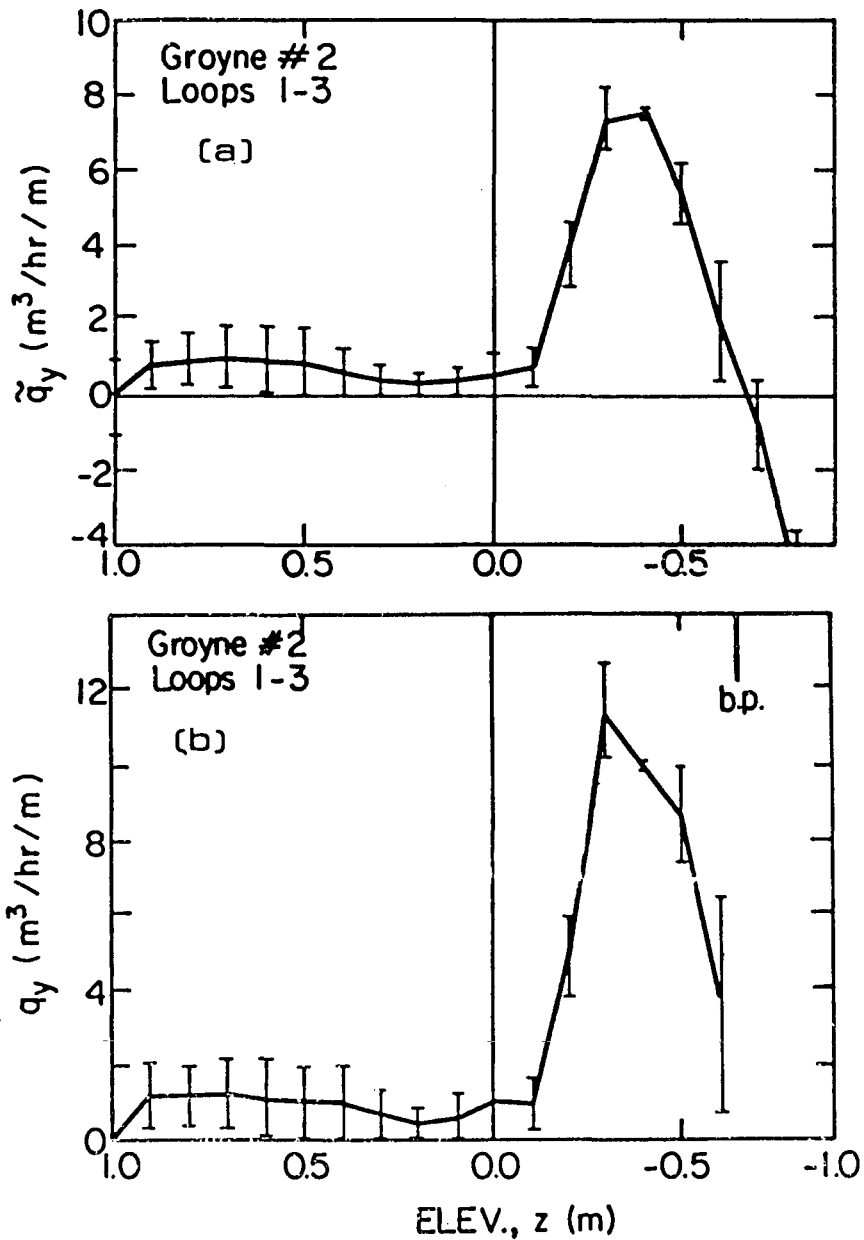


Figure 5-1: Distribution of longshore sediment transport rate for still-water depth contours: (a) "non-adjusted" for relative trapping times; (b) "adjusted" for relative trapping times. Groyne #2, loops 1-3.

uncertainties in the identification of the cross-shore contribution and the updrift extent of impoundment along each depth contour, as described in the previous chapter.

The anomalous negative values of longshore transport rate calculated for elevations below  $z=-0.6$  m are suspect because these contours were apparently inadequately blocked by the barrier. Figure 5-2a illustrates the effective trapping time,  $\Delta t_g/\Delta t$ , for which each depth contour

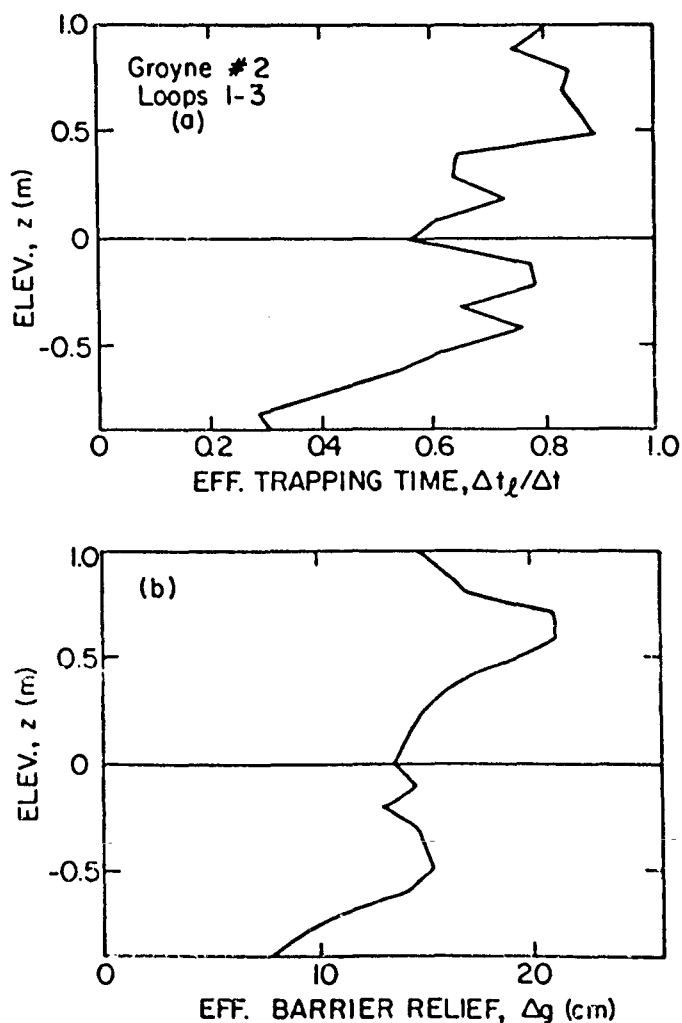


Figure 5-2: (a) Effective relative trapping time for which each depth contour was bounded by the groyne; (b) effective time-weighted barrier relief for each depth contour. Groyne #2, loops 1-3.

was bounded by the barrier during the loop 1 to loop 3 survey interval. Figure 5-2b illustrates the effective time-weighted barrier relief for each of the contours. It is noted that the effective trapping time and barrier relief are relatively constant for elevations above  $z=-0.6$  m, and abruptly decrease for elevations less than  $z=-0.6$  or  $-0.7$  m where the total transport function becomes erratic and indicates negative impoundment near the barrier. This may be a seaward end-effect of the barrier, such as scour. The correspondence between the abrupt decrease in calculated barrier effectiveness and the appearance of suspect impoundment data was not considered coincidental; similar correspondence was observed for other data sets presented in the following pages. Accordingly, transport values at elevations below  $z=-0.6$  m were deemed suspect and were excluded from further analysis. (Conservatively, data at  $z=-0.6$  m may be suspect as well, since it is close to the presumed effective end of the barrier.)

The first estimates of the local longshore transport rate (Figure 5-1a) were "adjusted" by the effective trapping time at each depth contour through Eq. (4.34) out to the limiting depth  $z=-0.6$  m. The resulting estimate of the longshore sediment transport distribution is shown in Figure 5-1b. The approximate significant breaking depth (or breakpoint, "b.p.") is also indicated in the figure.

Loops 1-2. The measured beach profile changes between the surveys during groyne construction (loop 1) and several hours after construction (loop 2) were poorly conditioned such that smoothed least-squares matrix tidal deconvolution yielded unrealistic results for the total transport functions. Instead, the total transport functions were calculated by the simple tidal deconvolution technique. The cross-shore component was

identified from data collected 18.3 and 36.5 m updrift of the barrier. The non-adjusted estimate of the longshore transport rate was then calculated and is shown in Figure 5-3a.

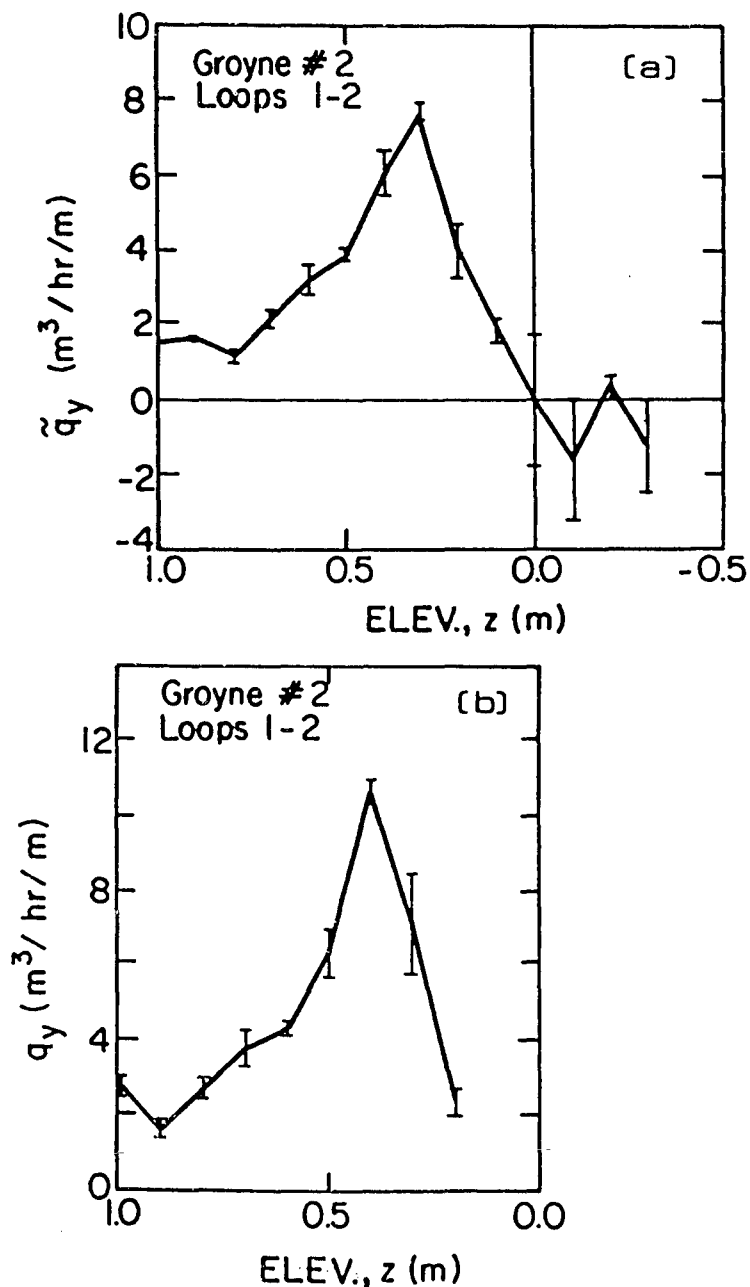


Figure 5-3: Distribution of longshore sediment transport rate for still-water depth contours: (a) "non-adjusted" for relative trapping times, (b) "adjusted" for relative trapping times. Groyne #2, loops 1-2. (Simple tidal deconvolution used.)

Through calculation of the effective relative trapping time and barrier elevation for each depth contour of this impoundment interval, an abrupt decrease in barrier effectiveness was noted below  $z=0.2$  or  $0.1$  m (for which  $\Delta t_g/\Delta t < 0.5$  and  $\Delta g < 13$  cm). The impoundment data seaward of these contours is correspondingly suspect and was therefore excluded from further consideration. The barrier was found to be ineffective at such a shallow depth contour because much of the loop 1 to 2 survey interval included time when the seaward section of the groyne was not yet complete and/or the tide was low. (This may also explain why the measured profile changes were ill-conditioned for matrix tidal deconvolution). The "non-adjusted" longshore transport rates shown in Figure 5-3a were modified by the effective trapping time calculated for each contour to produce the distributed longshore sediment transport profile shown in Figure 5-3b.

Comparison of loops 1-2 and 1-3. The distributed longshore transport calculated from profile loops 1 and 3 demonstrates a peak just landward of the breaker position and relatively little transport above the still water level. On the other hand, the data of loops 1 to 2 indicates considerable longshore transport above the still water level, (the only region where data were reasonable).

Inspection of the beach profiles (Figure 3-12) indicates that the profiles closest to the barrier accreted considerably about the (NGVD) foreshore during groyne construction, but remained relatively stable after construction. The profiles further updrift remained relatively stable during groyne construction, but accreted about the foreshore after construction. Inspection of all of the available profile data indicates that the latter was most likely unrelated to the presence of

the barrier. It is thought that the (NGVD) foreshore area near the barrier reached a "maximum" impoundment level during the latter stages of the groyne deployment. Accordingly, the data of survey loops 1 to 2 indicate considerable swash zone longshore transport, whereas relatively little impoundment occurred along the swash zone contours during the long interval which elapsed after groyne deployment between survey loops 1 and 3. It is possible, then, that the most likely estimate of the longshore sediment transport distribution for Groyne #2 is reflected by the data of loops 1-3 (Figure 5-1b) but with an additional contribution to the transport over the swash contours  $z=0.6$  m to 0.1 m.

#### 5.2.2 Groyne #3

For the third field experiment (Groyne #3) a pyramid-style groyne of high integrity was deployed during a falling neap tide. Sets of beach profiles were taken before groyne deployment (loop 1) and several hours after deployment on the subsequent rising and falling tides (loops 2 and 3, respectively).

Loops 2-3. As described earlier, waves were breaking landward of the end of the groyne during the interval between survey loops 2 and 3 such that the surf zone was "bounded" by the barrier. Accordingly, beach profile changes measured during this interval ideally represent the highest quality impoundment data for Groyne #3.

The total transport function was calculated along the beach for the loop 2 to loop 3 survey interval using smoothed least-squares matrix tidal deconvolution. Total rms errors between measured profile changes and profile changes calculated from the tidally deconvolved transport functions were relatively small, i.e., between 13% and 33%. Figure 5-4

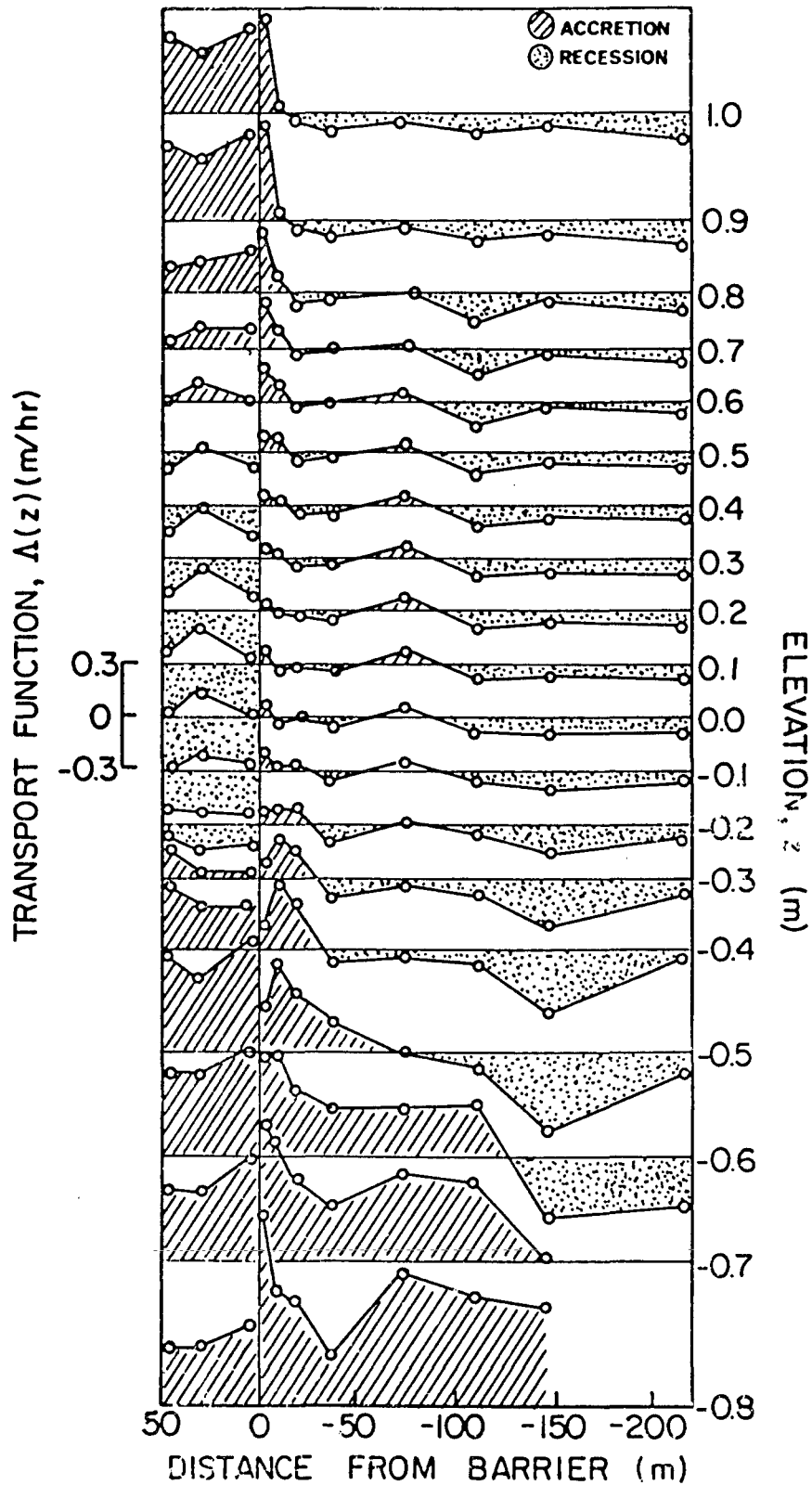


Figure 5-4: The total transport function,  $\Delta(z)$ , calculated for each of eleven profiles, and illustrated along various depth contours. Groyne #3, loops 2-3.

illustrates the total transport function along each depth contour both updrift and downdrift of the barrier. When examining Figure 5-4 (and similar illustrations of the total transport function), it is helpful to recall that the transport function  $\Lambda(z)$  represents the rate of horizontal accretion or recession per unit longshore beach width and per unit depth, along depth contour  $z$ . Accordingly, figures such as 5-4 depict the local rate of beach profile growth or recession both along and across the beach study site.

The total transport function exhibits an exponential-form impoundment against the barrier (right-side) for all contours analyzed. However, there are some local depressions in the impoundment immediately next to the barrier at  $z=-0.1$  to  $-0.5$  m. Large-valued accretion signals are also noted at the seaward end of the groyne on both the updrift and downdrift sides. These latter two features suggest the presence of a rip current which flows along both sides of the barrier and moves sand offshore from just below the still water level to the breaker region. Significant local accretion and recession downdrift of the groyne is also observed. Correlation between updrift and downdrift effects is unclear from the figure. The appearance of the total transport function, which is directly related to the sediment transport pattern about the barrier, is discussed in conjunction with the laboratory results in Chapter 7.

The relative trapping time,  $\Delta t_q/\Delta t$ , and effective time-weighted barrier relief,  $\Delta g$ , for each contour, are shown in Figure 5-5. The range of values shown for  $\Delta g$  (Fig. 5-5b) reflects the change in effective barrier relief at each depth contour as the beach profile immediately updrift of the barrier accreted during the survey interval.

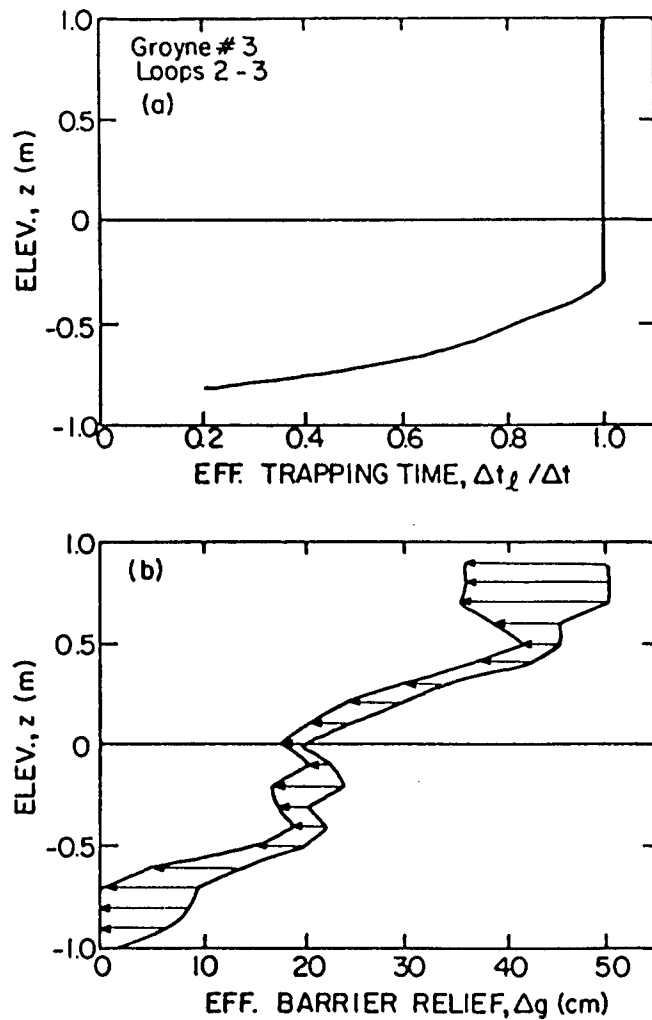


Figure 5-5: (a) Effective relative trapping time for which each depth contour was bounded by the groyne; (b) effective time-weighted barrier relief for each depth contour, (arrows indicate variation with time). Groyne #3, loops 2-3.

The cross-shore component of the total transport function was identified and removed for each depth contour. The resulting longshore component was integrated updrift from the barrier to yield the "non-adjusted" longshore transport rate for each contour (shown in Figure 5-6a). Anomalous (negative) transport estimates at contours deeper than  $z=-0.7$  m correspond to low relative trapping time ( $\Delta t_l / \Delta t < 0.56$ ) and

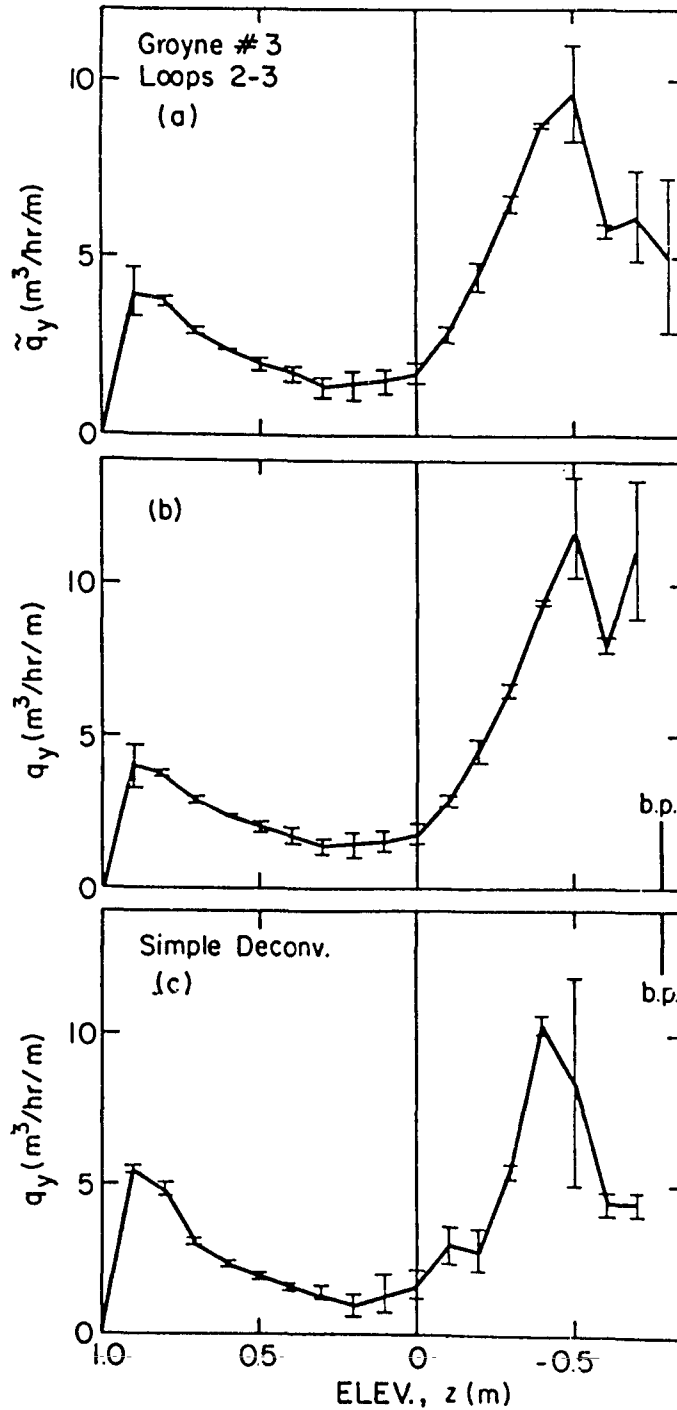


Figure 5-6: Distribution of longshore sediment transport rate for still-water depth contours: (a) "non-adjusted" for relative trapping times (least-squares matrix technique), (b) "adjusted" for relative trapping times (least-squares matrix technique), and (c) result of simple tidal deconvolution technique. Groyne #3, loops 2-3.

low barrier relief ( $\Delta g < 10$  cm). Accordingly, the non-adjusted impoundment rates shown in Figure 5-6a were modified by the effective trapping time only for elevations at or above  $z = -0.7$  m. The resulting estimate of the distribution of longshore sediment transport is shown in Figure 5-6b.

The loop 2 to loop 3 survey data were also analyzed using the "simple" tidal deconvolution technique. The total transport functions calculated by the "simple" technique did not reproduce the measured profile changes as accurately as did the functions developed by the smoothed least-squares matrix technique: specifically, rms errors were 22% to 50%. However, the transport functions calculated from each technique were relatively similar. The estimate of the longshore sediment transport distribution using "simple" tidal deconvolution, is shown in Figure 5-6c. The magnitude and shape of the longshore transport profile is similar to that calculated using the smoothed least-squares matrix deconvolution (Figure 5-6b). The results of both tidal deconvolution techniques indicate a transport peak just landward of the breakpoint. A secondary peak is noted in the upper swash zone.

Loops 1-2. Beach profile changes during and immediately after groyne deployment were obtained from the loop 1 to loop 2 survey data. The relative trapping time,  $\Delta t_{\ell}/\Delta t$ , and effective barrier relief,  $\Delta g$ , are shown for various depth contours in Figure 5-7. The former suggests that the barrier's effectiveness as an impoundment agent was diminished for elevations below  $z = -0.1$  m ( $\Delta t_{\ell}/\Delta t < 0.5$ ), while the latter suggests diminished barrier effectiveness for elevations below  $z = -0.5$  m ( $\Delta g < 10$  cm). The relative trapping times and effective barrier relief are relatively low-valued for this survey interval (considering the high

quality of the barrier) because this interval is dominated by the entire period during which the groyne was under construction.

The total transport function was calculated for the loop 1 to 2 survey interval using smoothed least-squares matrix tidal deconvolution. Cross-shore components were identified and removed, and the "non-adjusted" longshore sediment transport rate was calculated for each depth

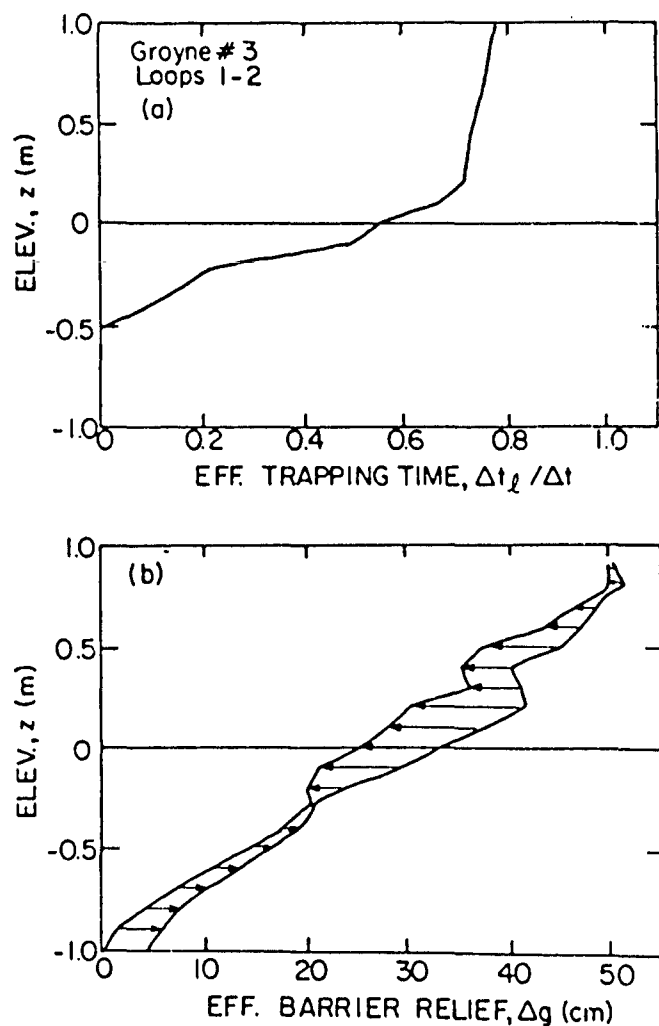


Figure 5-7: (a) Effective relative trapping time for which each depth contour was bounded by the groyne; (b) effective time-weighted barrier relief for each depth contour (arrows indicate variation with time). Groyne #3, loops 1-2.

contour (shown in Fig. 5-8a). The "non-adjusted" values were modified by the effective time for which each contour was bounded by the barrier out to elevation  $z=-0.4$  m. The resulting estimate of the distribution of longshore sediment transport is shown in Figure 5-8b. The validity

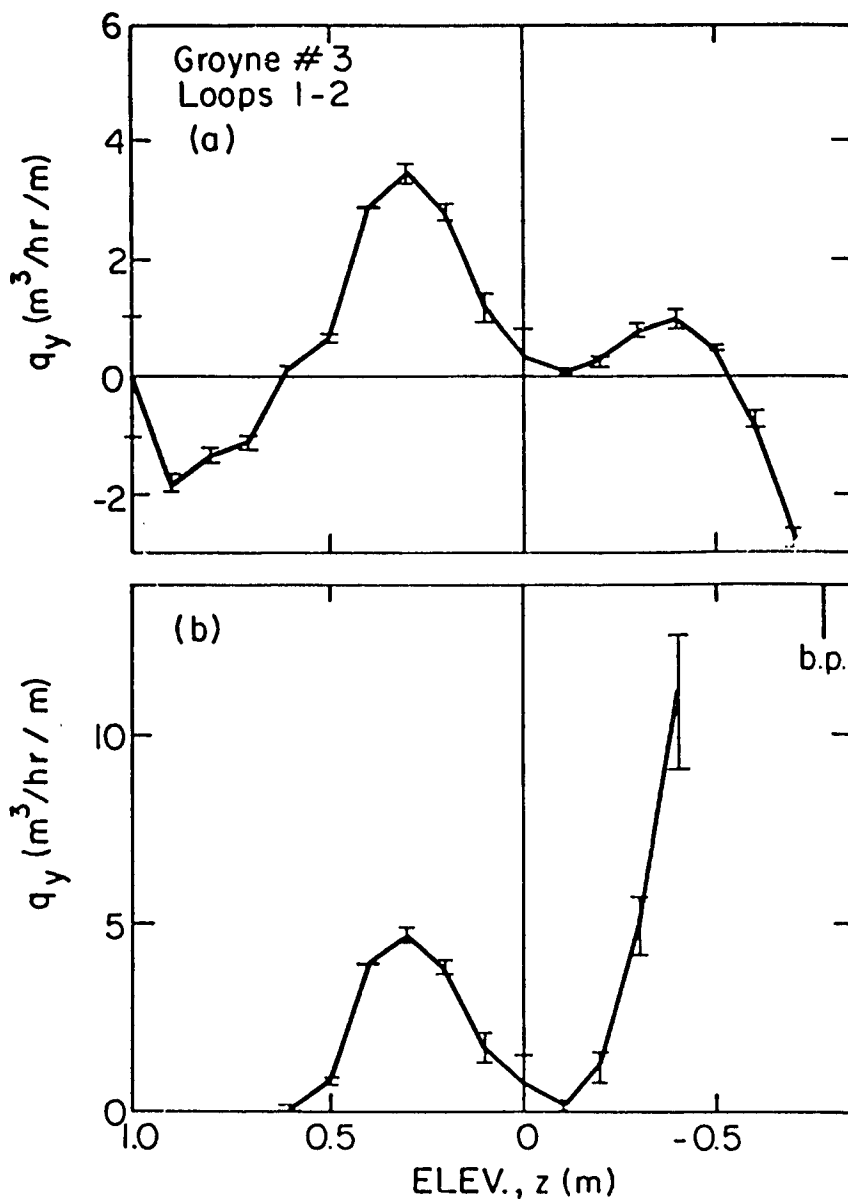


Figure 5-8: Distribution of longshore sediment transport rate for still-water depth contours: (a) "non-adjusted" for relative trapping times, (b) "adjusted" for relative trapping times. Groyne #3, loops 1-2.

of estimates below  $z=-0.1$  m is questionable due to the short time intervals for which these contours were bounded by the barrier.

It is noted that significant negative-valued estimates of the "non-adjusted" longshore transport were obtained for the upper swash zone during the groyne construction interval. This anomaly may be due to erosion of the foreshore immediately adjacent to the groyne caused by the bag-filling operation. The significant positive-valued longshore transport obtained over these upper contours for the post-construction survey interval (loop 2 to 3) may therefore be somewhat biased to the high side. That is, "scour" created during groyne construction rapidly filled in during the loop 2 to loop 3 survey interval while the tide was high. However, it is noted that a strong longshore-related impoundment signal was also calculated further updrift of the "scour" (i.e., 9 m updrift of the barrier) for these swash-zone contours. Hence, the somewhat surprisingly large estimates of longshore transport along the upper swash contours found for loop 2 to loop 3 may not be completely unrealistic.

Loops 1-3. The overall profile changes between the pre-groyne survey (loop 1) and the post-impoundment survey (loop 3), were also analyzed. The effective trapping time,  $\Delta t_g/\Delta t$ , and the effective barrier elevation,  $\Delta g$ , are shown in Figure 5-9 for relevant depth contours during the loop 1 to 3 survey interval. After calculation of the total transport function through least-squares matrix tidal deconvolution, and identification and removal of cross-shore signals, the "non-adjusted" longshore transport rate  $\tilde{q}_y$  was calculated and is shown in Figure 5-10a. The "non-adjusted" values were modified by the effective trapping time along each contour out to  $z=-0.5$  m, beyond which

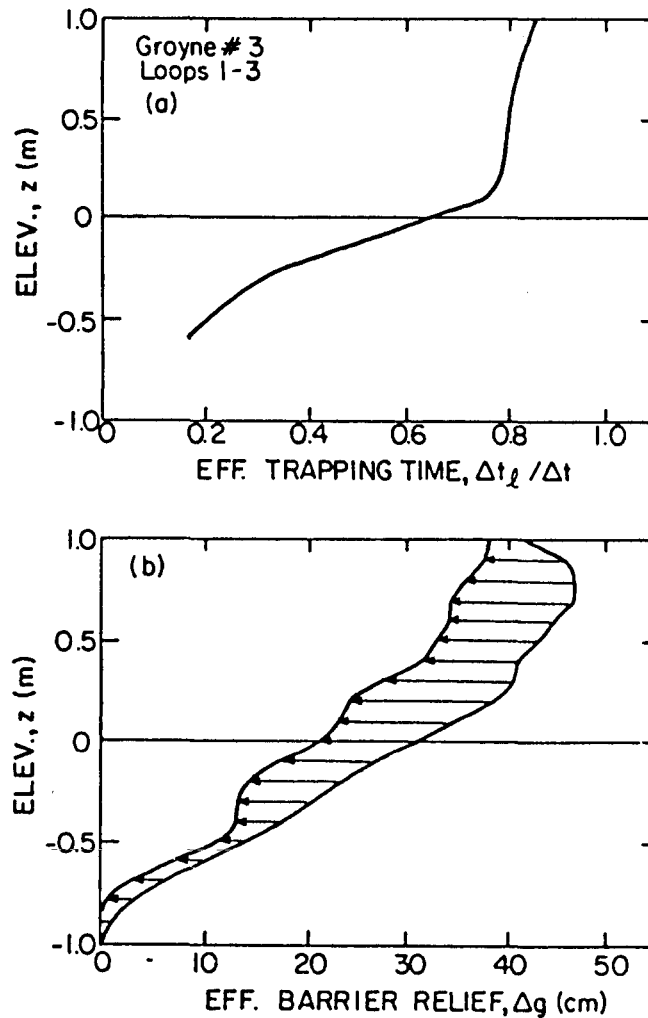


Figure 5-9: (a) Effective relative trapping time for which each depth contour was bounded by the groyne; (b) effective time-weighted barrier relief for each depth contour (arrows indicate variation with time). Groyne #3, loops 1-3.

the effective barrier relief fell below 13 cm. The resulting estimate of the distribution of longshore sediment transport is shown in Figure 5-10b. Estimates for  $z < -0.1$  m are questionable due to the relatively short time intervals for which these contours were trapped by the barrier ( $\Delta t_g / \Delta t < 0.5$ ).

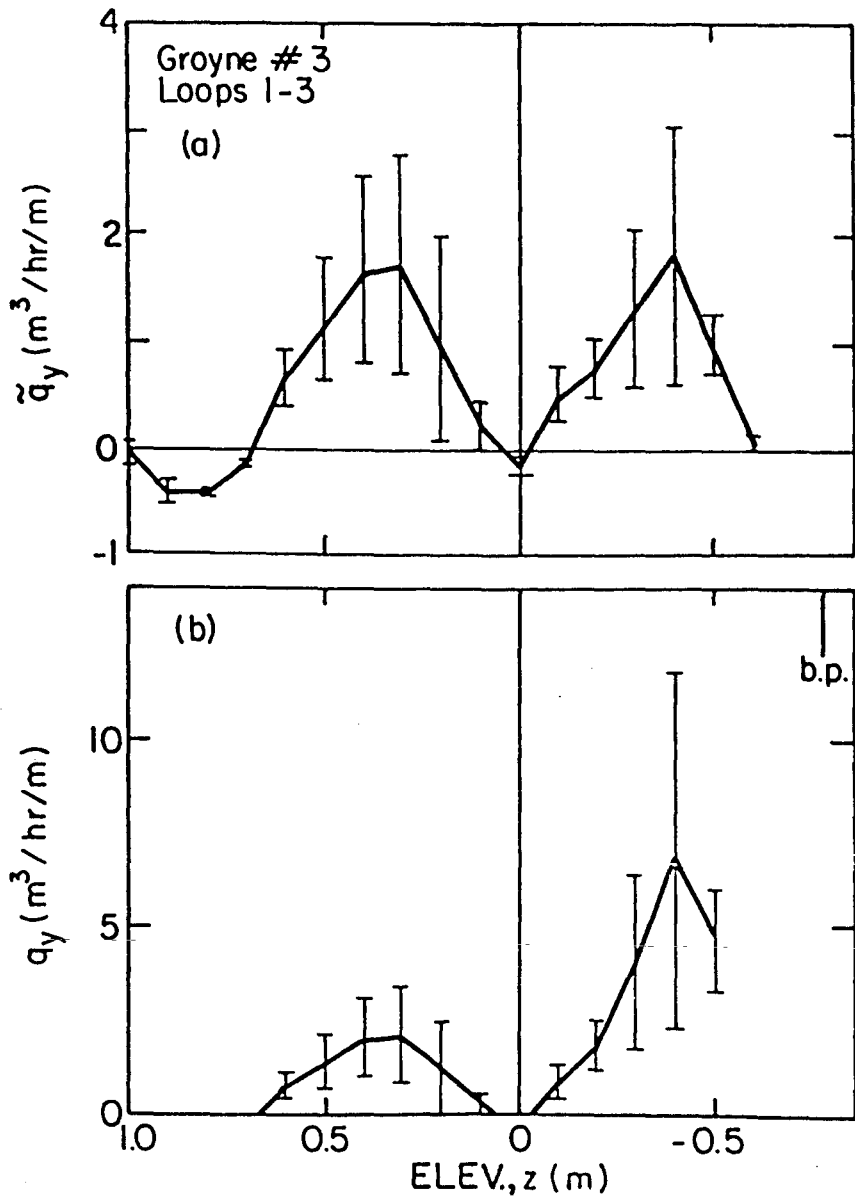


Figure 5-10: Distribution of longshore sediment transport rate for still-water depth contours: (a) "non-adjusted" for relative trapping times, (b) "adjusted" for relative trapping times. Groyne #3, loops 1-3.

Essentially zero longshore transport was calculated for the upper swash contours for the loop 1 to 3 survey interval. This suggests that construction of the groyne (or some other localized process) removed more material from the near-barrier profile than was replaced by

longshore (or cross-shore) processes. As described above, this is very likely since the pumping activity of groyne construction often leads to significant localized erosion high upon the foreshore--an area which is wetted for only brief intervals during the high tide. Accordingly, the estimate of the longshore transport for the upper-most depth contours derived from loops 1 to 3 is probably biased to the low side.

Best estimate of distribution. Bearing in mind the comments made above regarding each of the three survey intervals which were analyzed, the most probable description of the longshore sediment transport distribution is given by the loop 2 to loop 3 data (Fig. 5-6b). However, as mentioned, the relative contribution to the longshore transport by the uppermost swash contours may be overestimated. The relative contribution just above the still-water level ( $z = 0$  to  $+0.5$  m) may be slightly under-estimated, since the loops 1-2 and 1-3 results indicate transport peaks over these shoreline/swash contours.

#### 5.2.3 Groyne #4

For the fourth impoundment experiment (Groyne #4), a pyramid-style groyne of high integrity was deployed across the beach on a falling spring tide. Beach profiles were surveyed before groyne deployment (loop 1), three to eight hours after deployment on the subsequent rising and falling tide (loops 2 and 3, respectively), and sixteen to twenty-one hours after deployment on the next rising and falling tide, (loops 4 and 5, respectively). Like loops 2 and 3 of Groyne #3, the profile changes measured between loops 2-3 and loops 4-5 ideally represent high quality impoundment data since the surf zone was "bounded" by the barrier during the predominantly high-tide condition which existed during these survey intervals.

Loops 4-5. Figure 5-11 illustrates the smoothed total transport functions calculated along several depth contours from the measured loop 4-5 beach profile changes (using least-squares matrix tidal deconvolution). The loop 4 to loop 5 impoundment interval represents the most complete set of potentially meaningful field survey data; that is, calculation of the total transport function was possible out to considerable depths ( $z < -1.4$  m) because profile data were collected out to NGVD elevations of  $-0.70$  m and the high tide reached an NGVD elevation of  $+0.75$  m during the survey interval. Furthermore, these depth contours were relatively well bounded by the groyne during the survey interval because of the great length and relief of the groyne. The effective trapping times and barrier relief calculated for the loop 4-5 interval (Figure 5-12) indicate that impoundment data for elevations above  $z = -1.3$  m are potentially reasonable ( $\Delta t_g / \Delta t > 0.8$  and  $\Delta g > 15$  cm). The relatively large offshore spacing between measurements for the two farthest updrift profiles did not allow reasonable resolution of profile changes and so portions of these profiles ( $z_0 < -0.1$  m NGVD) were excluded from data analysis.

Cross-shore components of the total transport functions were identified and removed, and the "non-adjusted" longshore transport rate,  $\tilde{q}_y(z)$ , was calculated out to  $z = -1.3$  m. Because depth contours above  $z = -1.2$  m were blocked by the barrier for the entire survey interval ( $\Delta t_g / \Delta t = 1.0$ ), the "non-adjusted" longshore transport rate,  $\tilde{q}_y(z)$ , is essentially identical to the "adjusted" longshore transport rate  $q_y(z)$ . The latter is shown in Figure 5-13. The distribution of transport is slightly bimodal, with peaks immediately landward of the breakpoint and the shoreline. Considerable transport is noted above the shoreline.

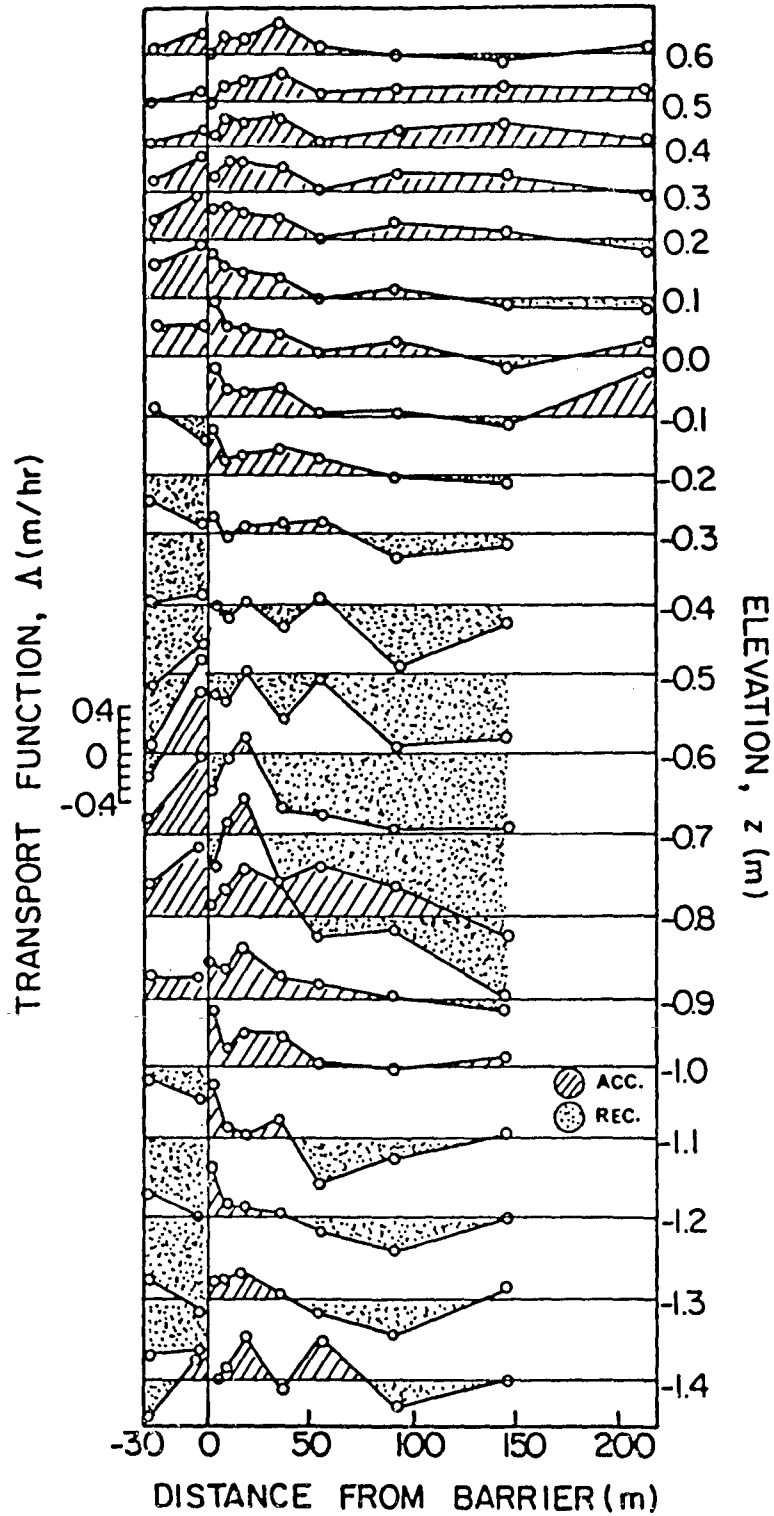


Figure 5-11: Total transport function,  $\Lambda(z)$ , calculated for each of 10 profiles, and illustrated along various depth contours. Groyne #4, loops 4-5.

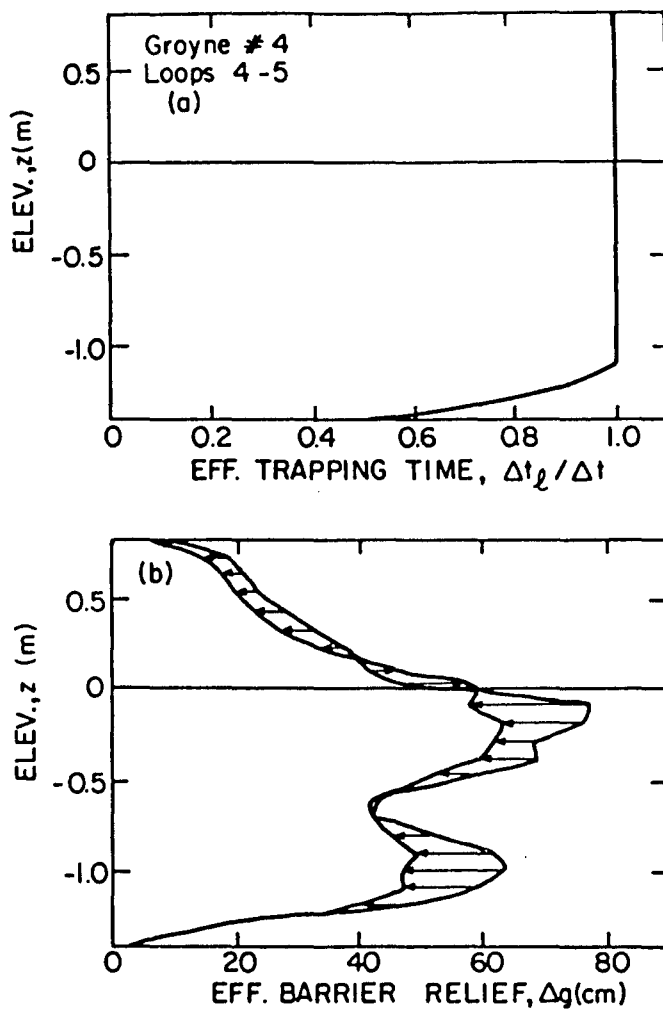


Figure 5-12: (a) Effective relative trapping time for which each depth contour was bounded by the groyne; (b) effective time-weighted barrier relief for each depth contour (arrows indicate variation with time). Groyne #4, loops 4-5.

Loops 2-3. As described above, the loop 2 to loop 3 survey interval should also represent a high quality impoundment data set. Although the depth contours for which data were available were well blocked by the barrier for practically the entire survey interval, the measured beach profile data are poorly conditioned for analysis. Specifically, the total transport functions calculated for half of the profiles by either "simple" or matrix tidal deconvolution were of poor quality

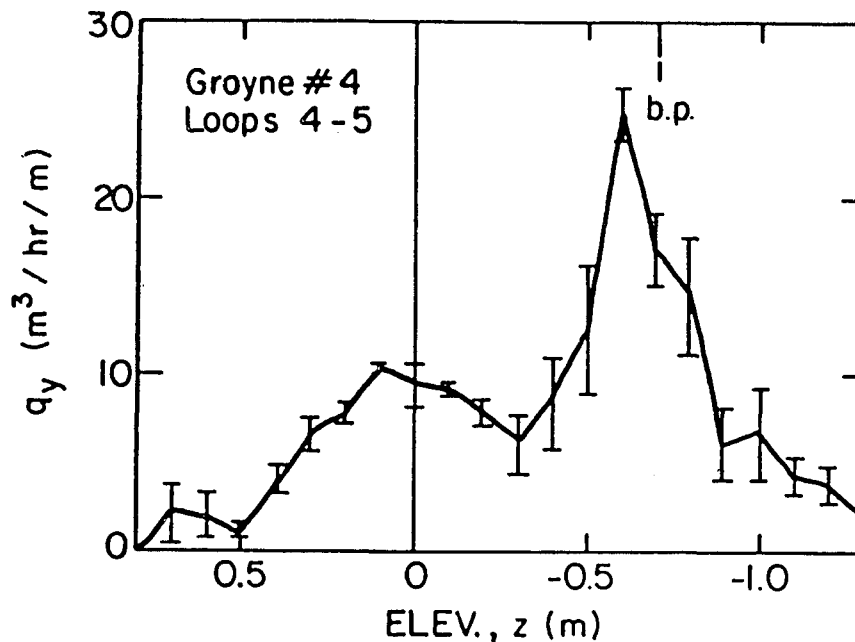


Figure 5-13: Distribution of longshore sediment transport rate for still-water depth contours (essentially identical to the "non-adjusted" estimate since practically all contours shown were blocked for the entire impoundment interval). Groyne #4, loops 4-5.

(i.e., total rms errors > 50%). Irregularities of the tidally deconvolved transport functions along most depth contours precluded the rational estimation of cross-shore signal identification. Furthermore, the loop 2 beach profile survey immediately updrift of the barrier is suspect because the profile does not "close" above the foreshore with other profiles at this location. Overall, it is thought that the signal to noise ratio of the loop 2-3 survey data and deconvolved transport values is not sufficiently large enough for meaningful data analysis.

Loops 1-3. Analysis of beach profile changes which occurred during groyne construction and the first high-tide impoundment interval, loops 1-3, avoids use of the suspect loop 2 survey data. However, the depth contours for which data are available were, of course, not always

effectively blocked by the groyne during the loop 1-3 interval. Figure 5-14 illustrates the relative trapping time,  $\Delta t_{\ell}/\Delta t$ , and the (minimum) effective time-weighted barrier relief,  $\Delta g$ , for relevant depth contours during the loop 1-3 interval.

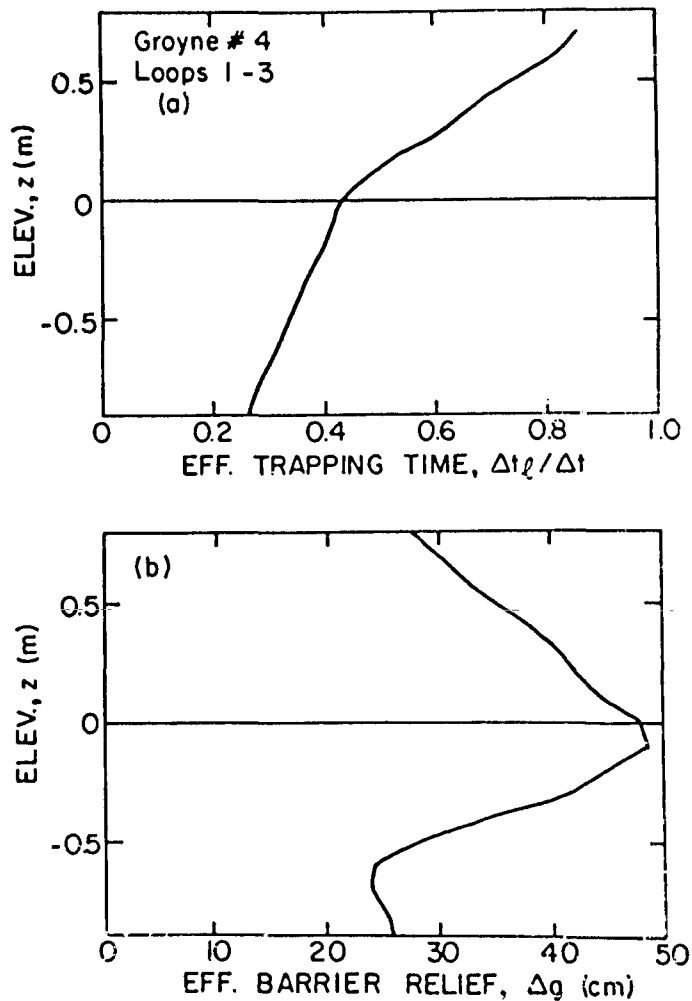


Figure 5-14: (a) Effective relative trapping time for which each depth contour was bounded by the groyne; (b) effective (minimum) time-weighted barrier relief for each depth contour. Groyne #4, loops 1-3.

Least-squares matrix tidal deconvolution produced total transport functions for each set of profiles which, when smoothed, appeared reasonable and fairly accurate (i.e., total rms error of 20% to 40%). Estimates of the cross-shore contribution to the transport function along each depth contour were made and subsequently removed. The "non-adjusted" longshore sediment transport rate was then calculated for each depth contour. The results are illustrated in Figure 5-15a. Anomalous negative-valued estimates were obtained for depths greater than  $z = -0.6$  m; accordingly, transport data beyond this depth was excluded from further analysis. Relative trapping times below  $z = -0.6$  m fell below  $\Delta t_g / \Delta t = 0.3$ , while the effective barrier relief was reduced to  $\Delta g \approx 25$  cm or less. The "non-adjusted" longshore transport values were modified by the relative trapping time  $\Delta t_g / \Delta t$  for each depth contour; the resulting estimate of the distribution of longshore transport rate is shown in Figure 5-15b. Peak values are associated with the breaker location, and significant levels of longshore transport are again observed above the shoreline.

Loops 1-5. The "non-adjusted" longshore transport distribution developed from profile changes measured between the pre-deployment survey loop (loop 1) and 21 hours after groyne deployment (loop 5) is shown in Figure 5-16a. These estimates were modified by the relative trapping time calculated for each contour and the results are shown in Figure 5-16b. Estimates below  $z = -0.6$  m were excluded (for which  $\Delta t_g / \Delta t < 0.43$  and  $\Delta g < 22$  cm). The distribution is similar to that calculated for loop 1-3, with maxima about the break point and significant transport above the shoreline. However, the error bars (associated with uncertainties in identification of cross-shore contributions

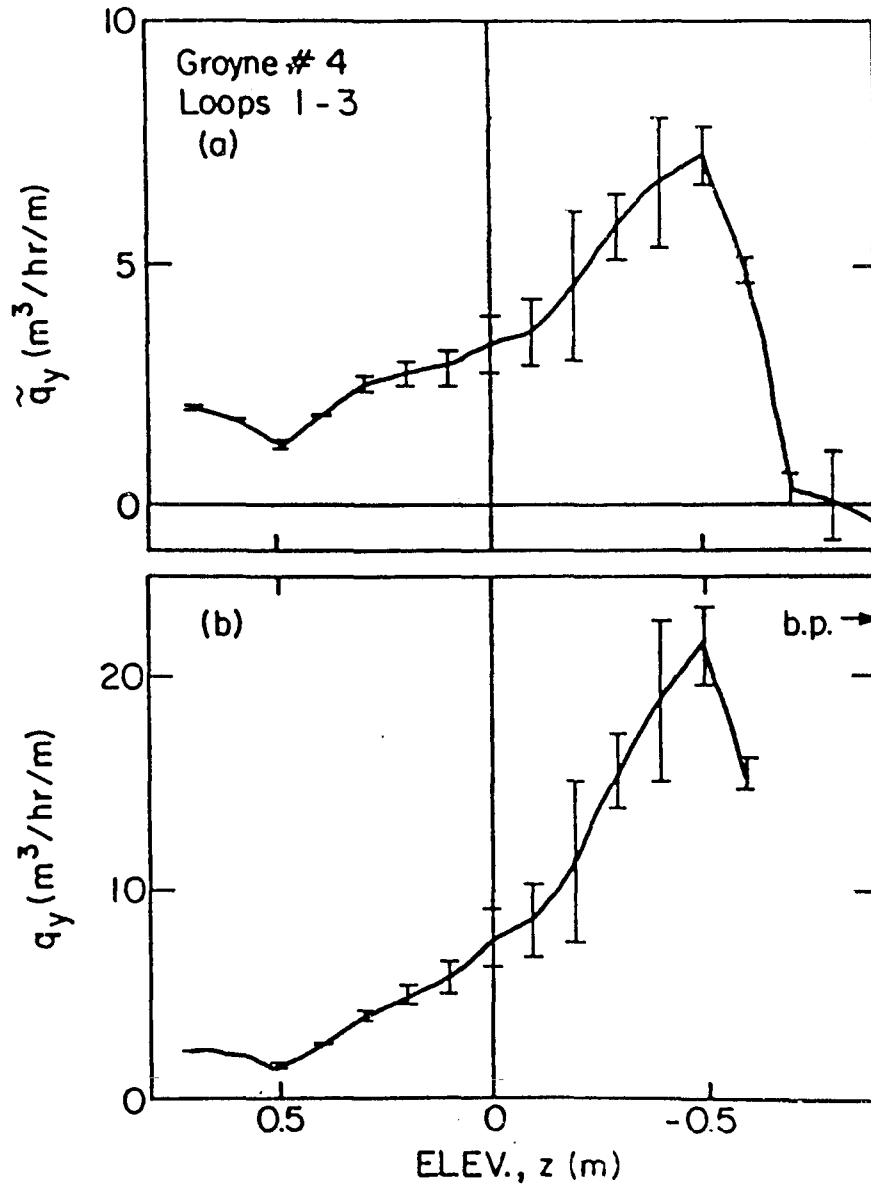


Figure 5-15: Distribution of longshore sediment transport rate for still-water depth contours: (a) "non-adjusted" for relative trapping times, (b) "adjusted" for relative trapping times. Groyne #4, loops 1-3.

and the updrift extent of impoundment) obscure much of the distribution profile. The severity of the error bars is not unexpected in this case, since the directional wave characteristics changed somewhat between the loop 1-3 and loop 4-5 survey intervals (see Table 3.2).

### 5.3 Total Longshore Sediment Transport

Table 5-1 lists the total longshore sediment transport rate,  $Q_L$ , calculated for the results of each field experiment impoundment interval. These values were obtained through integration of the local longshore sediment transport rate from maximum run-up to the depth contour

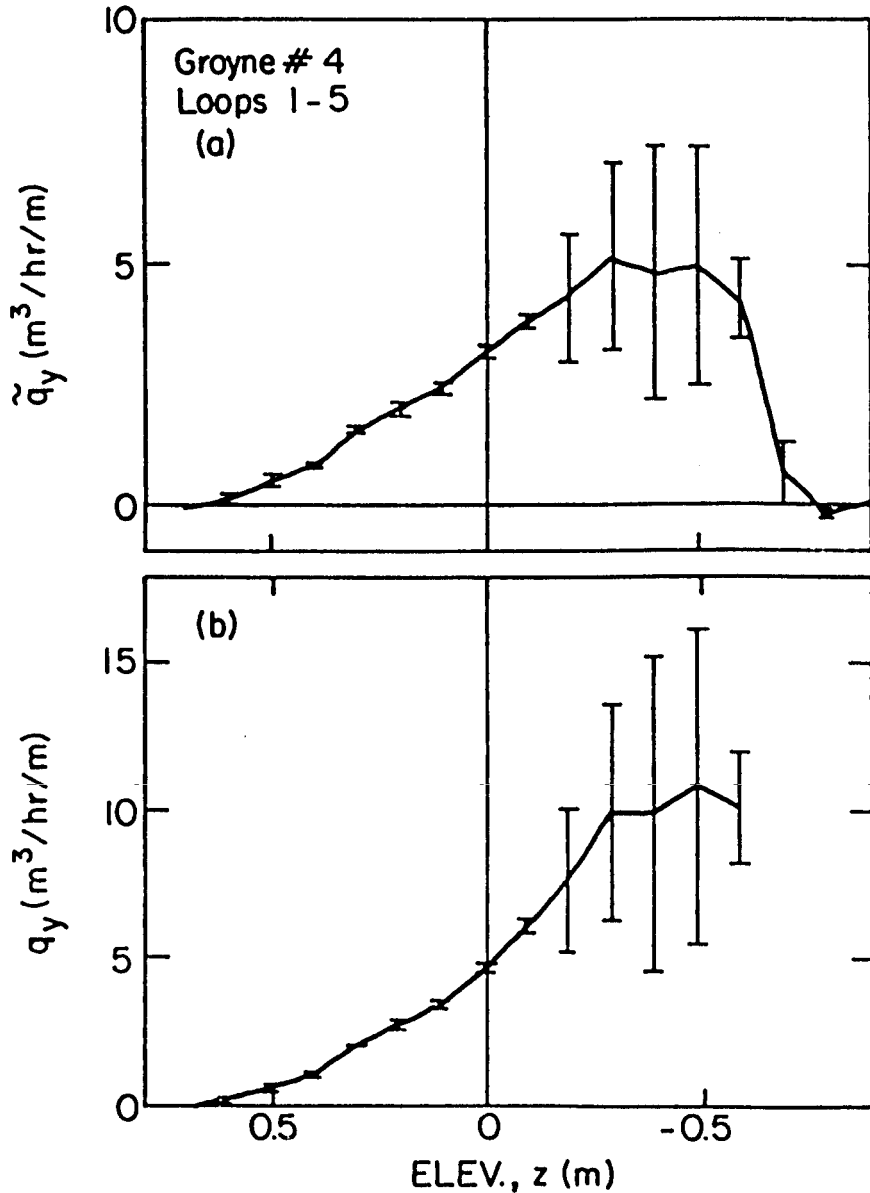


Figure 5-16: Distribution of longshore sediment transport rate for still-water depth contours: (a) "non-adjusted" for relative trapping times, (b) "adjusted" for relative trapping times. Groyne 4, loops 1-5.

for which the groynes were considered to be reasonable barriers (as described in the preceding pages for each experiment and survey interval). Approximate values of the longshore wave energy flux factor were obtained from the visual and radar estimates of the surf conditions (Table 3-2) and are also listed in Table 5-1. The range of K values from the CERC Formula for each result is also listed, where

$$K = \frac{I_{\ell}}{P_{\ell}} = \frac{(\rho_s - \rho)g a' Q_{\ell}}{\frac{1}{16} \rho g H^2 \sqrt{gh_b} \sin 2\alpha_b} \quad (5.1)$$

The sediment porosity factor  $a'$  was taken as 0.6. Since the values for the surf parameters were taken from visual measurements, the term  $P_{\ell}$  is most closely related to the significant longshore flux factor  $P_{\ell S}$ , for which the "recommended" value of K is 0.39 (CERC, 1984).

Table 5-1: Total Longshore Transport--Field Data

Study (Gr#/Loop)	$Q_{\ell}$ ( $m^3/hr$ )	$P_{\ell S}$ ( $N/s$ )	K	$h_*/h_b$	$\Delta t$ (hr:min)	$\frac{\Delta t_{\ell}}{\Delta t}$	$\Delta g$ (cm)
Groyne#2/1-3	4.2-5.1	89-103	.11-.15	0.94	18:35	> 0.54	> 14
#2/1-2	3.8-5.1	89-103	.10-.15	-.16	5:25	> 0.43	> 10
Groyne#3/2-3	7.3-9.0	105-119	.16-.23	0.90	4:30	> 0.56	> 10
#3/1-2	2.8-3.7	105-119	.06-.09	0.51	13:00	> 0.10	> 18
#3/1-3	1.2-4.1	105-119	.03-.11	0.64	17:30	> 0.21	> 13
Groyne#4/4-5	13.5-19.9	64- 69	.52-.83	1.44	3:10	> 0.50	> 16
#4/1-3	10.5-14.8	167-202	.14-.24	0.67	15:30	> 0.30	> 24
#4/1-5	4.9-9.2	140-167	.08-.18	0.89	28:45	> 0.40	> 23

The total longshore transport values calculated from the field data are generally smaller than the corresponding values calculated using the CERC Formula. Two notable exceptions are Groyne #3, loops 2-3, and Groyne #4, loops 4-5. It is recalled that these two data sets represent "ideal" impoundment intervals during which the surf zone was effectively bounded by a high-integrity barrier. Accordingly, longshore transport values were obtained for depth contours out to breaking (Groyne #3, loops 2-3) or past breaking (Groyne #4, loops 4-5), and so it is reasonable to believe that most of the total longshore drift across the surf zone was accounted for (neglecting losses over the top of the groyne). In addition, the survey intervals for these two data sets were very short (3 to 4-1/2 hours each); therefore, the calculated total transport functions for each data set,  $\Lambda = \Delta x / \Delta t$ , are generally larger-valued, since  $\Delta t$  is smaller. Although estimates of the longshore transport rate were made almost out to the break point for Groyne #2, loops 1-3, the quality of the groyne for this experiment was relatively poor compared to the third and fourth experiments, and so bypassing was probably more severe. Accordingly, the calculated K value is relatively small. The majority of the total longshore transport estimates in Table 5-1 were calculated for survey intervals for which data were not available out to breaking and/or for longer times between the survey loops. Hence it is not surprising that the estimates of the total longshore drift appear low for these data sets. The approximate time between survey loops,  $\Delta t$ , and the normalized depths to which the total longshore transport rates were calculated,  $(h_*/h_p)$ , are also listed in Table 5-1.

Finally, it is most probable that the total longshore transport rates calculated from the field impoundment data underestimate the

actual longshore transport rate because none of the groynes were complete longshore barriers. As described previously, the relief of each groyne was between 10 and 90 cm above the bed. Suspended sediment was observed to flow over the groynes--especially about the still-water level and along those contours for which the trap was relatively full. The magnitude of the "overwash" bypassing near the still-water level can appear visually significant. A similar phenomenon was observed by this author across a wooden weir at Rudee Inlet, Virginia. Measurements of the sediment flow over the top of the non-filled portions of the weir (made by this author as well as Dr. T. Walton, CERC) suggested that the amount of sediment which bypassed the high-relief sections of the weir was small relative to the total transport across the weir.

Regarding suspended load bypassing for deeper contours, initial results from a field investigation by Dr. N. Kraus of CERC (personal communication) suggest that about 40% of the total suspended longshore transport load is carried in water depths above a level 20 cm beyond the bed, as well as in the wave crest. Since the contribution of the suspended load to the total transport is not known for the field experiments, it is difficult to estimate the extent to which the groynes bypassed suspended load.

It is believed that no bypassing occurred for the upper swash contours. However, the effects of the groyne construction and its presence across the beach may have potentially altered the measured impoundment along these contours. Spurious effects of the groyne upon the measured sediment impoundment are discussed in conjunction with the laboratory results in Chapter 7.

#### 5.4 Limiting Effectiveness of the Groynes

The limiting values for which the relative trapping time,  $\Delta t_g/\Delta t$ , and the effective time-weighted barrier relief,  $\Delta g$ , indicate ineffective trapping by the barrier were not known a priori. Accordingly, for a first estimate, the values of  $\Delta t_g/\Delta t$  and  $\Delta g$  were noted for the depth contours beyond which the calculated longshore impoundment rates were anomalous (i.e., indicated small signal to noise ratio or were negative-valued). These values are shown for each data set in Table 5-1. Generally, it appears that impoundment data were unreasonable for depth contours bounded by the barrier for less than half the survey interval (i.e.,  $\Delta t_g/\Delta t < 0.5$ ) or bounded by a time-weighted barrier relief  $\Delta g$  of less than 10 to 20 cm. The field experiments did not encompass a wide range of wave heights or surf conditions; however, the results suggest that minimum barrier relief should be greater than 22% to 30% of the breaking wave height for reasonable impoundment measurements.

#### 5.5 Offshore Distribution of Longshore Transport for the Two "Best" Data Sets

The results of Groyne #3, survey loops 2-3, and Groyne #4, survey loops 4-5, are considered by the author to be the most complete and best estimates of the longshore transport distribution from the available field data of this study. It is recalled that these two data sets include impoundment data taken over a relatively short-term period when the surf zone was fairly completely "bounded" by a substantial barrier. Of the two, the results of Groyne #4, survey loops 4-5, are preferred because the data analysis extended beyond the breaking depth contour. Additionally, the distribution calculated across the swash zone for the data of Groyne #3 is also slightly suspect, as previously

discussed. Figures 5-17 and 5-18 illustrate the longshore transport distribution across the width of the surf zone for the two data sets. The values of the local longshore transport (per unit offshore distance) in each figure were calculated as described in Chapter 4, Section 8. Additionally, the approximate longshore current distribution, wave

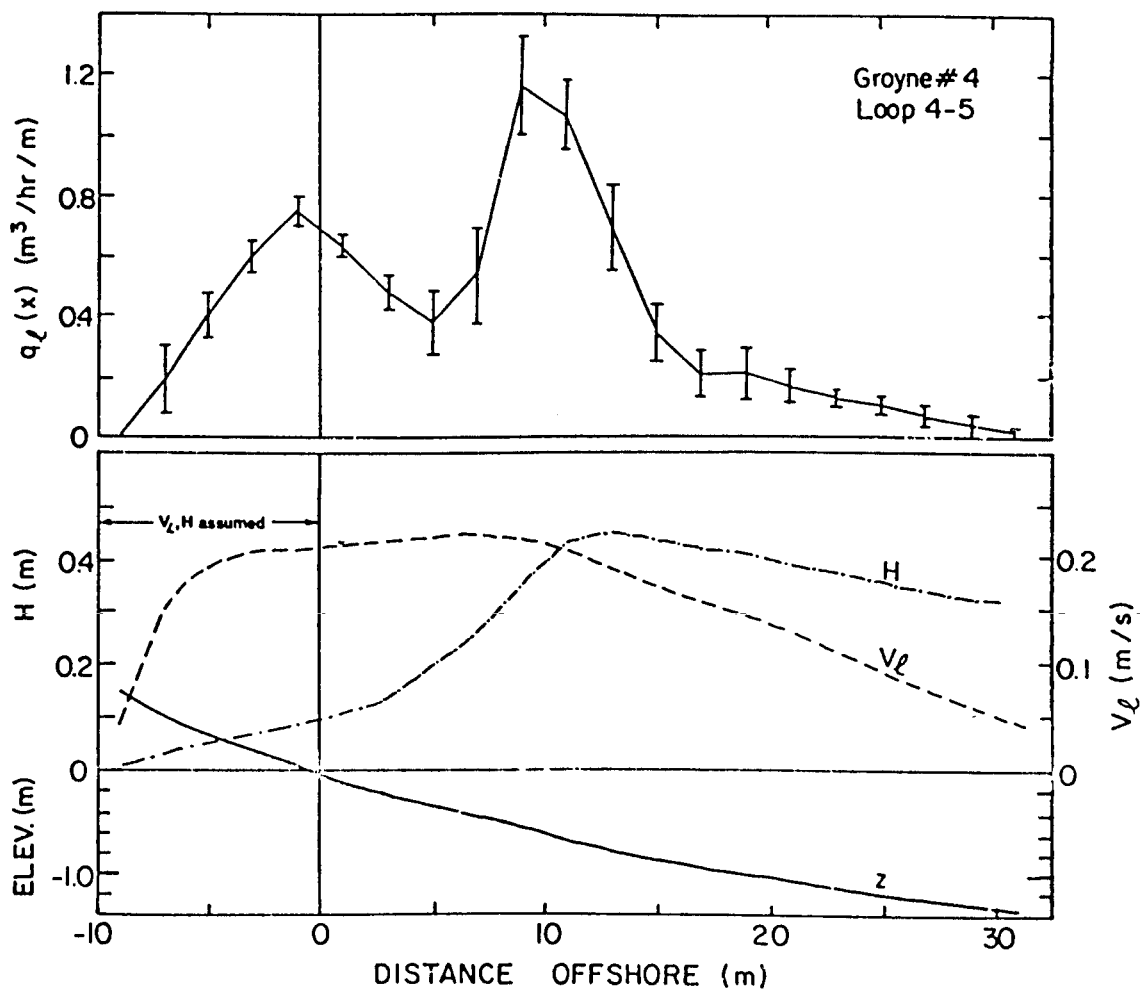


Figure 5-17: The longshore transport distribution, longshore current, wave height, and average beach profile across the surf zone for Groyne #4, loops 4-5 (the better of the two "best" field data sets).

height distribution, and the average beach profile are shown for each data set in the figures. The longshore current and wave height distributions were roughly estimated from the data presented as a function of depth in Figures 3-17 and 3-26. The longshore current and wave height at any particular depth  $z_i$  was then "mapped" to the corresponding offshore location on the average beach profile for which the tidally-averaged depth was equal to  $z_i$ .

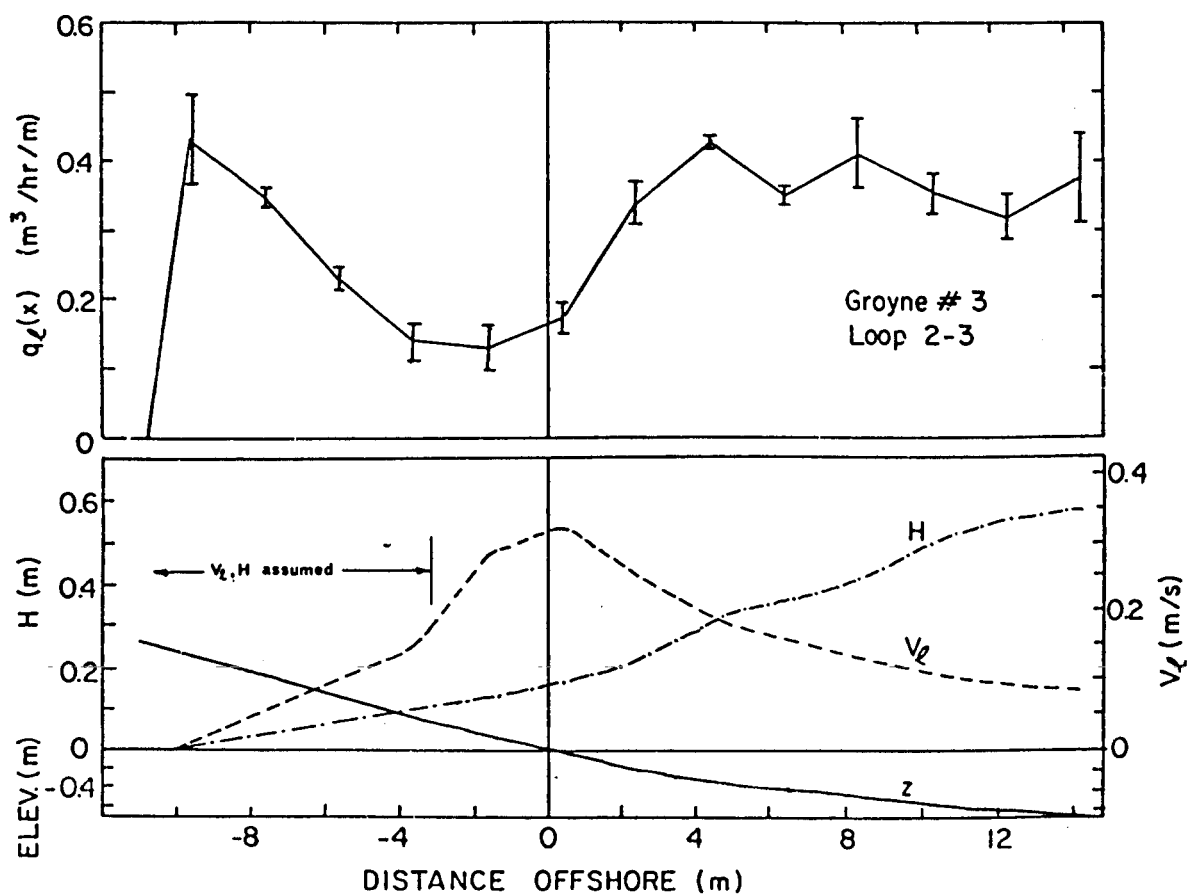


Figure 5-18: The longshore transport distribution, longshore current, wave height, and average beach profile across the surf zone for Groyne #3, loops 2-3 (the poorer of the two "best" field data sets).

## CHAPTER 6

### LABORATORY INVESTIGATION: MODEL APPARATUS AND EXPERIMENTAL METHOD

#### 6.1 Introduction

In order to better interpret the field results and to enhance understanding of the processes which affect the longshore sediment transport distribution, short-term longshore transport impoundment experiments were conducted in the laboratory. For the experiments, a fine-sand moveable-bed beach was constructed in the main wave basin at the University of Florida Coastal and Oceanographic Engineering Laboratory. The basin is approximately 28 m x 28 m in planform, bounded by a 1 m-high concrete wall, and is equipped on one end with an 88-paddle directional "snake" wavemaker capable of producing regular waves with a single desired direction.

Briefly stated, the approach of the field investigation was reproduced on the laboratory beach, but with several alterations intended to increase control. The model beach was pre-equilibrated to desired (regular) wave conditions and beach profiles along the model were surveyed. A sheet-metal groyne was then inserted in the absence of the waves and five to forty minutes of waves (actual time) were run in the model. The resulting sediment impoundment against the groyne was estimated from subsequent "post-impoundment" surveys of the beach. Details of the physical model and experimental techniques used in the laboratory investigation are described in this chapter.

## 6.2 The Physical Model

The beach was composed of 125 tons of well-sorted fine quartz sand ( $D_{50} = 0.16$  mm, sorting coefficient  $S_o = \sqrt{D_{75}/D_{25}} = 1.27$ ) of median fall velocity  $w_s = 1.7$  cm/sec. The beach was positioned in the middle of the wave basin such that the shoreline and toe of the beach made a 10-degree angle to the directional "snake" wavemaker (see Figure 6-1). The back-shore of the model was supported by an 81 cm-high block wall while the

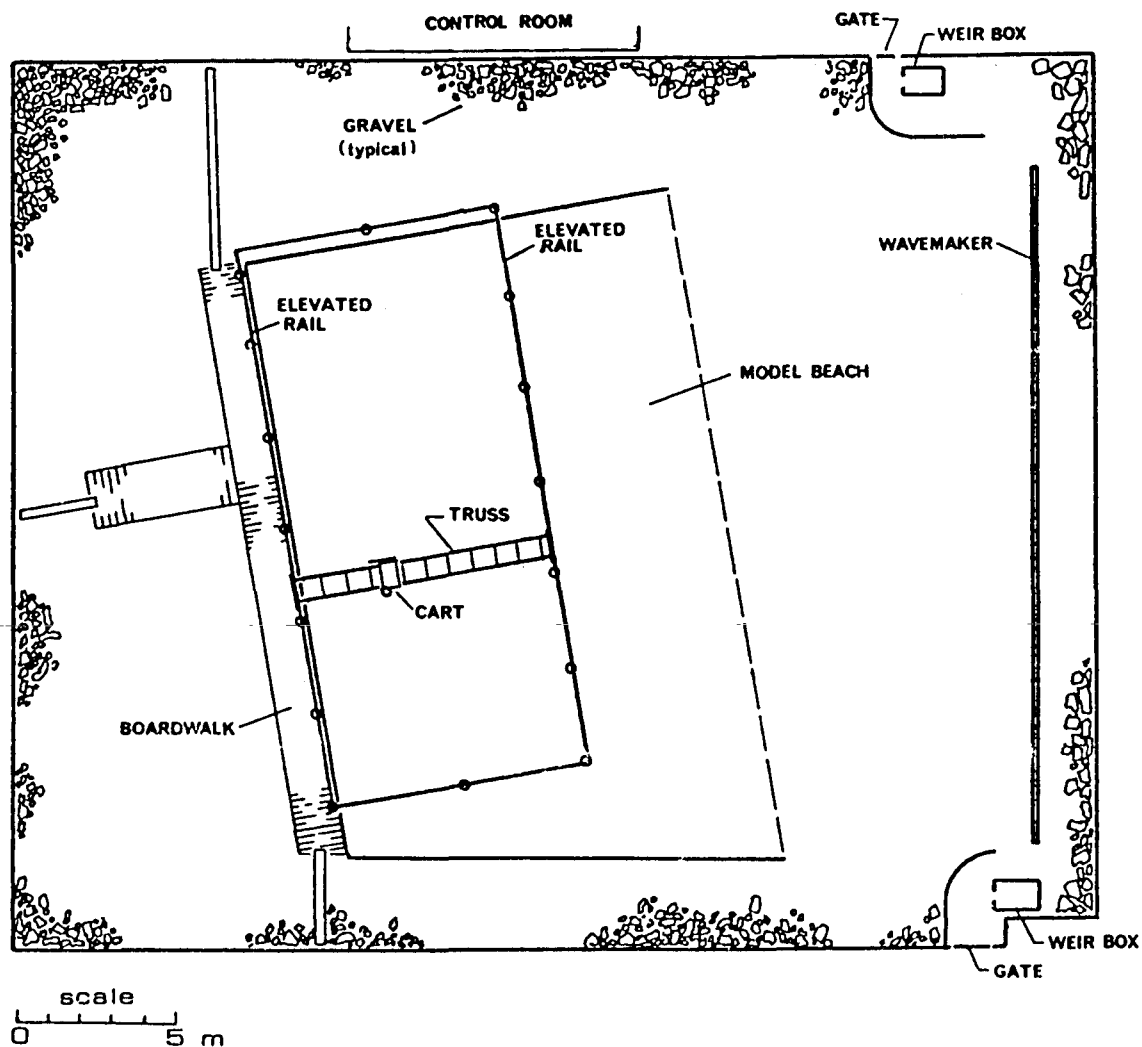


Figure 6-1: Plan view of the laboratory model.

the sides were supported by concrete-block and wooden templates cut to a "design" beach profile shape (described below). The approximate shoreline length was 19 m; the distance from the backshore to the toe was 14 m. The remainder of the basin consists of a level concrete floor with a short downward-sloping section immediately in front of the wavemaker. Roughly 75 cubic meters of gravel were spread along the inside of the basin walls to act as a wave absorber.

The "snake" wavemaker in the basin consists of 88 coupled paddles, 24 cm wide, which are driven by one shaft but which may be phased individually in order to create a wave train from any single desired direction (within practical limits of  $\pm 30^\circ$ ). Regular waves are created within a range of periods  $T = 0.5$  to 2.0 seconds.

The placement and orientation of the model beach relative to the wavemaker was decided through an optimization procedure. Specifically, it was desired that wave directions between normal incidence through 20-degrees breaking wave incidence could be applied to the model for maximum coverage of the shoreline and for maximum shoreline length.

Hughes' (1983) moveable-bed modeling law was utilized to scale the model beach based upon typical prototype profiles measured during the field investigation at the FRF. (It is noted that the model was not intended to completely replicate the field site; that is, the effects of the pier and other indigenous FRF beach morphology were not included in the model.) The fall-velocity scale was established as  $N_w = 1.47$ , and the time scale was selected as  $N_T = 6$ . After Hughes, this resulted in vertical and horizontal length scales of  $N_\mu \approx 9$  and  $N_\lambda \approx 18$ , respectively, and therefore a 2:1 horizontal/vertical distortion. The time scale was chosen such that the short-term (high tide) field

impoundment intervals could be modeled in a 30-50 minute period. From experience, this seemed to be an adequate time span for which a significant level of impoundment might be observed in the laboratory before the updrift beach (which was not "fed") became depleted or unacceptably irregular. The time scale was also chosen such that the corresponding vertical and horizontal length scales, applied to the field profiles, suggested a model geometry which closely resembled an equilibrium profile for the model's median grain size. Specifically, Dean (1977), among others, has suggested an equilibrium beach profile:

$$h(x) = A x^{2/3} \quad (6.1)$$

where the depth  $h$  at a distance offshore  $x$  is described as a function of the dimensional parameter  $A$ . Moore (1982) described the value of  $A$  as a function of sediment size. For the model sand,  $A \approx 0.078 \text{ m}^{1/3}$ . The best-fit  $A$  parameter for the field profiles was found to be  $A = 0.13 \text{ m}^{1/3}$ , which, when scaled to the model, becomes  $A = 0.1 \text{ m}^{1/3}$ . Accordingly, for the submerged portion of the "design" model beach profile, the average value  $A = 0.089 \text{ m}^{1/3}$  was selected. Based upon (scaled) foreshore characteristics of the field site, the subaerial portion of the "design" model profile was selected as an approximately planar slope. Precisely, the "design" model beach profile was

$$h(x) = \begin{cases} 0.152 x & -2.5 < x \leq -1.22 \text{ m} \\ 0.135 x & -1.22 < x \leq -0.61 \text{ m} \\ 0.130 x & -0.61 < x \leq 0.095 \text{ m} \\ 0.089 x^{2/3} & x > 0.095 \text{ m} \end{cases} \quad (6.2)$$

where Eq. (6.2) is expressed in meters and in model scale. In practice, this "design" profile proved relatively stable for all wave conditions

which were tested; that is, the foreshore and shallow contours responded to various surf conditions, while contours deeper than about 23 cm (model scale) remained fairly stationary.

The "design" basin water depth was 44.5 cm such that the toe of the model corresponded to the 4-meter depth contour of the prototype. Table 6-1 summarizes the physical model design parameters.

Fresh water was supplied to the basin through two V-notched weir boxes located on either side of the wavemaker. The weir box discharge areas were partially separated from the main basin by splash walls. Water could be emptied from the basin through either of two gates located near the weir box discharge areas. The water level in the basin could be changed during a wave trial, if desired.

Selection of appropriate wavemaker parameters to achieve a desired surf condition was aided by a computer-based algorithm. In particular, for given values of wavemaker stroke, paddle phase, period, and water depth, the height and angle of the waves generated by the paddle were calculated after Dean and Dalrymple (1984). The corresponding deepwater wave parameters were calculated using linear theory and the breaking wave height was then estimated after Weishar and Byrne (1978). The corresponding breaking depth was found through Weggel's (1972) approximation of the breaker index,  $\kappa = H_b/h_b$ , and the wave angle at breaking was then estimated using Snell's law. From the "design" beach profile, the bed slope at the estimated breaking depth was next calculated in order to approximate the surf similarity parameter,  $\xi_b = m/\sqrt{H_b/L_o}$ , from which the breaker type was predicted after Battjes (1974). In practice, this algorithm predicted surf parameters with reasonable accuracy (generally within 10% to 40%).

Table 6-1: Physical Model Design Parameters

Median sediment size . . . . .	$D_{50} = 0.16$ mm
Sorting coefficient . . . . .	$S_o = 1.27$
Median Fall Velocity . . . . .	$w_s = 1.7$ cm/sec
Shoreline Length . . . . .	$\sim 19$ m
Backshore to toe length . . . . .	$\sim 14$ m
Time scale . . . . .	$N_T = 6$
Vertical length scale . . . . .	$N_\mu = 9$
Horizontal length scale . . . . .	$N_\lambda = 18$
Distortion (horizontal:vertical) . . . . .	2:1
Design water depth . . . . .	$h_{\text{basin}} = 44.5$ cm
Design foreshore slope . . . . .	$m_f \approx 0.13$
Design (submerged) profile . . . . .	$h(x) = Ax^{2/3}$
Design "A" parameter . . . . .	$A = 0.089$ m <sup>1/3</sup>

### 6.3 Profiling Apparatus

Two shore-parallel rails were installed along the beach as shown in Figure 6-2. Spanning the rails was an 8.5 m-long wheeled truss which could be moved along the rails (and therefore along the beach) using a single loop of cable wound about a winch. Another pair of rails extended along the top of the truss (i.e., shore-perpendicular). A cart was built to move along these top rails (and therefore across the beach), via a pulley positioned at the shoreward end of the truss.

The cart supported a profiling device which operated as described below. The horizontal position of the cart along the top rails was indicated by the voltage drop across a potentiometer geared to a fifth "tracking wheel" on the cart. The elevation of the bed was measured by a "profiling arm," which was attached to the cart through another potentiometer. At the bottom end of the profiling arm was a small freely

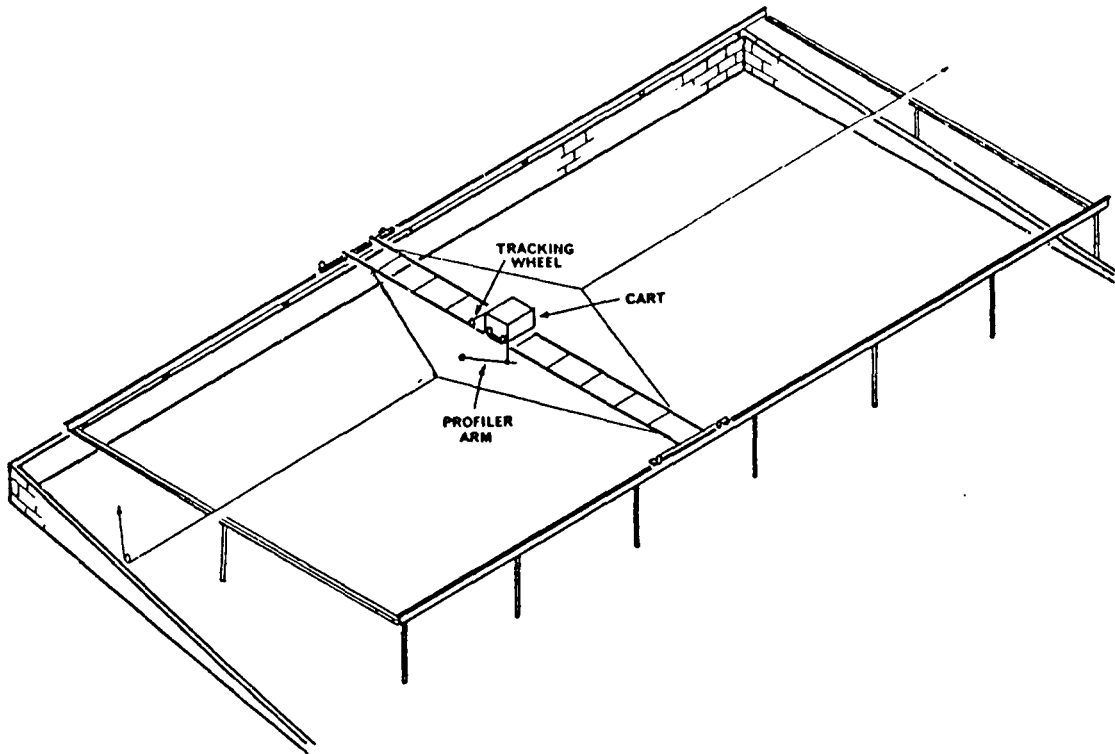


Figure 6-2: Oblique sketch of the support walls, rail system, cart, and profiler used in the laboratory model.

rotating PVC wheel (3.8 cm. dia x 2 cm tread width). As the cart was moved seaward, the profiling arm swung behind and below the cart-- following the beach profile as the small wheel at the bottom of the arm rolled along the bed. The angle which the profiling arm made with the cart-horizontal was indicated by the voltage drop across the potentiometer through which the arm was connected. Using simple geometry, this angle was interpreted as the distance between the bed and the cart's horizontal reference. Thus, the elevation of the bed was determined at any point over the portion of the beach which was covered by the rails. The location of the profiler along the shoreline was determined from a marker which indicated the position of the truss along the bottom

rails. The geometric considerations required to determine bed coordinates from the profiling system are described in Appendix E.

The potentiometers utilized a  $\pm 15$  V power supply with individual provisions for separate two sided (+/-) zero offset and profiler-arm signal amplification. If so desired, the offset and amplification features provided increased profile resolution across any portion of the beach. The profiler circuit diagram is shown in Appendix E.

The profiling apparatus on the cart was hard-wired to a data acquisition system using 50 meters of cable. The cable was strung along a steel line above the model via springs and pulley-blocks, and was thereby free to follow the movement of the cart. The analog signals from the potentiometers were digitized using an 11-bit A/D converter interfaced to a Hewlett-Packard HP-85 computer. This provided for standard horizontal and vertical profiler resolution of 3.3 mm and 0.35 mm, respectively. In practice, profile measurements could be repeated within 1 mm rms vertical deviation.

The cart and profiling arm were operated manually from a boardwalk behind the model. For each profile, reference (bench-mark) signals were taken from the potentiometers; then the cart was slowly moved seaward. Constant-speed motion was not necessary, as horizontal-tracking and profiler arm signals were taken at any point along the rails within less than 0.01 seconds of one another. The signal pairs were interrogated by the HP-85 computer at any desired burst interval. Typical sample rate was 1.25 Hz for a horizontal spacing of 5 to 15 cm between points on a profile. At the end of a profile, the arm was raised and locked in its "up" position by pulling a thin nylon line through a cam-cleat located near the rear of the cart. Profiles were always taken towards the

seaward direction so that the profiler wheel generally travelled "downhill" (else the wheel could gouge the bed). The profiler arm was counter-balanced so that the wheel would roll just over the top of the bed and leave a barely discernible track. Sand would occasionally contaminate the bearing of the profiler wheel and cause it to drag along the bed instead of roll. This problem was avoided by generously washing the profiler wheel and axle with water at the beginning of each profile. During all profiling operations, the water was drained from the basin to the deepest profile depth.

Use of the profiler was limited to the area of the model bounded by the rail system (i.e., the landward 8.5 m of the beach). However, screeding and inspection of the beach after many tests indicated that bed changes seaward of the rail system were negligible for the wave conditions used in the laboratory experiments.

The seaward-most bottom rail was supported by 2.5 cm-diameter pipes located on 3 m centers. The presence of these pipes was not observed to significantly affect the surf zone as they were relatively small compared to the model wavelengths (diameter/wavelength  $< 0.02$ ). The landward-most bottom rail was supported by the back wall of the model. The entire rail system was horizontally leveled to within  $\pm 1.5$  mm.

#### 6.4 Wave Measurement

Wave measurements over the basin floor were made by a capacitance wave probe located between the toe of the beach and the wavemaker. Wave measurements across the surf zone were made by a second capacitance probe mounted upon the profiling cart. The cross-shore position of the latter probe was indicated by the cart's horizontal tracking system.

The wave height envelope across the swash zone and very close to shore was measured using a so-called "wave board". For each "wave board" measurement, a plywood board was cut to the measured shape of the foreshore. The bottom of the board was positioned upon the foreshore and the level of the still water line across the board was marked. The board was then soaked in water, covered with sand, and briefly returned to its position on the foreshore in order to record the passage of several waves/swash. The crest envelope of the waves and swash were clearly indicated upon the board by the absence of sand. The width of this envelope--referenced to the still water mark or the bottom of the board--was taken as an estimate of the wave height or swash height, respectively, along the board. The "wave board" measurements potentially under-estimate wave heights due to lack of a trough envelope, but potentially over-estimate wave heights due to wicking, splash, and wave induced set-up. Wave height data established from the capacitance probe and the "wave board" agreed within 5% to 30% for those locations where the two measurement systems overlapped.

#### 6.5 Longshore Current and Wave Angle Measurement

Longshore currents across the surf zone were estimated from the time-rate of movement of a cross-shore injection of rhodamine dye into the water. The dye was mixed with water from the basin before injection and so was fairly neutrally buoyant. Movement of the dye injection along the beach was recorded by still-photography from a platform 8 m above the model. Bright markers and a large clock were laid upon the beach for distance- and time-scaling in the photographs. The breaking wave angle, relative to the rear retaining wall of the model, was also

estimated from the photographs. Since the seaward face of the retaining wall was established as the survey baseline, the wave angle relative to the breaking depth contour could be then estimated from inspection of the model's surveyed bathymetric contours.

#### 6.6 Flourescent Sand Tracer

Ninety kilograms of sand were tagged with four different colors of fluorescent dye and subsequently ground and re-sieved to match the grain size distribution of the native model material. When needed, approximately uniform strips of this tracer, 2 cm in width, were injected across the bed. The distribution of the time-rate of movement of the tracer after three to six minutes of wave action was to be used as a qualitative estimate of the distribution of longshore sediment transport across the surf zone and to assess the extent of groyne by-passing. The field of tracer dispersion was illuminated by flooding the model with intense black light provided by two filtered mercury-vapor lamps mounted 8 m above the model. Illumination was accomplished late at night while the laboratory was otherwise completely dark. Isolines of both "major" and "minimal" concentrations of fluorescent tracer were marked by different-colored ropes laid along the beach. These ropes were then photographed from above in daylight to indicate the approximate tracer dispersion field. Color photography of the black-lit tracer fields (using 1600 ASA high-speed film at long-exposures) provided rather eerie-looking images of the major tracer dispersion but did not adequately indicate the typically large areas of small tracer concentration.

Visual estimation of the tracer dispersal is both approximate and subjective because it relies on the eyes' ability to detect relative levels of illumination. However, the visual technique was preferred over conventional tracer-counting methods because counting techniques are extremely difficult and time-consuming for small diameter sands such as used in this model. In many cases, it was found that the tracer studies often yielded poor quality transport signals--principally because of the difficulty in discerning and/or quantifying the tracer field. Accordingly, the results of the tracer studies are not typically emphasized in the discussion of the laboratory results.

#### 6.7 Experimental Procedure

Preparation for a typical laboratory experiment began with draining all of the water out of the basin. Four plywood templates, cut to the "design" beach profile, were then inserted into and across the beach at approximately 3.6 m spacing along the beach. Insertion of the templates was accomplished by trenching the model down to the basin floor. The trenches along the templates were re-filled and the beach was then screeded in 3.6 m-wide sections at a time to the "design" beach profile. Screeding was accomplished by dragging a 4 m-long wooden board over the plywood templates. After screeding, the templates were removed and sand was replaced and smoothed across the long, narrow spaces left by the templates. Sediment deposited upon the floor from the sides of the model during previous tests was replaced onto the back-beach.

The basin was re-filled with water to a level several centimeters above the "design" water level (in order to saturate the upland beach) and then dropped to the "design" water level. The wavemaker was then

configured for the desired wave height, period, and direction for the experiment. In the absence of any shoreline obstructions, twenty to thirty minutes (model scale) of waves were run in the basin to establish a beach state of cross-shore quasi-equilibrium. Sediment which flowed off the sides of the model was usually collected from the basin floor and replaced to the back-beach. The water was then drained to the seaward limit of the rails and beach profiles were measured along the beach with intensive concentration in the vicinity of the proposed groyne site. A single, low-profile, sheet-metal groyne was then installed across the beach and the water level was raised to the "design" level. Five to forty minutes of waves were then run in the basin. During this time, waves and longshore current were measured as described previously, and the beach and groyne were carefully observed for surf-zone anomalies and barrier by-passing. After the impoundment interval associated with the wave run, the water was again drained from the basin to the seaward limit of the rails, and the earlier set of beach profiles was re-measured.

For some tests, the water level was then raised once again to the "design" level and another wave run and subsequent post-impoundment beach profiling loop were executed. For tests in which a new but similar wave condition was to be investigated, the groyne was removed and the beach was crudely re-screeded by distributing impounded sand evenly across beach contours defined by various water levels in the basin. For those cases in which the beach was greatly perturbed by the previous experiment or a greatly different wave condition was to be tested, the basin was completely drained and re-screeded using the "design" profile templates described previously.

In all cases there was no updrift artificial "supply" of sand during the short-term impoundment intervals, nor was a longshore current introduced artificially in the basin, nor were wave training walls used. The extent of end-effects and anomalous features along the model were determined by inspection of dye injections along the surf zone. In all cases, the groyne was established in a location where the longshore current appeared well-established and the beach was relatively free of anomalies for at least two or three surf zone widths updrift of the groyne.

#### 6.8 Laboratory Data Analysis

The beach profiles measured in the laboratory experiments were analyzed in a similar manner to the field data in order to establish total transport functions (related to the impoundment rate along the beach). Tidal deconvolution was not necessary except for those tests which included simulated tidal changes. Although the beach was pre-established in a state of cross-shore quasi-equilibrium for each test, cross-shore transport contributions to the total transport function (i.e., the profile changes) were still considered. As expected, these contributions were relatively small. Deviations from the previously described data analysis are described where appropriate in the next chapter.

## CHAPTER 7

### LABORATORY INVESTIGATION: RESULTS

#### 7.1 Introduction

This chapter describes the experimental conditions and immediate findings of the laboratory investigation of the distribution of long-shore sediment transport using impoundment techniques. For discussion purposes, the laboratory experiments are separated into five test series. Each series represents a single type breaking wave condition: spilling, plunging/spilling, plunging, plunging/collapsing, or collapsing. The effect of tidal fluctuation was investigated in the plunging/collapsing series. The plunging/spilling series most closely models the tideless field experiment conditions. The laboratory experiments were not necessarily executed in the order with which they are described below.

It is noted that all results are presented in prototype scale unless otherwise noted. The model/prototype scaling relationships are described in the previous chapter and are summarized in Table 6-1. Representative surf conditions for each laboratory test series are presented in both prototype and model scales in Table 7-1.

Table 7-1: Representative Surf Conditions  
for Laboratory Test Series

<u>Prototype Scale</u>										
Exp't.	$H_b$ (m)	$h_b$ (m)	$\alpha_b$ (deg)	T (s)	$x_b$ (m)	$H_o'$ (m)	$m_f$	R (m)	$\xi_b$	$h_{basin}$ (m)
PL/SP	1.11 0.83*	1.04 0.60*	12.0 ~11*	8.1	30.5 18.4*	0.64	0.104	0.63	0.30 0.35*	4.0
PL	1.10	1.04	16.2	11.9	25.6	0.91	0.075	0.81	0.37	4.0
PL/CLPS	0.80	0.59	14.5	9.6	12.3	0.25	0.102	0.73	0.45	4.1
CLPS†	0.53	0.48	14.2	10.8	7.6	0.30	0.066	0.50	0.69	4.0
SP	0.94	1.29	10.8	5.1	39.5	0.69	0.054	0.36	0.15	4.1
<u>Model Scale</u>										
Exp't.	$H_b$ (cm)	$h_b$ (cm)	$\alpha_b$ (deg)	T (s)	$x_b$ (m)	$H_o'$ (cm)	$m_f$	R (cm)	$\xi_b$	$h_{basin}$ (cm)
PL/SP	12.3 9.2*	11.6 6.7*	12.0 ~11*	1.35	1.7 1.0*	7.1	0.208	7.0	0.30 0.35*	44.5
PL	12.2	11.6	16.2	1.98	1.4	10.1	0.150	9.0	0.37	44.5
PL/CLPS	8.9	6.6	14.5	1.60	0.7	2.8	0.204	8.1	0.45	45.5
CLPS†	5.9	5.3	14.2	1.80	0.4	3.3	0.132	5.5	0.69	44.5
SP	10.4	14.3	10.8	0.85	2.2	7.7	0.108	4.0	0.15	46.0

Notes:

- Breaking wave types: PL=plunging, SP=spilling, CLPS=collapsing  
 $x_b$ : average surf zone width (still water shoreline to breakpoint)  
 $m_f$ : average foreshore slope  
R: vertical wave run-up  
 $\xi_b$ : surf similarity parameter (using average breakpoint bed slope)  
\* inner break position  
† conditions at mean water (i.e., non-tidal test).

## 7.2 Plunging/Spilling Series--Field Experiment Conditions Without Tide

### 7.2.1 Description of Experiment

As described in the previous chapter, the laboratory beach profile was modeled after typical profiles characteristic of the field experiment site. For the plunging/spilling test series, the wave conditions were similarly selected to represent typical field experiment conditions; i.e., plunging and/or spilling breakers between 0.5 and 1.0 meters in height, 8 to 9 seconds in period, and 6 to 10 degrees in shoreline angle. During the model tests, the breaker position migrated irregularly. This was most probably due to the presence of a long wave in the model basin, but the migration was not significant in the other test series. In Table 7-1, the wave conditions for this series are reported for both the extreme seaward ("outer") and landward ("inner") locations of the break. It is noted that the "inner" break was not the second breaking of the reformed wave associated with the "outer" break.

The model beach was screeded to the "design" profile, as described in the preceding chapter, and equilibrated to the series' wave conditions in the absence of any groyne for approximately 3 hours (prototype time). The pre-impoundment survey loop, "A", was executed, a single groyne was installed, and waves were run for 3 hours and 12 minutes, after which survey loop "B" was taken. Another 4-1/2 hours of the same wave conditions were run, after which survey loop "C" was taken. This series therefore resulted in two successive impoundment intervals. The profile of the groyne, and beach profile changes adjacent to the groyne are shown in Figure 7-1.

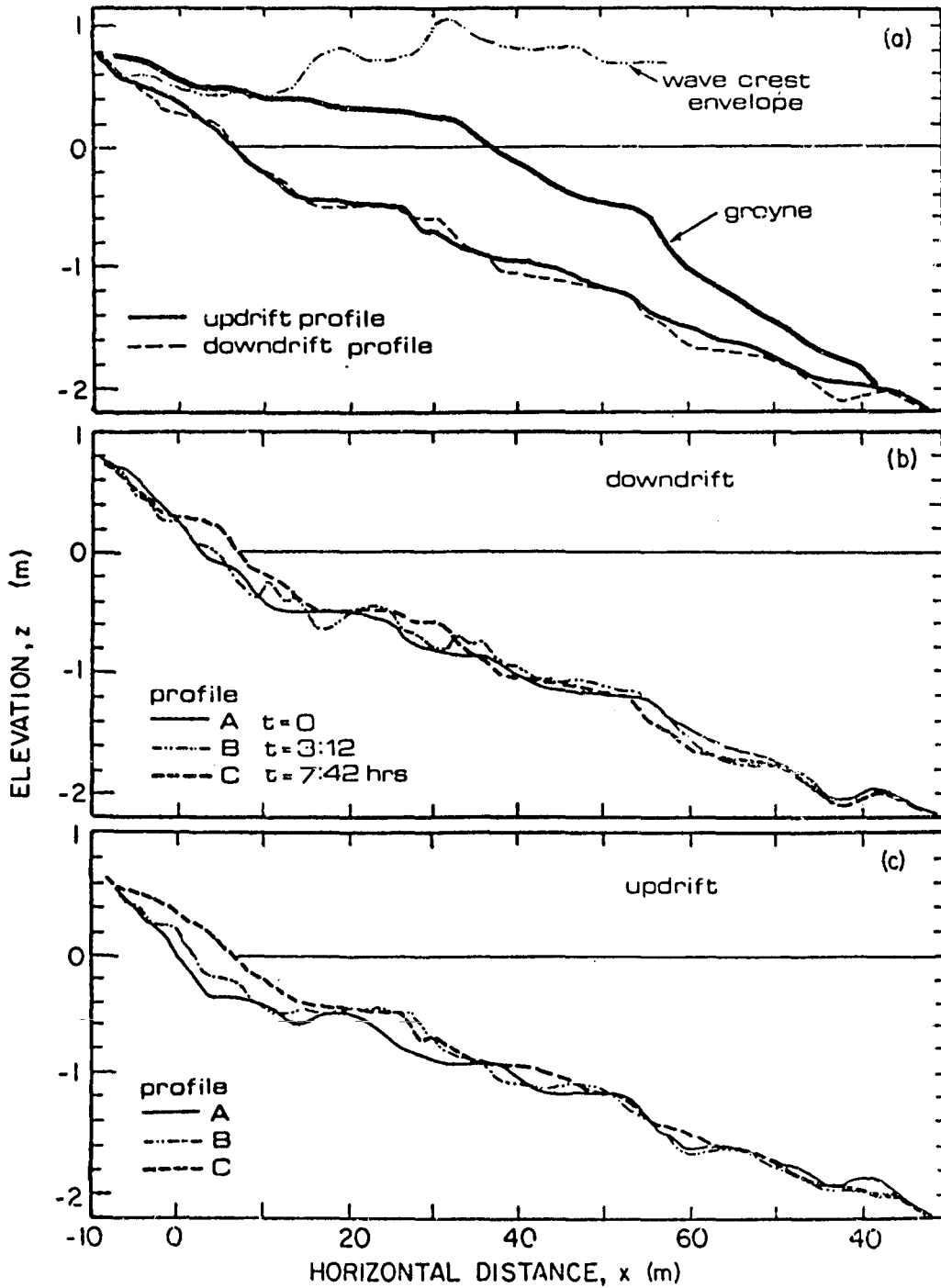


Figure 7-1: (a) Profile of groyne and adjacent beach profiles (survey loop "C"), and beach profile changes immediately (b) downdrift and (c) updrift of the groyne. Plunging/spilling test series (prototype scale).

### 7.2.2 Appropriate Groyne Profile

In an earlier (un-reported) laboratory trial, it was observed that a groyne which extends well above the swash wave height on the lower foreshore and/or well above the still water level elsewhere creates a very strong rip along the groyne and significant (observable) wave reflection from the updrift side of the groyne. The strong rip steepens the waves near the end of the groyne thereby altering the local breaking wave condition. The strong rip is also thought to transport considerable amounts of sediment seaward thereby skewing the impoundment profile towards the offshore direction. The significant wave reflection off the groyne can lead to the formation of a cusp-like feature updrift of the groyne where the reflected waves interfere with the incident waves at the shoreline. This cusp-like feature interrupts littoral transport along the shoreline. Decreasing the groyne elevation (such that at least most of the wave crest passes over the groyne) significantly reduces the updrift rip and wave reflection caused by the groyne's presence. After experimenting with several groyne profiles, it was concluded that wave crest overtopping and suspended-load losses associated with a low-profile groyne compromised experimental quality much less severely than the alteration of the sediment transport field caused by a high-profile groyne. Additionally, the low-profile groyne is a fairly accurate representation of the groynes constructed for the field experiments (for high tide conditions in the field.)

In view of the above, a low-profile groyne was used in all of the laboratory tests. When necessary, the groyne was locally reinforced in height during a wave run in order to crudely maintain a constant local groyne relief above the bed and to prevent by-passing as sand impounded against the updrift side.

### 7.2.3 First Impoundment Interval

The total transport function  $\Lambda(z)$  as determined from the horizontal displacement of the model beach contours between survey loops "A" and "B" is illustrated for most of the entire beach in Figure 7-2. The transport function is similar to those presented for the field experiment results described in Chapter 5. As the transport function is shown here primarily for purposes of qualitative discussion, as follows, Figure 7-2 illustrates the transport function in model scale.

Downdrift changes. Like the field results, the transport function indicates considerable localized accretion against the downdrift side of the barrier. Although some localized accretion (or at least stability) was expected on the downdrift side due to "shadow zone" effects of the groyne, the magnitude and distribution of this accretion as observed in the field results was initially perplexing. However, the benefit of greater observational clarity and the increased quantities of profile data possible in the laboratory revealed the processes associated with this downdrift accretion. On the downdrift side of the barrier, a strong current was observed to flow along the shoreline towards the groyne in addition to a strong rip which flowed offshore along the downdrift side of the groyne (see Figure 7-3). The magnitudes of the longshore current and rip were equal to or greater than the longshore current and rip, respectively, observed on the updrift side of the groyne. The longshore current began flowing updrift about one groyne length leeward of the groyne. Further downdrift, the current flowed in the downdrift direction, as expected. The rip began in the swash zone and extended well past the break point. It is thought that the updrift-flowing longshore current was partly a diffraction current flowing into

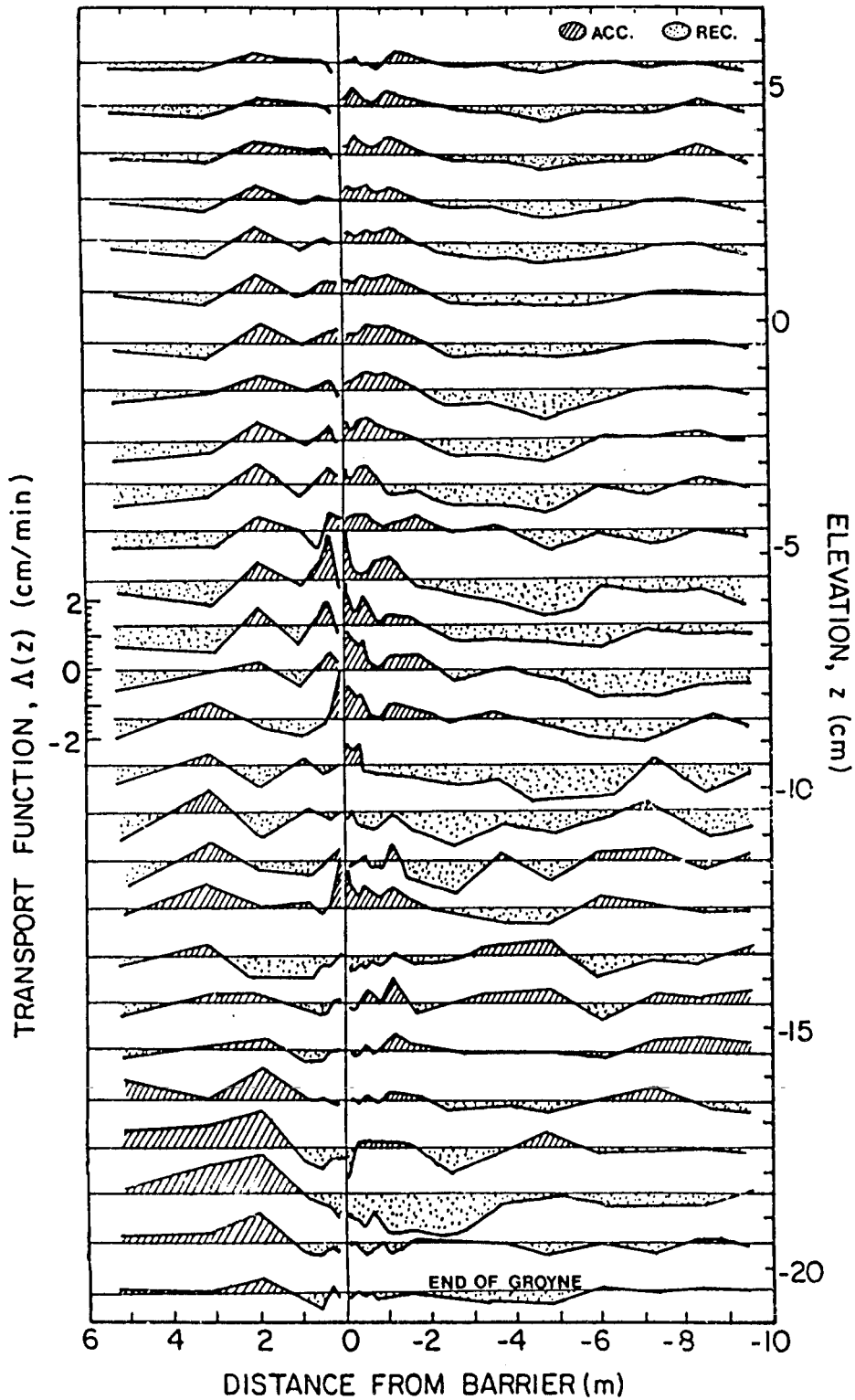


Figure 7-2: The total transport function determined for the first impoundment interval of the plunging/spilling test series, (model scale).

the shadow zone of the groyne. This current was diverted by the groyne as a rip which flowed against the incoming waves and induced an effective refraction of the waves around the end of the groyne. The waves were observed to refract into the downdrift area of the groyne at an angle opposite in sign to that of the updrift side. This induced a longshore current (opposite in sense to that on the updrift side) which enhanced the downdrift-side diffraction current and which therefore enhanced the downdrift-side rip. As one might imagine, the wave/current pattern on the downdrift side was quite remarkable to observe. If the sediment transport corresponded in magnitude and complexity to that of the downdrift-side current field, then considerable amounts of sediment were carried towards the groyne and subsequently smeared in the

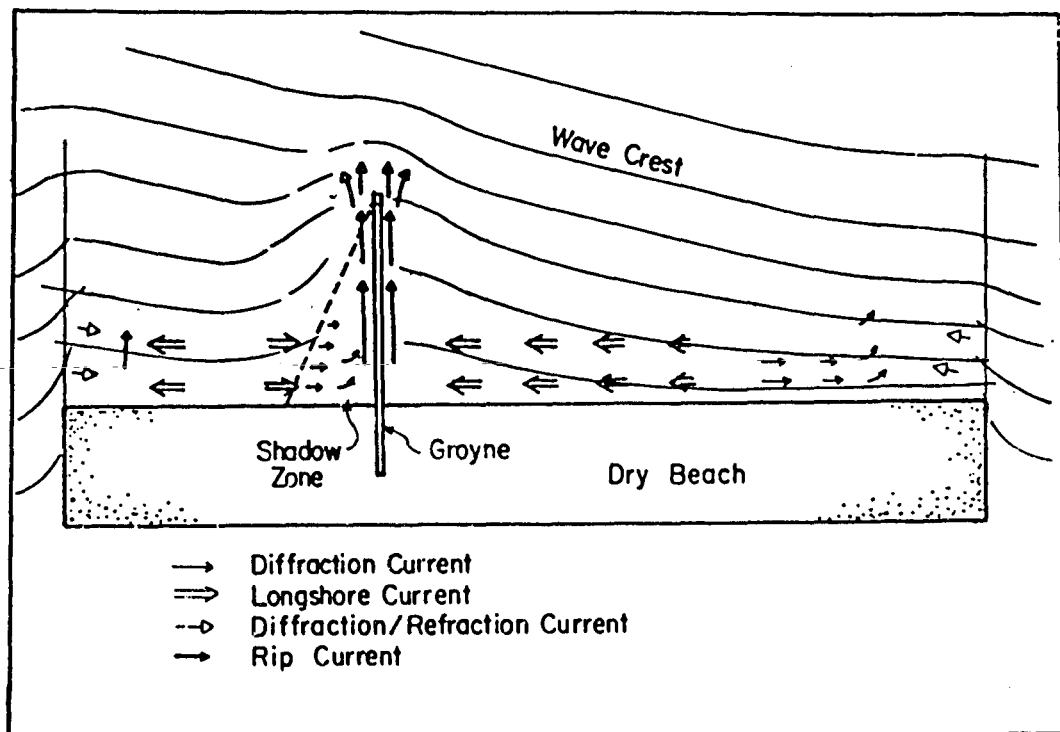


Figure 7-3: Illustrative sketch of wave and current pattern around the impoundment barrier in the laboratory model. Not to scale.

offshore direction by the rip. This may explain the significant magnitude and unusual distribution of accretion observed on the down-drift side of the groynes in both the field and this test series' laboratory results. Localized recession on the downdrift side might be viewed as localized profile steepening in response to the altered wave conditions caused by the rip at the groyne. The transport function appears quasi-symmetric across the groyne at some depth contours; however, this is not typical of the laboratory test results. In summary, it is thought by this author that local downdrift-side profile changes are generally misrepresentative of updrift-side transport processes; therefore, downdrift-side profile changes should not be used to interpret local updrift-side processes until an improved understanding of wave and current patterns in the vicinity of a shore-perpendicular barrier is achieved.

Updrift changes. The total transport function and associated profile changes on the updrift side of the groyne are also generally similar to those observed in the field experiments. Like the field results, accretion is noted against the groyne at most contours within the surf zone. Recession near the groyne (mostly outside of the surf zone) is generally consistent with recession all along the contour and so probably reflects fairly alongshore-uniform cross-shore processes at these contours. Like the field results, some recession or relatively low accretion signals are noted immediately adjacent to the groyne. Observation of the model suggested that these impoundment "anomalies" are associated with localized scour and offshore transport due to the rip and associated wave steepening along the updrift side of the groyne.

End effects. An important difference between the profile changes measured in the field and in the laboratory experiments comes about because of the finite length of the laboratory beach. Whereas it may be assumed that the field site had an infinite supply of sediment for longshore impoundment, the supply in the model was limited to the updrift length of beach for which the longshore current was developed. The finite lengths of the wavemaker and the updrift stretch of beach in the model basin resulted in an updrift end effect manifest as an along-shore diffraction current which flowed towards the updrift end of the beach. Hence a nodal point in the longshore current (and sediment transport) clearly existed on the updrift side. For this series' tests, the nodal point was identified by dye injections at approximately 4.8 m updrift of the groyne (model scale). Presumably because the nodal point was induced by an unnatural model end effect, the gradient of longshore current (and sediment transport) was unusually large at the nodal point; accordingly, considerable recession was observed here (see Figure 7-2). Downdrift of the node, sediment was carried towards the groyne by the prevailing longshore current generated by the obliquely incident waves and was deposited against or bypassed over/around the barrier. Updrift of the node, sediment was carried updrift by the diffraction currents and deposited near the updrift end of the model. This updrift area accreted because sand was mostly prevented from flowing off the updrift end of the model due to very localized wave refraction at the model's ends; furthermore, the diffraction current lost some of its transporting power as it diffused in the low wave energy environment of the far updrift area. Similarly, losses off the far downdrift end of the beach were much less than expected because the localized wave

refraction at the far downdrift end prevented some of the sand from spilling onto the basin floor. This resulted in a local accretion at the far downdrift end (not shown in Figure 7-2) which reinforced the localized wave refraction there.

Data analysis methodology. Most beach profiles measured in this test series were characterized by a steep planar foreshore with considerable terracing below the still water level--but with few bar features. Accordingly, profile changes were analyzed in the same manner as described for the field data; that is, the total transport function  $\Lambda(z)$  was developed from the horizontal displacement of depth contours along the beach. Specifically, for the most general case, where a depth contour of either or both surveys of a particular beach profile was uniquely described, terraced, or rippled, the horizontal displacement  $\Delta x$  was calculated from

$$\Delta x = (x_{2c} - x_{1c}) - (x_{2b} - x_{1b}) + (x_{2a} - x_{1a}) \quad (7.1)$$

where the offshore locations  $x$  are described graphically in Figure 7-4. For a uniquely defined contour of profile number 'n',

$$x_{na} = x_{nb} = x_{nc} \quad (7.2)$$

such that  $\Delta x$  in Eq. (7.1) is simply given by  $x_2 - x_1$  if the depth contour is uniquely defined for both surveys of a profile. For a contour which includes a terrace feature for profile number 'n',

$$x_{na} = x_{nb} \quad (7.3)$$

and  $x_{nc}$  represents the seaward limit of the terrace. For a profile contour "contaminated" by a single ripple feature, each of the  $x$  terms for the profile are uniquely valued.

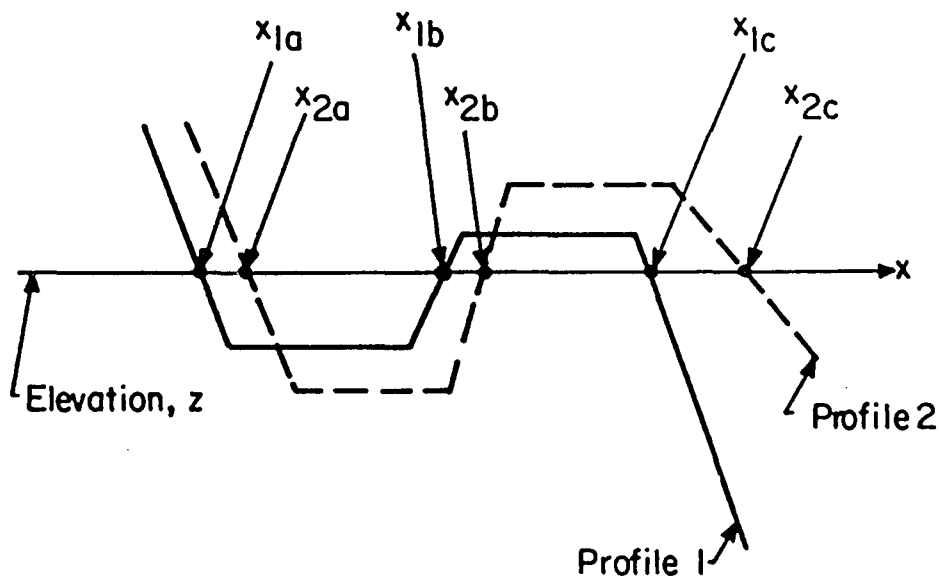


Figure 7-4: Graphical description of variables used to calculate the horizontal displacement  $\Delta x$  between two beach profiles for the general case of a non-uniquely defined contour.

Identification of the cross-shore component of transport and the longshore impoundment signal from the laboratory transport functions was similar to the approach used for the field data. As with the field data, the laboratory data analysis was restricted to the updrift side of the groyne. An idealized total transport function along a contour  $z$  is illustrated in Figure 7-5 for the updrift side of the groyne. The transport  $q(y)$  (a cumulative function obtained by integrating the transport function along the beach and updrift from the barrier) is also shown. The local transport  $q(y_e)$  is the cumulative value of the transport function at the far-updrift end of the beach, and therefore represents the net local rate of updrift volumetric sediment loss or gain along the depth contour. The labelled regions approximately correspond to (A) fillet due to longshore transport impoundment by the

barrier, (B) recession associated with supply of impoundment fillet, (C) longshore transport losses over the barrier and updrift transport due to diffraction current, and (D) accretion due to updrift end effect. The alongshore location  $y_*$  corresponds to the near-barrier maxima of the cumulative function  $q(y)$ , which is also the updrift limit of impoundment caused by the barrier. If there were no losses off the beach or across the barrier, and no net cross-shore transport processes, the cumulative function at the end of the beach,  $q(y_e)$ , would be zero-valued. Since very little sediment was ever recovered from the basin floor next to the

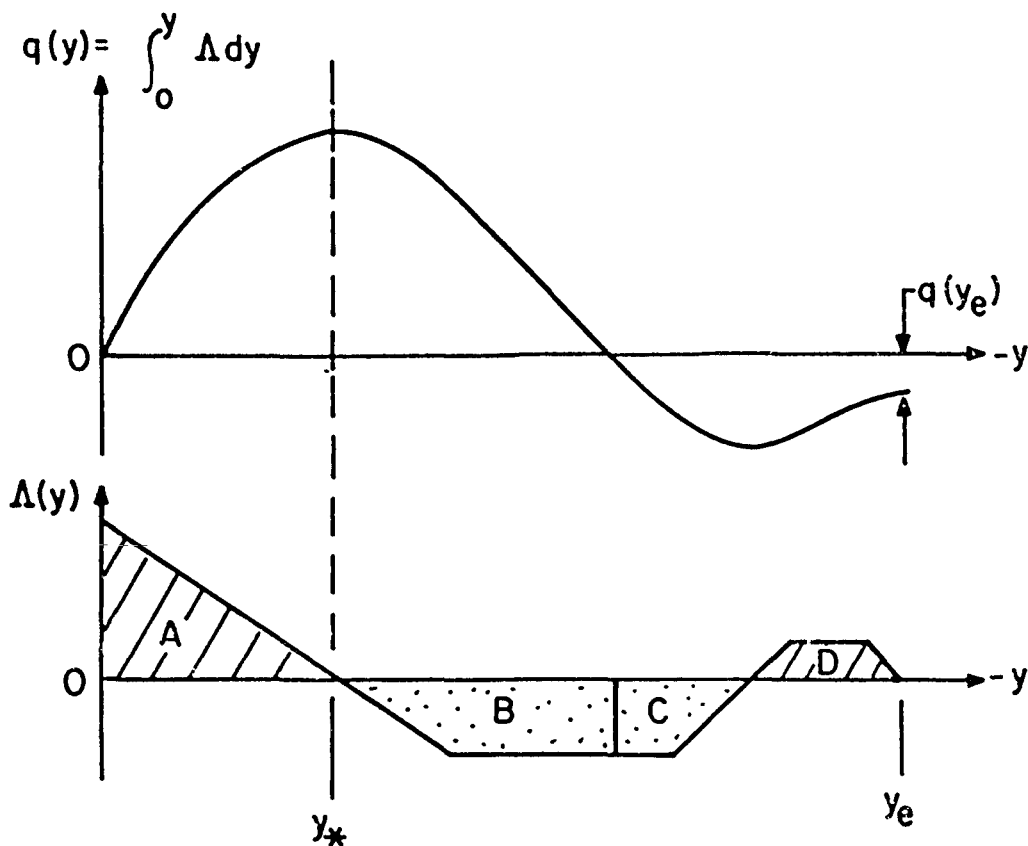


Figure 7-5: Idealized total transport function,  $\Lambda(y)$ , and associated transport,  $q(y)$ , along a given depth contour (or offshore location) updrift of the barrier on the laboratory beach.

far updrift end of the model, updrift losses may be assumed as small. Hence, a non-zero value of  $q(y_e)$  would indicate that cross-shore transport processes or barrier bypassing was present.

If bypassing is neglected and the cross-shore processes are assumed to be fairly uniform along the beach, then the cross-shore component  $C$  of the total transport function is  $q(y_e) \cdot y_e$ . This value is removed from the total transport function and the result is integrated updrift from the barrier to  $y_*$ . This yields one estimate of the local longshore transport rate  $q_l(z)$  at the contour.

If cross-shore processes are neglected and bypassing is instead considered, the local rate of bypassing is simply  $q(y_e)$ . A second estimate of the local longshore transport rate is therefore given by the bypassing rate  $|q(y_e)|$  plus the impoundment rate, where the latter is obtained by integrating the "raw" total transport function updrift from the barrier to  $y_*$ .

These two estimates, respectively, represent the low and high estimates of the local longshore transport rate at the contour of interest. A potentially better estimate, which includes both cross-shore processes and bypassing, is also described. The average value of the total transport function, estimated far updrift of the groyne (regions C and D) is assumed to approximate the cross-shore component  $C$  and is subsequently subtracted from the total transport function along the contour. The local longshore transport rate is then taken as the impoundment rate (calculated as described for the first estimate) plus the bypassing rate  $|q(y_e)|$ , where the latter is adjusted by the cross-shore contribution  $C \cdot y_e$ . This third estimate of the local longshore transport rate is possible only if the total transport function along the contour is well-conditioned.

The actual profile data yields total transport functions which are similar to the ideal case shown in Figure 7-5. However, signal quality varies between contours/offshore locations and between tests. As an example, the updrift-side total transport functions shown in Figure 7-2 are fairly typical of the laboratory test results. Error bars shown throughout this chapter for the estimates of local longshore transport rate generally reflect the difference between the low- and high-valued estimates described above, and/or uncertainties in the updrift extent of the impoundment fillet. Slight differences in analysis methodology for other test series are discussed individually for each series where appropriate.

Longshore sediment transport distribution profile. The profile change data from the first impoundment interval of the plunging/spilling test series were analyzed along 1 cm depth contours (model scale) as described above. The resulting estimate of the local longshore transport rate per unit depth,  $q_\ell(z)$ , was transformed to the local rate per unit offshore distance,  $q_\ell(x)$ , as described in Chapter 4, Section 8. In Figure 7-6, the offshore distribution of the longshore sediment transport rate is illustrated, along with the measured wave height and longshore current data, and the average representative beach profile. The agreement between the laboratory model results and the "best" field results (Figures 5-17 and 5-18) is good, particularly if the break point in the laboratory test is taken as the average location of the "inner" and "outer" migrating break locations. The longshore transport distribution is bimodal for both field and laboratory results with one peak in the outer surf zone and another near the approximate shoreline. Approximately 30% of the total transport is observed above the shoreline

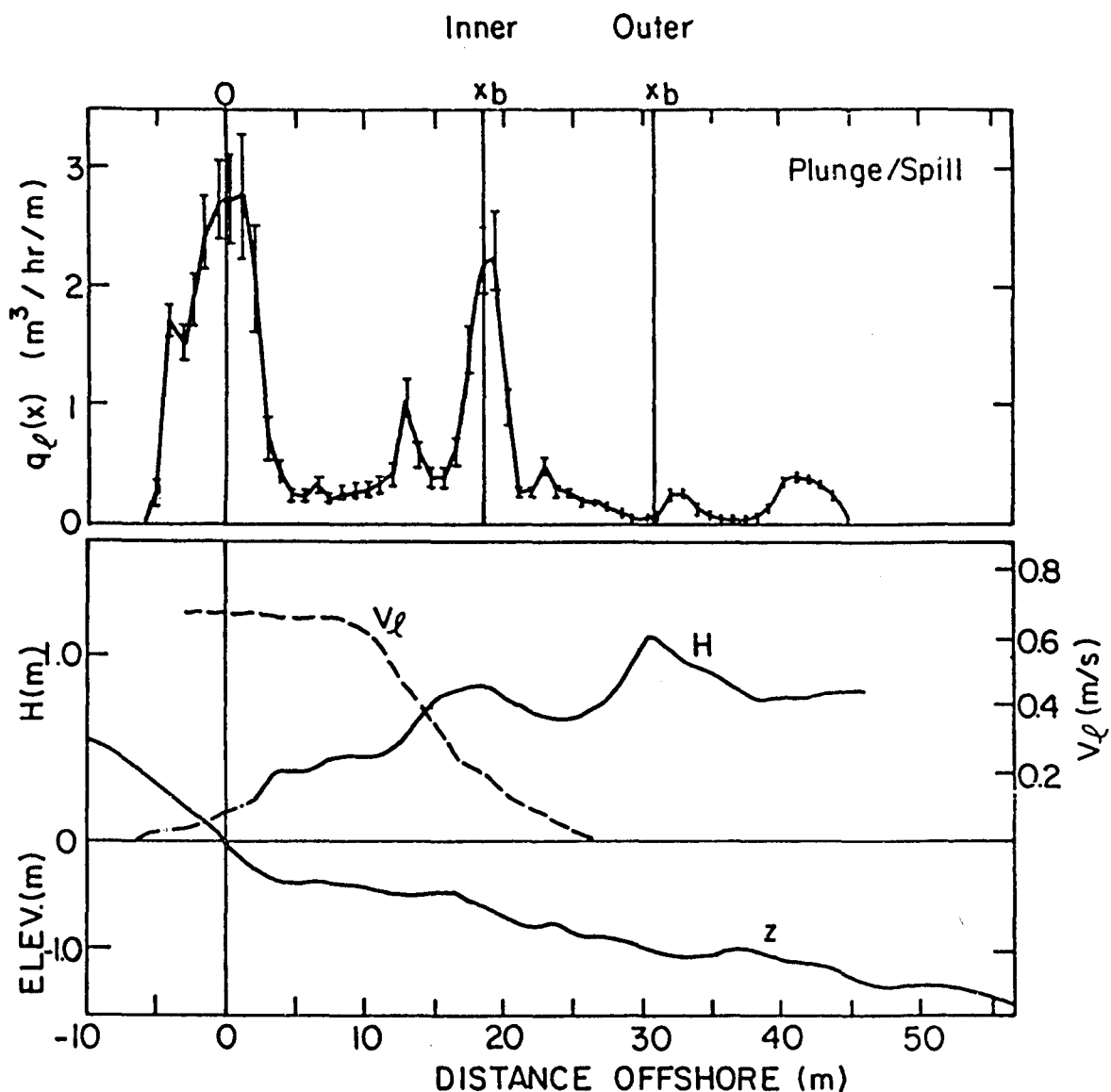


Figure 7-6: The longshore transport distribution, longshore current, wave height, and average beach profile across the surf zone for the first impoundment interval of the plunging/spilling test series (prototype scale).

with about 10% to 20% seaward of the break point. The total longshore transport for the laboratory test results is 27.5 to 38.5  $\text{m}^3/\text{hr}$ . (For comparison, the total transport rate found for the most complete field impoundment experiment was 13.5 to 19.9  $\text{m}^3/\text{hr}$ .) The impoundment fillet

typically extended to about 29 m updrift of the groyne. This is approximately equal to the average surf zone width.

Longshore current profile. The Lagrangian measurement of the longshore current indicated that the local maxima was located near the shoreline (Figure 7-6). This feature, as well as the overall longshore current profile, is consistent with that predicted by McDougal and Hudspeth (1981) for an equilibrium beach of the same general shape used in all of the laboratory tests. Figure 7-6 also indicates a strong longshore current in the swash zone. More precisely, the longshore movement of the dye observed above the mean shoreline was not associated with a temporally continuous current, but was instead associated with the longshore component of the swash water particle motion upon the beachface. For the present, however, the latter is treated as a longshore current.

#### 7.2.4 Second Impoundment Interval

The analysis methodology described above and utilized for the profile change data of the first impoundment interval was applied to that of the second interval (survey loops "B" to "C"). The local longshore transport distribution (calculated per unit depth) was transformed to a distribution across shore and is shown in Figure 7-7. The longshore transport distribution found for the first impoundment interval is also shown for comparison; the error bars have been deleted for clarity of presentation. It is noted that the longshore transport distribution derived from the second impoundment interval is skewed seaward compared to that of the first interval. More detailed investigations of this effect (discussed in the following pages in

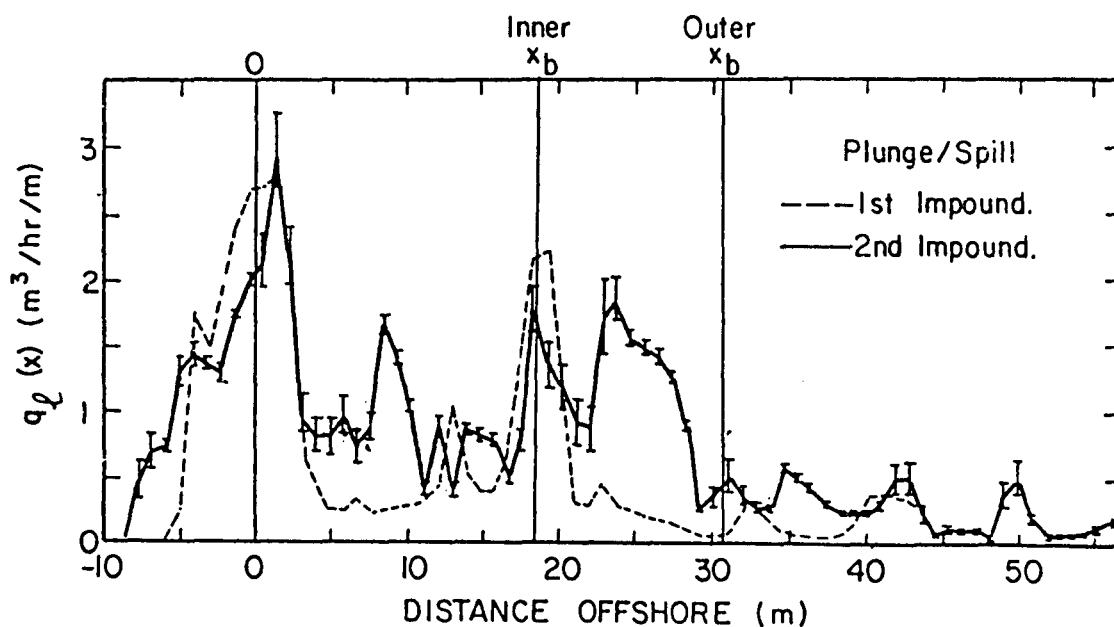


Figure 7-7: Comparison of the longshore transport distribution found from the first and second impoundment intervals of the plunging/spilling test series (prototype scale).

conjunction with other test series) suggest that the distribution of sediment impounded against the groyne is progressively smeared with time--primarily offshore--as the trap becomes full and the waves and groyne-rip act to equilibrate the profile updrift of the groyne.

The total longshore transport calculated for the second impoundment interval is 46.7 to 57 m<sup>3</sup>/hr, which is considerably greater than that calculated for the first interval. This may be due to the slight heightening of the groyne undertaken between the first and second impoundment intervals and/or mis-interpretation of the profile change data from either or both intervals. Subsequent investigations of impoundment-smearing over time do not show a discrepancy in the total transport rate between impoundment intervals.

### 7.3 Plunging Series

#### 7.3.1 Description of Experiment

After screeding the beach to the approximate "design" profile described in the previous chapter, a plunging breaker wave condition was established in the basin of 1.1 m height, 11.9 s period, and approximately  $16.2^\circ$  in shoreline angle (prototype scale). The complete series' test conditions are listed in Table 7-1. The beach was equilibrated to the series' wave conditions for approximately 3 hours in the absence of the groyne, after which the first survey loop ("A") was taken. Another 60 minutes of waves were run in the absence of the groyne and the second survey loop ("B") was taken. A low-profile groyne was then installed, 30 minutes of waves were run, and the third survey loop ("C") was taken. Another 42 minutes of waves were run, and the final survey loop ("D") was taken. This series therefore resulted in a no-groyne "control" interval ("A to B") and two successive impoundment intervals ("B to C" and "C to D"). Alternately, a single impoundment interval ("B to D") may be considered. A different trapping technique, using combination bedload and suspended-load traps, was also tried during this test series, and is described in Section 7.3.6.

Each survey loop of the impoundment trials of this series included sixteen profile lines: four within 5.4 m downdrift of the groyne and twelve within 52.2 m updrift, where the spacing between lines increased from 1.08 m near the groyne to 10.8 m far updrift. The profiles were limited to an area free of end-effects such that, essentially, only the impoundment fillet would be reflected in the profile data.

### 7.3.2 No groyne "control" interval

Profile changes between survey loops "A" and "B", during which no groyne was present, were interpreted as an indicator of the degree to which the model beach was equilibrated with the wave conditions before the impoundment tests were begun. In addition, the profile changes were taken as an estimate of cross-shore transport processes which may have been present in the impoundment survey data.

The pre-impoundment profile change ("A to B") at the eventual site of the groyne is illustrated in Figure 7-8. The profile change illustrated in the figure is typical of all of the profiles surveyed for the "A to B" interval. It is observed that the beach was well equilibrated with the wave conditions since the profile changes measured before the barrier installation were relatively small.

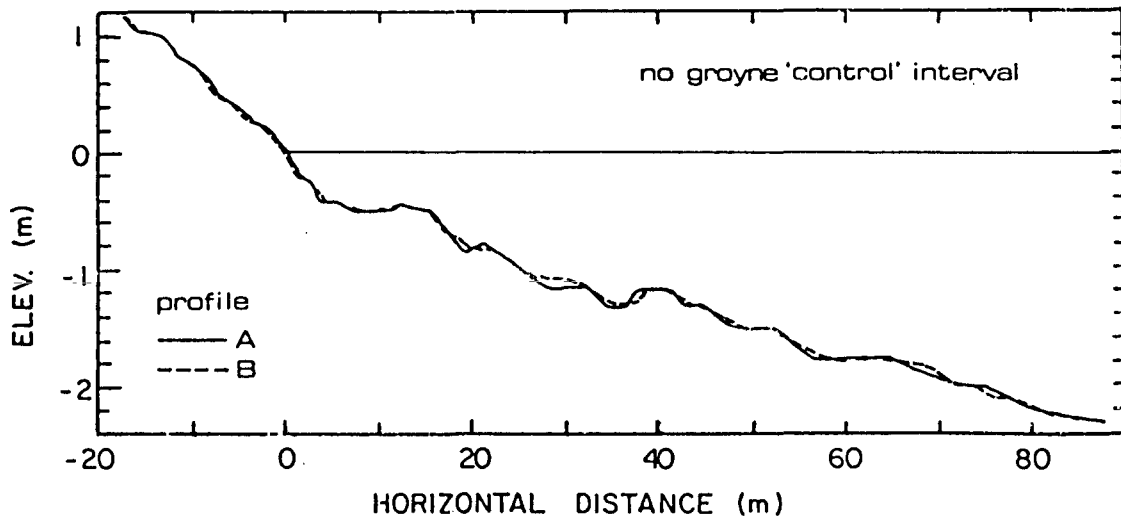


Figure 7-8: Beach profile change before groyne deployment at the site of the groyne for the plunging test series (prototype scale).

### 7.3.3 Impoundment Data Analysis Methodology

The profiles measured during the second survey loop of the impoundment interval (loop "C") exhibited strong bar features. Hence, analysis along depth contours for impoundment intervals "B to C" and "C to D" was problematic because the locations of the contours were not uniquely defined by offshore distances,  $x$ . Instead, the data analysis for these intervals was conducted along a series of offshore locations (at 0.9 m spacing, prototype scale). In general, it is preferable to consider horizontal profile changes along contours or elevations  $z$  (as has been done up to this point) rather than to consider vertical profile changes along fixed offshore locations  $x$ . This is because beach processes are related to the depth contours--not necessarily the distance offshore--and the depth contours shift along the beach during impoundment. As an example, let a chosen offshore location originally correspond to a particular depth contour along the beach. After the beach accretes near the groyne due to impoundment (and possibly recedes farther updrift due to a lack of sediment supply) location  $x$  corresponds to a shallow depth near the groyne, (and possibly to a greater depth farther updrift of the groyne). However, analysis along fixed offshore locations was deemed a reasonable approach for this test series since the contours near the groyne did not shift seaward appreciably (due to the relatively short impoundment intervals) and so the depth was relatively uniform along each offshore location of interest. The profile change data for the interval "B to D" were analyzed along both fixed offshore locations and along depth contours; the longshore transport distribution found for each approach agreed satisfactorily.

The total transport function,  $\Lambda(x)$ , for analysis along offshore locations is expressed from the "conservation of sand" equation as:

$$\begin{aligned} \left. \frac{\partial z}{\partial t} \right|_x &= -\left( \frac{\partial q_x(y)}{\partial x} + \frac{\partial q_y(x)}{\partial y} \right) \\ &= \vec{V} \cdot \vec{q} \equiv \Lambda(x) \end{aligned} \tag{7.4}$$

where  $\vec{q}$  represents the local transport rate per unit offshore width at location  $(x,y)$ . From Eq. (7.4) it is seen that the total transport function is actually calculated from the profile data as the vertical rate of change of the bed at location  $(x,y)$ .

Typically, the cross-shore component along each offshore location or depth contour was taken as both (i) zero, and (ii) the average-value calculated along the offshore location or depth contour for the no-groyne "control" interval "A to B." These estimates were subtracted from the total transport function along each offshore location, and the resulting values were integrated updrift from the barrier to the location where the cumulative transport function reached a maximum or became constant (i.e., the updrift extent of the impoundment fillet). This approach resulted in two estimates of the local longshore transport rate,  $q_l(x)$ , for each offshore location. Error bars presented in the calculated longshore transport values which follow reflect the difference between these two estimates as well as uncertainties in the updrift extent of the impoundment fillet.

### 7.3.4 First Impoundment Interval ("B to C")

The profile changes immediately updrift and downdrift of the groyne during the first impoundment interval (survey loops "B to C") are illustrated in Figure 7-9. The profile of the groyne is also shown. Although profile changes further downdrift of the groyne (5 m away) predominately indicated recession, downdrift profile changes poorly reflected impoundment-related updrift changes.

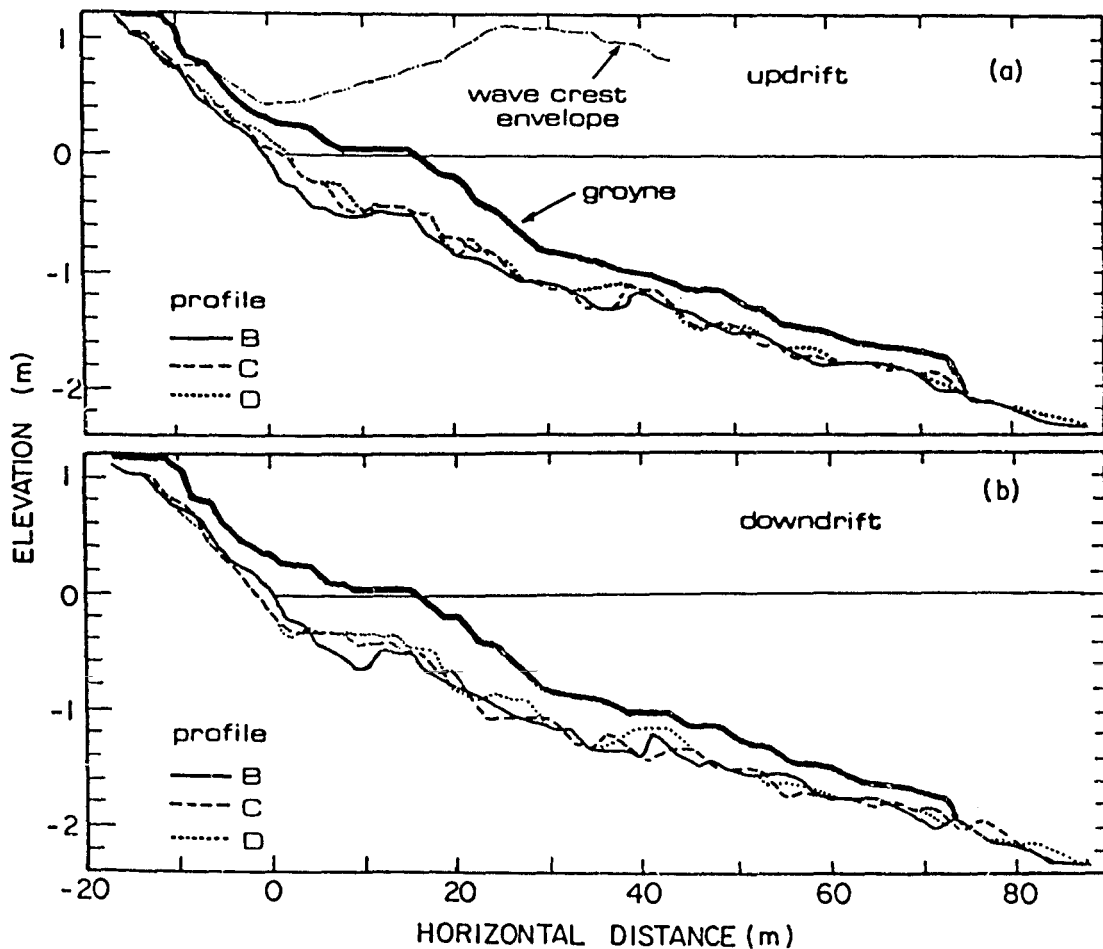


Figure 7-9: Beach profile changes at 5 meters: (a) updrift, (b) downdrift of the groyne for the first impoundment interval ("B to C") and for the second impoundment interval ("C to D"), plunging test series. (Prototype scale).

Figure 7-10 illustrates the local longshore sediment transport rate (per unit distance offshore) as calculated along fixed offshore locations. The wave height and longshore current distributions, and the average beach profile (determined by the average depth along each offshore location of interest) are also shown. A bimodal longshore transport distribution, with peaks about the break point and the

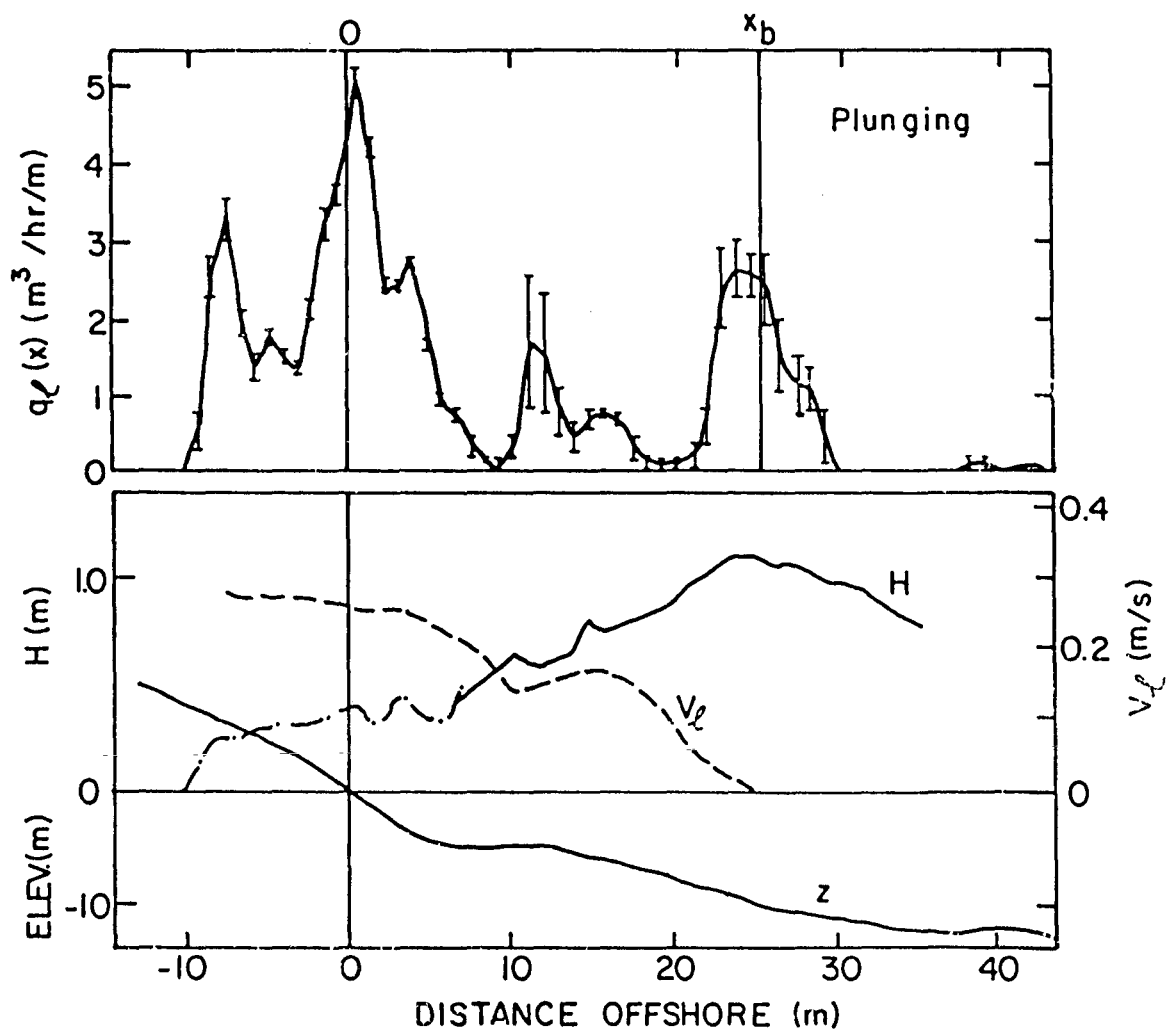


Figure 7-10: The longshore transport distribution, longshore current wave height, and average beach profile across the surf zone for the first impoundment interval of the plunging test series (prototype scale).

shoreline, is once again noted. A third peak is observed in the mid-surf zone and corresponds to the seaward face of a bar (the relief of which is smeared in the average-value beach profile shown in the figure). About 34% of the total transport occurs above the still water shoreline with less than 10% occurring seaward of the break point. The total longshore transport is between 56.3 and 73.5 m<sup>3</sup>/hr. The typical updrift extent of the impoundment fillet was about 23.5 m, or just less than one surf zone width.

#### 7.3.5 Second Impoundment Interval ("C to D") and Smearing

Profile changes immediately updrift and downdrift of the groyne for the second impoundment interval are shown in Figure 7-9. The local longshore transport rate (per unit distance offshore) as calculated along offshore locations for this interval is illustrated in Figure 7-11. The calculated longshore transport distribution for the first interval is shown for comparison. It is seen that the distribution for the second interval is shifted offshore. The total transport, 44.5 to 71.8 m<sup>3</sup>/hr, is approximately the same as for the first interval. As suggested previously, it is thought that the distribution of sediment impounded by the barrier is progressively skewed seaward with time due to smearing by wave action and the rip at the groyne. Specifically, as impoundment proceeds, the profiles nearest the groyne are progressively enriched with an overabundance of sediment relative to the equilibrium beach state for the wave conditions and water level. This sediment accumulation is concentrated about those contours associated with the greatest longshore transport. Therefore, the profiles nearest the groyne exhibit a shape which is dissimilar to the equilibrium profile,

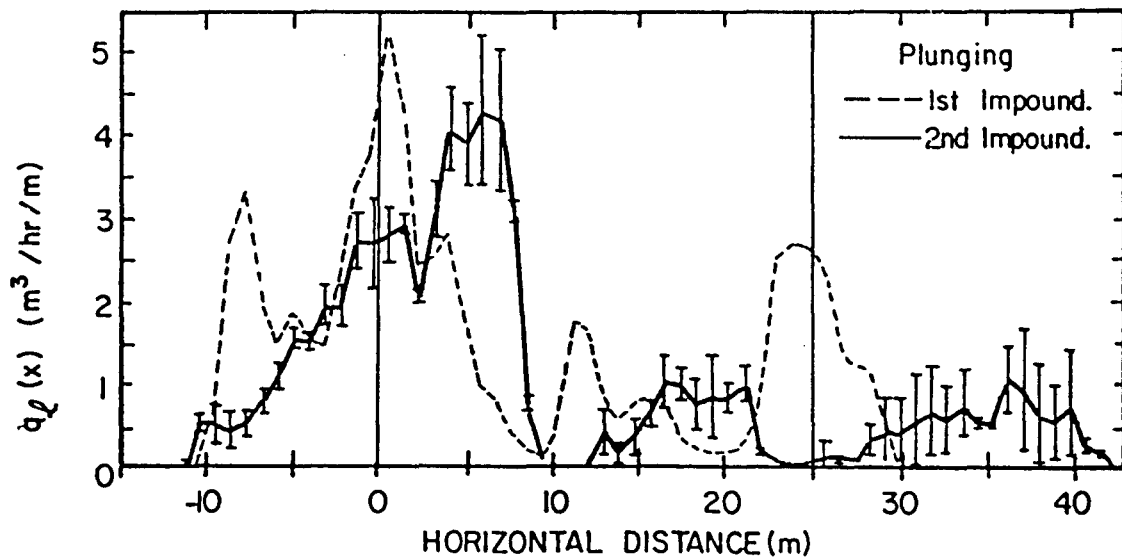


Figure 7-11: Comparison of the longshore transport distribution found from the first and second impoundment intervals of the plunging test series (prototype scale).

and contain a greater total volume of sediment than is associated with equilibrium conditions. The waves then act to rework the "surplus" sediment. One may expect that at least part of the surplus would be pushed onshore; however, this appears to be prevalent mainly for cases of significant foreshore steepening and increased runup just updrift of the groyne (see Section 7.5.2, collapsing test series). Instead, local profile steepening caused by impoundment at contours of large-magnitude longshore transport, along with wave steepening and offshore-directed stress associated with the rip at the groyne, promotes offshore transport which "smears" the impoundment profile towards the seaward direction. Accordingly, it is important that impoundment intervals be of short term if the distribution of longshore transport is to be derived from the sediment impoundment distribution before significant offshore

directed smearing occurs. For this case, offshore smearing of the impoundment fillet was observed in the second impoundment interval; that is, during the 212 waves which followed the first 150 waves.

#### 7.3.6 Bed and Streamer Traps

For the plunging wave series, an alternate longshore transport trapping technique was executed for comparison to the impoundment technique. A series of bedload and suspended load traps was deployed across the re-screeded and wave-equilibrated beach in lieu of a groyne. Waves were then run for 27 minutes and the weight and volume of sediment collected in each of the bed and streamer traps were measured (after squeezing the water out of each sample using nylon hosiery--see Kraus and Nakashima, in review). The bedload traps consisted of open-topped coffee cans or beer cans. The open tops of the coffee cans were bent into 11.4 cm × 6.5 cm rectangular shapes, and the open tops of the beer cans were bent into 5.3 cm × 5.3 cm square shapes (model scale). The streamer traps were made of 30 cm-lengths of nylon hosiery (model scale) closed at one end and held open at the other by a wire loop. The streamer traps were attached to the top downdrift edge of the bed traps using the wire loops. The assembled bed and streamer traps were dug into the beach such that the tops of the bed traps were flush with the bed. The streamer traps extended between half-way and completely through the still water column. The four traps highest on the foreshore were not equipped with streamer traps and had 1-cm high walls above the bed on all sides except the updrift opening side. The spacing between traps was 50 cm nearshore increasing to 3.6 m outside of the surf zone (prototype scale).

The distribution of the local rate of sediment accumulation for the combined bed and streamer traps (per unit offshore distance) is shown in Figure 7-12. The local longshore sediment transport rate derived from the first impoundment interval ("B to C") is shown for comparison. Both are normalized by their respective maxima. The local contribution of the suspended load, expressed as the streamer trap accumulation rate divided by the streamer plus bed trap accumulation rate, is also illustrated. The distributions of the trap accumulation and impoundment-derived longshore transport agree reasonably well. It is noted that the bed traps were not very efficient because they tended to lift up during the test such that their openings were no longer flush with the bed. This was most severe in the mid-surf zone on the seaward

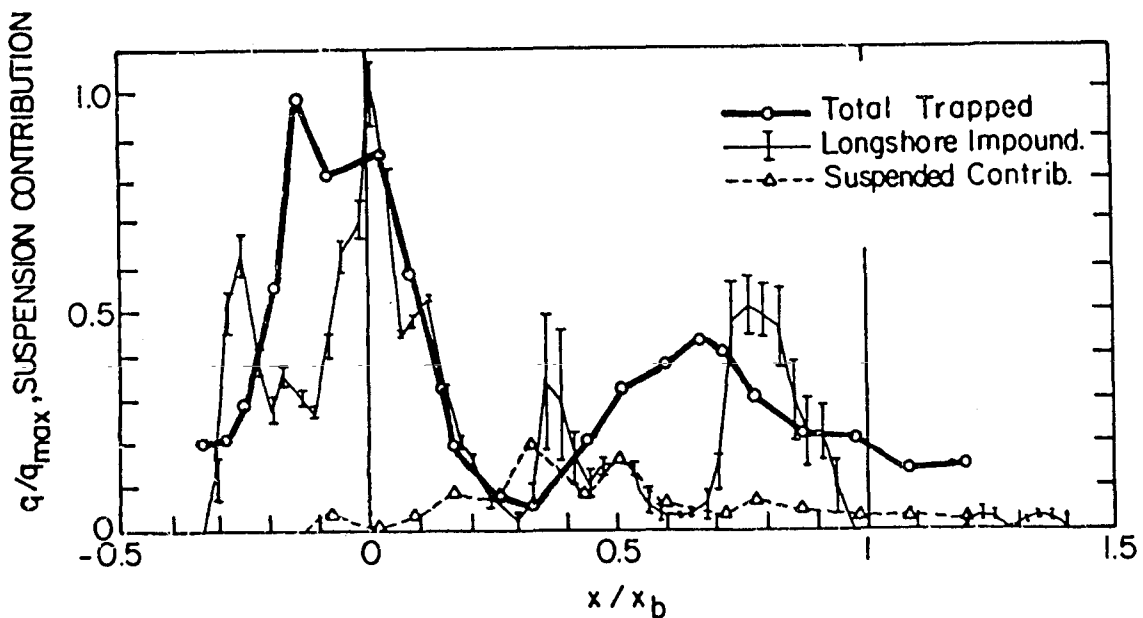


Figure 7-12: Comparison of combined bed and streamer trap sediment accumulation rate, suspended sediment contribution, and longshore sediment transport rate (from impoundment data) across shore. Values normalized by respective maxima. Plunging test series.

face of the bar. The streamer traps were not very efficient because of flow constrictions about the openings. Overall, the total volumetric accumulation rate of the traps,  $37 \text{ m}^3/\text{hr}$ , was 34% to 50% less than the total longshore transport rate determined by the impoundment technique. This is attributable to the inefficient operation of the traps and some unaccounted-for impoundment observed immediately updrift of the traps (presumably associated with the low barrier formed by the elevated bed traps). The relatively small contribution of the suspended load is possibly attributable to the inefficient operation of the streamer traps and inadequate modelling of suspension transport in the laboratory. Finally, it is not known how accurately the trapped sediment reflects solely longshore transport processes.

#### 7.4 Plunging/Collapsing Series and Tests with Simulated Tidal Fluctuations

##### 7.4.1 Description of Experiment

A plunging/collapsing breaking wave condition was established in the basin primarily to investigate the effect of tidal fluctuations and the effectiveness of tidal deconvolution. Additional insight to the distribution of longshore transport and to the potential smearing of the impoundment fillet was also gained.

The wave conditions in the basin were selected so as to create a bar-free beach and a relatively "stable" surf zone (i.e., non-migratory break point for steady water level). The test conditions so selected, are described in Table 7-1 for the tideless beach. Briefly, a plunging/collapsing breaker was developed with 0.8 m height, 9.6 second period, and  $14.5^\circ$  incidence angle. In order to simulate tidal fluctuations when desired, the basin's pumps and weir gates were configured to yield

average rates of water level rise and fall of 2.3 cm/min and 2.9 cm/min, respectively. The "design" tidal range was 0.45 m. The mean water level fluctuations in the basin were monitored inside a stilling well by a capacitance wave gauge connected to a strip chart recorder.

For the tidal simulation test, the beach was screeded and equilibrated to the series' wave conditions in the absence of the groyne during a 4 hour low-high-low tidal fluctuation. After equilibration, a pre-impoundment survey loop ("T-A") was taken and a low-profile groyne was deployed across the beach. Waves were run for 144 minutes during a low-high tidal fluctuation after which an intermediate survey loop ("T-B") was taken. Another 102 minutes of waves were subsequently run during the high-low portion of the simulated tide, and the final survey loop ("T-C") was taken. The time history of the mean water level fluctuation in the basin and the survey sequence is illustrated in Figure 7-13.

For the non-tidal tests, the water level was held constant at the average level of the tidal test. The wavemaker settings were identical for both the tidal and non-tidal tests. In the first non-tidal test, the beach was re-screeded and equilibrated with two hours of waves. The first survey loop ("NT-A") was taken and another 24 minutes of waves were run in the absence of the groyne. A survey loop ("NT-B") was then taken and a low-profile groyne was installed across the beach. For this test, 18 minutes of waves were run in the presence of the groyne after which the last survey loop ("NT-C") was taken. Profile changes between loops "NT-A" and "NT-B", and between "NT-B" and "NT-C", respectively, represent a no-groyne "control" interval and a tideless (short-term) impoundment interval.

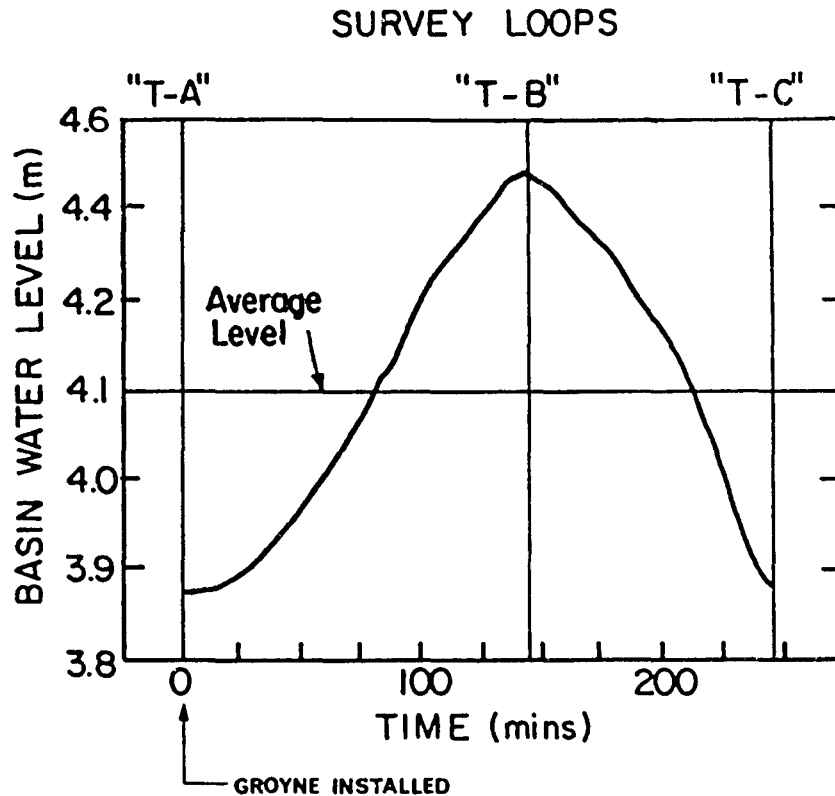


Figure 7-13: Time history of the mean water level fluctuation and survey loops for the laboratory investigation involving simulated tide effects (prototype scale).

In the second non-tidal test, the beach was again re-screeded and equilibrated with two hours of waves. An initial survey loop was taken, a low-profile groyne was installed, 96 minutes of waves were run, and a final post-impoundment survey loop was taken. This test represented a single (longer-term) impoundment interval.

For the tidal and second non-tidal tests, the survey loops included thirteen updrift and three downdrift profile lines. The furthest downdrift profile was 10.8 m from the groyne while the furthest updrift profile was 45 m from the groyne. For the first non-tidal tests, one downdrift and twelve updrift profile lines were included in the survey loops. The furthest updrift line was 32.4 m from the groyne. For all

tests, the updrift profiles were uniformly spaced 1.08 m apart within 5.4 m of the groyne. Profile spacing increased gradually to 8 m far from the groyne.

#### 7.4.2 Tests with Tidal Fluctuation

Beach profiles measured updrift and adjacent to the groyne during the pre-, intermediate, and post-impoundment surveys for the tidal test are illustrated in Figure 7-14a. The groyne profile and region of wave breaking during the tidal test are also shown. Beach profiles measured downdrift and adjacent to the groyne are illustrated in Figure 7-14b. The local downdrift recession demonstrated by the profile changes is a fair, but not reliable, indication of the updrift profile changes.

Data analysis methodology. Profile changes derived from the survey data for each impoundment interval, along with the time-history of the tidal water level fluctuation for each interval, were used to construct the total transport function across each profile using both the "simple" and smoothed (over-constrained) least-squares matrix tidal deconvolution techniques. These functions were then linearly interpolated to form the total transport function for a series of depth contours along the beach. Estimates of the cross-shore component of the transport function were identified and subtracted for each contour through inspection of the far-updrift transport function and/or through consideration of the cumulative transport function along each contour (see Section 7.2.3). The result was integrated from the barrier to the updrift extent of the impoundment fillet in order to form estimates of the local longshore transport rate (per unit depth) for each contour for both the "simple" and least-squares matrix tidal deconvolution techniques. As usual,

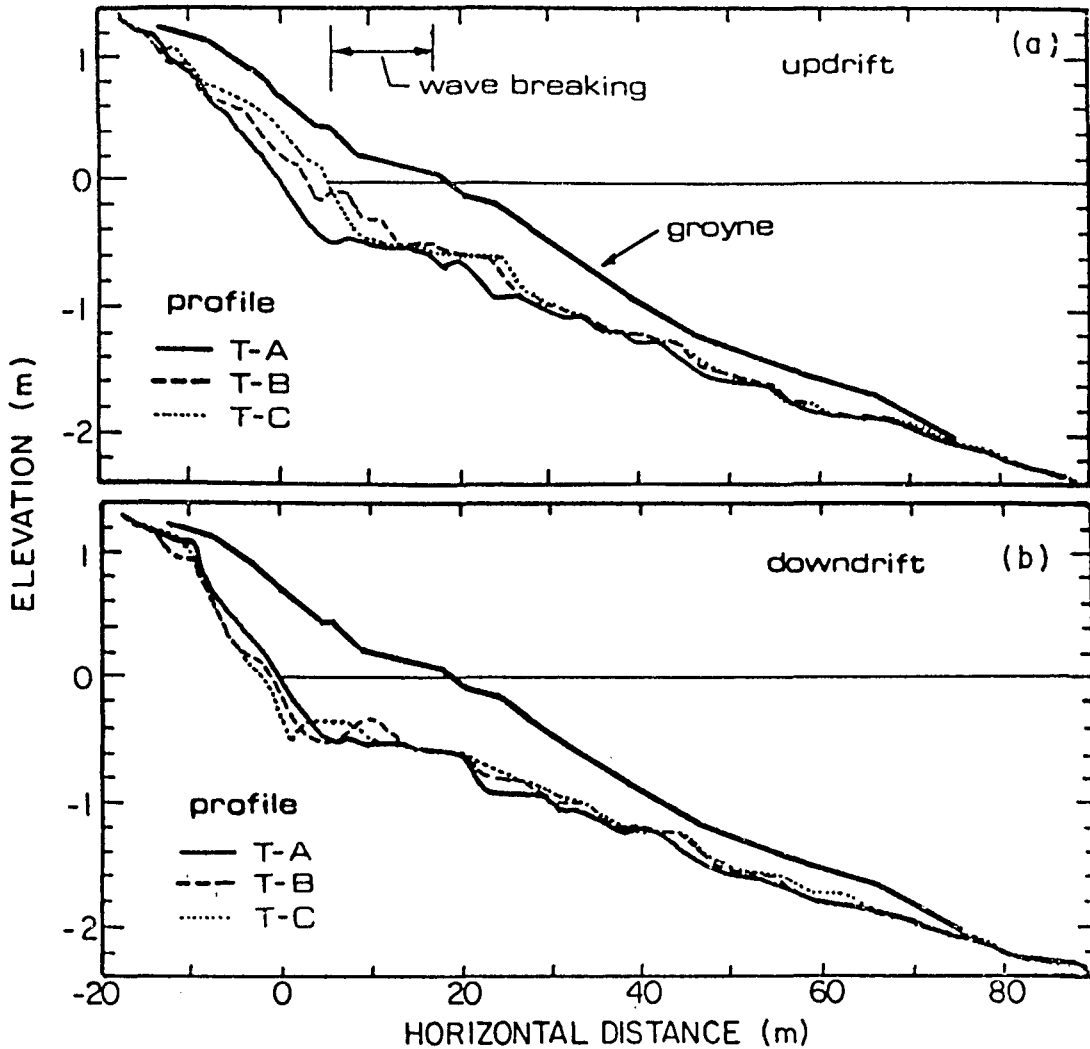


Figure 7-14: Beach profiles measured immediately (a) updrift, and (b) downdrift of the groyne during the pre-, intermediate, and post-impoundment surveys for the laboratory test involving simulated tidal fluctuations (prototype scale).

error bars presented in the longshore transport estimates represent uncertainties in the cross-shore contribution and/or the updrift extent of impoundment for each contour.

Before the tidal deconvolution step was executed, a sensitivity test was undertaken to explore the appropriate degree of over-constraint for the least-squares matrix tidal deconvolution technique. The profile

change data,  $\Delta z/\Delta t$ , was evaluated along 25 depth contours vertically spaced 9 cm apart (1 cm apart, model scale). Therefore, for each tidal impoundment interval, the 45 cm tidal variation (5 cm, model scale), encompassed five depth contours. Using the notation of Chapter 4, this corresponds to  $N=25$ ,  $K_b=5$  and  $\Delta z_o=0.009$  m. A relatively small degree of over-constraint,  $M>23$ , yielded unreasonable and erratic estimates of the transport function--even after smoothing. The over-constraint described by Eq. (4.17),  $M=N-(K_b-1)$ , suggests using  $M=22$ . This value (and to a lesser degree,  $M=23$ ) yielded fairly reasonable estimates of the transport function after smoothing. Greater constraint,  $18<M<21$ , did not significantly improve the stability of the transport function solution. Extreme constraint,  $M<18$ , resulted in coarse estimates of the transport function which poorly reproduced the measured profile changes when coupled with the tidal fluctuations. Accordingly, the constraint recommended by Eq. (4.17),  $M=22$ , was used in the data analysis.

Rising tide interval. The updrift profile changes measured between survey loops "T-A" and "T-B", which correspond to the rising tide impoundment interval, were analyzed as described above. The local longshore transport rate per unit depth, as determined by the "simple" and the smoothed least-squares matrix tidal deconvolution techniques, are shown in Figure 7-15a. The results of the two techniques are somewhat similar in trend although the least-squares matrix result exhibits more exaggerated variation. This is not unexpected since the "simple" technique is an averaging algorithm and inherently smooths across depth contours, whereas the matrix technique is more prone to oscillatory instability. Transport estimates for the upper swash, as developed by the simple technique, are exceptionally large because they

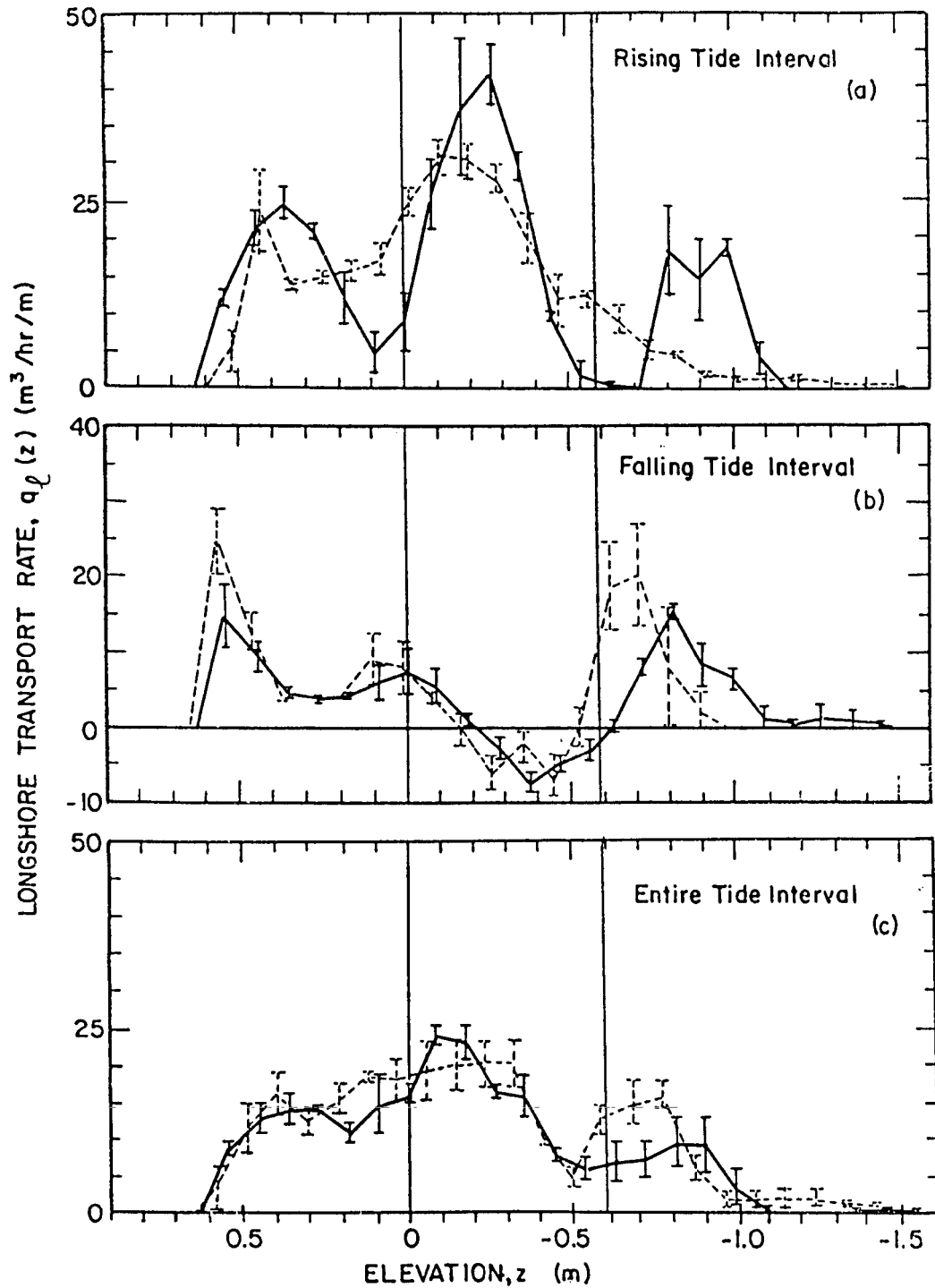


Figure 7-15: Distribution of longshore transport rate for still water depth contours derived from the (a) rising tide, (b) falling tide, and (c) entire tide impoundment intervals. Results of both simple (dashed line) and least-squares matrix (bold line) tidal deconvolution techniques are shown. (Prototype scale).

were developed from profile change data at beach elevations which were wetted for only short periods of time. The total longshore transport estimates for this interval agree fairly well between techniques: 20.9 to 26.9 m<sup>3</sup>/hr for the "simple" technique, and 22.9 to 32.4 m<sup>3</sup>/hr for the least-squares matrix technique. The estimates differ by about 15%. This is attributable to differences in the interpretation of the total transport function generated by each of the two techniques.

Falling tide interval. The updrift profile changes measured between survey loops "T-B" and "T-C," which correspond to the falling tide impoundment interval, were analyzed in the same manner as above for each of the two tidal deconvolution techniques. The estimates of the local longshore transport rate per unit depth for both the "simple" and least-squares matrix techniques are shown in Figure 7-15b. The results of each technique are similar. This is not surprising since the water level fluctuation for this interval was fairly linear over time. The short time for which the upper-most beach elevations were wetted is responsible for the large-valued transport estimates for the upper swash zone contours. Both techniques exhibit negative values across the outer surf zone. (It is recalled that the transport function analysis methodology does not constrain the longshore transport estimates to be positive-valued.) The negative-valued estimates are due to local recession of the impoundment fillet. The total longshore transport estimated by the "simple" and least-squares matrix techniques, 4.0 to 10.5 m<sup>3</sup>/hr and 4.9 to 9.4 m<sup>3</sup>/hr, respectively, are in good agreement but are about 30% to 40% smaller than the total transport estimates for the rising-tide impoundment interval. This is probably attributable to decreased longshore transport associated with a decrease in angle between the

incident waves and the rotating beach contours, where the latter is associated with increasing impoundment of sand against the barrier as the test progressed. Specifically, the mean shoreline contour had rotated  $3^\circ$  towards the incident wave field after the rising tide interval, and rotated another  $3.3^\circ$  after the falling tide interval. For the original breaking wave angle of  $14.5^\circ$ , this potentially represents a 19.4% decrease in longshore transport by the end of the rising tide interval, and another 27.6% decrease in transport by the end of the falling tide interval (assuming that the total longshore transport is proportional to the sine of twice the incident breaking wave angle).

Considerable dissimilarity of the transport distributions found for the rising and falling tide intervals is immediately apparent from Figure 7-15. Specifically, contours characterized by significant local longshore transport for the first portion of the tidal test (rising tide) are characterized by low- or negative-valued transport for the second portion of the test (falling tide). Conversely, contours of local low-valued longshore transport for the first portion of the test are associated with higher-valued estimates of transport for the second portion. Since the overall longshore transport capacity was diminished during the second portion of the test, it appears that the impoundment (survey) data for the second portion was dominated by local near-groyne cross-shore transport signals. That is, the large local "surplus" volumes of sand, centered near the groyne about those contours associated with strong longshore transport, were modified towards equilibrium and/or profile smoothing by local cross-shore processes. In the near-groyne survey data, these processes appear as local recession and accretion at contours initially associated with significant and low

valued impoundment signals, respectively. Seaward groyne by-passing and berm accretion (due to the local excess of sand across the profile immediately updrift of the groyne) are also expected; though only the latter is apparent in the data. Such local near-groyne cross-shore processes are difficult to address in the data analysis since the removal of cross-shore signals from the data, as described in this paper, typically relies upon the assumption that cross-shore transport is uniform along the beach at any given depth contour. Accordingly, it is thought that the impoundment data of the falling tide portion of the tidal test reflects considerable smoothing which can not be easily removed.

Entire tide interval. The updrift profile changes from survey loops "T-A" and "T-C," which include the entire tidal cycle, were analyzed as described above to yield the local longshore transport rate per unit depth for both the "simple" and least-squares matrix tidal deconvolution techniques (Fig. 7-15c). The longshore transport distribution and the total transport agree with the combined time-weighted results derived from the separate analyses of the rising and falling tide data sets within about 20% rms error and 10% error, respectively. This indicates that the data analysis and interpretation was fairly consistent between data sets.

#### 7.4.3 Non-Tidal Tests

No-groyne "control" interval. Profile changes measured over the no-groyne "control" interval of the first non-tidal test (survey loops "NT-A" to "NT-B") were used to indicate the degree to which the beach was equilibrated with the wave conditions before the first non-tidal

impoundment interval began. These profile changes were also used as one estimate of the cross-shore transport which would be removed from the survey data of the impoundment intervals. As seen from Figure 7-16a, only small and localized net beach profile changes occurred during the no-groyne "control" interval. This indicated that the beach was fairly well equilibrated with the wave conditions before the impoundment test was begun and that cross-shore transport "noise" in the impoundment survey data should be relatively small. The beach profiles shown in Figure 7-16a were measured 0.5 m updrift of the intended site of the groyne and were typical of the entire model beach survey area for this interval.

Impoundment interval--first test. The updrift beach profile changes measured over the (short-term) first non-tidal test impoundment interval (survey loops "NT-B" to "NT-C") were analyzed along depth contours. Estimates of the local longshore transport rate per unit depth were made after removal of cross-shore signals in a similar manner as described for the plunging wave test series. The estimates of the local longshore transport rates per unit depth,  $q_l(z)$ , were then transformed to estimates per unit offshore width,  $q_l(x)$ . Beach profile changes over the impoundment interval (0.5 m updrift of the groyne) are illustrated in Figure 7-16b. The groyne profile is also shown. Like the tidal tests, local downdrift profile changes (not shown) were only fair indicators of local updrift profile changes. The longshore transport distribution across the surf zone is illustrated in Figure 7-17, along with the average beach profile and the measured wave height and longshore current distributions.

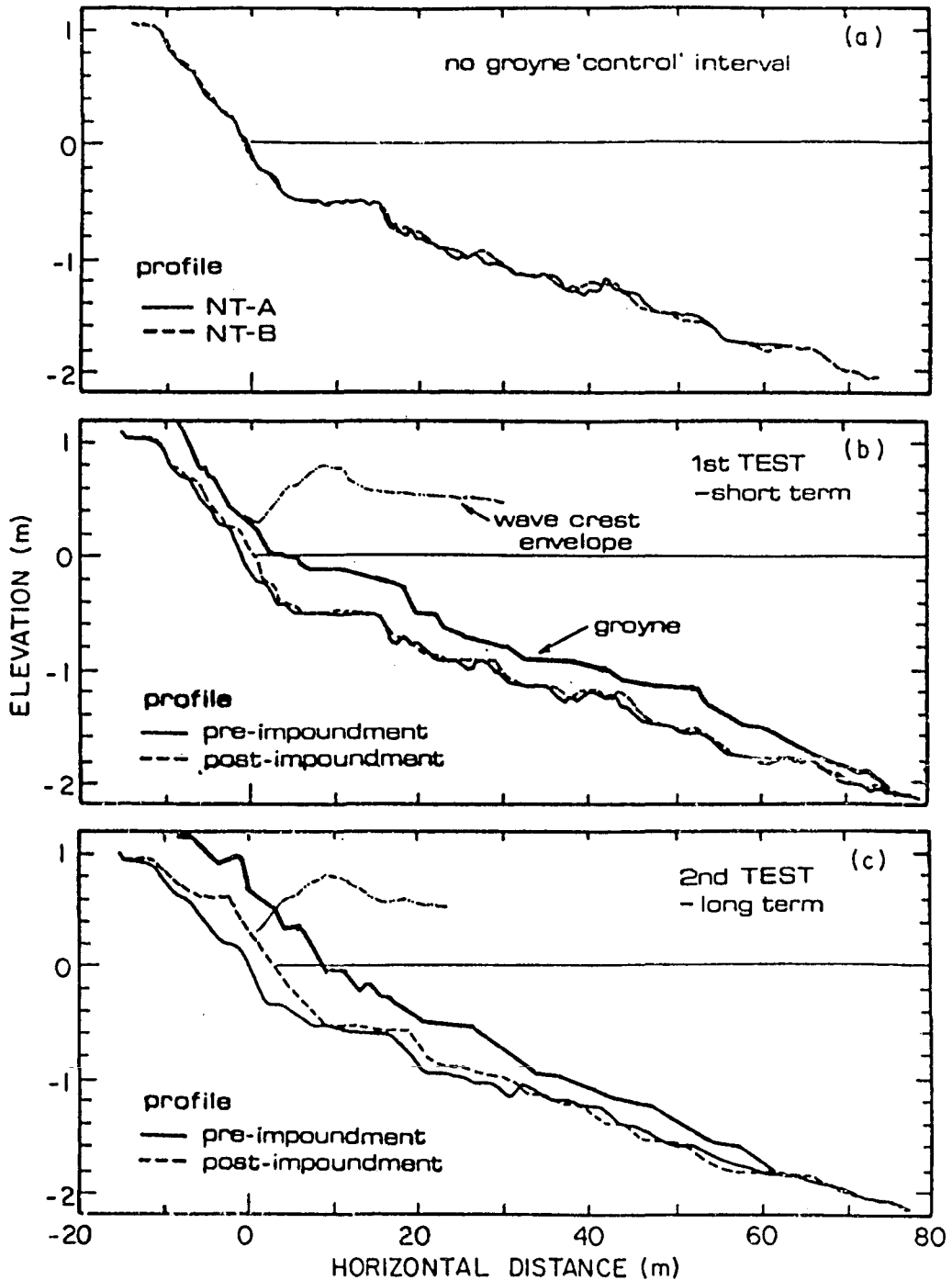


Figure 7-16: Beach profiles measured immediately updrift of the groyne site for the non-tidal plunging/collapsing test series: (a) prior to groyne deployment, (b) before and after the short-term, first impoundment interval, and (c) before and after the longer-term, second impoundment interval. (Prototype scale).

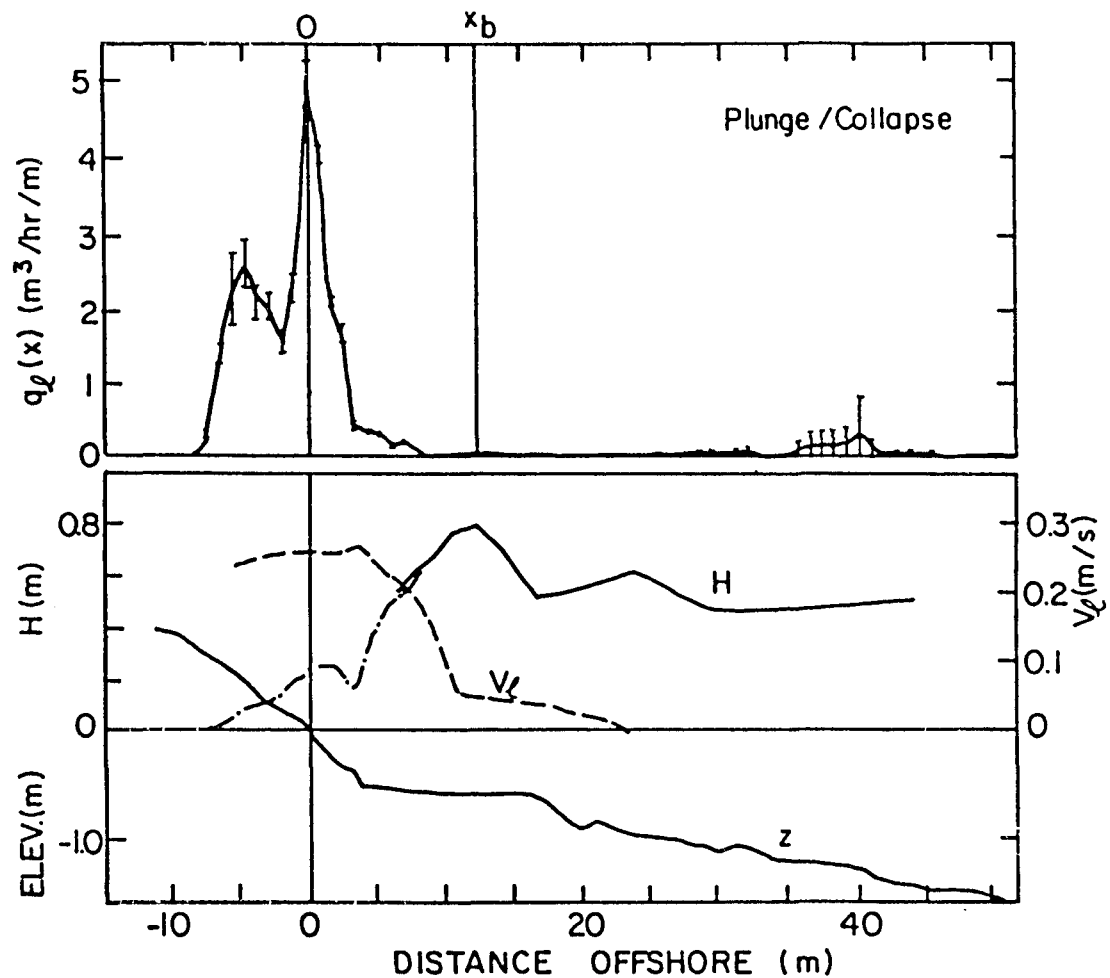


Figure 7-17: The longshore transport distribution, longshore current, wave height, and average beach profile across the surf zone for the short-term, first impoundment interval of the plunging/collapsing (non-tidal) test series. (Prototype scale).

Impoundment interval--second test. Figure 7-16c illustrates the beach profile changes measured 0.5 m updrift of the groyne over the impoundment interval of the (longer-term) second non-tidal test. The groyne profile for this test is also shown. Updrift profile changes were analyzed as described above to yield estimates of the local longshore transport rate per unit depth for this interval. These estimates were subsequently transformed to estimates per unit offshore width in

order to develop the longshore transport distribution across the surf zone, as shown in Figure 7-18a. The longshore transport distribution determined from the first non-tidal test is also shown in the figure for comparison.

The results of the (short-term) first impoundment test suggest a strong transport maxima at the shoreline and sharply decreasing transport toward the breakpoint. The longshore transport distribution found for the (longer-term) second impoundment test is generally similar to that of the (short-term) first test but is somewhat subdued about the shoreline and smeared offshore. The total longshore transport estimated for the first test, 24.5 to 32.0 m<sup>3</sup>/hr, is approximately equal to or slightly higher than that for the second test, 25.0 to 27.4 m<sup>3</sup>/hr. Two adverse effects of longer-term impoundment intervals were evident from the non-tidal tests. For the second, longer-term, test, the angle between the incident waves and the beach contours decreased with time as the contours rotated with the impoundment fillet in response to the oblique wave attack--thereby decreasing the longshore transport with time, as described previously for the falling tide test. Also, increasing impoundment with time created a large mound of sand against the groyne and about the foreshore and shoreline area which led to a "downhill" bed slope along the beach directed away from the groyne. Wave runup was increased over this steep mound and the subsequent backwash flowed downslope along the beach--forming a run-out at the shoreline amidst the impoundment fillet. This runout carried impoundment material offshore and deposited it in the mid-surf zone thereby smearing the impoundment distribution profile ever further.

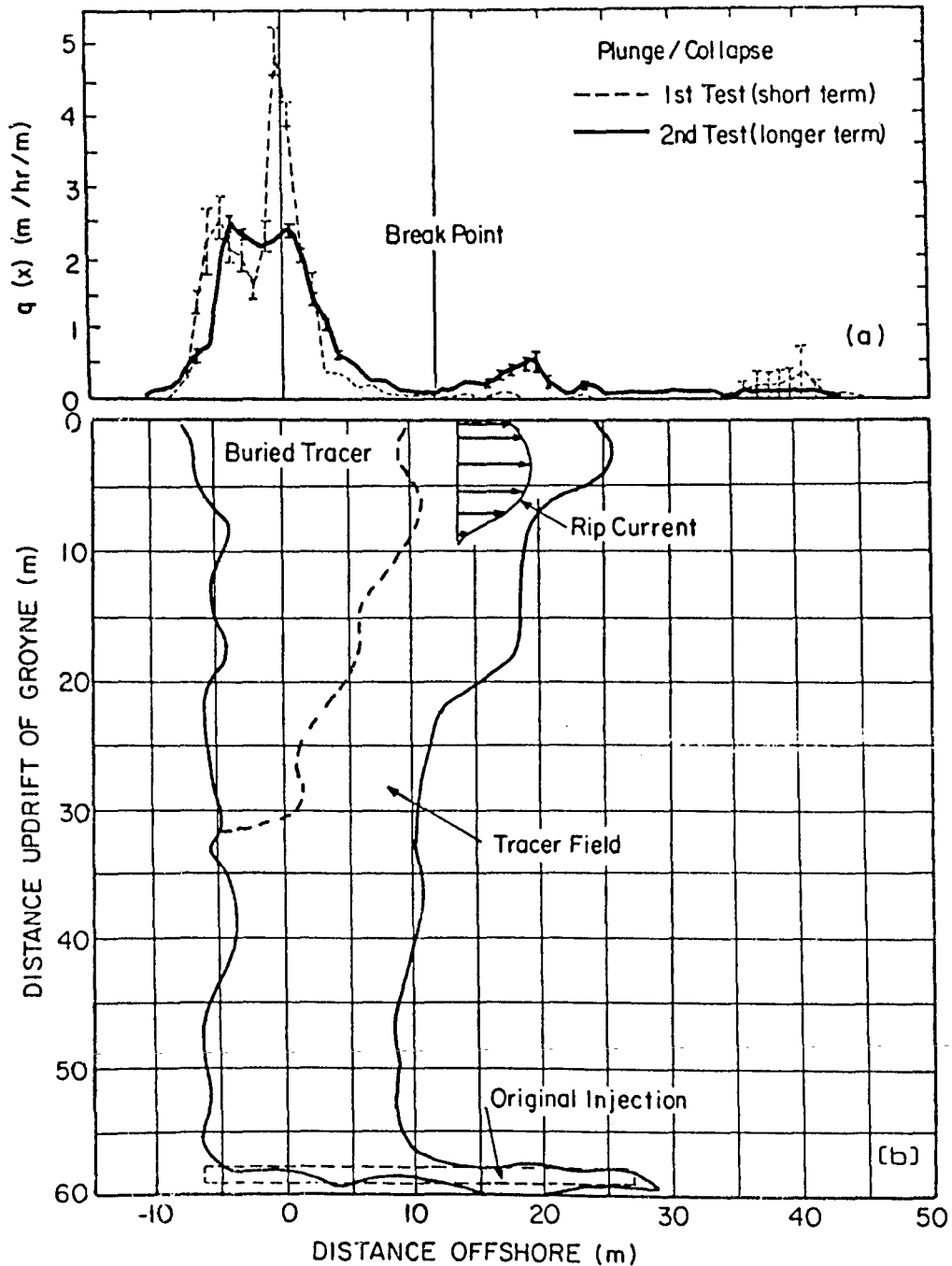


Figure 7-18: (a) Comparison of the longshore transport distribution across the surf zone for the short-term, first impoundment interval and the longer-term, second impoundment interval; (b) fluorescent tracer field after 18 minutes of wave action during the second impoundment interval. Plunging/collapsing (non-tidal) test series. (Prototype scale).

The smearing of the second test's longer-term impoundment is consistent with that observed for the previously described test series. Fluorescent tracer, injected as a uniform cross-shore strip 60 m updrift from the groyne during the second test, demonstrated the offshore-directed shift of the longshore sediment transport in the vicinity of the groyne. Figure 7-18b illustrates the major field of tracer visually discerned under black flood lights after 18 minutes of wave action. The tracer injection was made 18 minutes prior to the end of the second non-tidal impoundment test. The distribution of longshore transport across shore (estimated from the impoundment data of the non-tidal tests and transformed from  $q_L(z)$  to  $q_L(x)$ ) are shown in Figure 7-20a for comparison. Far updrift of the groyne (near the injection), the offshore limit of longshore transport is readily seen. Closer to the groyne, an offshore movement of the tracer is noted. Photographs of dye movements over the same area occupied by the tracer field indicated that a rip current was concentrated within 9 m updrift of the groyne. The maximum estimated current was 0.16 m/s (5.2 cm/s, model scale). The approximate scalar velocity distribution of the rip, as determined by the photographs of the dye movement, is shown in Figure 7-18b. Adjacent to the groyne, the magnitude of the rip current decreases seaward as the water depth increases and the relief of the groyne decreases (because for groyne elevations well below the still water level, the rip is no longer constrained to flow along the groyne nor are the surface longshore currents impeded by the barrier). From inspection of the rip and tracer fields, it appears that the rip greatly enhances the near-groyne seaward transport of the impounded sediment.

The longshore transport distribution determined from the second non-tidal impoundment test reflects offshore smearing (as observed through tracer visualization) more than the distribution determined from the first, short-term, test. Accordingly, the results of the first test are considered most representative of the actual longshore sediment transport distribution for the non-tidal plunging/collapsing case investigated here.

As indicated in Figure 7-18b, the nearshore tracer was buried under a thin lamina of non-fluorescent sand updrift to a distance of about 30 m from the groyne. The updrift extent of the impoundment fillet was about 18 to 25 m updrift of the groyne (i.e., about 1.5 to 2 surf zone widths). For the first, short-term, non-tidal impoundment test, the updrift extent of the fillet was about 14 m (i.e., roughly equal to the surf zone width).

#### 7.4.4 Effectiveness of the Tidal Deconvolution

In Figure 7-19, the longshore transport distributions developed from the tidally-deconvolved data of the rising tide impoundment intervals are compared to the distributions developed from the data of the first and/or second non-tidal impoundment intervals. For clarity, the average-values of the local transport are shown for each distribution (i.e., the error bars have been omitted).

Since the rising-tide interval of the tidal test was longer in duration than the second non-tidal test (which exhibited impoundment smearing), it may be expected that the rising-tide test should also exhibit considerable smearing. However, as seen in Figure 7-19, the longshore transport distributions determined for the rising-tide test

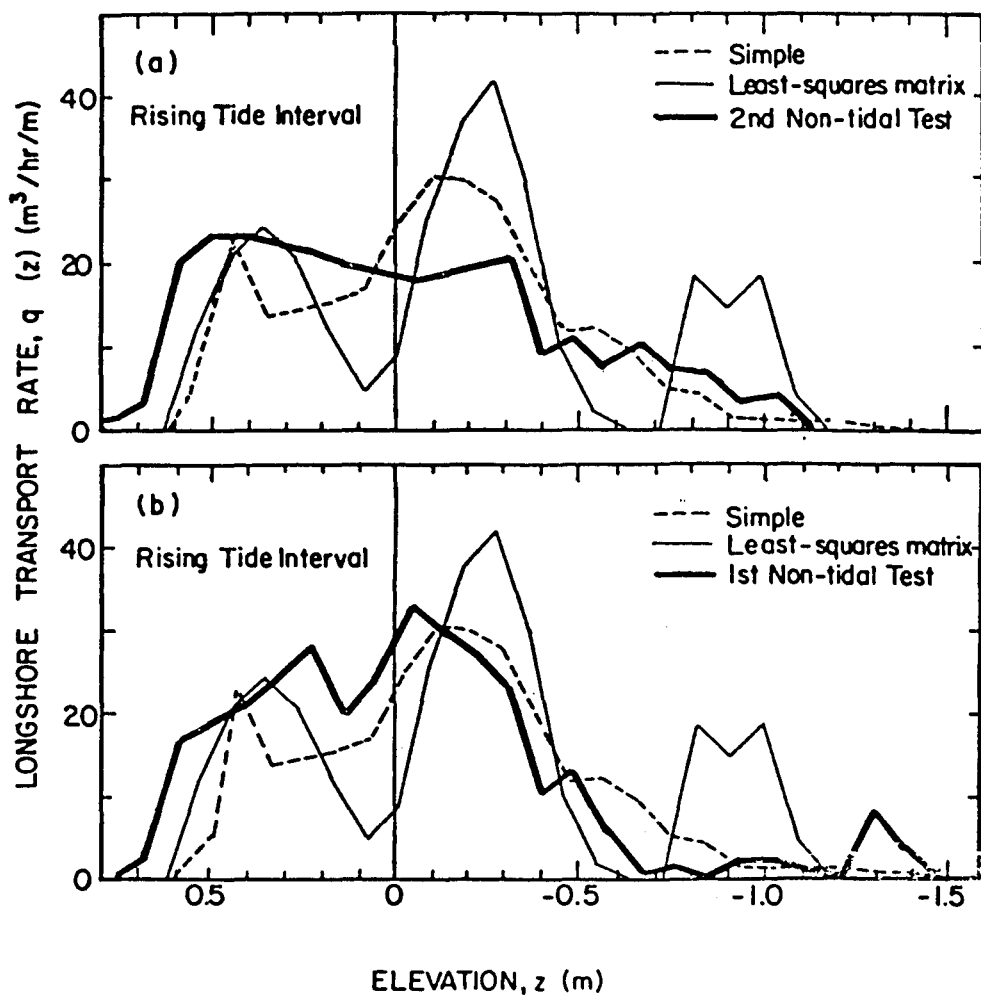


Figure 7-19: Comparison of the longshore transport distributions across shore developed using tidal deconvolution for (a) rising tide and longer-term, second non-tidal impoundment intervals, and (b) rising tide and short-term, first non-tidal impoundment intervals. Plunging/collapsing test series. (Prototype scale).

match the first non-tidal test (which was short-term and presumably not badly smeared) more closely than they match the second non-tidal test. This suggests the possibility that impoundment tests with tidal fluctuations are somewhat more resistant to impoundment smearing than non-tidal tests (at least to a point, viz., the smearing observed over the later falling-tide interval). Physically, this may be because the

impoundment is distributed more evenly across the beach profile as the fluctuating tide moves the longshore transport distribution across the beach (assuming that the transport distribution is depth dependent). An additional factor, for the case of rising tide, is that the active transport shifts to previously unaffected contours and materials. In the simplest sense, impoundment is smeared by water level fluctuations for tidal cases and smeared by near-groyne cross-shore wave and current processes for non-tidal cases. Theoretically, the smearing due to tidal fluctuations may be removed through tidal deconvolution, while smearing by localized wave and current processes is much more difficult to remove. For longer-term tidal impoundment tests, both types of smearing are likely and so the effects of smearing are difficult to address.

Both tidal deconvolution techniques discussed herein develop longshore transport distribution profiles which are fairly similar to that developed for the non-tidal tests. For the relatively simple tidal fluctuation tested and the abundant profile data available in the laboratory, the "simple" technique yielded results which are at least as good as the least-squares matrix technique. However, it is recalled that for the depth-limited profile data of the field studies, the "simple" technique developed transport values over shallower depth contours than the matrix technique and therefore represented a less "powerful" deconvolution technique.

The matrix tidal deconvolution techniques were developed on the assumption that the total transport function (i.e., the local rate of profile change) is strictly depth dependent for a given surf condition. If the transport is also dependent upon the local bed slope, then application of the matrix techniques is valid for planar beaches but not

for non-planar beaches. The impoundment survey data tidally-deconvolved for the field experiments were collected over a portion of the prototype beach which was relatively planar compared to that portion of the model beach over which the laboratory survey data were collected (see Figure 7-20). Consideration of all the laboratory test results (discussed later) suggests that the longshore transport distribution is dependent upon both local water depth and bed slope. Accordingly, the results of the matrix tidal deconvolution are probably more valid for the field data sets than for the laboratory (tidal) data sets.

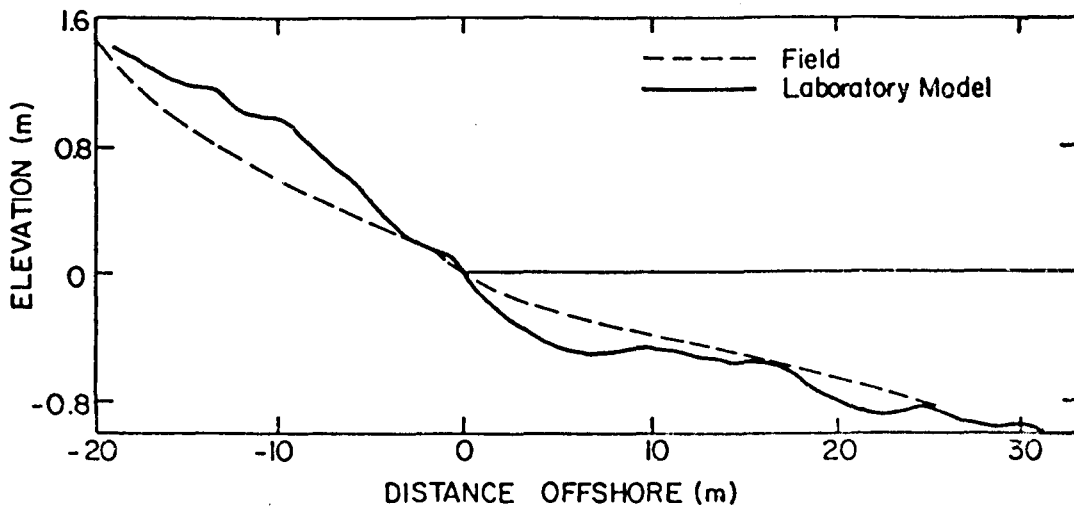


Figure 7-20: Comparison of typical beach profiles updrift of the groyne for the field studies (9 m updrift of Groyne #4, survey loop 4) and the laboratory studies (10.8 m updrift of the groyne, prototype scale, pre-impoundment, plunging/collapsing test series with tide).

## 7.5 Collapsing Series

### 7.5.1 Description of Experiment

A collapsing wave condition was established in the basin with a breaking wave height of 0.53 m, 10.8 seconds period, and 14.2° angle to

the shoreline. The complete test conditions are listed in Table 7-1. The model beach was screeded and equilibrated to the series' wave conditions for two hours in the absence of the groyne. A pre-impoundment survey loop was taken, a low-profile groyne was installed across the beach, waves were run for 90 minutes, and the post-impoundment survey loop was taken. The survey loops included 3 profile lines downdrift of the groyne, and 11 lines updrift of the groyne. Spacing between the updrift lines increased from 1.08 m near the groyne to about 10 m far updrift (45 m total).

#### 7.5.2 Impoundment Results

The beach profiles at the groyne site before impoundment, and 0.5 m up- and downdrift of the groyne before and after the impoundment interval are illustrated in Figure 7-21. The profile of the groyne is also

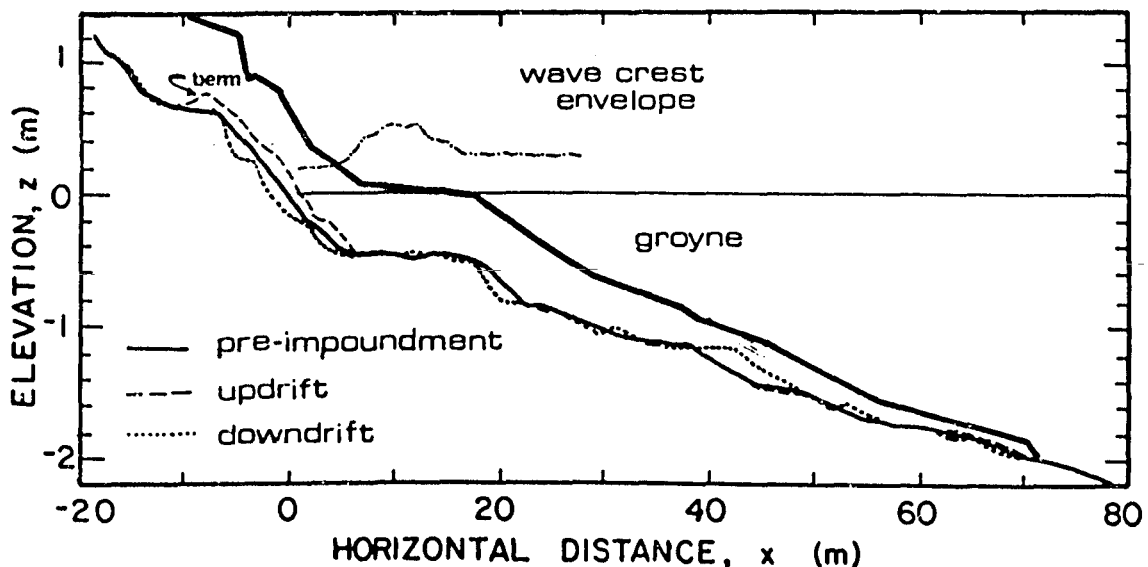


Figure 7-21: Beach profiles at the groyne deployment site before impoundment, and immediately updrift and downdrift of the groyne after the impoundment interval for the collapsing test series. (Prototype scale.)

shown. Updrift beach profile changes were utilized to develop the total transport function along a series of depth contours, from which were removed possible cross-shore transport contributions as determined from profile changes far updrift of the groyne. (As was usual for the laboratory results, these contributions typically represented less than 10% of the total transport function values in the impoundment area.) The longshore transport rate for each depth contour was then determined as usual by integrating the longshore component of the total transport function along each depth contour up to the apparent limit of the impoundment fillet. Beach profile changes in the vicinity of a localized runout, 8.1 m updrift of the groyne, were excluded from the data analysis. This runout was caused by the swash backrush over a large, steep impoundment feature which formed immediately updrift of the groyne (similar to that described for the second non-tidal impoundment interval in the plunging/collapsing series). This steep impoundment feature, or mound, increased wave runup immediately updrift of the groyne and led to the formation of a significant localized berm-like feature (see Figure 7-21). Impoundment material was progressively deposited on the landward side of this "berm" in a narrow ponding area. Accretion in this area cannot be considered as a local longshore transport because this area was landward of or higher than the maximum runup for the undistributed portion of the beach. Instead, this accretion must be viewed as an onshore smearing of longshore-impounded sediment caused by enhanced wave runup near the groyne.

The estimate of the distributed longshore sediment transport across the surf zone for this test series is illustrated in Figure 7-22. The beach profile, wave heights, and longshore current across the surf zone

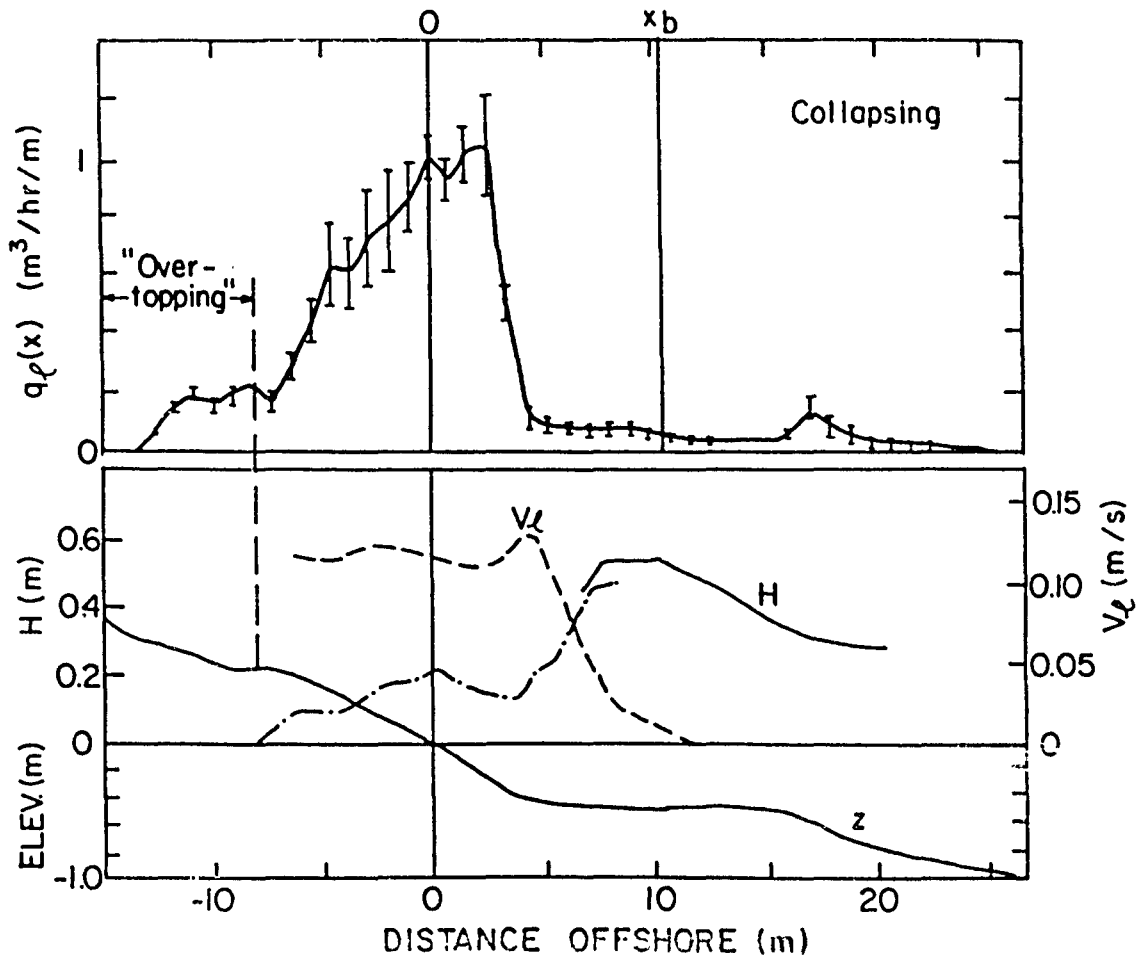


Figure 7-22: The longshore transport distribution, longshore current, wave height, and average beach profile across the surf zone for the collapsing test series. (Prototype scale).

are also shown. The total longshore transport was between 8.1 and 11.3  $\text{m}^3/\text{hr}$ . The impoundment fillet extended between about 14 and 25 m updrift of the groyne for the mid-foreshore and breaking contours, and the shoreline and inner surf zone contours, respectively. These lengths approximately represent one to two surf zone widths. The width of the surf zone plus the swash zone was about 18 m.

As expected for a collapsing wave case, practically all of the transport is observed near the shoreline. Almost 65% of the total transport is observed above the still water shoreline. The small peak well seaward of the break point is likely associated with smearing where sediment from the impoundment area was carried offshore and deposited at an antinode of a long wave in the basin. The presence of an antinode at this point was substantiated by a local apparent node of the measured wave height envelope (not shown). Of course, it is also possible that the velocity and/or pressure field associated with a long wave antinode mobilizes sediment for downdrift advection by small longshore currents, or possibly transports sediment downdrift by the longshore component of the long wave velocity field. However, the effect of long waves on the longshore sediment transport was not specifically investigated in this study.

## 7.6 Spilling Series

### 7.6.1 Description of Experiment

Considerable difficulty was encountered in creating a spilling surf zone in the basin which was suitable for impoundment studies. Severe rips were usually observed as soon as the breaking waves were changed from spilling/plunging to pure spilling conditions (by re-configuration of the wavemaker). Visual observation suggested that the rips were caused by the high phase difference of the swash; that is, the uprush time was greater than about 0.7 of the wave period and so the swash was not completed before the next shore break occurred. This rapidly led to over-saturation of the foreshore. The excess volume of water from the uprush flowed along the beach (and eventually back into the surf zone)

via any available alongshore gradient. This created fairly stable runouts, and eventually rips, irregularly spaced along the shoreline. Runouts and rips interrupt the longshore transport and/or smear the impoundment fillet offshore if they are located updrift of a groyne. It was sometimes possible to create a spilling wave condition in the basin which was less prone to form rips; however, the introduction of a groyne usually perturbed the surf zone sufficiently such that an irregularly spaced rip field eventually appeared.

After several trials, a spilling wave condition was established which did not exhibit visually discernable runouts or rips within about one and a half surf zone widths along the beach. Breaking wave height was just under 1 m with a period of 5.1 seconds and shoreline angle of  $10.8^\circ$ . The complete surf conditions are listed in Table 7-1. The beach was screeded and equilibrated with three hours of the above-described wave conditions, the pre-impoundment survey loop was executed, a low-profile groyne was installed near the downdrift end of the rip-free section of beach, 186 minutes of waves were run, and the post-impoundment survey loop was taken. A cross-shore strip of fluorescent tracer sand was injected about 40 m updrift of the groyne 36 minutes before the end of the test. A small rip intermittently appeared 18 m updrift of the groyne throughout the test. The survey loops included one profile line immediately downdrift of the groyne, and nine lines extending up to 52.2 m updrift of the groyne. Profile spacing was 2.7 m near the groyne increasing to 10.8 m far updrift.

### 7.6.2 Impoundment Results

Profile changes 0.9 m, 3.6 m, and 7.2 m updrift of the groyne over the impoundment interval are illustrated in Figure 7-23. A pronounced bar was formed near the groyne presumably from local impoundment of longshore transport as well as from erosion of the toe of the terrace. This terrace erosion was observed only within about 4 m of the groyne, (elsewhere the terrace accreted) and is attributed to (i) offshore transport caused by the near-groyne rip and related wave steepening, and (ii) wave breaking over the emergent bar. It is not clear whether the accretion seaward of the bar, observed only along the profiles closest to the groyne, is due primarily to local longshore transport impoundment or to offshore smearing. The bar was also observed downdrift of the groyne site before the groyne was installed. Its pronounced appearance was somewhat unexpected for the spilling wave conditions established in the basin and suggested that the bar was enhanced or "fed" by rip currents along the beach.

The updrift profile changes were analyzed along fixed locations offshore because of the presence of the bar. Cross-shore contributions along each location were estimated and removed as described for the plunging series (except that estimates from a no-groyne "control" interval were not available). The longshore transport was estimated as usual by the **alongshore** integration of the longshore component of the total transport function. The resulting estimate of the longshore transport distribution across the surf zone is illustrated in Figure 7-24, along with the average beach profile and the wave height and longshore current distributions.

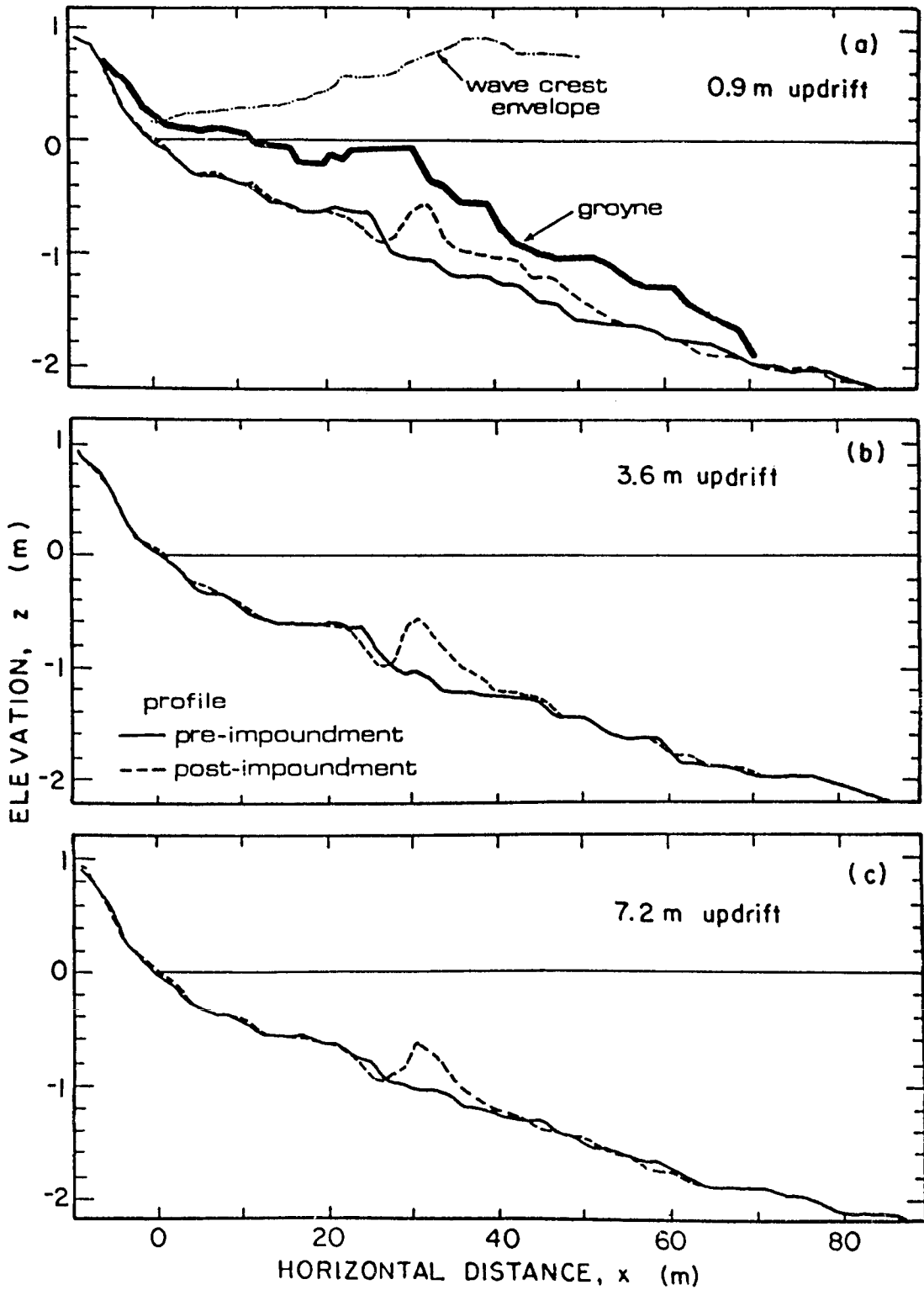


Figure 7-23: Beach profiles measured before and after impoundment for the spilling wave test series: (a) 0.9 m, (b) 3.6 m, and (c) 7.2 m updrift of the groyne (prototype scale).

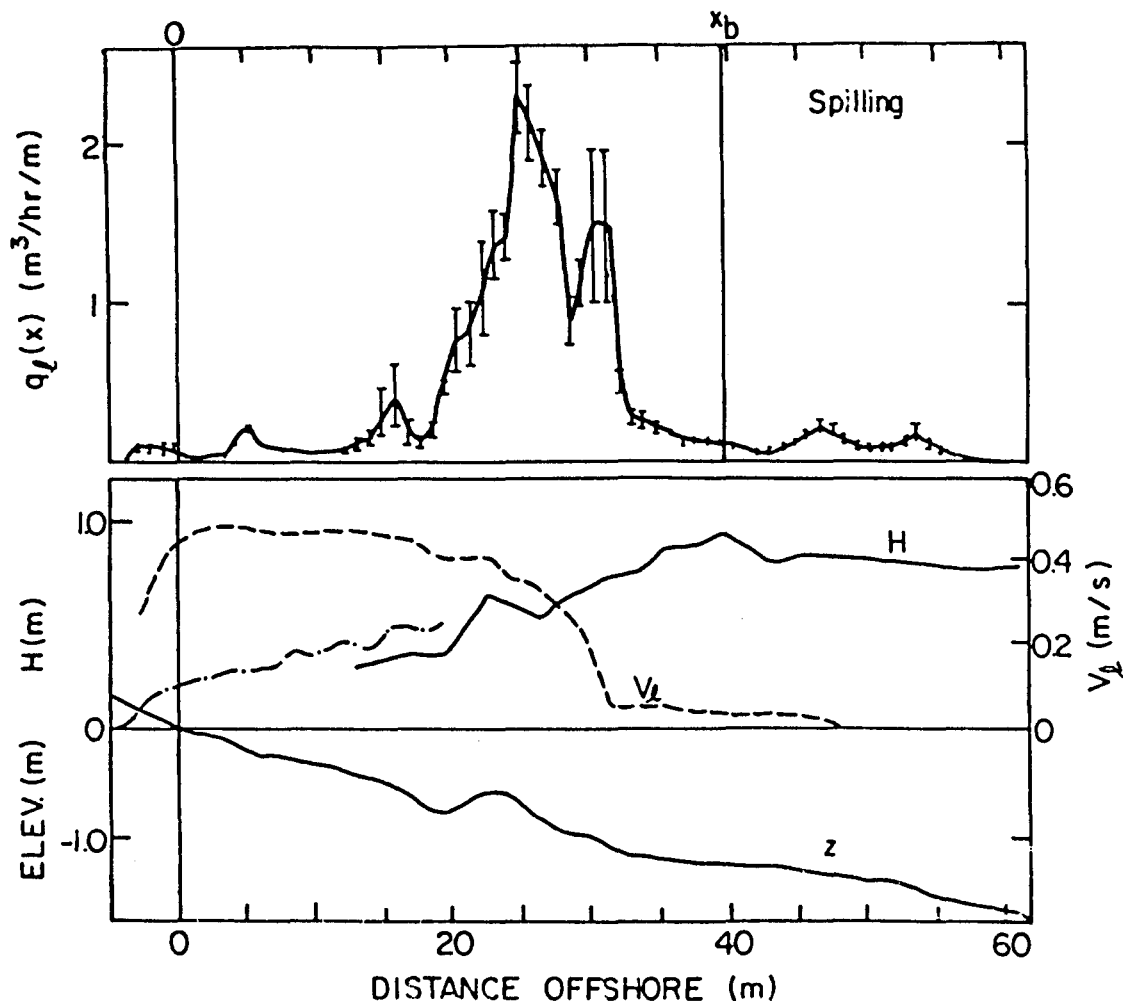


Figure 7-24: The longshore transport distribution, longshore current, wave height, and average beach profile across the surf zone for the spilling test series. (Prototype scale).

The estimated distribution indicates that virtually all of the longshore transport occurred between half-way and three-quarters of the way across the surf zone. However, it is thought that the distribution as derived from the impoundment data is biased seaward. Specifically, it is likely that intermittent and/or visually indiscernable rips carried sediment offshore that was being transported along the beach face. These rips then deposited the sediment in the mid-surf zone.

However, visual observation indicated that alongshore swash transport did not appear nearly as large as for the previous reported tests, so that the possible underestimate of the near-shoreline longshore transport (and associated overestimate of the mid-surf transport) is probably not extreme. Additionally based upon observation, the relatively "chaotic" appearance of the swash suggested that high phase difference swash (such as for this test series) may not be sufficiently longshore-uniform or sufficiently organized to promote significant longshore transport across the foreshore.

The distribution of fluorescent tracer observed after 36 minutes of wave action is illustrated in Figure 7-25b. Regions of relatively high and low concentrations of tracer are outlined in the figure as visually determined from long-exposure photographs of the beach under black flood lights. Some by-passing of material over the crest of the groyne is evident from the figure. This was fairly unique to the spilling test series. The tracer distribution generally agrees with the longshore transport distribution determined from the impoundment data, although considerable tracer is observed seaward of the distribution peak found from the impoundment data. The presence of tracer far offshore may be misleading if the offshore patch of tracer was predominately finer-grained fluorescent material transported from the impoundment area and deposited offshore--while much of the rest of the tracer was buried amidst the peak impoundment area. The validity of this possibility was not determined because the small median grain size of the model beach material made tracer identification and burial evaluation (among the mid-surf zone bed forms) difficult. The relatively sharp downdrift gradient of tracer near the shoreline and the apparent absence of buried

tracer on the foreshore near the groyne suggests that nearshore tracer was carried seaward at a point midway between the injection and the groyne--thus reinforcing the notion that the near-shoreline longshore transport was underestimated by the impoundment data.

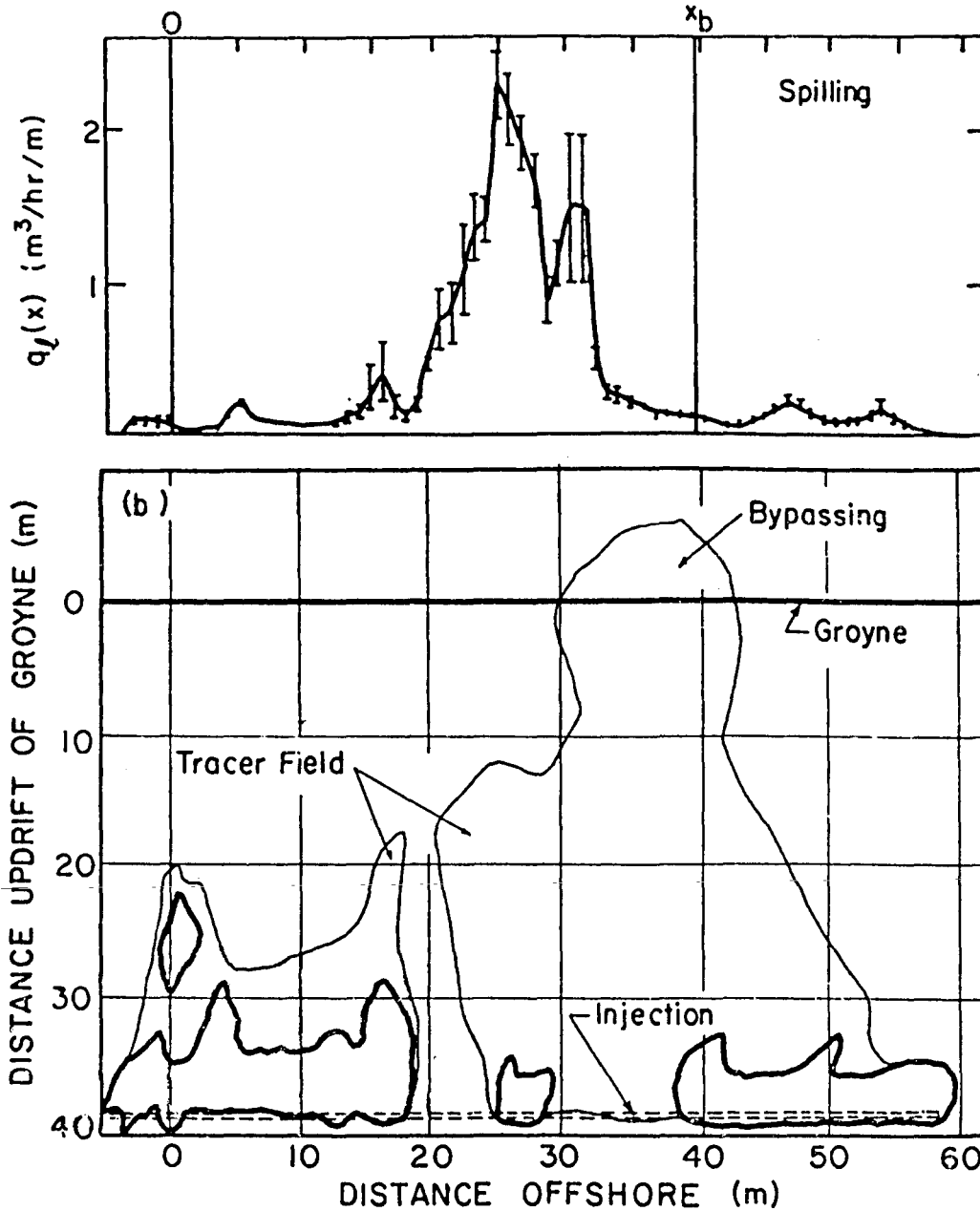


Figure 7-25: (a) Longshore transport distribution developed from impoundment data, and (b) fluorescent tracer field after 36 minutes of wave action for the spilling test series. (Prototype scale.)

The total transport for the spilling wave test series experiment was estimated between 16.3 and 21.4 m<sup>3</sup>/hr. The updrift extent of the impoundment fillet was about 16 m and 40 m for the lesser and greater regions of impoundment, respectively. The latter value is roughly equal to one surf zone width for this test series.

### 7.7 Total Transport

The experiments executed in this study were not intended as a measure of the total longshore sediment transport. However, for completeness, Table 7-2 lists the values of the proportionality constant K from the CERC Formula (which relates the total immersed weight longshore sediment transport rate  $I_\ell$  and the so-called longshore component of wave energy flux at breaking  $P_{\ell b}$  as in Eq. (5.1)). The volumetric rates of transport  $Q_\ell$  determined from the best impoundment interval of each test series were converted to immersed weight transport rates  $I_\ell$  for sediment density  $\rho_s=2.7 \text{ g/cm}^3$  and porosity  $a'=0.6$ . A trend of the proportionality constant K with the surf similarity parameter  $\xi_b$  is weakly indicated. In general, the values of the proportionality constant K determined from the laboratory tests (scaled to prototype) are about one-fourth the value of most field studies and about one-half the value found from most other laboratory studies (CERC, 1984). The comparatively small values of K from this study may be partly due to the finite-length of the model beach, that is, because the longshore current and sediment supply were not artificially introduced updrift in the basin.

Table 7-2: Total Longshore Transport Estimates  
from the Laboratory Impoundment Data Sets  
(Prototype Scale)

Experiment	$P_{\ell b}$ (N/s)	$I_{\ell}$ (N/s)	K	$\xi_b$
PL/SP				
1st Imp.	977	76.4-107.0	0.08 - 0.11	0.30
	415*	"	0.18*- 0.26*	"
2nd Imp.	977	129.8-158.4	0.13 - 0.16	"
	415*	"	0.31*- 0.38*	"
PL				
1st Imp.	1280	156.5-204.3	0.12 - 0.16	0.37
2nd Imp.	"	123.7-199.6	0.10 - 0.16	"
PL/CLPS				
Rising Tide	~ 410	58.1- 90.0	0.14 - 0.22	0.45
Falling Tide	~ 350	11.1- 29.2	0.03 - 0.08	"
1st non-tidal	455	68.1- 88.9	0.15 - 0.20	"
2nd non-tidal	~ 430	69.5- 76.1	0.16 - 0.18	"
CLPS	180	22.5- 31.4	0.13 - 0.17	0.69
SP	703	45.3- 59.5	0.06 - 0.09	0.15

\* Inner wave break

### 7.8 Characteristic Features of the Longshore Transport Distributions

Figure 7-26 illustrates the normalized longshore transport distributions as determined from the best impoundment intervals of the field studies and each of the laboratory test series. For the laboratory plunging/spilling series, the offshore coordinate  $x$ , was normalized by the outer location of the observed migratory breakpoint. Generalizing, the results shown in the figure suggest that the longshore transport distribution is generally bimodal with peaks about the shoreline and

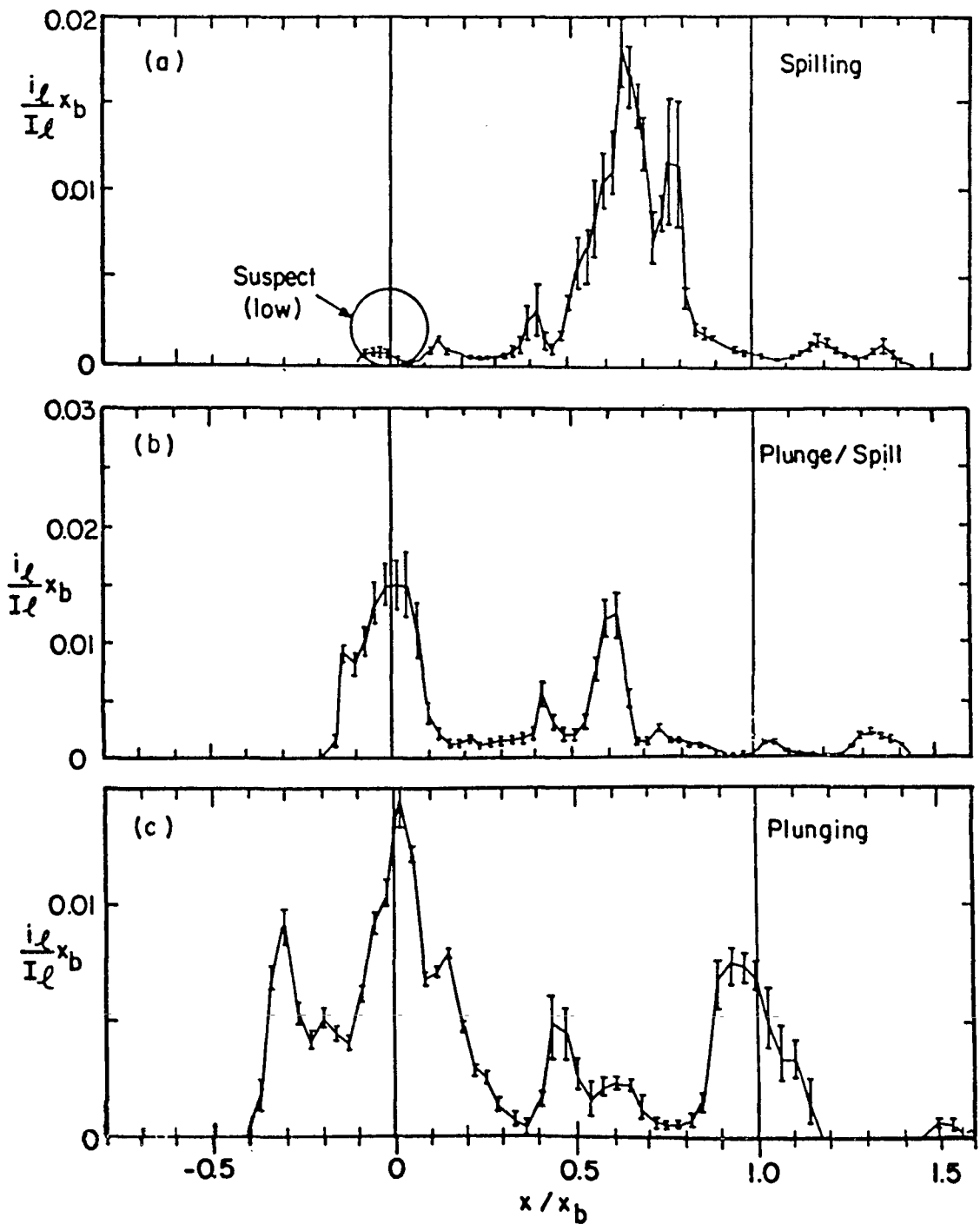


Figure 7-26: Normalized longshore transport distribution across the surf zone developed from the best impoundment data sets of the laboratory and field experiments (continued on following page).

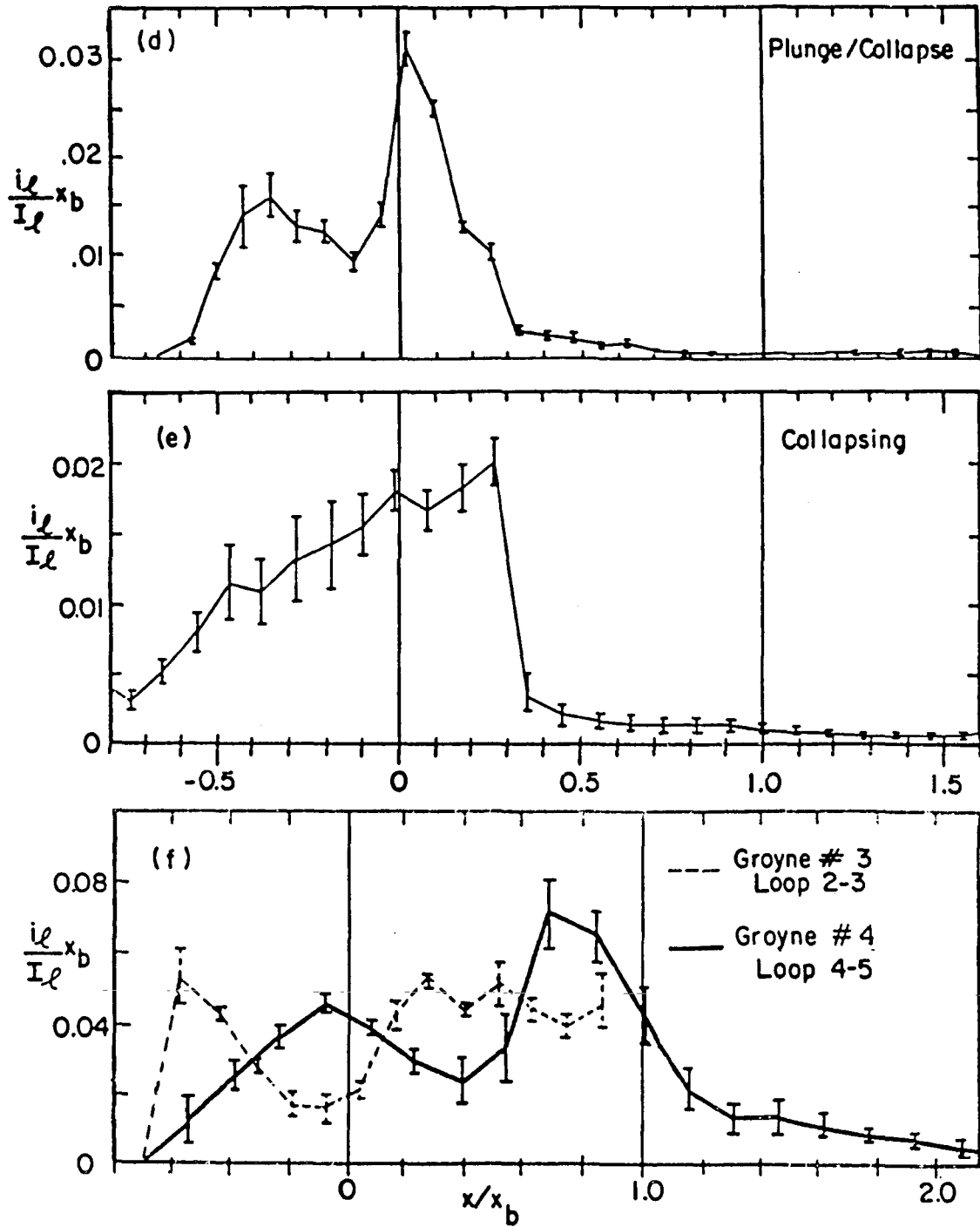


Figure 7-26: Continued from previous page.

about three-quarters of the distance from the shoreline to the breakpoint; however, the relative significance of the peaks shifts from the near-breakpoint peak to the near-shoreline peak as the surf zone changes from spilling to collapsing wave conditions. In the collapsing condition limit, the near-breakpoint peak tends towards zero. The contribution of above-shoreline longshore transport to the total longshore transport progressively increases from less than 5% for the spilling condition to more than 60% for the collapsing condition. Longshore transport seaward of the breakpoint increases somewhat as the wave conditions vary from the collapsing to spilling condition, but generally represents a 10% to 20% contribution to the total transport.

In Figures 5-17, 5-18, 7-6, 7-10, 7-15, 7-17, and 7-24, the average beach profiles and the non-normalized longshore sediment transport, wave height, and longshore current distributions across shore have been illustrated for the best field and laboratory impoundment data sets. Inspection of these figures suggests nearshore correlation between the local longshore transport and the local bed slope, longshore current, and inverse-depth. In particular, for the laboratory data, the longshore transport increases dramatically over the steep beachface slope which was usually clearly defined above the terrace.

## CHAPTER 8

### MODELING THE LONGSHORE SEDIMENT TRANSPORT DISTRIBUTION

#### 8.1 Introduction

In this chapter, several distributed longshore sediment transport models previously proposed in the literature, as well as several alternate models, are evaluated with the wave, current, and average beach profile data measured in the field and laboratory and are compared to the longshore sediment transport distributions developed from the field and laboratory impoundment data. Additionally, the significance of nonlinearities to the total and distributed longshore transport is briefly discussed.

#### 8.2 Bagnold Model

Bagnold's (1963) energetics-based model of local immersed weight longshore sediment transport, previously described by Eq. (2.11), is rewritten below

$$i_{\ell B} = k_B \frac{d}{dx}(E C_g) \frac{V_{\ell}}{u_o} \quad (8.1)$$

where small angle of wave incidence is assumed, and where  $k_B$  is a dimensionless transport coefficient,  $C_g$  is the wave group celerity,  $V_{\ell}$  is the local longshore current,  $E$  is the wave energy density  $E = \rho g H^2 / 8$ , and  $u_o$  is typically taken as the near bed horizontal wave orbital velocity.

The Bagnold model is first expressed separately for the surf zone and for the swash zone and without wave induced set-up. For the surf zone,  $u_o$  is taken as the maximum near bed horizontal wave orbital velocity, and linear wave theory and shallow water conditions are assumed such that  $u_o = gH/2C$  and the wave celerity  $C = C_g \approx \sqrt{gh}$ . For the swash zone, it is assumed that  $u_o = \sqrt{gH}$  and  $C_g = \sqrt{gH}$ . The Bagnold model is then written

$$i_{lB} = \begin{cases} \frac{5}{16} k_B \rho g V_\ell H \frac{dH}{dx} & x < 0 \\ \frac{1}{4} k_B \rho g V_\ell (2h \frac{dH}{dx} + H \frac{dh}{dx}) & 0 < x < x_b \\ 0 & x > x_b \end{cases} \quad (8.2)$$

for no wave energy dissipation seaward of the breakpoint  $x_b$ . The values (but not necessarily the gradients) of the surf and swash expressions are continuous at  $x=0$  if the bed slope relative to the gradient of the wave height,  $dh/dH$ , is 2.5 at the shoreline. (For the laboratory data,  $dh/dH \approx 3.0$  to 5.3 at the shoreline.) It is assumed that the local maximum elevation of water during the uprush and backwash of the swash (i.e., values from the wave board) is equal to the wave height  $H$ , for  $x < 0$ . Equation (8.2) was evaluated with the smoothed wave height, longshore current, and profile data from the best laboratory impoundment intervals. In Figure 8-1 the results for three cases are compared to the measured longshore transport distributions developed from the impoundment data for each case. As for all similar figures which follow, the calculated and measured distributions are normalized by their respective total longshore transport values. As seen in the figure, agreement is generally poor especially for the plunging/

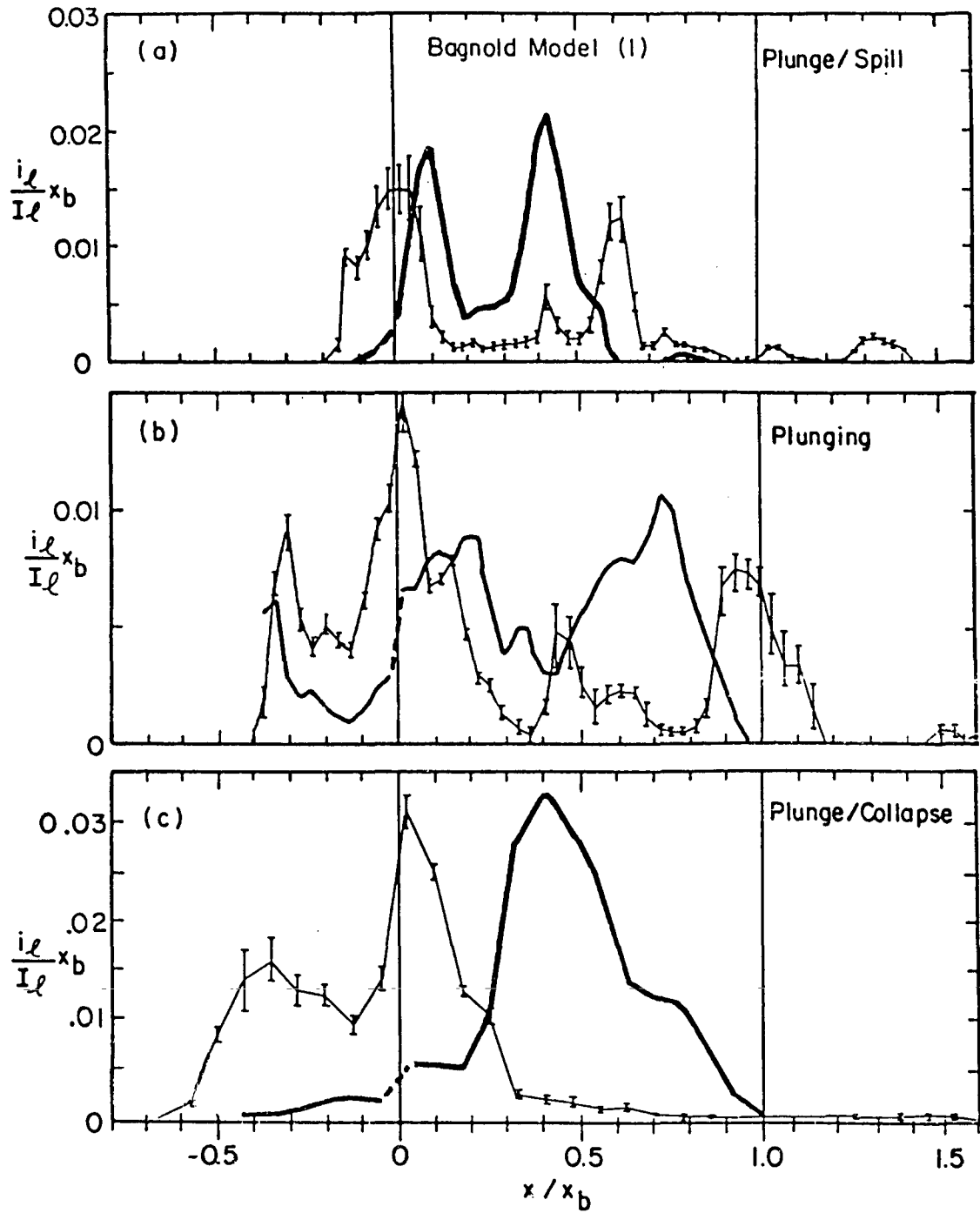


Figure 8-1: Comparison of normalized measured longshore transport distributions from laboratory data (light) with the Bagnold model (bold). No set-up, shoreline-discontinuous evaluation.

collapsing case. The worst and best agreement was for the collapsing and spilling cases, respectively (not shown); however, it is recalled that the measured distribution for the spilling case is suspect. For the calculated distributions, the breakpoint discontinuity is indiscernible because the longshore current tends to zero landward of the breakpoint for the laboratory data.

The Bagnold model is also written so as to be continuous across the shoreline and evaluated for the inclusion of wave induced set-up. Specifically, for both the surf and swash zones, the maximum horizontal orbital velocity from linear theory is assumed for  $u_0$ , but the phase and group celerities,  $C$  and  $C_g$ , (assuming shallow water) are taken as:

$$C = C_g = \sqrt{g(H+d)} \quad (8.3)$$

from solitary wave theory, and where  $d$  is the total depth including wave induced set-up,  $d=h+\bar{\eta}'$ . The Bagnold model is then written

$$i_{\ell B}' = \frac{1}{4} k_B \rho g V_{\ell} \left[ 2(H+d) \frac{dH}{dx} + \frac{1}{2} H \frac{d}{dx}(H+d) \right] \quad (8.4)$$

for all  $x < x_b$ , and where  $i_{\ell B}' = 0$  for  $x > x_b$  assuming no energy dissipation seaward of the breakpoint.

Wave induced set-up (which was not measured in the field or laboratory experiments) is given by

$$\bar{\eta}' = \left[ \frac{3\kappa^2}{8+3\kappa^2} \left( 1 - \frac{h}{h_b} \right) - \frac{\kappa^2}{16} \right] h_b \quad (8.5)$$

for assumptions of small angle of wave incidence, shallow water, and constant proportion  $\kappa$  between local wave height and water depth (Dean

and Dalrymple (1984), among others). The set-up for each data set of interest is initially estimated from Eq. (8.5) using the average beach profiles and breaking depths from the laboratory data, and for  $\kappa=0.8$ . The actual set-up in the laboratory experiments was probably less than that described by Eq. (8.5) because of the finite water mass and beach end-conditions in the model basin. Accordingly, only half the magnitude of the set-up predicted across the surf zone by Eq. (8.5) is used for the laboratory evaluation of the local longshore transport models. The removal of the full magnitude of set-up (predicted by Eq. (8.5)) from the nearshore wave board results in negative-valued wave height estimates--lending support to the assumption that the set-up was not fully developed in the laboratory basin.

The shoreline-continuous Bagnold model, Eq. (8.4), was evaluated with the laboratory data as described above, and in Figure 8-2 is compared to the measured longshore transport distribution for the three cases previously shown. In Figure 8-2, as in all figures of this paper,  $x=0$  refers to the still water shoreline. The agreement is similar or slightly worse than for the shoreline-discontinuous, no set-up Bagnold model (Eq. (8.2)). Agreement for the spilling and collapsing cases (not shown) is also similar or slightly worse.

One measure of the quality of agreement between the predicted and measured longshore transport distributions is the total rms distribution error, defined here as

$$\epsilon_{\hat{i}_l} = \sqrt{\frac{\sum_n^N (\hat{i}_{lc_n} - \hat{i}_{lm_n})^2}{\sum_n^N (\hat{i}_{lc_n})^2}} \quad (8.6)$$

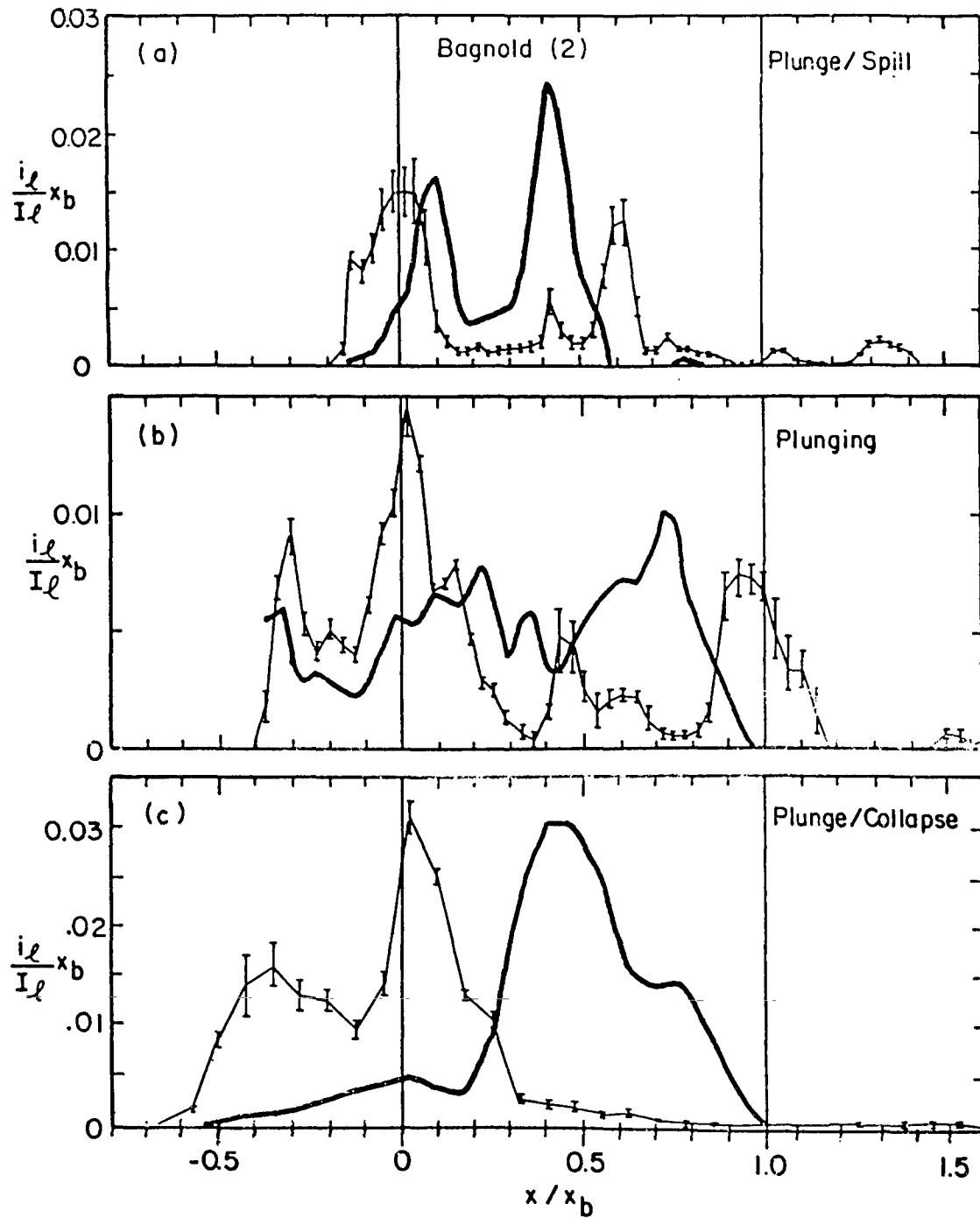


Figure 8-2: Comparison of normalized measured longshore transport distributions from laboratory data (light) with the Bagnold model (bold). Set-up, shoreline-continuous evaluation.

where  $\hat{i}_{lc_n}$  and  $\hat{i}_{lm_n}$  are the normalized predicted (i.e., calculated) and measured local longshore transport values, respectively, at N discrete, uniformly-spaced locations across the surf zone. The normalized values  $\hat{i}_l$  refer to  $i_l/(I_l/x_b)$ . Based upon Eq. (8.6), the average total normalized rms distribution error for each of the laboratory test series is 0.92.

For purpose of comparison to other models, it is noted that if  $H=kd$  and  $h=d$  across the beach, the two Bagnold models evaluated above, Eqs. (8.2) and (8.4), are of the form

$$i_{lB} \sim h V_l \frac{dh}{dx} \quad (8.7)$$

### 8.3 Stress Model

Komar (1971, 1975, 1977) and Bailard and Inman (1981) proposed distributed longshore sediment transport models which are based conceptually upon the energetics approach of Bagnold. Whereas the Bagnold model assumes that sediment is mobilized for transport by the orbital wave motion and carried alongshore by existing currents, the Komar and Bailard/Inman models assume that the existing currents carry sediment alongshore which is mobilized as a function of the bottom stress. Accordingly, the latter two models are termed "stress models" by McDougal and Hudspeth (1981) who presented a generalized stress model for local longshore transport,

$$i_{ls} = k_s \rho |\vec{u}_o| V_l^2 \sin\theta \quad (8.8)$$

for the assumption of small wave angle and weak longshore current, and

where  $\hat{k}_s$  is a dimensionless coefficient which is a function of sediment properties and transport efficiency. Replacing the near-bed wave orbital velocity by its maximum value from linear theory, and further assuming shallow water conditions and the validity of Snell's Law, Eq. (8.8) is written

$$i_{ls} = \frac{1}{2} k_s g H v_l^2 \left( \frac{\sin \theta}{C} \right)_b \quad (8.9)$$

where the subscript b denotes breaking conditions, as usual. Equation (8.9) was taken as a generic description of the Komar and Bailard and Inman models, and was evaluated with the (smoothed) wave and longshore current data from the laboratory experiments. The normalized results are shown in Figure 8-3 for the three test series previously illustrated. The normalized measured transport distributions developed from the laboratory impoundment data are also shown for comparison. The agreement is very poor for all cases (including the spilling and collapsing cases, not shown). Whereas the Bagnold model exhibits some ability to predict large localized transport contributions such as are prevalent in the data (see Figures 8-1 and 8-2), the stress model generally predicts smoother, more uniform transport distributions. This may be due to over-simplification of the stress model as expressed by Eq. (8.9). In application, the smooth appearance of the stress model's predictions result primarily from its non-dependence upon local bed slope and the local gradient of wave height.

A condensed description of the generic stress model, Eq. (8.9), for  $H=kh$ , is

$$i_{ls} \sim h v_l^2 \quad (8.10)$$

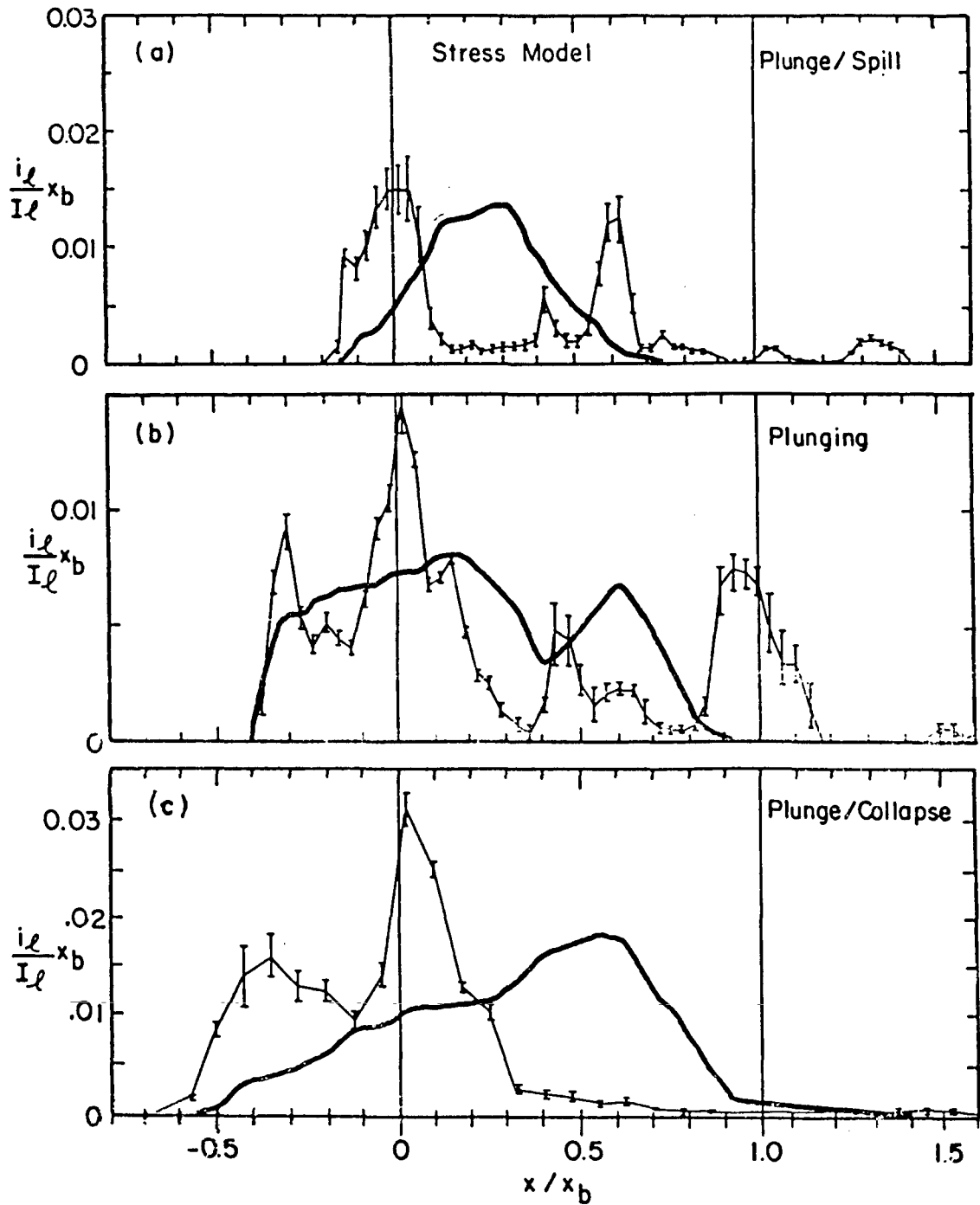


Figure 8-3: Comparison of normalized measured longshore transport distributions from laboratory data (light) with the stress model (bold).

8.4 Alternate Model #1

An alternate model is proposed which is somewhat similar in concept to both the Bagnold and stress models, described above. The local longshore transport is assumed proportional to the local work done by shear stress acting on the bottom, i.e.,

$$i_{\ell 1} = k_1 \tau_b V_{\ell} \quad (8.11)$$

where  $k_1$  is a dimensionless coefficient. The bottom shear stress,  $\tau_b$ , is taken as the cross-shore gradient of the average onshore flux of the longshore component of momentum  $S_{xy}$ :

$$\tau_b = \frac{\partial S_{xy}}{\partial x} \quad (8.12)$$

where

$$S_{xy} = \overline{\int_h^{\eta} \rho uv \, dz} \quad (8.13)$$

and  $u$  and  $v$  represent the cross-shore and alongshore components of wave orbital velocity, respectively. The overbar denotes time-averaging. Assuming small amplitude linear wave theory, straight and parallel depth contours, and small angles of wave incidence, Eq. (8.13) may be written

$$S_{xy} = E C_g \left( \frac{\sin \theta}{C} \right)_b \quad (8.14)$$

such that the proposed local longshore transport model is written

$$i_{\ell 1} = k_1 \frac{d}{dx} (E C_g) V_{\ell} \left( \frac{\sin \theta}{C} \right)_b \quad (8.15)$$

Assuming  $C_g = \sqrt{g(H+d)}$  so as to ensure continuity across the shoreline, Eq. (8.15) becomes

$$i_{\ell 1} = \frac{1}{8} k_1 \rho g^{3/2} \left(\frac{\sin\theta}{C}\right)_b H \left[2\sqrt{H+d} \frac{dH}{dx} + \frac{H}{2\sqrt{H+d}} \frac{d}{dx}(H+d)\right] V_{\ell} \quad (8.16)$$

for all  $x < x_b$ , and  $i_{\ell 1} = 0$  for  $x > x_b$  assuming that wave energy is conserved seaward of the breakpoint.

Eq. (8.16) was evaluated with the laboratory data including an estimate of set-up as described above. In Figure 8-4, the results are compared to the measured longshore transport distributions for the three cases previously shown. Noting its similarity to the Bagnold model, it is not surprising that the proposed model's predicted transport distributions are very similar to those of the second evaluation of the Bagnold model (Fig. 8-2). Like the Bagnold model, agreement between the calculated and measured distributions is fair for the spilling case but deteriorates for the non-spilling cases due to overprediction of transport in the mid- or outer surf zone. Based upon the total rms distribution error, the normalized longshore transport distributions from the Bagnold model, as expressed by Eq. (8.4), agree with the normalized (measured) laboratory distributions, on average, 13% better than the results of the proposed model. This is based upon the data of the best impoundment intervals of all five laboratory test series except the spilling case, for which the proposed model is 20% better than the Bagnold model.

For  $H=kd$  and  $d=h$ , the proposed model, Eq. (8.16), is of the form

$$i_{\ell 1} \sim h^{3/2} V_{\ell} \frac{dh}{dx} \quad (8.17)$$

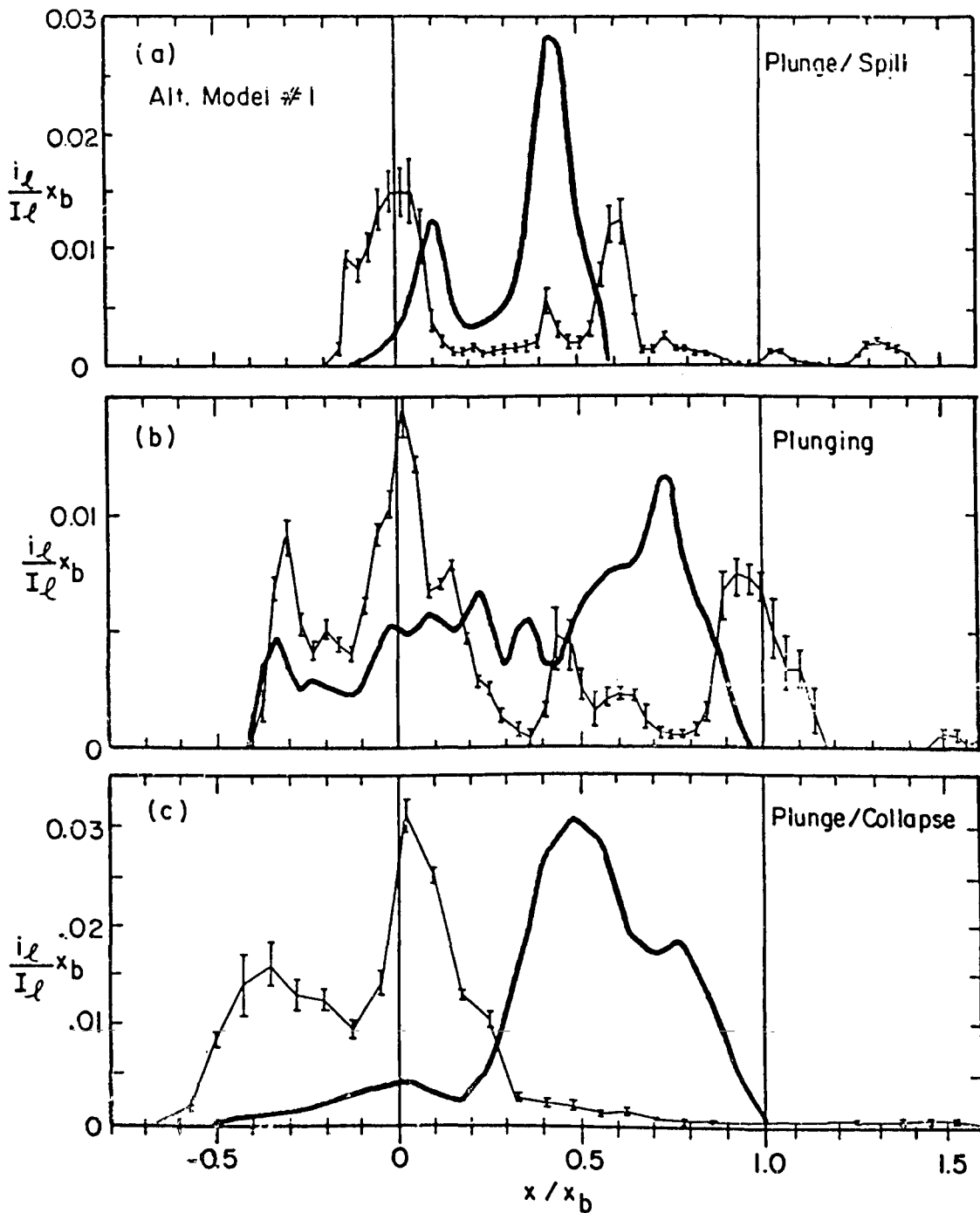


Figure 8-4: Comparison of normalized measured longshore transport distributions from laboratory data (light) with alternate model #1 (bold). Set-up, shoreline-continuous evaluation.

8.5 Alternate Model #2

A second distributed longshore transport model is proposed which assumes that sediment is mobilized in proportion to the local rate of wave energy dissipation per unit volume and transported alongshore by an existing current, i.e.,

$$i_{L2} = k_2 \frac{1}{h} \frac{\partial}{\partial x} (E C_g) V_L \quad (8.18)$$

where  $k_2$  is a constant of proportionality with units of time.

In order to avoid a singularity and ensure continuity at the shoreline, it is assumed that the height of the water column which defines the local surf zone volume (per unit area) is given by  $H+h$ . Further assuming shallow water conditions, small angles of wave incidence, and taking  $C_g = \sqrt{g(H+h)}$ , Eq. (8.18) may be written

$$i_{L2} = \frac{1}{8} k_2 \rho g^{3/2} \frac{H}{\sqrt{H+d}} \left[ 2 \frac{dH}{dx} + \frac{H}{2(H+d)} \frac{d}{dx} (H+d) \right] V_L \quad (8.19)$$

for  $x < x_b$ , and  $i_{L2} = 0$  for  $x > x_b$  assuming no energy dissipation seaward of the breakpoint. The still water depth,  $h$ , has been replaced by the total depth,  $d$ , for completeness.

Eq. (8.19) was evaluated with the laboratory data including an estimate for set-up as described earlier. In Figure 8-5 the results are compared to the measured longshore transport distributions for all five of the laboratory test series. The agreement is fair, but the model generally overpredicts transport in the mid-surf zone (especially for the plunging/collapsing and collapsing cases) and poorly models the near-shoreline transport distribution. The average total normalized rms

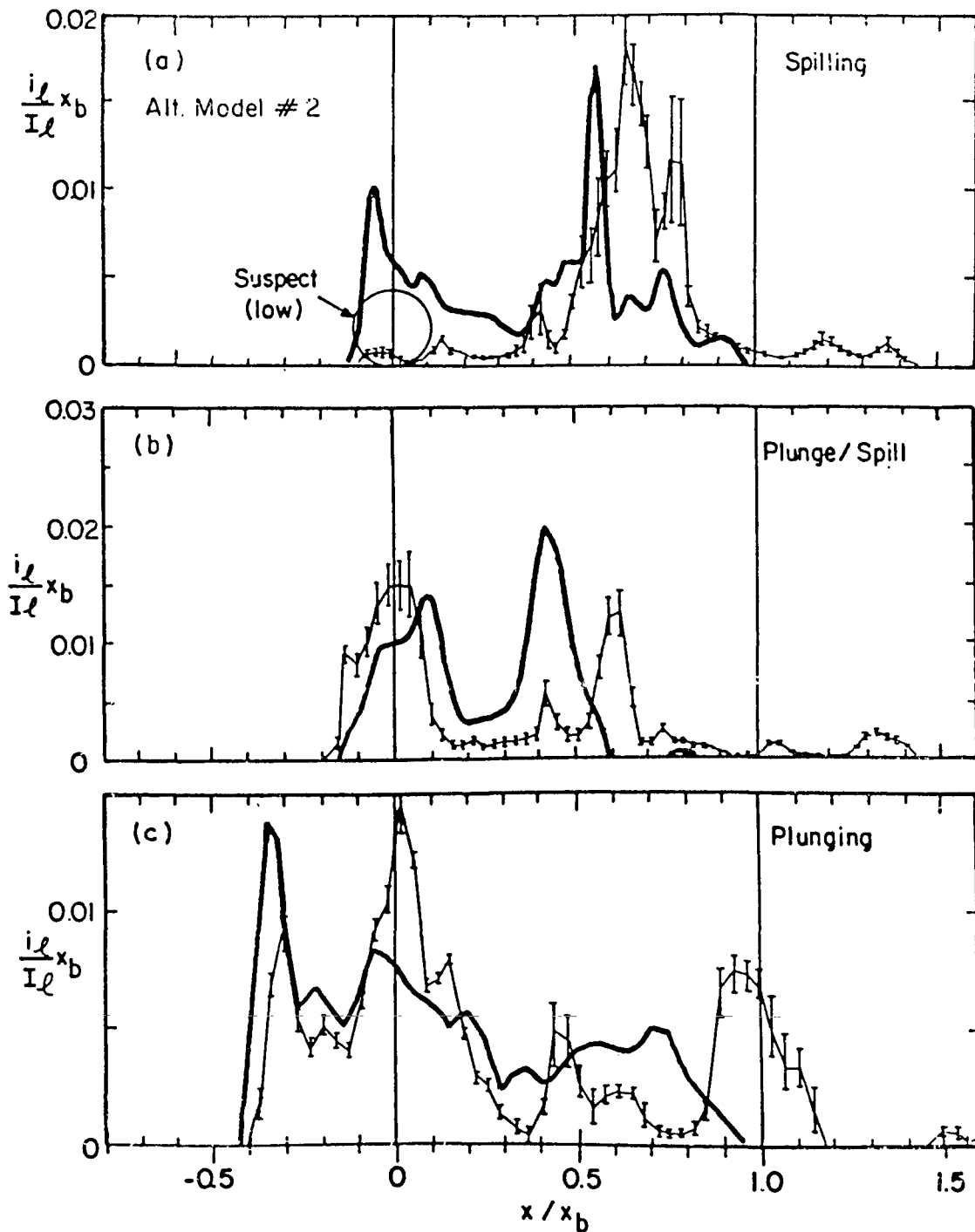


Figure 8-5: Comparison of normalized measured longshore transport distributions from laboratory data (light) with alternate model #2 (bold). Set-up, shoreline-continuous evaluation. (Continued on following page.)

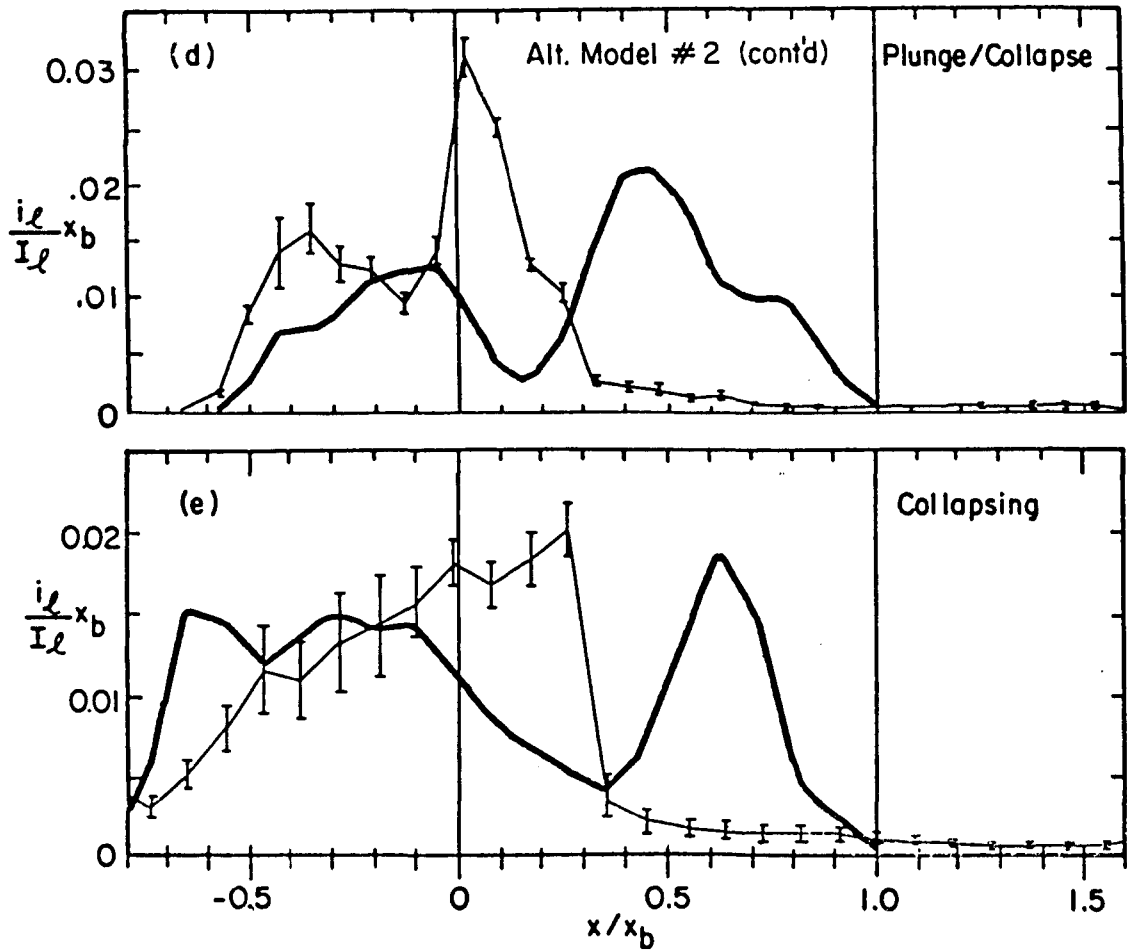


Figure 8-5: Continued from previous page.

distribution error is 15.5% better than for the Bagnold model. This excludes the spilling case, for which the Bagnold model is 5% better.

A condensed description of the proposed model, for  $H=kd$  and  $d=h$  is

$$i_{l2} = h^{1/2} v_l \frac{dh}{dx} \tag{8.20}$$

8.6 Alternate Model #3

The third proposed model is identical in concept to alternate model #2, but includes a factor of the local bed slope,

$$i_{L3} = k_3 \frac{1}{h} \frac{\partial}{\partial x} (E C_g) v_L \left( \frac{dh}{dx} \right)^{1/2} \quad (8.21)$$

where  $k_3$  is a constant of proportionality with units of time. The factor  $(dh/dx)^{1/2}$  is, for now, empirically introduced to reflect the relatively strong correlation observed between the longshore transport distribution data and the local bed slope. Theoretically based arguments which support the inclusion of a factor of bed slope are presented later in this chapter.

For the same assumptions described for alternate model #2, Eq. (8.21) is written:

$$i_{L3} = \frac{1}{8} k_3 \rho g^{3/2} \frac{H}{\sqrt{H+d}} \left[ 2 \frac{dH}{dx} + \frac{H}{2(H+d)} \frac{d}{dx} (H+d) \right] v_L \left( \frac{d(d)}{dx} \right)^{1/2} \quad (8.22)$$

Eq. (8.22) was evaluated with the laboratory data including an estimate for set-up as described earlier. In Figure 8-6 the results are compared to the measured longshore transport distributions for all five of the laboratory test series. The agreement is fairly good for all cases. There is some overprediction in the surf zone for the plunging/ collapsing and collapsing cases, and underprediction near the breakpoint and inner breakpoint, respectively, for the plunging and plunging/ spilling cases. Recalling that the measured distribution for the spilling case is believed to be biased towards the outer surf zone, the disagreement between the predicted and actual distributions for the spilling case is probably not as severe as is observed in the figure. It is thought,

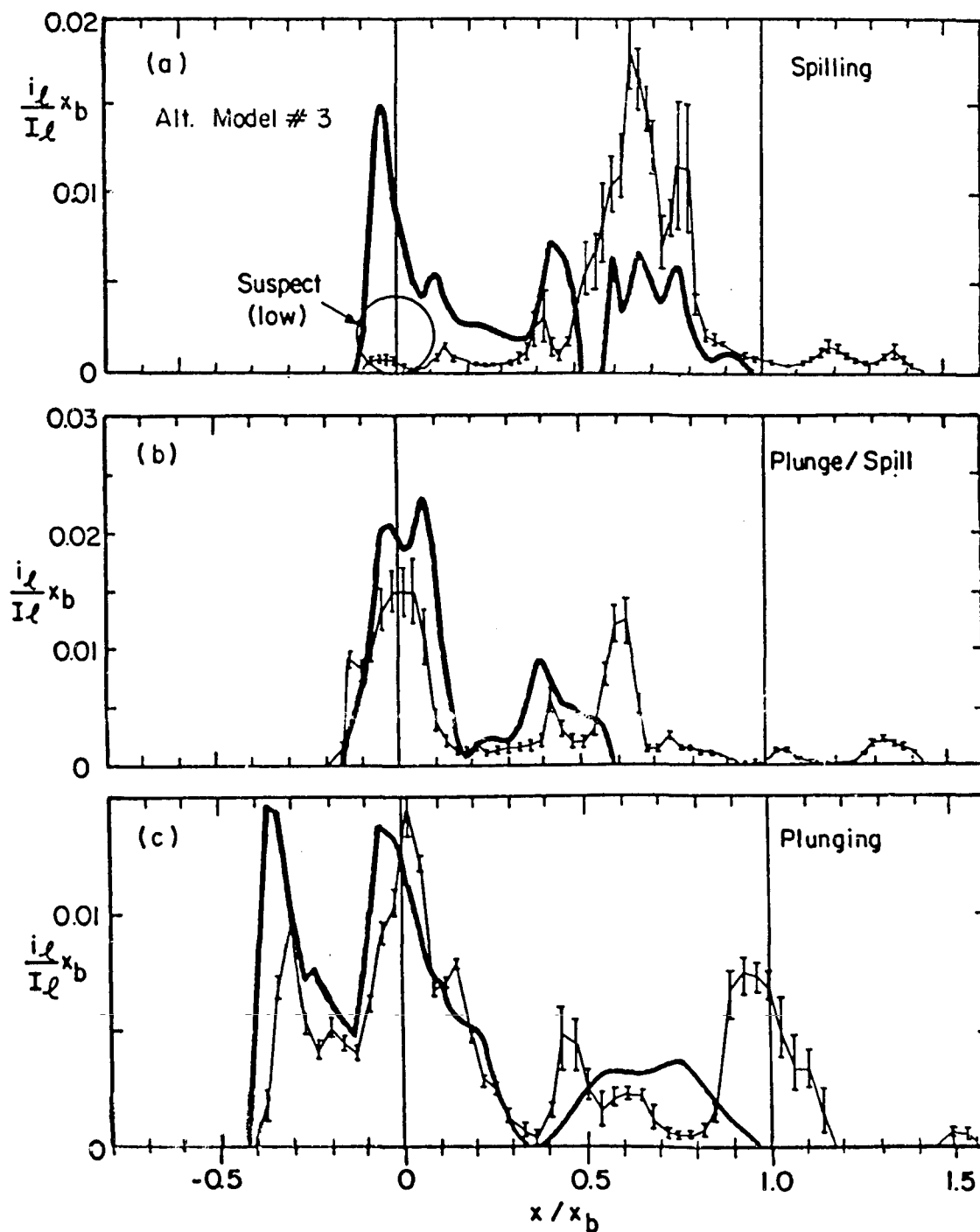


Figure 8-6: Comparison of normalized measured longshore transport distributions from laboratory data (light) with alternate model #3 (bold). Set-up, shoreline-continuous evaluation. (Continued on following page.)

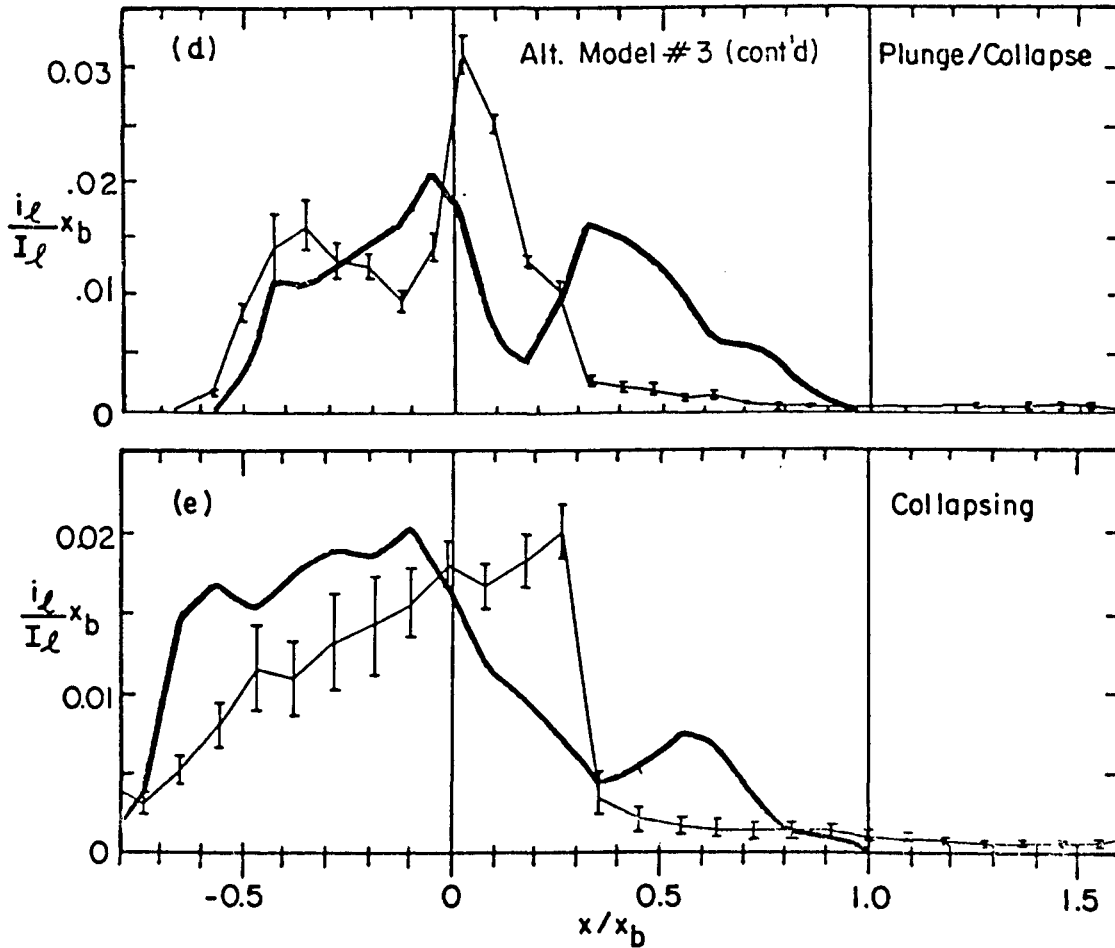


Figure 8-6: Continued from previous page.

however, that the peak predicted in the swash zone for the spilling case may be unrealistically large.

On average (excluding the spilling case) this model exhibits a 16.8% improvement in total rms normalized distribution error over alternate model #2, and a 32% improvement over the Bagnold model. Individually, the greatest improvement is observed for the plunging/collapsing and collapsing cases (about 20% for alternate model #2, and 43% for the Bagnold model). The least improvement (less than 10% for both models) is observed for the plunging case.

Evaluation of the model for the full magnitude of set-up, given by Eq. (8.5), generally improved agreement for the spilling and spilling/plunging cases, but worsened agreement for the plunging/collapsing and collapsing cases. Conversely, evaluation for no set-up degraded agreement for the former cases while improving agreement for the latter.

For  $H=kh$  and  $d=h$ , alternate model #3 is of the form

$$i_{l3} = h^{1/2} V_l \left( \frac{dh}{dx} \right)^{3/2} \quad (8.23)$$

#### 8.7 Alternate Model #4

A fourth model is proposed primarily as a sensitivity test of the bed slope factor introduced in the previous model; that is,

$$i_{l4} = k_4 \frac{1}{h} \frac{\partial}{\partial x} \left( E C_g \right) V_l \frac{dh}{dx} \quad (8.24)$$

where  $k_4$  is a constant of proportionality with units of time. This model was evaluated following the same assumptions and approach of the previous two models. The results for all five of the laboratory test series are shown in Figure 8-7 along with the measured longshore transport distributions.

As the majority of the laboratory beach profiles exhibited a steep foreshore relative to the rest of the profile, alternate model #4--which heavily weights bed slope--consistently predicts the longshore transport maxima about the foreshore. This results in improved agreement between the predicted and measured distributions for the plunging/collapsing and collapsing cases. However, it simultaneously results in substantial overprediction of foreshore contributions for the non-collapsing cases. Given the limited data and the possibility that the measured transport

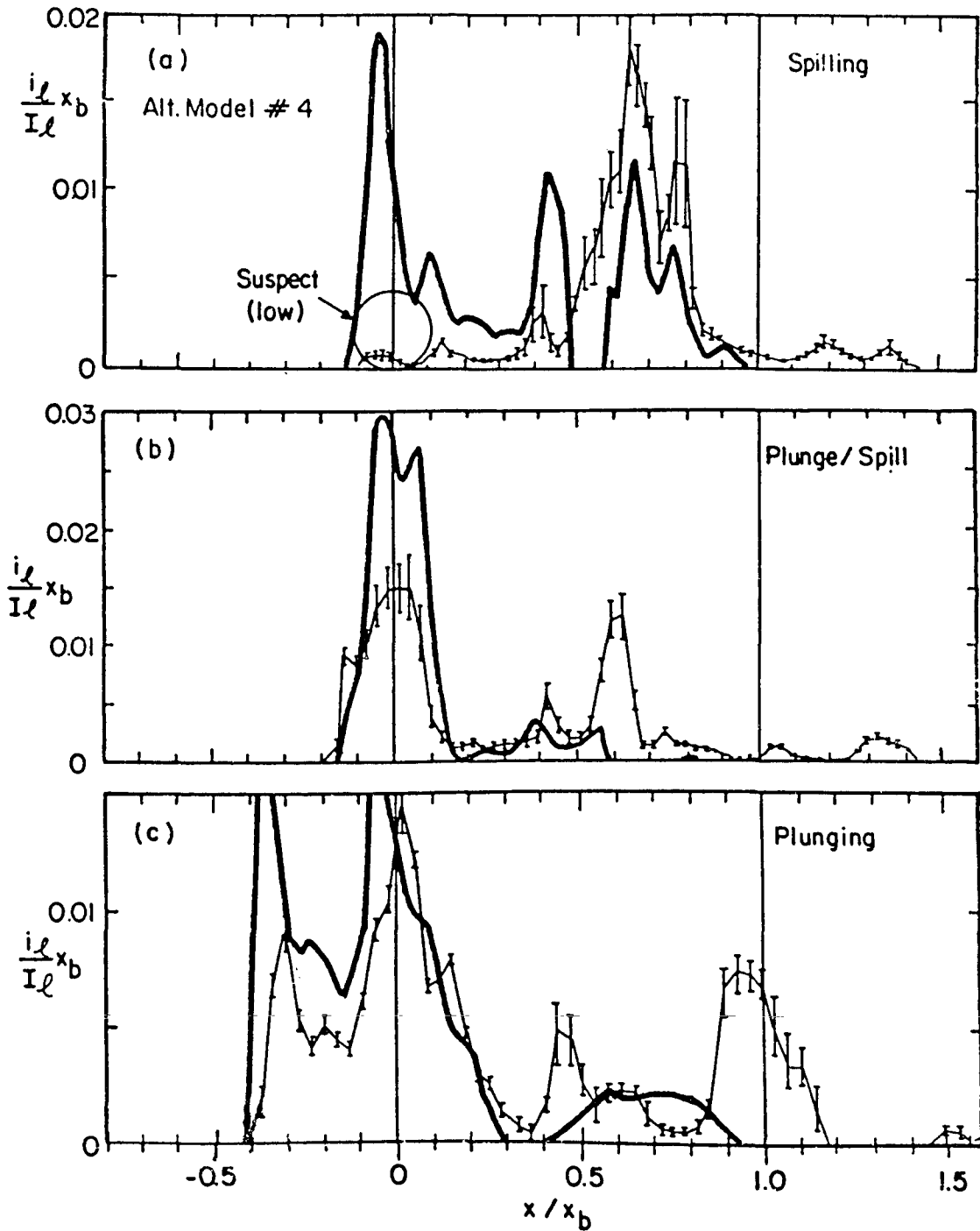


Figure 8-7: Comparison of normalized measured longshore transport distributions from laboratory data (light) with alternate model #4 (bold). Set-up, shoreline-continuous evaluation. (Continued on following page.)

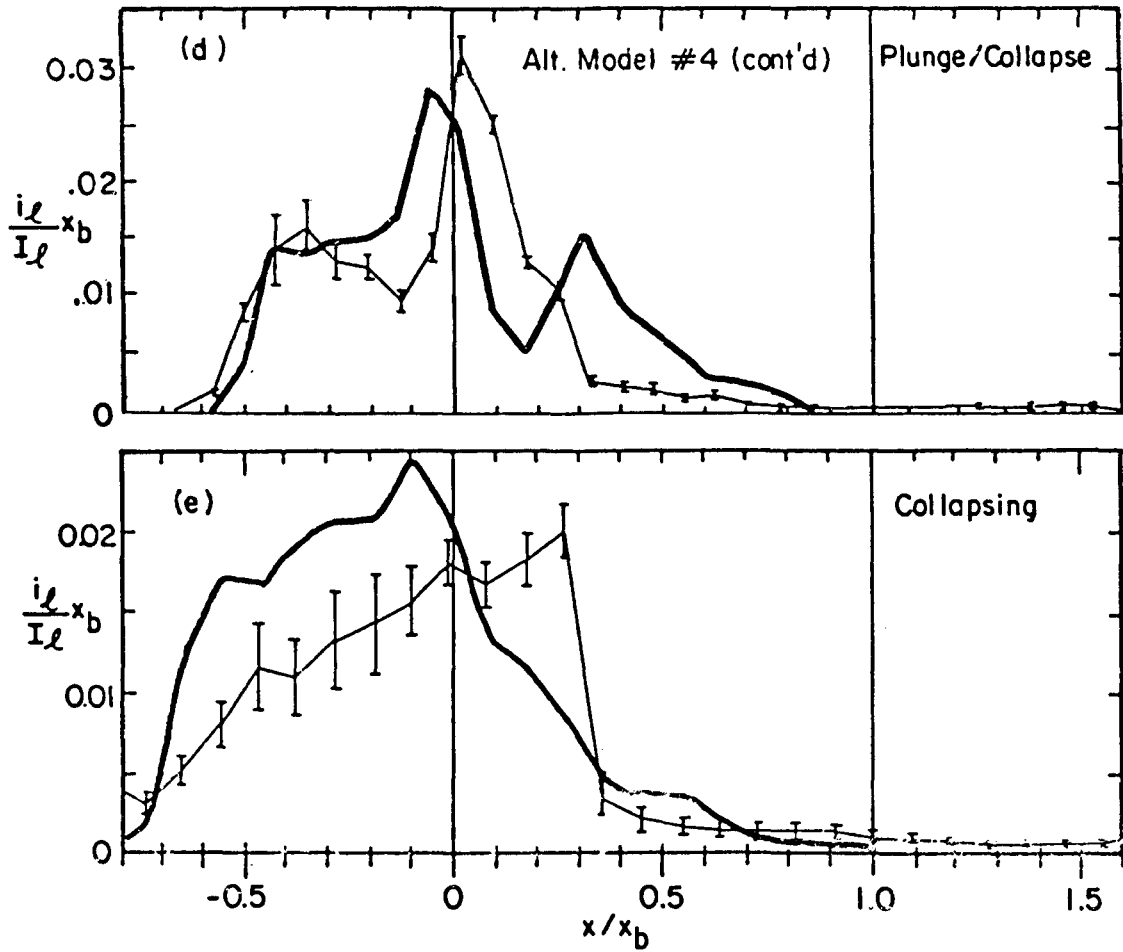


Figure 8-7: Continued from previous page.

distributions for the longer-term impoundment experiments may be somewhat skewed offshore due to smearing (i.e., for the spilling and plunging/spilling cases), it is difficult to say whether this overprediction at the foreshore is significantly unrealistic.

The average total normalized rms distribution error for this model is 0.67, or 3.7% better than for alternate model #3. (The average error is 0.57 if the spilling case is excluded.) However, since this model may significantly overpredict local longshore transport about the foreshore for non-collapsing cases (i.e., those cases which are of more

frequent interest to coastal engineers), alternate model #3 is preferred to this model.

### 8.8 Alternate Model #5

Finally, a fifth model is proposed which is conceptually similar to the Bagnold model:

$$i_{L5} = k_5 \frac{1}{h} \frac{\partial}{\partial x} (E C_g) \frac{V_L}{u_o} \left( \frac{dh}{dx} \right)^{1/2} \quad (8.25)$$

where  $k_5$  is a constant of proportionality with units of length, and the factor of bed slope is introduced as for alternate model #3. Bagnold assumed that the sediment transport rate is proportional to the rate of energy dissipation (per unit area) within the shearing bedload layer, whereas in the present model, it is assumed proportional to the rate of energy dissipation per unit volume of surf.

Bailard and Inman (1979) re-derived the general form of the original Bagnold expression through consideration of the rate of energy dissipation (per unit volume) in the bedload shear layer. They found that the total rate of energy dissipation within the layer is composed of two terms: the contribution from the downslope gravity component and the contribution from the applied stress. The first term is proportional to  $\sin(\beta)$  where  $\beta$  is the angle which the bed makes with the horizontal. The Bagnold model is developed by assuming small bed slope such that the first term is neglected and the second term remains. Accordingly, for relatively steep local bed slopes such as upon the foreshore or the face of a bar, the inclusion of a factor of bed slope in the present model (as well as in the previous alternate models #3 and

#4) is somewhat justified. However, it follows that the local bed slope term may be more properly included in the model in the form

$$i_{\ell} \sim \left\{ \frac{\partial}{\partial x} D + \Phi \left( \frac{dh}{dx} \right) \right\} \frac{v_{\ell}}{u_0} \quad (8.26)$$

where the applied stress is assumed proportional to the local rate of wave energy dissipation per unit volume,  $D$ , and where  $\Phi \left( \frac{dh}{dx} \right)$  represents a term which is a function of the local bed slope and other sediment and flow parameters.

Alternate model #5, though lacking the form of Eq. (8.26) suggested above, was evaluated for the same assumptions and conditions of the previous four models, and for  $u_0$  taken as the near bed horizontal orbital velocity from linear theory. Accordingly, Eq. (8.25) was written

$$i_{\ell 5} = \frac{1}{4} k_5 \rho g \left[ 2 \frac{dH}{dx} + \frac{H}{2(H+d)} \frac{d}{dx} (H+d) \right] v_{\ell} \left( \frac{d(d)}{dx} \right)^{1/2} \quad (8.27)$$

Eq. (8.27) was evaluated with the laboratory data and for wave induced set-up as described earlier. The resulting predicted (normalized) distributions were very similar to those of alternate model #3. However, the average agreement between the predicted and measured (normalized) distributions was 9% poorer than for alternate model #3. Individually, the plunging and collapsing cases, respectively, were 20% and 12% poorer than for model #3, while the other cases were less than 5% poorer.

### 8.9 The Proportionality Constants

As previously described, the laboratory experiments were not intended to measure the total longshore transport rate. However, it will be assumed that the total longshore transport rate measured for each laboratory test series,  $I_{\ell m}$ , is reasonably approximated by the cross-shore integration of the local longshore transport rates developed from the best impoundment intervals of each test series. The local volumetric rates are converted to immersed weight rates through Eq. (2.5), where  $\rho_s=2.7$  and  $a'=0.6$ . The constant of proportionality  $k$ , in an existing or proposed local longshore transport model is evaluated by

$$k = I_{\ell m} / I_{\ell c} \quad (8.28)$$

where

$$I_{\ell c} = \int_{x_0}^{\infty} i_{\ell c} dx \quad (8.29)$$

and  $i_{\ell c}$  refers to the calculated values of the local longshore transport rate from the existing or proposed model. The term  $x_0$  is the landward limit of longshore transport calculated from the model.

The mean value of the proportionality constant  $k_3$  in alternate model #3 (Eq. (8.21)) is 0.48 secs (prototype scale) and 0.057 secs (model scale). The normalized standard deviation of  $k_3$  for all five laboratory test series is 31.8%. The value of  $k_3$  generally increases as the wave type varies from the spilling cases to the collapsing case but a clear trend is not seen. (The prototype-scale value of  $k_3$  listed above is not really meaningful because the distortion of the laboratory model precludes proper scaling of the proportionality constant.)

For comparison, the average value of the proportionality constant  $k_B$  in the Bagnold model (as evaluated through Eq. (8.4)) is 0.123. This

is about half the value suggested by the field data of Komar and Inman (1970). The normalized standard deviation of  $k_B$  for all five laboratory test series is 64%. Again, a weak and poorly defined trend is observed as  $k_B$  increases by a factor of about 4 from the spilling case to the collapsing case.

The smallest range of values calculated for the proportionality constant for each of the proposed models was associated with alternate model #4, for which the normalized standard deviation of  $k_4$  was found to be 28%. Alternate model #3 was second smallest (31.8%).

#### 8.10 Comparison to Field Data

Each local longshore transport model described above was evaluated with the wave, longshore current, and average beach profile data of the two best field impoundment experiments. Tidal effects were not included. The results were compared to the measured longshore transport distributions developed for these experiments. Specifically, the data of Groyne #3, loops 2-3, and of Groyne #4, loops 4-5, were selected for analysis. The total magnitude of the wave induced set-up, described by Eq. (8.5), was included in the model evaluations.

The normalized longshore transport distributions predicted by alternate models #2 and #3 (as evaluated using Eqs. (8.19) and (8.22), respectively) exhibited the best overall agreement with the normalized measured distributions from the field data (see Figures 8-8 and 8-9). Both models #2 and #3 predict the general trend of the measured transport distribution fairly well for the Groyne #4 case, although the predicted distributions are shifted slightly shoreward relative to the measured distributions. Unlike the laboratory cases, the agreement for

model #2 is slightly better than for model #3. Neither model reflects the general trend of the measured distribution from Groyne #3 very well; however, the validity of the measured distribution may be suspect. As described in Chapter 5, the large-valued transport peak at the landward-most edge of the swash zone may reflect groyne-local accretion high on the beach which followed localized erosion due to the groyne deployment operation.

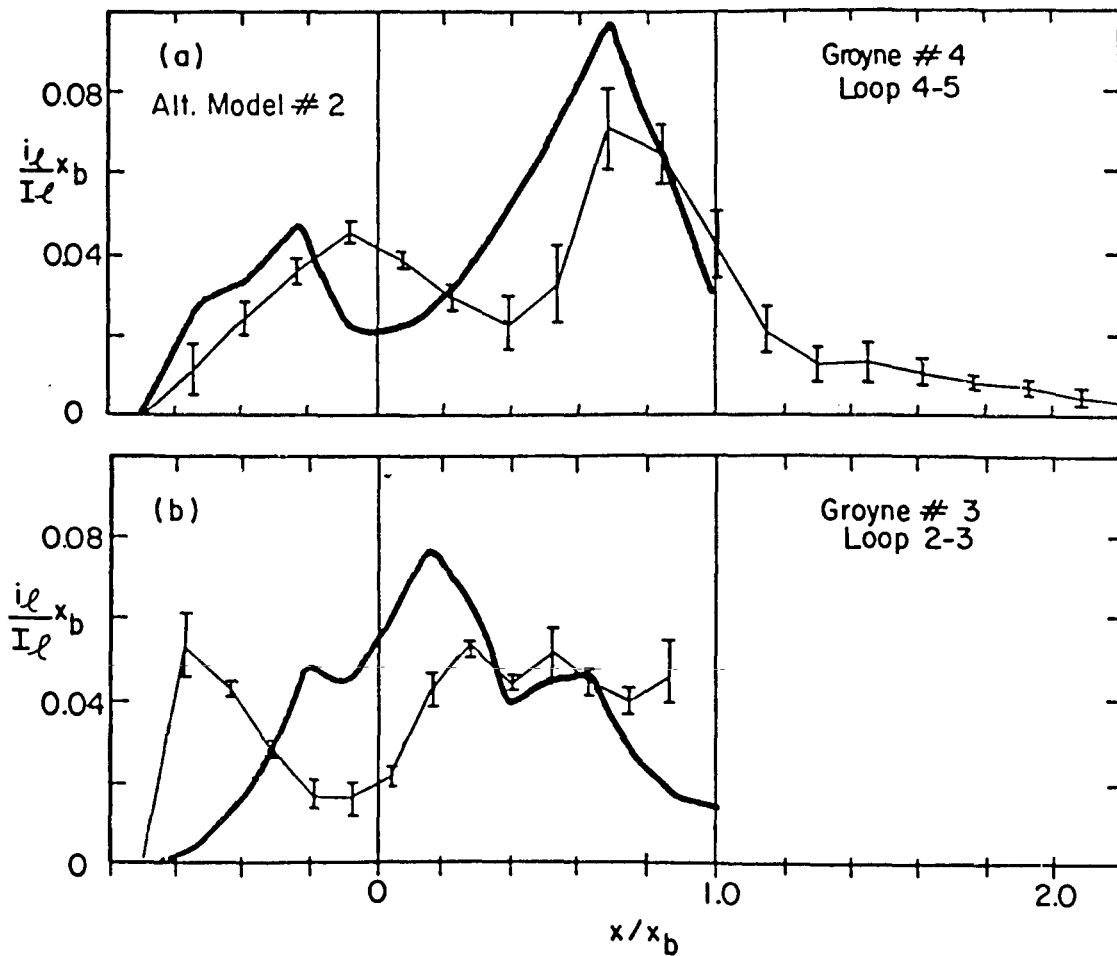


Figure 8-8: Comparison of normalized measured longshore transport distributions from the two best field data sets (light) with alternate model #2 (bold). Set-up, shoreline-continuous evaluation without tidal influence.

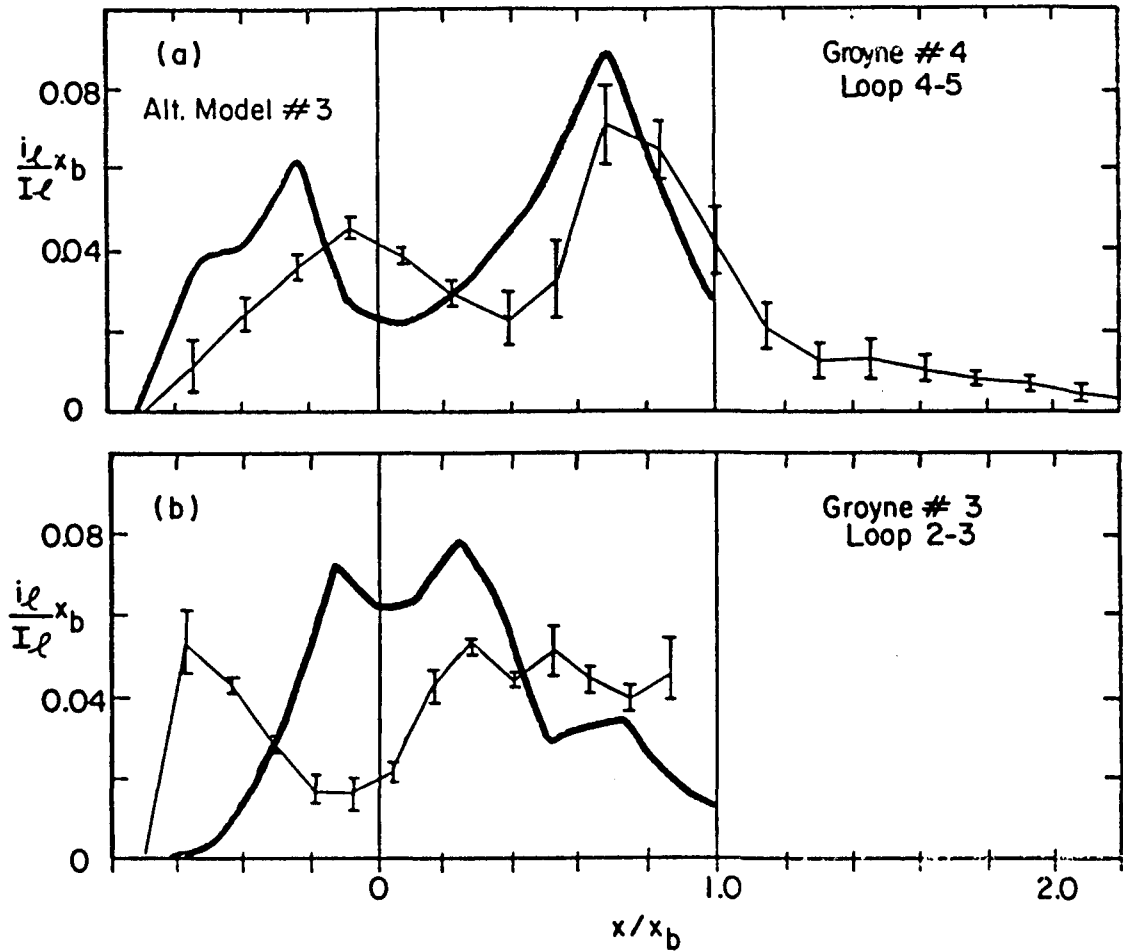


Figure 8-9: Comparison of normalized measured longshore transport distributions from the two best field data sets (light) with alternate model #3 (bold). Set-up, shoreline-continuous evaluation without tidal influence.

As was also observed for the laboratory data, alternate model #4 substantially overpredicted the swash and near-shoreline contributions for the two field cases. The stress model and alternate model #1 also poorly predicted the general trend of the two field cases. The results of alternate model #5 (evaluated using Eq. (8.27)) were similar to those of alternate model #3.

The results of the Bagnold model as evaluated using Eq. (8.4) for the two best field data sets are shown in Figure 8-10. Agreement with

the measured field distributions is generally fair for the surf zone, but swash and near-shoreline contributions are not predicted.

For the Groyne #4 results, the constants of proportionality for the two best models were found to be  $k_2=0.14$  secs and  $k_3=0.53$  secs for alternate models #2 and #3, respectively. For the Bagnold model,  $k_b=0.115$ .

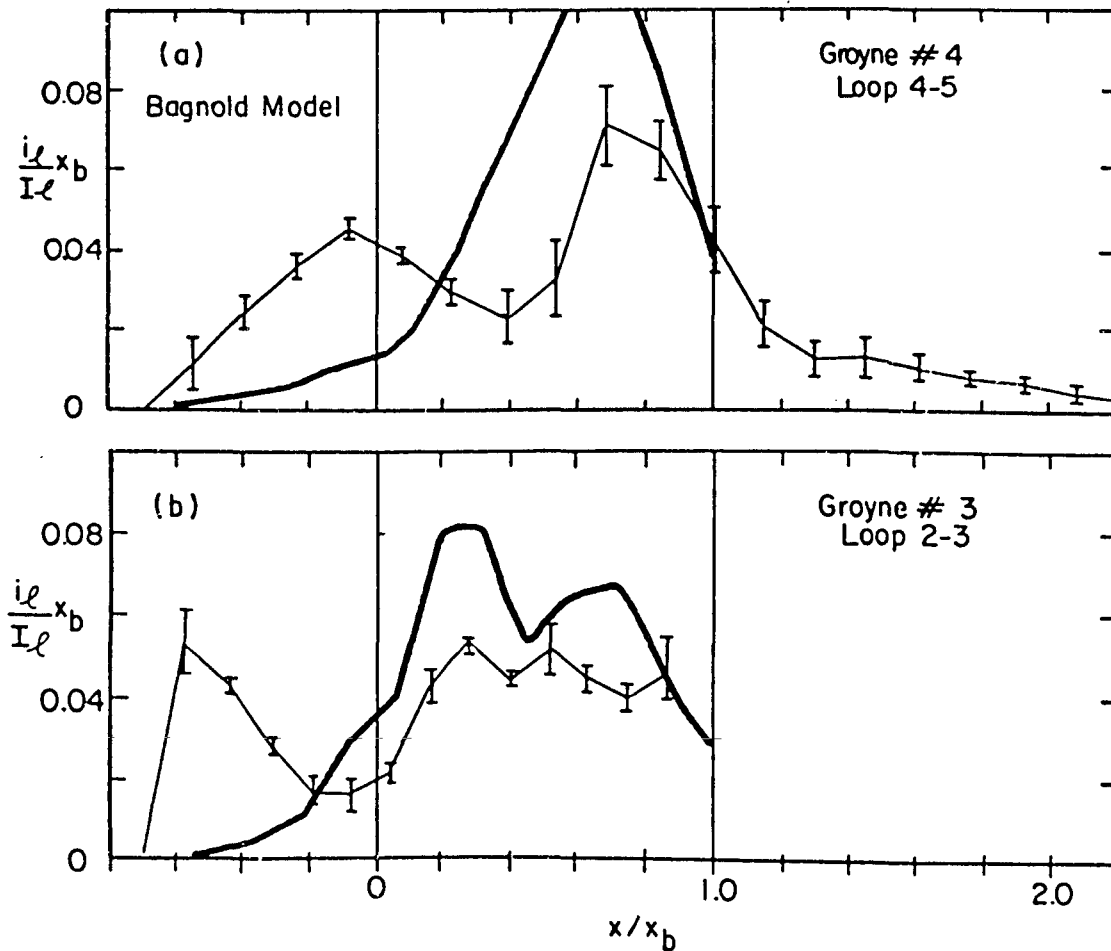


Figure 8-10: Comparison of normalized measured longshore transport distributions from the two best field data sets (light) with the Bagnold model (bold). Set-up, shoreline-continuous evaluation without tidal influence.

While comparing the models' predicted results with measured long-shore transport distributions from the field data, it is important to bear in mind the limitations of the data. First, the wave and longshore current data for the field experiments as used in the model evaluation, are very crude. The raw wave and current data (limited in the first place) were plotted against the tidally-adjusted depth at which they were observed, smoothed, then transformed to approximate wave height and longshore current profiles across shore. Values in the swash zone were simply assumed based upon laboratory observations. Second, the measured longshore transport distributions were in part developed through tidal deconvolution--the validity of which has not yet been firmly established.

#### 8.11 The Preferred Model

Of all the models described and evaluated above, alternate model #3, originally expressed by Eq. (8.21), appears to predict the longshore transport distributions measured in the laboratory most consistently. Additionally, model #3 predicts the measured distribution from one of the two best field data sets reasonably well; none of the models reasonably predict the other. Based upon the laboratory data, alternate model #4 overestimates near-shoreline contributions because it includes the greatest dependence upon bed slope of any of the models. Alternate model #2, which includes less dependence on bed slope than model #3, overestimates surf zone contributions and poorly models the nearshore distribution. The normalized distributions predicted by model #5 are very similar to those of model #3. However, the total rms distribution error is 9% worse for model #5 than for #3, and the values

of the proportionality constant estimated for model #5 vary over a range which is twice as great as for model #3. Overall, of the models tested, alternate model #1 and the Bagnold and stress models exhibit the poorest agreement with the measured distributions. In summary, it appears that alternate model #3, on average, best predicts the measured longshore transport distributions of all the models considered.

## 8.12 Some Considerations of Non-Linear Effects

### 8.12.1 Preliminary Remarks

Evaluation of all of the models described above more or less relied upon linear wave theory. While the use of linear theory greatly simplifies application of the models, it is recognized that non-linear wave theories are more appropriate for evaluating nearshore wave related beach processes. Accordingly, a few implications of non-linear wave theory on total and distributed longshore transport are discussed in the following pages.

### 8.12.2 Total Transport

Dean (1974) has shown that the average energy  $E$  per unit surface area for a non-linear (stream function) wave is much less than for a linear wave. Similarly, it can be shown that the quantities  $P_{lb}$  and  $S_{xy}$  most often associated with prediction of the total longshore transport are also much less for non-linear (stream function) theory than for linear theory.

From Eq. (2.2),

$$P_l = E C_g \cos \alpha \sin \alpha \quad (8.30)$$

Denoting stream-function quantities by the subscript  $\psi$ , the ratio between the stream function and linear theory expressions of the so-called longshore energy flux at breaking can be written

$$\frac{P_{\ell b \psi}}{P_{\ell b}} = \left( \frac{E_{\psi}}{E} \frac{n_{\psi}}{n} \frac{L_{\psi}}{L_o} \frac{h}{L} \right)_b \left( \frac{h}{L_o} \right)_b^{-1} \quad (8.31)$$

where  $n=C_g/C$  as usual, and where wave properties not subscripted by  $\psi$  refers to linear theory values.

From Eq. (8.13),

$$S_{xy} = \frac{1}{2} E n \sin 2\alpha \quad (8.32)$$

so that the ratio between the stream function and linear theory expressions of the onshore flux of the longshore component of momentum (longshore radiation stress) at breaking can be written

$$\left( \frac{S_{xy \psi}}{S_{xy}} \right)_b = \left( \frac{E_{\psi}}{E} \frac{n_{\psi}}{n} \right)_b \quad (8.33)$$

For selected values of  $h/L_o$ , Dean (1974) presents values of the ratios  $E_{\psi}/E$ ,  $n_{\psi}$ , and  $L_{\psi}/L_o$  for a breaking condition defined by  $H_b \approx 0.78h_b$  ("case D" in the stream function tables). For the first seven tabulated conditions in Dean, where  $h/L_o = 0.002$  to  $0.2$ , the non-linear to linear ratios of  $P_{\ell b}$  and  $S_{xy}$  (as given by Eqs. (8.32) and (8.33), respectively) are shown in Figure 8-11. The suspiciously large values calculated for  $h_b/L_o = 0.02$  ("case 4-D") are not unexpected as they reflect an error or anomaly in the stream function tables for this case (Dean--personal communication). It is seen that the quantities  $P_{\ell b}$  and  $S_{xy}$  calculated by stream function theory, are as much as 3 to 4 times smaller than

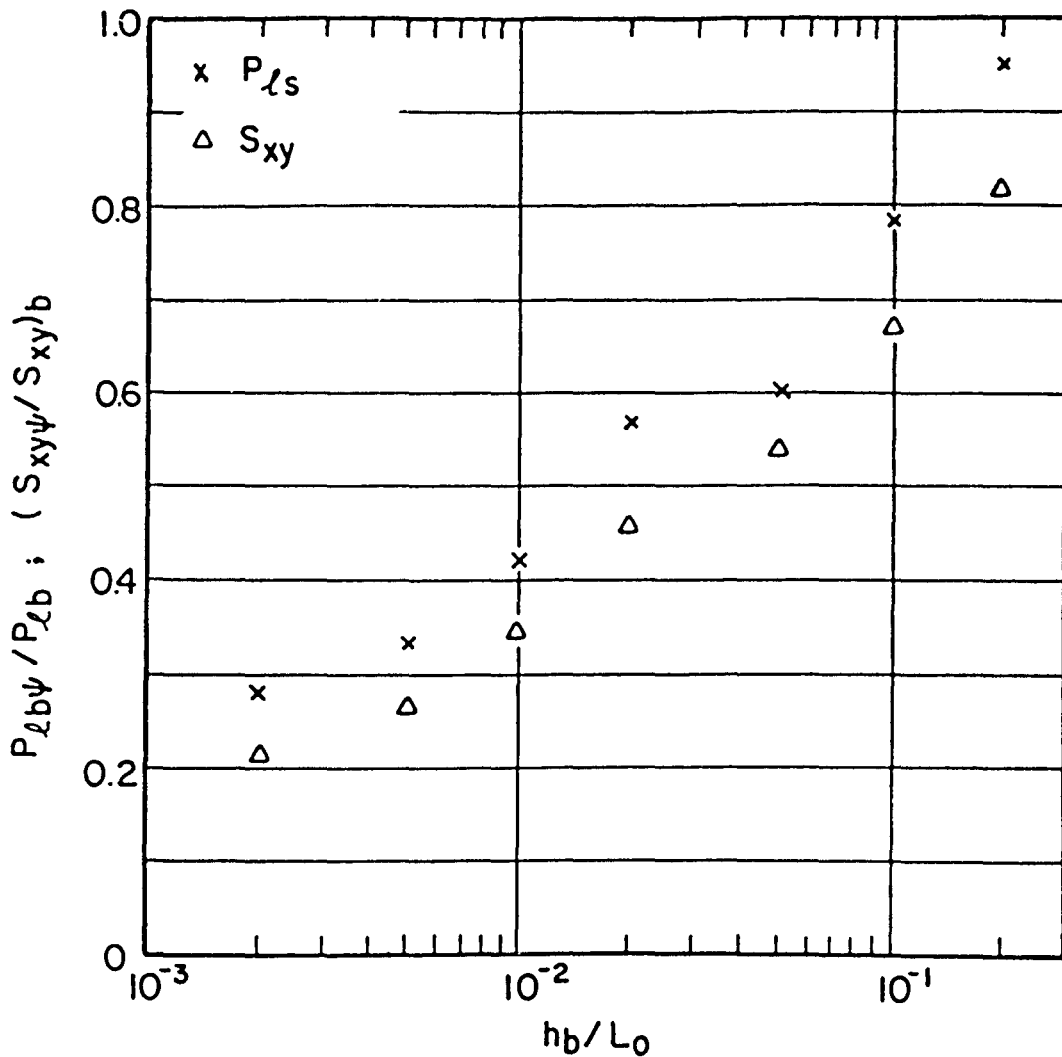


Figure 8-11: Ratio of the stream function and linear theory values of the longshore wave energy flux,  $P_{\ell}$ , and the longshore radiation stress,  $S_{xy}$ , for several cases evaluated at breaking.

calculated by linear theory for very shallow water waves. If the well known expressions for total longshore transport,  $I_{\ell} = K P_{\ell b}$  and  $I_{\ell} = K^* S_{xy}$ , are not simply functional relationships (that is, if the total longshore transport is actually related to physical quantities expressed by  $P_{\ell b}$  and  $S_{xy}$ ) then one would expect less longshore transport than predicted

by linear theory for very shallow water waves (smaller  $h_b/L_0$ ). For a less shallow water wave (larger  $h_b/L_0$ ), one would expect that the total longshore transport is better predicted by linear theory. This of course overlooks the point that  $P_{\ell b}$  has no obvious physical meaning and assumes that the constants of proportionality,  $K$  and  $K^*$ , are actually treated as constants. Conversely, if  $K$  and  $K^*$  are not really constants and  $P_{\ell b}$  and  $S_{xy}$  are evaluated by linear theory as usual, then one would expect  $K$  and  $K^*$  to decrease with decreasing  $h_b/L_0$ .

As described in Chapter 2, however, the laboratory data of Kamphuis and Readshaw (1978), Vitale (1981), and Ozhan (1982) suggest that the opposite may be true. Each of these investigators found that the constants of proportionality  $K$  and  $K^*$  increase with increasing surf similarity parameter  $\xi_b = m/\sqrt{H_b/L_0}$ . Therefore, for a given beach slope  $m$ , if  $H_b$  is proportional to  $h_b$ ,  $K$  and  $K^*$  should increase with decreasing  $h_b/L_0$ .

This disagreement implies that either (i) the longshore transport is not related to the physical quantities expressed by  $P_{\ell b}$  and  $S_{xy}$ , or (ii) the dependence of the longshore transport upon the surf similarity parameter is significant enough to outweigh the non-linear vs. linear argument presented above. If the former is true, then the simple expression  $I_{\ell} = KP_{\ell}$  and  $I_{\ell} = K^*S_{xy}$  are only functional relations. If the latter is true, then one might expect that swash zone processes are even more significant to longshore sediment transport than has been previously recognized in the literature. That is, large values of the surf similarity parameter correspond to collapsing or surging conditions and imply larger values of  $K$  and  $K^*$  (i.e., greater longshore transport for given linear theory values of  $P_{\ell b}$  and  $S_{xy}$ ). Since most of the

longshore transport occurs at or above the shoreline for collapsing or surging cases, the efficiency of the longshore swash transport must be very high in order to produce relatively larger magnitudes of total transport. Likewise, it was found from the laboratory experiments that relatively less longshore transport occurs at or above the shoreline for spilling or spilling/plunging conditions (i.e., small surf similarity parameter). Since the  $K$  and  $K^*$  values are purportedly smaller for these conditions, relatively less longshore transport is expected (for given values of  $P_{\ell b}$  and  $S_{xy}$ ). It follows, then, that the total longshore transport decreases (for given  $P_{\ell b}$  and  $S_{xy}$ ) as the relative contribution of swash zone and near-shoreline longshore transport decreases. As an example, previous investigations have suggested that the value of  $K$  increases about five-fold from plunging/spilling to collapsing conditions (see Figure 2-5). From this study's laboratory investigation, the contribution of the swash transport to the total transport was similarly found to increase by about two- to three-fold from plunging/spilling to collapsing conditions. Hence, swash and inner surf zone longshore transport must play a central role in the determination of the total longshore transport.

It is of interest to note that the preferred longshore transport distribution model, described above as alternate model #3, implies that the total longshore transport is proportional to the surf similarity parameter or at least increases as the waves tend from spilling to collapsing conditions for a given value of  $P_{\ell b}$  for a planar beach. From Eq. (2.12), and assuming linear wave theory, straight and parallel depth contours, weak longshore current with no mixing,  $C_g = \sqrt{gh}$ , and that the local wave height is in constant proportion to the local water

depth,  $H=\kappa h$ , the longshore current profile is given by

$$v_{\ell} = \frac{5\pi}{16} \frac{g \kappa}{C_f} h \frac{dh}{dx} \left( \frac{\sin \alpha}{C} \right)_b \quad (8.34)$$

after Longuet-Higgins (1970). For the above assumptions the longshore sediment transport distribution from alternate model #3 (Eq. (8.22)) is given by

$$i_{\ell 3} = \frac{5}{16} k_3 \rho g^{3/2} \kappa^2 h^{1/2} \left( \frac{dh}{dx} \right)^{3/2} v_{\ell} \quad (8.35)$$

where set-up has been neglected. Combining Eqs. (8.34) and (8.35) and integrating from the shoreline to the breakpoint yields the total longshore transport in the surf zone. For a planar beach of slope  $m$ ,

$$I_{\ell 3} = \frac{5}{16} k_3 \frac{\pi g^{1/2} \kappa m^{3/2}}{C_f h_b^{1/2}} P_{\ell b} \quad (8.36)$$

where shallow water conditions and small wave angle have been further assumed such that  $\cos \alpha \approx 1$  and  $C_b = \sqrt{gh_b}$ . For a given value of  $P_{\ell b}$ , Eq. (8.36) implies that the total longshore transport (at least in the surf zone) should increase with increasing beach slope and decreasing breaking water depth. Since it is well known that the breaking wave condition tends from spilling to collapsing as the beach slope and breaking depth increase and decrease, respectively, Eq. (8.36) implies greater total transport for collapsing conditions compared to spilling conditions. Alternately, Eq. (8.36) may be written

$$I_{\ell 3} = K_3 P_{\ell b} \quad (8.37)$$

where

$$K_3 = \frac{5}{16} k_3 \frac{\pi\sqrt{2\pi} \kappa^{3/2}}{C_f} \frac{m}{T} \xi_b \quad (8.38)$$

As described by Eq. (8.38), correlation of the total transport proportionality constant  $K_3$  with the surf similarity parameter  $\xi_b$  appears when the wave period  $T$  is introduced. The correlation of the total longshore transport proportionality constant with the surf similarity parameter is consistent with the findings of other recent investigators as described in Chapter 2.

### 8.12.3 Shoreward Convection of Longshore Current by Wave Mass Transport

The longshore current profiles measured by Eulerian and Lagrangian methods in the field and laboratory, respectively, suggest that the longshore current is maximum near the shoreline. This is consistent with the longshore current profile predicted for a concave-up equilibrium beach shape (McDougal and Hudspeth, 1981) which was the characteristic beach shape of the field and laboratory conditions. However, the laboratory longshore current profiles appeared to be displaced shoreward from the break point relative to the profiles predicted by theory (see Chapter 9). This may be due to a shoreward convection of the longshore current associated with mass transport in the surf zone (a phenomenon originally suggested to this author by Robert Dean). Specifically, if both the horizontal wave orbital velocity  $u$  and an existing longshore current  $V_\ell$  are considered, the average flux in the onshore direction of the longshore component of momentum is given by

$$\hat{S}_{xy} = \int_0^{h+\eta} \rho u \cos\alpha (V_\ell + u \sin\alpha) ds \quad (8.39)$$

after Eq. (8.12), where  $s$  is oriented vertically upwards from the bed,  $\alpha$  is the local wave angle, and the over-bar denotes time-averaging. It is instructive to rewrite Eq. (8.39) in two terms

$$\hat{S}_{xy} = \overline{\int_0^{h+\eta} \rho u^2 \cos\alpha \sin\alpha ds} + \overline{\int_0^{h+\eta} \rho u V_\ell \cos\alpha ds} \quad (8.40)$$

Assuming that  $u$  is given by linear theory and that  $V_\ell$  is steady and uniform over depth, Eq. (8.40) becomes

$$\hat{S}_{xy} = \frac{1}{2} E n \sin 2\alpha + \frac{E}{C} V_\ell \cos\alpha \quad (8.41)$$

where only terms up to second order have been retained and use has been made of the expansions for the hyperbolic terms  $\cosh(k\eta)$  and  $\sinh(k\eta)$ . In Eq. (8.41) the first term is identical to the usual expression of the longshore radiation stress,  $S_{xy}$ . Recognizing that  $E/C$  is the mass transport, the second term (which is developed from the second integral of Eq. (8.40)) represents an onshore transport of the longshore current (or alternately, a longshore convection of the onshore component of wave mass transport). Physically, from an Eulerian viewpoint, the second term arises because the longshore current is assumed to exist up to the free surface; i.e., the longshore current exists above the wave trough level during passage of the crest (onshore particle motion), but does not always exist above the trough level during passage of the trough (offshore particle motion). Therefore, a net onshore movement of the near-surface longshore current is observed.

The implications of the second term in Eq. (8.41) are twofold. First, there is a shoreward displacement of the longshore current

profile (as was observed in the laboratory experiments). Second, longshore stresses may be convected towards shore thereby enhancing longshore transport near the shoreline. Specifically, the onshore component of the mass transport diffuses downwards through the water column and is returned seaward through an undertow which flows near the bottom. Nearshore, in very shallow depths, the mass transport which streams to the bottom to form the return flow includes a large component of longshore velocity (i.e., due to the shoreward convection of longshore current by the mass transport). If the longshore current is in reality concentrated near the surface (and not depth-uniform as originally assumed), then further from shore, in relatively deeper water, the near-bottom seaward return flow includes a smaller component of longshore velocity. If this conceptual model is valid, then the near-bottom return flow is rich in longshore current near the shoreline and relatively poorer in longshore current further offshore. Hence, the near-bottom longshore stress and longshore sediment transport are expected to be greater near the shoreline than near the outer surf zone.

It may also be argued intuitively that the downward diffusion of the shoreward-directed mass transport increases for steeper bed slopes since the vertical eddy diffusivity is generally thought to increase with increasing bed slope. Accordingly, the longshore current convected shoreward by the mass transport is more rapidly and/or effectively diffused towards the bed over steeper slopes. Therefore, longshore stress or longshore transporting capability is increased near the bed for regions of steep bed slope. This may explain the strong correlation between local bed slope and local longshore transport which is observed in the data and is reflected in the preferred distributed longshore transport model, Eq. (8.21).

The implications of the onshore convection of the longshore current are slightly different for the swash zone. The swash zone may be thought of as a "sink" for longshore stress which is convected shoreward and which has not been otherwise applied or returned seaward across the surf zone. Specifically, it is hypothesized that water particles entering the swash zone include a longshore component of velocity due to incomplete refraction of the translatory broken wave,  $u_s \sin \alpha_s$ , as well as longshore current which exists and/or is convected towards the shoreline,  $V_{ls}$ . (The subscript s refers to quantities at the shoreline.) The water particles therefore swash up and along the beachface with angle  $\alpha_{sw}$  to the shore-normal as illustrated in Figure 8-12 and where

$$\alpha_{sw} = \arctan\left( \tan \alpha_s + \frac{V_{ls}}{u_s \cos \alpha_s} \right) \quad (8.42)$$

Since it is typically observed in the laboratory and in nature that the backrush returns down the beach with an angle less than  $\alpha_{sw}$  to the shore-normal, longshore stress must be exerted upon the bed during the swash.

The contention that the near-shoreline longshore current is carried into the swash is supported by two sets of evidence. First, Lagrangian measurements in the laboratory experiments of this study indicate that the longshore current is continuous across the shoreline and is fairly uniform over at least the seaward half of the swash (for the uprush, anyways). Second, measurements made by this author near Virginia Beach, Virginia, in 1981 (unpublished) substantiate Eq. (8.42). In the Virginia Beach study, the uprush angle of the swash,  $\alpha_{sw}$ , and the angle

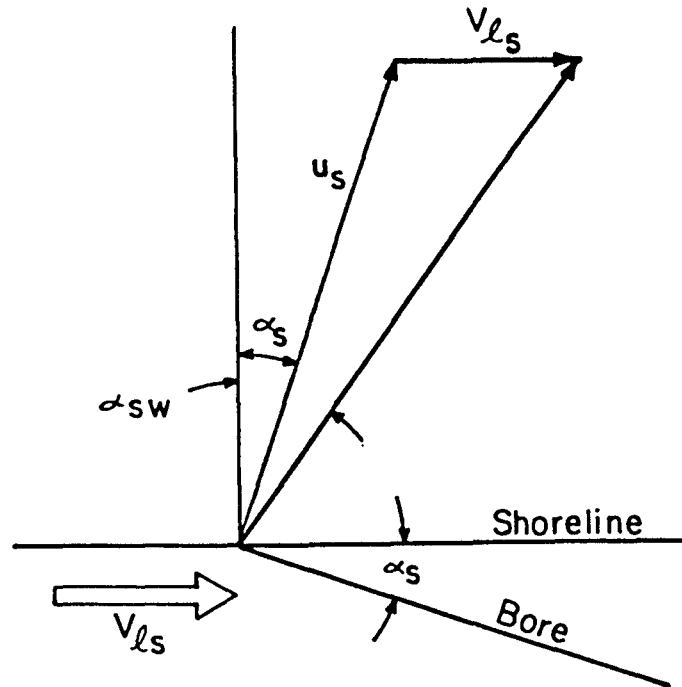


Figure 8-12: The uprush angle  $\alpha_{sw}$  for water particles entering the swash zone with velocity  $u_s$  associated with a bore arriving at the shoreline with angle  $\alpha_s$  in the presence of a near-shoreline longshore current  $v_{ls}$ .

which the bore made with the shoreline just before breaking,  $\alpha_s$ , were visually estimated with the aid of a compass and an array of stakes and tethered floating balls positioned across the beachface. The longshore current several meters from the shoreline was estimated by the along-shore rate of movement of a slightly buoyant sphere. The height of the bore at the shoreline,  $H_{bs}$ , was estimated using a meter stick just seaward of the shorebreak. With the assumption that the velocity of the bore at the shoreline can be approximated by  $u_s = \sqrt{gH_{bs}}$ , the uprush angle of the swash,  $\alpha_{sw}$ , was calculated from Eq. (8.42) for each set of measurements and was then compared to the measured angle. The results

from five data sets, collected over a large range of wave conditions and foreshore slopes, are listed in Table 8-1. On average, the agreement between the measured and calculated uprush swash angles is fairly good. At the least, the data clearly indicates that the uprush angle of the swash is greater than the angle which the arriving bore makes with the shoreline. This indicates that some or all of the near-shoreline longshore current must be convected and/or advected into the swash zone during the uprush. Due to the extreme turbulence of the shore break and

Table 8-1: Comparison of Swash Uprush Angle and Angle of Bore at the Shoreline.  
(From field data of Bodge, unpublished).

$H_{bs}$	$\alpha_s$ - bore	$V_{ls}$	$\alpha_{sw}$ - measured	$\alpha_{sw}$ - Eq.(8.42)
0.27 m	15°	0.20 m/s	27°	21.6°
0.13 m	17°	0.60 m/s	32°	41.0°
0.20 m	5°	0.35 m/s	12°	18.7°
0.25 m	10°	0.33 m/s	18°	21.3°
0.41 m	5°	0.28 m/s	13°	12.8°

the relatively thin layer of the swash, it is reasonable to assume that the longshore current is fairly depth-uniform throughout the swash. Hence, longshore stress is immediately and effectively applied to the bed during the swash.

In summary of this discussion, it appears that longshore transport near and above the shoreline may be particularly significant because of shoreward convection of the longshore current by the onshore component

of the waves' mass transport. This longshore current is more effectively diffused to the bed for shallower depths and steeper bed slopes. Some or all of the near-shoreline longshore current is carried into the swash zone during the uprush and represents a very effective longshore shearing and/or transporting agent because of the turbulence and shallow depths associated with the shorebreak and swash.

#### 8.12.4 Net Longshore Bottom Stress Induced by Non-Linear Wave Orbital Motion

A brief investigation was initiated to determine the relative contribution to the net longshore stress in the surf zone of both longshore currents and non-linear wave orbital motion. Longshore sediment transport is doubtlessly related to either or both components of the longshore stress, but perhaps not equally so.

The total longshore component of momentum flux which can be transferred to the surf zone bed is the total amount which enters the surf zone at the breakpoint,  $(S_{xy})_b$ . The average longshore shear stress across the surf zone width  $W$  is therefore  $(S_{xy})_b/W$ . Recognizing that the average bottom longshore shear stress is composed of both the mean longshore current contribution  $\overline{\tau_{V_\ell}}$  and the net non-linear orbital motion contribution  $\overline{\tau_u}$ , one may write

$$\frac{(S_{xy})_b}{W} = \overline{\tau_{V_\ell}} + \overline{\tau_u} \quad (8.43)$$

Equation (8.43) implies that an increase in the net non-linear wave orbital contribution to the bottom shear stress must be accompanied by a decrease in the longshore current (or at least a decrease in the bottom shear stress due to longshore current).

The relative contribution of the average net longshore bottom shear stress due to non-linear wave orbital motion to the total average bottom shear stress is given by

$$\frac{\overline{\tau_u}}{(\overline{S_{xy}})_b/W} \quad (8.44)$$

This ratio is liberally estimated if the maximum value of  $\overline{\tau_u}$  is taken (i.e., at the breakpoint) where

$$(\overline{\tau_u})_b = (\rho C_f \overline{|u|u} \sin\alpha)_b \quad (8.45)$$

where  $u$  is the bottom non-linear wave orbital velocity,  $C_f$  is a bed friction coefficient, and the over-bar denotes time-averaging. Assuming shallow water conditions, small angle of wave incidence, a beach profile of the shape  $h=Ax^{2/3}$  such that  $W=(h_b/A)^{3/2}$  and that the breaking wave height is related to the breaking depth by  $\kappa=H_b/h_b$ , the ratio of Eq. (8.44) is re-written

$$\frac{\overline{\tau_{u_b}}}{(\overline{S_{xy}})_b/W} = \frac{8 C_f (\overline{|u|u})_b}{\hat{\psi} g \kappa^2 A^{3/2} h_b^{1/2}} \quad (8.46)$$

where  $\hat{\psi}$  is a factor relating the non-linear quantity  $(\overline{S_{xy}})_b$  to the linear theory estimate of  $(S_{xy})_b$ . For stream function theory, from Figure 8-11,  $\hat{\psi}$  is typically between 0.2 and 1.0 in value.

Eq. (8.46) may be evaluated for stream function theory by multiplying through by  $C_b^2/C_b^2$ , where  $C_b^2 = gh_b$ ,

$$\frac{\overline{\tau_{u_b}}}{(\overline{S_{xy}})_b/W} = \frac{8 C_f \left( \left| \frac{u}{C} \right| \frac{u}{C} \sqrt{h} \right)_b}{\hat{\psi} \kappa^2 A^{3/2}} \quad (8.47)$$

The expression  $(u/C)_b$  may be re-written

$$\left(\frac{u}{C}\right)_b = \left(\frac{uT}{L}\right)_b = \frac{\left(\frac{u}{H/T}\right)_b}{\left(\frac{L}{L_0}\right)_b} \kappa \left(\frac{h}{L_0}\right)_b \quad (8.48)$$

where the stream function values of  $u/(H/T)$  and  $L/L_0$  at breaking are given for selected values of  $h/L_0$  in Dean (1974). Therein, the breaking condition is defined for  $\kappa=0.78$  ("case D"). For  $(h/L_0)_b = 0.002$  to  $0.1$ ,

$$\left[ \left| \frac{u}{C} \right| \frac{u}{C} \right]_b = 0.005 \quad (8.49)$$

where near-bottom non-linear wave orbital velocities are implied. Substitution of Eq. (8.49) into Eq. (8.47) yields

$$\frac{\overline{\tau_{u_b}}}{(S_{xy})_b/W} = \frac{0.066 C_f \sqrt{h_b}}{\hat{\psi} A^{3/2}} \quad (8.50)$$

Equation (8.50) suggests that the longshore stress contribution of the net non-linear bottom orbital velocities increases for larger, increasingly shallow-water waves and for more gently sloping beaches (i.e., smaller profile parameter  $A$ ). As an example, if  $\hat{\psi}=0.3$ ,  $A=0.2 \text{ m}^{1/3}$ ,  $h_b=2 \text{ m}$ , and  $C_f=0.02$ , Eq. (8.50) suggests that the net non-linear bottom orbital velocities at the breakpoint represent less than 7% of the total average longshore stress.

In general, it appears that the net non-linear wave orbital velocity contribution to the average longshore stress is typically small compared to the longshore current contribution. Accordingly, further investigation of the longshore sediment transport relationship to the fluctuating non-linear wave motion induced stress was not pursued.

## CHAPTER 9

### LONGSHORE CURRENT AND SEDIMENT TRANSPORT ACROSS A SET-UP NON-SINGULAR CONCAVE-UP BEACH

#### 9.1 Introduction

In this chapter, the wave induced set-up, longshore current, and longshore transport are considered for a concave-up equilibrium beach profile. For most existing expressions of the equilibrium beach profile, the beach slope at the shoreline is described as infinite. In many applications this leads to singularities at the shoreline. For the present study, a "non-singular concave-up equilibrium beach profile" is proposed which includes a planar foreshore of finite slope which is matched to the concave-up portion of the profile just below the mean water level. For brevity, the profile is termed a "non-singular equilibrium profile."

#### 9.2 Non-Singular Equilibrium Profile

Bruun (1954) and Dean (1977) have suggested that equilibrium beach profiles are described by the form

$$h = A x^{2/3} \tag{9.1}$$

as previously presented in Eq. (6.1), where Moore (1980) has shown that the dimensional parameter  $A$  is related to sediment size. A disadvantage of Eq. (9.1) is that the beach slope is infinite at the shoreline. Inspection of most natural and laboratory equilibrium profiles indicates that this is unrealistic. Instead, most profiles are characterized by a relatively planar beachface which extends from the berm to just below the mean low water level. Accordingly, a concave-up equilibrium beach profile is herein proposed which is not infinitely-sloped (i.e., singular) at the shoreline. The profile is characterized by a planar foreshore and an  $Ax^{2/3}$ -type profile seaward of the foreshore; namely,

$$h = \begin{cases} m_f x & x < x_m \\ A(x-\Delta)^{2/3} & x > x_m \end{cases} \quad (9.2)$$

as illustrated in Figure 9-1. The foreshore slope is characterized by  $m_f$ , and  $x_m$  is the distance from the shoreline to the "match point" where the planar foreshore and the concave-up, ( $Ax^{2/3}$ -type), beach profile intersect. Requiring that both the depth and the bed slope be continuous at the match point,

$$x_m = \frac{4 A^3}{9 m_f^3} \quad (9.3)$$

such that the shoreline "offset" of the concave-up portion of the profile must be

$$\Delta = \frac{x_m}{3} \quad (9.4)$$

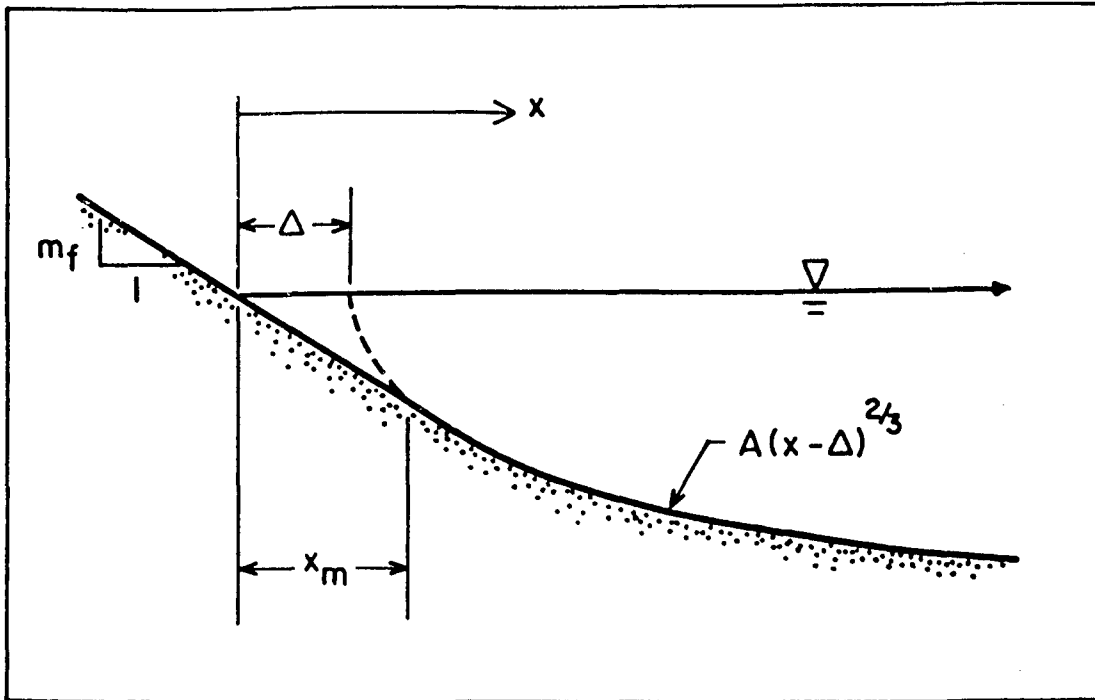


Figure 9-1: The "non-singular concave-up equilibrium beach profile."

In Figure 9-2, the average measured beach profiles from three of the laboratory test series are compared to non-singular equilibrium profiles. The latter were calculated using the average measured fore-shore slope  $m_f$  and the "design" value of the profile parameter  $A$  for the laboratory beach (described in Chapter 6). The three examples shown in Figure 9-2 are representative of all of the laboratory test series. It is seen that the non-singular equilibrium profiles are a reasonable representation of the average measured profiles. The slightly low elevations of the calculated non-singular equilibrium profiles (relative to the measured profiles) are due to the use of the "design" value of  $A$ . During the laboratory beach equilibration executed before each impoundment test, the nearshore portion of the beach profiles rotated about the shoreline slightly such that the profiles became more gently-sloped. Therefore, the value of the profile parameter  $A$  for the

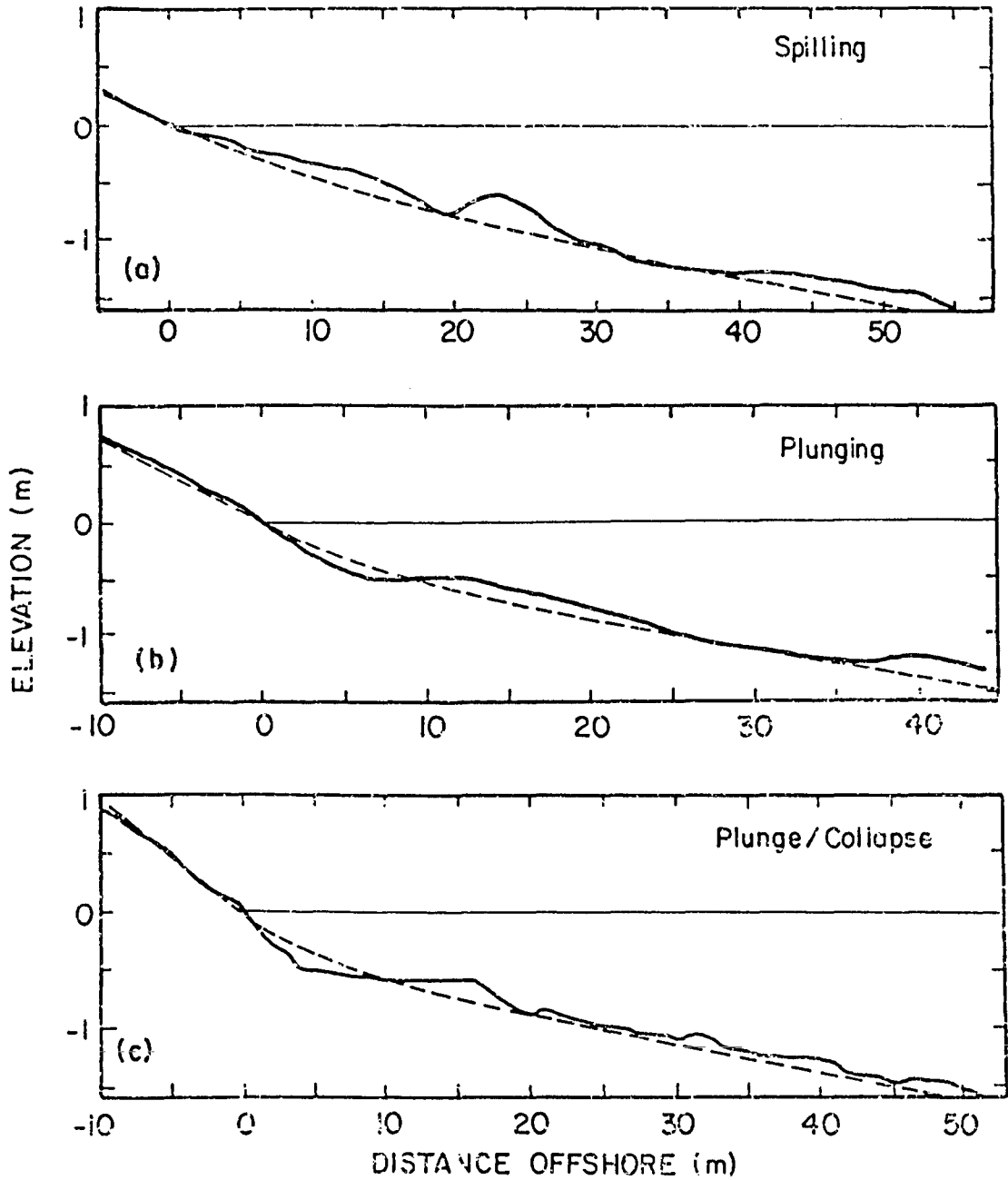


Figure 9-2: Comparison of average beach profiles from three of the laboratory test series with a non-singular equilibrium profile.

equilibrated beach became slightly smaller than the "design" value. (This was not completely surprising since the "design" value for A was slightly larger than the value suggested for the sediment size used in the laboratory model.)

### 9.3 Wave Induced Set-Up and Set-Down

The general expression for wave induced set-up and set-down,  $\overline{\eta'}$ , assuming constant proportion between local wave height and total water depth,  $H = \kappa d$ , was previously presented in Eq. (8.5). Evaluating this expression for the non-singular equilibrium profile, Eq. (9.2), yields

$$\overline{\eta'} = \begin{cases} \left[ v \left( 1 - \frac{m_f x}{A x_b^{2/3}} \right) - \frac{\kappa^2}{16} \right] A x_b^{2/3} & x_o < x < x_m \\ \left[ v \left( 1 - \frac{(x-\Delta)^{2/3}}{x_b^{2/3}} \right) - \frac{\kappa^2}{16} \right] A x_b^{2/3} & x_m < x < x_b \\ \frac{-H^2 k}{8 \sinh 2kh} & x > x_b \end{cases} \quad (9.5)$$

where  $k$  is the wavenumber, and

$$v = \frac{3 \kappa^2}{8 + 3\kappa^2} \quad (9.6)$$

In Eq. (9.5), as well as in all expressions which follow, the concave-up profile offset  $\Delta$  is assumed to be small relative to the breaking distance  $x_b$  such that

$$x_b = (h_b/A)^{3/2} \quad (9.7)$$

This leads to slight discontinuities at the breakpoint  $x_b$  which become increasingly significant as the profile match point  $x_m$  approaches  $x_b$ . (For the laboratory data of this study,  $x_m < 0.3x_b$  for all cases.) In Eq. (9.5), the location  $x_0$  is the landward limit of set-up for which  $\overline{\eta'} = -m_f x_0$ , i.e.,

$$x_0 = \frac{\left(u - \frac{\kappa^2}{16}\right) h_b}{(u-1) m_f} \quad (9.8)$$

The total water depth,  $d = h + \overline{\eta'}$ , across the non-singular equilibrium profile is given by

$$d = \begin{cases} \left(u - \frac{\kappa^2}{16}\right) h_b + (1-u) m_f x & x_0 < x < x_m \\ \left(u - \frac{\kappa^2}{16}\right) h_b + (1-u) A(x-\Delta)^{2/3} & x_m < x < x_b \\ A(x-\Delta)^{2/3} - \frac{H^2 \kappa}{8 \sinh 2kh} & x_b < x \end{cases} \quad (9.9)$$

McDougal and Hudspeth (1981) found that the best least-squares fit to the total water depth  $d$  across a beach profile completely characterized by  $h = Ax^{2/3}$  is:

$$d = AB x^{1/2} \quad (9.10)$$

where  $B/x_b^{1/6} = 0.949$  for  $0 < x < x_b$ . In Figure 9-3 the calculated total water depth profile for the complete  $Ax^{2/3}$ -type beach is compared to the approximation, Eq. (9.10). The fit is generally good for  $x/x_b > 0.15$ , but deteriorates towards the shoreline as one might expect since  $d$  is

non-zero at  $x=0$  in reality--whereas  $d$  tends to zero at  $x=0$  in the approximation, Eq. (9.10).

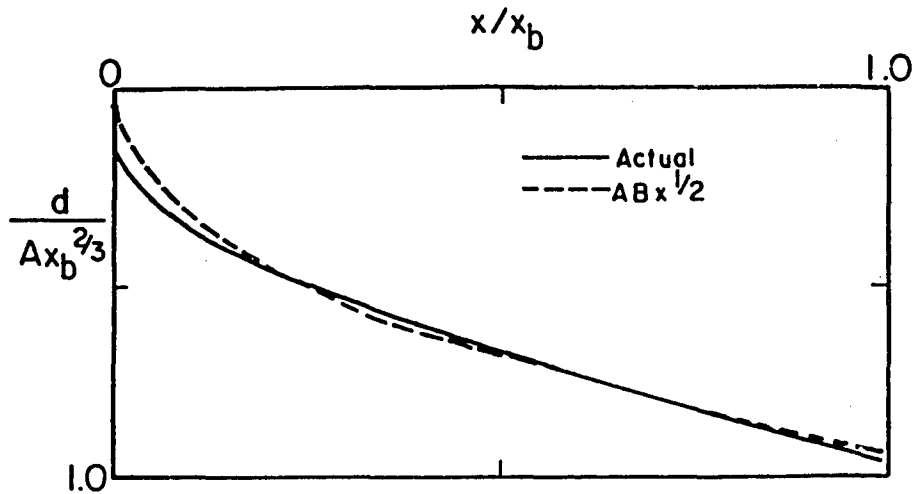


Figure 9-3: The calculated total water depth across the surf zone for an  $h=Ax^{2/3}$ -type beach profile compared with the approximation  $d=ABx^{1/2}$ . (Adapted from McDougal and Hudspeth, 1981).

If Eq. (9.10) is taken as the approximate total water depth over the concave-up portion of the non-singular equilibrium profile, and the "actual" predicted total water depth is taken over the planar foreshore portion (Eq. (9.9) for  $x_0 < x < x_m$ ), then the poor fit of Eq. (9.10) near the shoreline becomes irrelevant. That is, for most cases, the region of poor fit for the approximation  $d=ABx^{1/2}$  is located over the planar foreshore section of the non-singular equilibrium profile--for which the "actual" predicted total water depth can be used in lieu of the approximation. Therefore, the total water depth across the non-singular equilibrium profile is well approximated by

$$d \approx \begin{cases} m_f(1-u)(x-x_0) & x_0 \leq x < x_m \\ AB(x-\hat{\Delta})^{1/2} & x_m \leq x < x_b \\ A(x-\hat{\Delta})^{2/3} - \frac{H^2 k}{8 \sinh 2kh} & x_b \leq x \end{cases} \quad (9.11)$$

where  $B$  and  $\hat{\Delta}$  are determined so as to ensure continuous total water depth and mean surface slope at the profile match point  $x_m$ ; that is,

$$B = \frac{\sqrt{2}}{A} (1-u) m_f \sqrt{x_m - x_0} \quad (9.12a)$$

$$\hat{\Delta} = \frac{1}{2} (x_m + x_0) \quad (9.12b)$$

A similar matching constraint is not imposed at the breakpoint; however, the consequent discontinuity in the total water depth at this point is typically small for most cases of practical interest.

#### 9.4 Longshore Current

Longuet-Higgins (1970) and McDougal and Hudspeth (1981), respectively, presented solutions for the wave induced longshore current over planar beach profiles and concave-up ( $d=ABx^{1/2}$ ) beach profiles. Both solutions assume shallow water wave conditions within the surf zone, small angle of wave incidence, straight and parallel depth contours, a linear expression for the bottom shear stress, constant proportion between local wave height and total water depth,  $H=kd$ , and include lateral mixing where the eddy viscosity is assumed to be proportional to a characteristic velocity and a turbulent mixing length. Following the

non-dimensional presentations of these authors, all quantities of length are non-dimensionalized by the breaker distance,  $x_b$ , while all quantities of velocity are non-dimensionalized by the no-mixing planar beach velocity at the breaker line,  $V_{\ell b}$ . From Longuet-Higgins (1970),

$$V_{\ell b} = \frac{5}{16} \frac{\pi \kappa}{c_f} d s \sqrt{g d_b} \sin \alpha_b \quad (9.13)$$

where  $s$  is the planar beach slope including set-up.

Making direct use of the Longuet-Higgins and McDougal and Hudspeth solutions for the planar foreshore and concave-up portions of the profile, respectively, the longshore current across the non-singular equilibrium profile (including set-up) is given by

$$v'_\ell = \begin{cases} B_1 (x' - x'_0)^{P_1} + A_1 (x' - x'_0) & x'_0 < x' < x'_m \\ \frac{C_1}{\gamma^2} \left[ \frac{\gamma \cosh(\gamma(x' - \hat{\Delta}')^{1/4})}{(x' - \hat{\Delta}')^{1/2}} - \frac{\sinh(\gamma(x' - \hat{\Delta}')^{1/4})}{(x' - \hat{\Delta}')^{3/4}} \right] + \frac{1}{2} & x'_m < x' < 1 \\ C_2 \left[ \frac{1}{(x' - \hat{\Delta}')^{1/2}} + \frac{1}{\gamma(x' - \hat{\Delta}')^{3/4}} \right] e^{-\gamma(x' - \hat{\Delta}')^{1/4}} & x' > 1 \end{cases} \quad (9.14)$$

where the prime notation denotes non-dimensional terms, such as  $x' = x/x_b$  and  $v'_\ell = v_\ell/V_{\ell b}$ , and where

$$P_1 = \frac{-3}{4} + \left( \frac{9}{16} + \frac{1}{P} \right)^{1/2}; \quad P \neq \frac{2}{5} \quad (9.15)$$

$$C_1 = \frac{-1}{2} \left( \gamma + 3 + \frac{3}{\gamma} \right) e^{-\gamma} \quad (9.16)$$

$$C_2 = \frac{1}{2} \left[ \left( 1 + \frac{3}{\gamma^2} \right) \sinh \gamma - \frac{3}{\gamma} \cosh \gamma \right] \quad (9.17)$$

and

$$\gamma = 4/\sqrt{P_2} \quad (9.18)$$

The term  $P$  is the familiar longshore current mixing parameter from Longuet-Higgins (1970),

$$P = \frac{N\pi s}{C_f \kappa} \quad (9.19)$$

except that the slope  $s$  includes the effect of set-up as described earlier. For the planar foreshore (for which Longuet-Higgins' solution was utilized),

$$s = (1-\nu)m_f \quad (9.20)$$

A separate expression of the mixing parameter,  $P_2$ , comes about because the planar (set-up) slope  $s$ , above, is replaced by  $AB$  for the  $ABx^{1/2}$  portion of the profile. Accordingly, from Eqs. (9.3), (9.8), (9.12a), (9.19), and (9.20),

$$P_2 = \sqrt{2(x'_m - x'_0)} P \quad (9.21)$$

The constants  $C_1$  and  $C_2$  were presented by McDougal and Hudspeth such that the longshore current is continuous across the breakpoint ( $x'=1$ ). However, because of the  $x$ -axis offsets  $\Delta$  and  $\hat{\Delta}$  for the concave-up portion of the non-singular equilibrium beach, a discontinuity in the longshore current exists at the breakpoint for Eqs. (9.14), (9.16), and (9.17), as written. As mentioned previously, this discontinuity is typically small, but becomes more apparent as the match point  $x_m$  approaches  $x_b$ .

The constants  $B_1$  and  $A_1$  are evaluated by requiring that the magnitude and gradient of the longshore current be continuous across the profile match point,  $x_m$ . From Eq. (9.14),

$$B_1 = \frac{Y_1 - Y_2 (x'_m - x'_o)}{(1-p_1) (x'_m - x'_o)^{p_1}} \quad (9.22a)$$

$$A_1 = Y_2 - p_1 B_1 (x'_m - x'_o)^{p_1 - 1} \quad (9.22b)$$

where

$$Y_1 = \frac{C_1}{\gamma^2} \left[ \frac{\gamma \cosh(\gamma(x'_m - \hat{\Delta}')^{1/4})}{(x'_m - \hat{\Delta}')^{1/2}} - \frac{\sinh(\gamma(x'_m - \hat{\Delta}')^{1/4})}{(x'_m - \hat{\Delta}')^{3/4}} \right] \quad (9.23)$$

$$Y_2 = \frac{C_1}{\gamma^2} \left[ \frac{3 + \gamma^2 (x'_m - \hat{\Delta}')^{1/2} \sinh(\gamma(x'_m - \hat{\Delta}')^{1/4})}{4 (x'_m - \hat{\Delta}')^{7/4}} - \frac{3\gamma \cosh(\gamma(x'_m - \hat{\Delta}')^{1/4})}{4 (x'_m - \hat{\Delta}')^{3/2}} \right] \quad (9.24)$$

The solution for  $A_1$  and  $B_1$  as given above is tedious; however, the solutions can be parameterized in terms of  $x_m/x_b$  for various values of the mixing parameter,  $P$ . Specifically, from Eqs. (9.3) and (9.7),

$$\frac{x_m}{x_b} = \frac{4 A^{9/2}}{9 m_f^3 h_b^{3/2}} \sim \frac{A^{9/2}}{m_f^3 h_b^{3/2}} \equiv \Pi \quad (9.25)$$

where  $\Pi$  is a similarity parameter. In Figure 9-4, computed values of the constants  $A_1$  and  $B_1$  are presented graphically as a function of the term  $\Pi$ , defined above, and for selected values of the mixing parameter  $P$ . Note that the longshore current equations were not developed for the special case of  $P = 0.4$ . For the case of no lateral mixing,  $P = 0$ ,  $V'_l = 0.5$  for  $x'_m < x' < 1$ , and decreases linearly to zero from  $x'_m$  to  $x'_o$ .

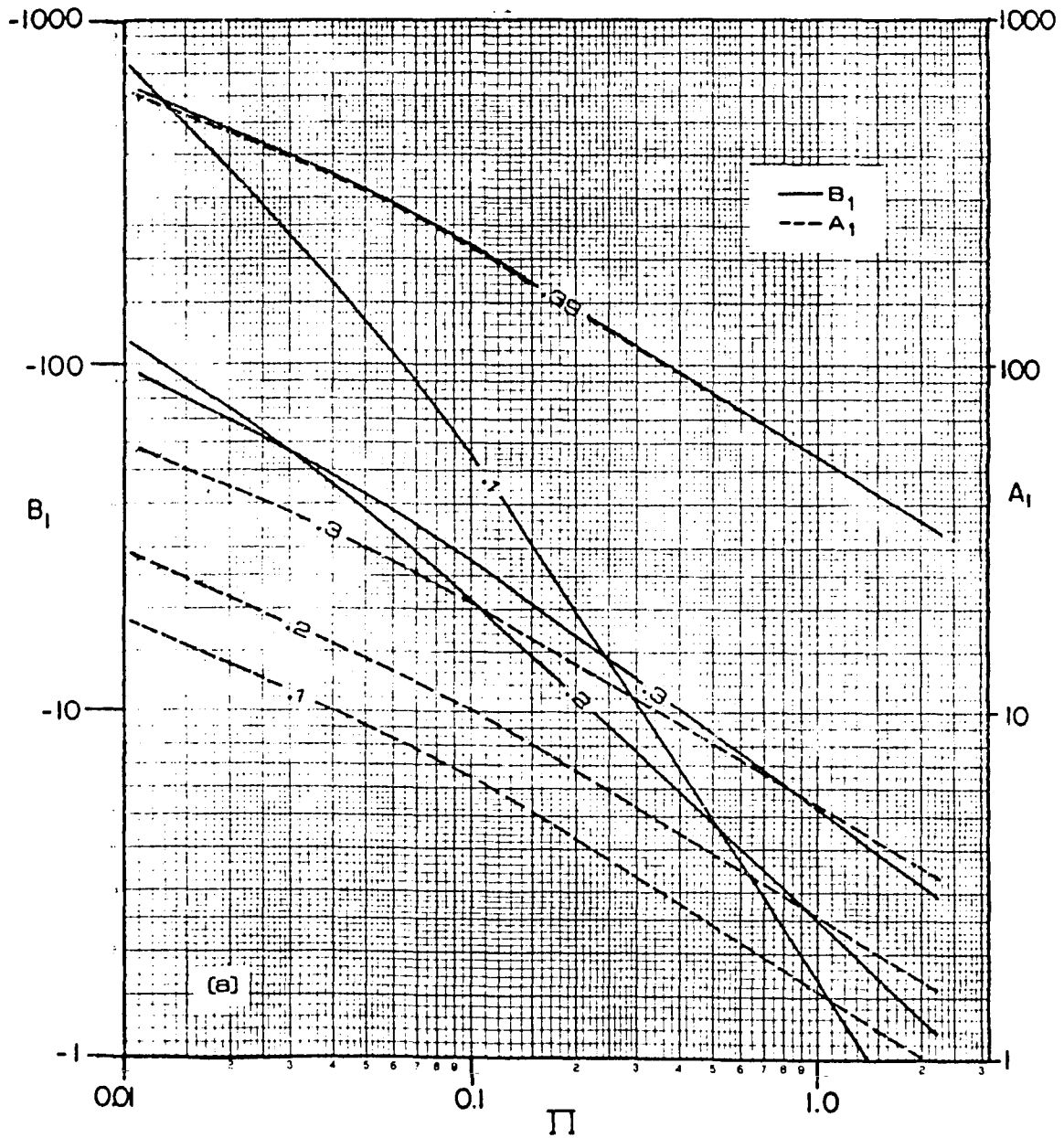


Figure 9-4: Coefficients  $A_1$  and  $B_1$  of the longshore current expression for the planar foreshore portion of the non-singular equilibrium beach profile. Numbers on curves represent values of the mixing parameter  $P$ ; (a)  $0.1 < P < 0.4$ , and (b)  $0.4 < P < 1$ , (next page).

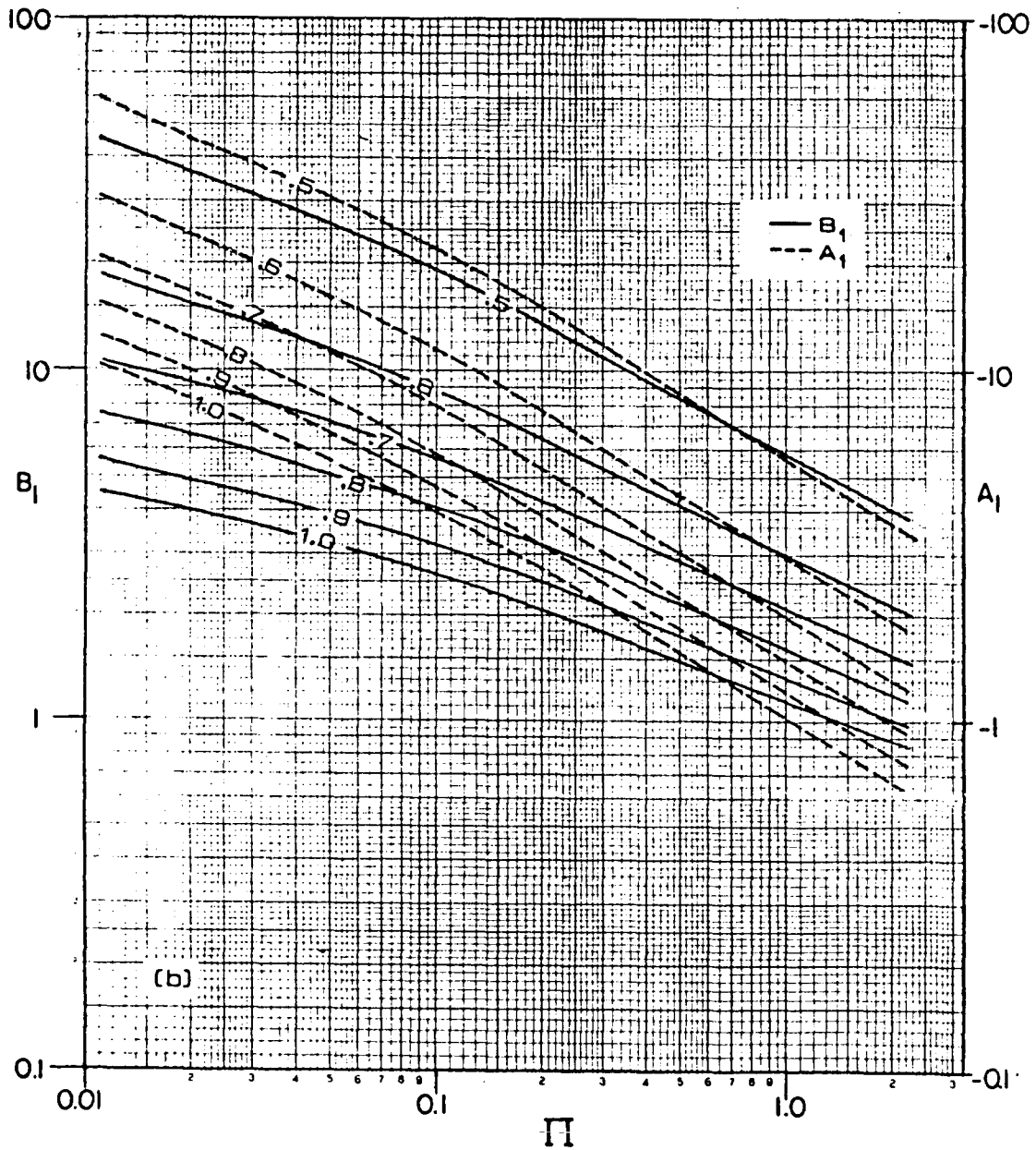


Figure 9-4: Continued from previous page.

It is also noted that the results for the non-singular equilibrium profile described here are not valid if the profile match point  $x_m$  is seaward of the breakpoint  $x_b$ ; that is, if  $x_m > x_b$ . From Eq. (9.25), for the requirement  $x_m/x_b < 1$ ,

$$\Pi < 2.25$$

(9.26)

Physically, Eq. (9.26) is a condensed expression of the requirement that the planar foreshore and the concave-up portions of the profile must intersect shoreward of the breakpoint. Obviously, if the intersection is seaward of the breakpoint, the entire surf zone may be modelled as for a planar beach. For the quasi-equilibrated profiles of this study's laboratory tests,  $0.06 < x_m/x_b < 0.28$  and  $0.08 < \Pi < 0.77$ .

#### 9.5 Comparison of the Predicted Longshore Current with Laboratory Observations

The model for the (normalized) longshore current across a non-singular equilibrium profile, Eq. (9.14), was evaluated for the prototype scale conditions of each of the laboratory test series. Specifically, the characteristic foreshore slope  $m_f$  and breaking depth  $h_b$  were taken from the data of each laboratory test series, and the profile parameter  $A$  was taken as the prototype-scale "design" beach profile value. The wave height to total water depth ratio  $\kappa$  was taken as 0.8. These four parameters, as well as an estimate of the mixing parameter,  $P$ , are all that are necessary for evaluation of the normalized longshore current model. It is noted that for the plunging/spilling test, the average breaking depth was taken between the inner and outer breakpoint locations.

In Figure 9-5, the normalized longshore current profiles calculated by Eq. (9.14) are compared to the normalized measured profiles from the laboratory tests (estimated from Lagrangian dye tracking). The measured longshore current profiles were scaled to the prototype and normalized

by  $V_{\ell b}$  for the conditions of each test series. Specifically, the slope  $s$  in  $V_{\ell b}$  (Eq. (9.13)) was taken as  $d_b/x_b$ , and the friction coefficient  $C_f$  was selected such that the maximum surf zone value of the normalized longshore current was equal to 0.5 for each test (i.e., the no lateral-mixing value). For this approach, the prototype scale values of  $C_f$  were found to be fairly reasonable; that is,  $0.05 < C_f < 0.15$ . The ratios  $s/C_f$  and  $m_f/C_f$  were found to vary over a range of 0.6 to 2 and 0.8 to 3.3, respectively.

From inspection of Figure 9-5, it is evident that the calculated longshore current profiles are fairly good representations of the observed laboratory profiles for a mixing parameter  $P \approx 0.05$  to 0.1. However, two major differences are evident between the observed and calculated longshore current profiles. First, the observed laboratory profiles are shifted shoreward by about  $0.2x_b$  relative to the calculated profiles. Second, the observed longshore current is relatively uniform across the shoreline and at least the lower swash zone, whereas the calculated longshore current decreases sharply to zero from the profile match point to the shoreward limit of set-up. These two features, respectively, may be indicative of (i) onshore movement of the longshore current by mass transport, and (ii) convection and/or advection of the near-shoreline longshore current into the swash zone by uprushing water particles. Each of these ideas has been discussed previously in Section 8.12.3. Additionally, the shoreward-shift of the observed longshore current profile may be associated with a lag in the initiation of the longshore current. Bowen, Inman, and Simmons (1968) and Battjes (1972) among others, have each reported a similar lag in the initiation of set-up. Svendsen (1984) and Battjes and Stive (1985) suggest that this is

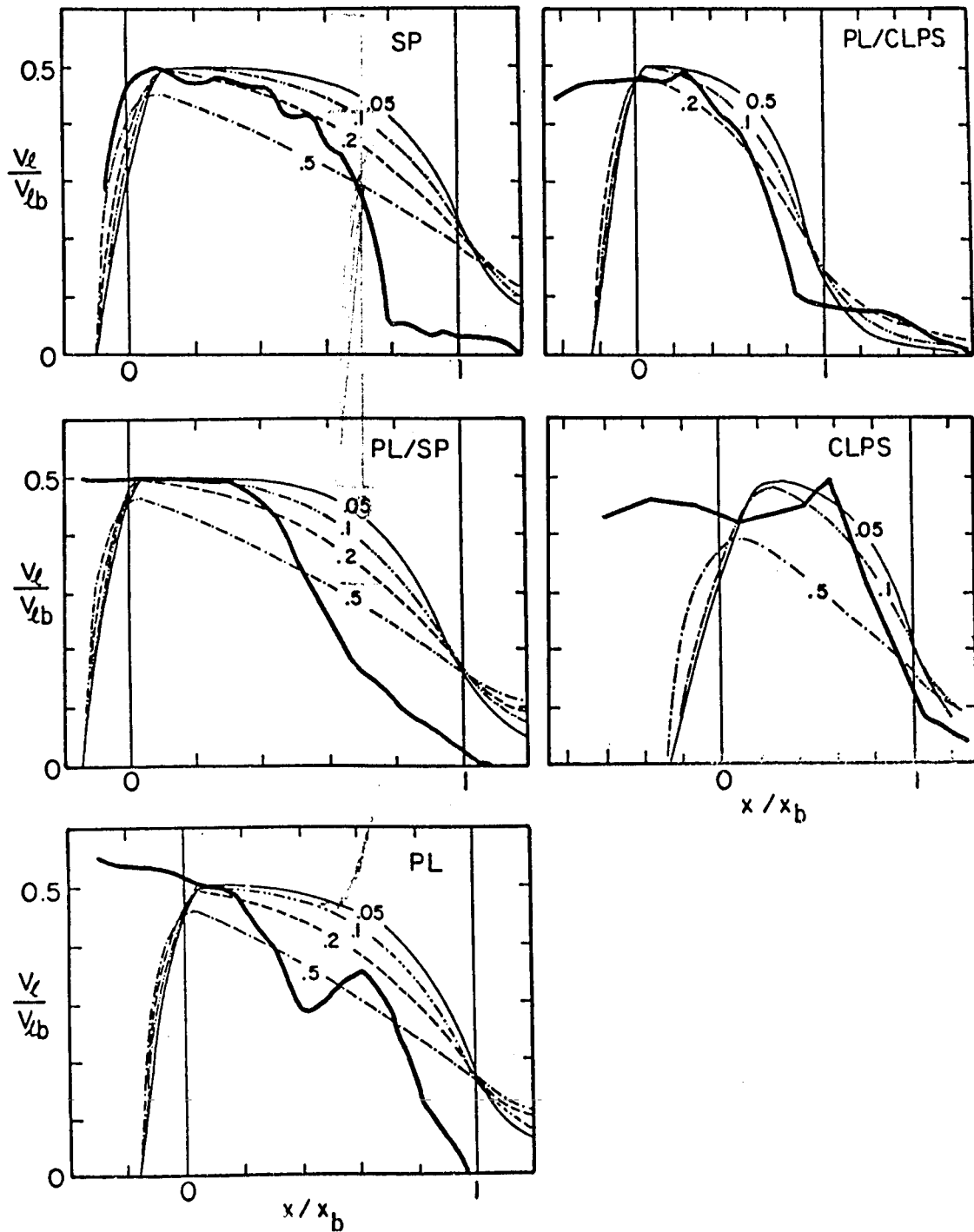


Figure 9-5: Normalized (Lagrangian) measured longshore current across the surf zone from the laboratory test series (bold) compared to the calculated longshore current for a non-singular equilibrium beach profile for various values of the mixing parameter  $P$  (light).

because energy originally represented by the initial breaking wave height is converted to organized and/or turbulent kinetic energy through the water column--and is not all immediately dissipated. Since both longshore current and set-up are associated with radiation stress, it may not be unexpected that the longshore current should show an initiation lag which is similar to that of set-up.

The absence of longshore current seaward of the breakpoint and the related low value of the mixing parameter observed for the laboratory data may also be partly due to the finite longshore end conditions of the laboratory beach. The longshore current measurements from the field experiments contain considerable scatter and are somewhat incomplete across the beach; however, they suggest greater lateral mixing than found for the laboratory data. Figure 9-6 illustrates the normalized longshore current measured during the two "best" field impoundment intervals compared to the calculated longshore current for non-singular equilibrium beach profiles fit to the average field beach profiles. Overall agreement between the measured and calculated longshore current profiles is fair to poor. However, it is recalled that the quality of the measured longshore current distributions developed from the field data is questionable.

In light of the laboratory-observed longshore current features described above, it may be appropriate to shift the calculated longshore current profiles (predicted by Eq. (9.14)) shoreward by about  $x'=0.2$ . Additionally, the longshore current within the swash zone may be better described, for now, as uniform and equal in value to the shoreward-shifted longshore current predicted at the shoreline. With these empirically-based modifications, the "adjusted" normalized longshore

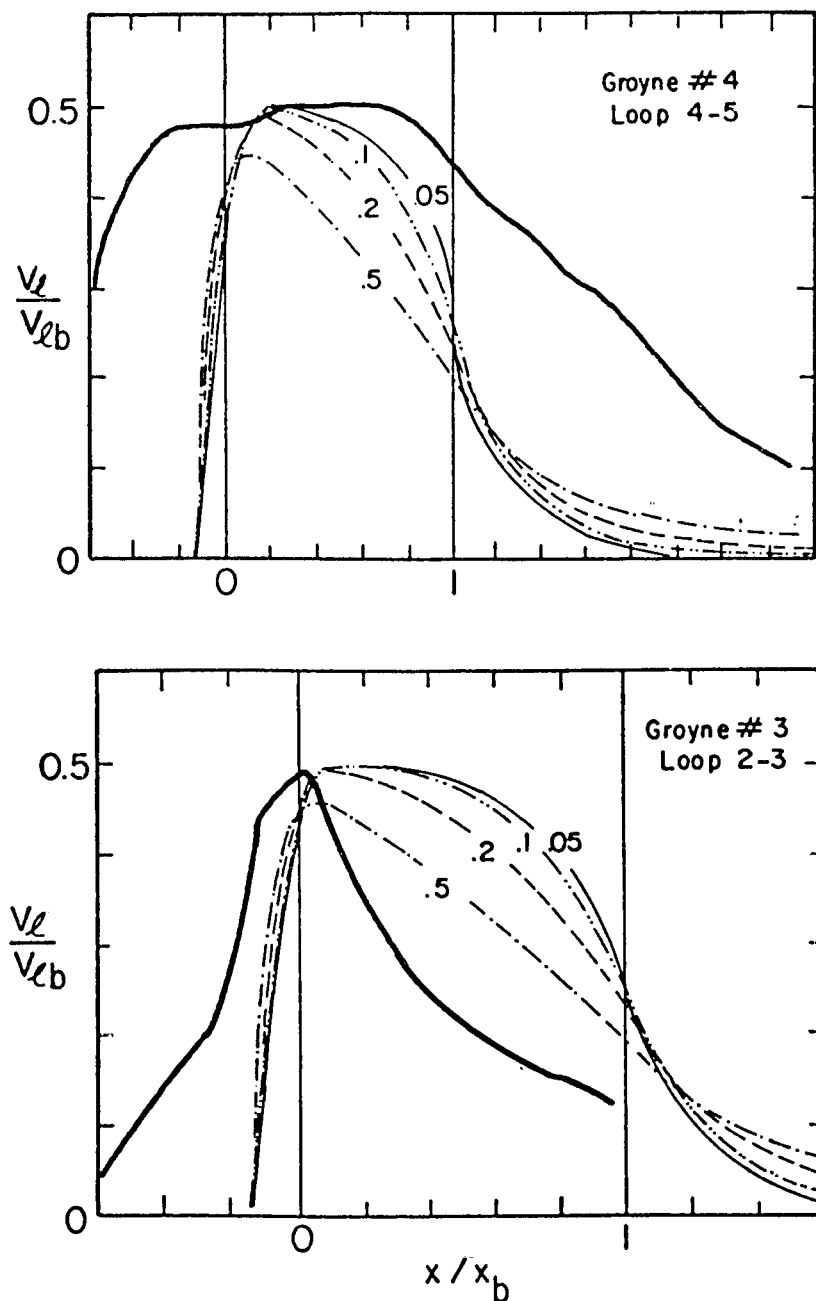


Figure 9-6: Normalized (Eulerian) measured longshore current across the surf zone from the two "best" field impoundment experiments (bold) compared to the calculated longshore current for a non-singular equilibrium beach profile (light). Numbers on the curves represent values of the mixing parameter P. The quality of the measured longshore current data is questionable.

current profile  $\tilde{V}'_l$  is written in terms of  $V'_l$  from Eq. (9.14) as

$$\tilde{V}'_l(x') = \begin{cases} V'_l(0) & x'_0 < x' < 0 \\ V'_l(x' + 0.2) & 0 < x' \end{cases} \quad (9.27)$$

In his surf zone modelling expressions, Svendsen (1984) uses a somewhat similar approach by "delaying" calculation of the set-up and wave decay within the surf zone to a location just landward of the breakpoint.

#### 9.6 Swash on a Planar Beachface

The results of the present and some previous investigations indicate that the swash zone is of potentially great significance to the total and distributed longshore sediment transport. Therefore, a reasonable three-dimensional swash model is pertinent to the consideration of longshore transport. Expressions or characteristic solutions of the cross-shore, two-dimensional swash motion have been presented by Keller, Levine, and Whitman (1960), Shen and Meyer (1963), Freeman and LeMehaute (1964), Meyer and Taylor (1972), Waddell (1973), Kemp and Plinston (1974), Wang and Yang (1980), and Mizuguchi (1984), among others. The former four models are non-linear and are typically evaluated numerically. The latter four are analytic but do not directly address the effect of the sloping swash surface nor the singularities associated with the shorebreak of the bore (see Meyer and Taylor, 1972). It is thought by this author that consideration of the free surface slope of the swash allows more realistic modeling of the fluid acceleration up the beachface after the shoreline collapse of the bore; additionally, it can lead to run-up predictions which more closely match available data. Regarding the latter point, models which do not

directly consider the slope of the swash across the beachface typically require unrealistic "amplification" of the initial particle velocities (usually assumed equal to the incident bore speed) in order to achieve measured run-up levels (e.g., Waddell, 1973).

The equations of motion, and some considerations thereof, for swash across and along a planar beachface are presented in Appendix F. Analytic (or at least transcendental) expressions for the depth-averaged velocity field and local instantaneous swash depth are potentially achievable from the proposed equations. However, to date, attempts by this author to properly describe all of the terms and subsequently solve the equations have not been satisfactory. Therefore, for present, the swash height and longshore velocity across the swash is simplistically assumed as described in the next section.

### 9.7 Longshore Sediment Transport

Alternate model #3, the preferred distributed longshore transport model, may be expressed as follows

$$i_{\ell} = \frac{1}{8} k_3 \rho g^{3/2} \frac{1}{d} \frac{d}{dx} (H^2 \sqrt{d}) v_{\ell} \left( \frac{d(d)}{dx} \right)^{3/2} \quad (9.28)$$

from Eq. (8.21), where shallow water conditions have been assumed. It is convenient to normalize Eq. (9.28) by the local longshore transport calculated at the breakpoint, where it is assumed that  $H_b = \kappa d_b$  and  $V_{\ell}$  is the no-mixing planar beach longshore current  $V_{\ell b}$ , as described previously by Eq. (9.13). Normalized as such, Eq. (9.28) becomes

$$i'_l = \frac{2}{5\kappa^2 d \sqrt{d_b}} \frac{d}{dx} (H^2 \sqrt{d}) v'_l \frac{\sqrt{d(d)/dx}}{(d(d)/dx)_b^{3/2}} \quad (9.29)$$

Assuming that the local wave height is in constant proportion to the local total water depth across the entire beach (consistent with the development of the set-up and longshore current expressions), Eq. (9.29) becomes

$$i'_l = \left(\frac{d}{d_b}\right)^{1/2} v'_l \left[\frac{d(d)/dx}{(d(d)/dx)_b}\right]^{3/2} \quad (9.30)$$

Of course, Eq. (9.30) does not describe swash zone contributions adequately because no transport is predicted landward of the mean (set-up) water line.

Equation (9.30) was evaluated for the non-singular equilibrium profile using Eqs. (9.11) and (9.14) as expressions of the total water depth and the normalized longshore current, respectively. (Note that Eq. (9.14) is not the shoreward-shifted longshore current profile.) The resulting estimates of the normalized longshore transport distributions are illustrated in Figure 9-7 for (a) different values of the mixing parameter  $P$  for a given profile, and (b) different values of the profile similarity parameter  $\Pi$  for a given mixing parameter. The transport peaks correspond to the intersection of the planar foreshore and concave-up portions of the profiles. This is not unexpected since immediately seaward of this intersection (or match point) the longshore current and the gradient of the total water depth are maximum. Landward of the match point, the gradient in the total water depth is constant, but the longshore current rapidly decreases towards shore (all according

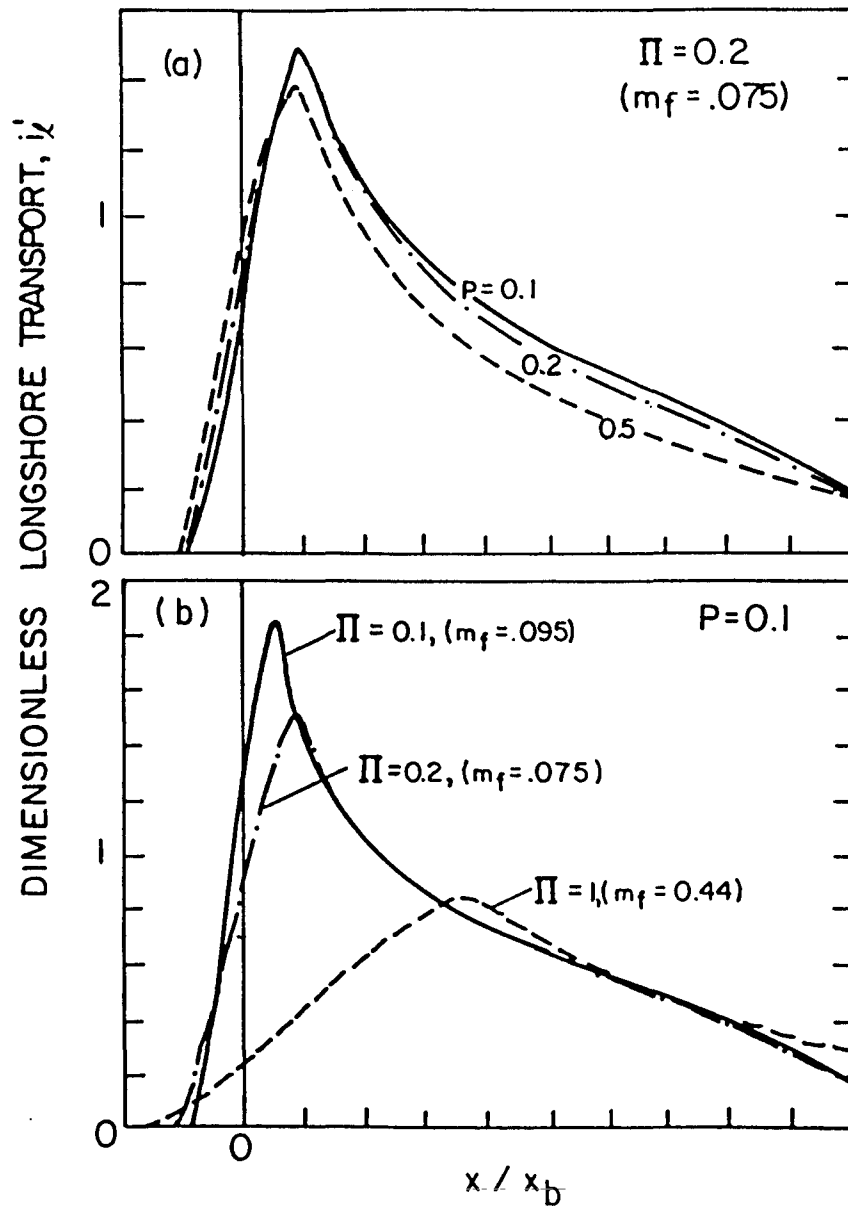


Figure 9-7: Dimensionless longshore transport across the surf zone for a non-singular equilibrium beach profile for (a) fixed profile similarity parameter  $\Pi$  and various longshore current mixing parameters  $P$ , and (b) fixed  $P$  and various values of  $\Pi$ . Evaluated for  $A=0.15 \text{ m}^{1/3}$ ,  $h_b=1.75 \text{ m}$ , and without inclusion of swash.

to the assumed expressions for the water depth and current). Therefore, the maximum transport is expected about the match point since the preferred model suggests that the local longshore transport increases with the local longshore current and gradient in total water depth.

The results shown in Figure 9-7b are interesting because they indicate that for a milder-sloped beachface (all other conditions equal), the peak transport shifts seaward and the total transport decreases. Since it is recognized that the beachface often flattens somewhat during an erosive storm event, one might expect that the longshore transport maxima is shifted further seaward during a storm event such that near shoreline contributions to the total transport become smaller. (However, one should not simultaneously presume that the total transport for a given energy level is decreased in a storm--since the simple evaluation here does not include the effects of a storm-related bar nor increases in turbulence which may mobilize additional sediment for transport.)

The preferred distributed longshore transport model was also evaluated for a crude inclusion of the swash zone. For this case, the local wave height was again assumed to be in constant proportion to the local water depth--but only over the concave-up portion of the profile. Over the planar foreshore, the wave height was assumed to decrease linearly from the value at the match point to zero at the shoreward limit of runup. Concisely,

$$H = \begin{cases} \kappa d_m (x-x_r)/(x_m-x_r) & x_r < x < x_m \\ \kappa d & x_m < x < x_b \end{cases} \quad (9.31)$$

where  $d_m$  is the total water depth at the intersection of the concave-up

and planar portions of the profile (i.e., the match point), and  $x_r$  is the shoreward limit of runup. (For illustrative purposes only,  $x_r$  was assumed to be  $2x_0$ .) Incorporating Eq. (9.11) with Eq. (9.31), the local wave height across the profile was expressed

$$H = \begin{cases} \kappa AB (x_m - \hat{\Delta})^{1/2} \frac{(x - x_0)}{(x_m - x_0)} & x_0 < x < x_m \\ \kappa AB (x - \hat{\Delta})^{1/2} & x_m < x < x_b \end{cases} \quad (9.32)$$

The longshore current profile was assumed to follow Eq. (9.27). It is recalled that this is the shoreward-shifted expression which also describes uniform longshore current across the swash zone that is equal in magnitude to the value calculated at the shoreline. The total water depth was assumed to follow Eq. (9.11) as before. Because the local wave height was not assumed proportional to the local depth over the planar portion of the profile, the more general form of the preferred longshore transport model (Eq. (9.29)) was utilized to calculate the local longshore transport shoreward of the match point, where the total depth  $d$  was replaced by  $d+H$  in order to avoid singularities above the mean water line. Eq. (9.30) was suitable for evaluation seaward of the match point.

In Figure 9-8, the normalized longshore transport distributions, calculated as described above, are illustrated for the cases shown in Figure 9-7. As expected, the longshore transport is less near the breakpoint and enhanced above the shoreline relative to the results shown in Figure 9-7 for the case which excluded the swash zone. Although the maximum longshore current occurs at or above the shoreline, the peak transport is still observed at the profile match point primarily because the gradient in wave height is relatively small landward of the match point.

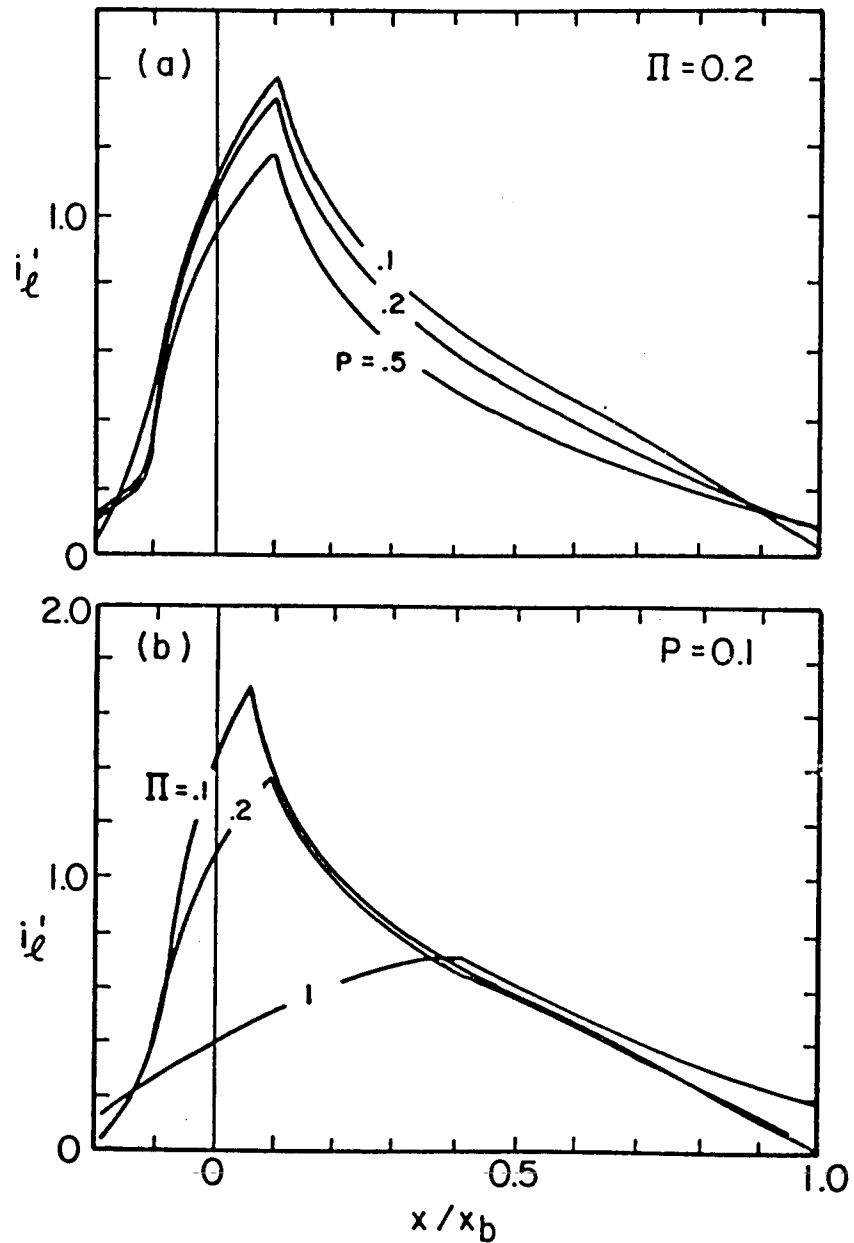


Figure 9-8: Dimensionless longshore transport across the surf zone for a non-singular equilibrium profile for: (a) fixed profile similarity parameter  $\Pi$  and various values of the longshore current mixing parameter  $P$ , and (b) fixed  $P$  and various values of  $\Pi$ . Evaluated for  $A=0.15 \text{ m}^{1/3}$ ,  $h_b=1.7 \text{ m}$ , shoreward-shifted longshore current profile, and linear decay of wave height from the profile match point to the shoreward limit of runup.

For purposes of comparison, the normalized longshore transport distribution expressed by the preferred model for a planar beach is written

$$i'_l = \left(\frac{x}{x_b}\right)^{1/2} v'_l \quad (9.33)$$

Eq. (9.33) is graphically represented in Figure 9-9 for the Longuet-Higgins (1970) expression of the longshore current across a planar beach (neglecting set-up) for various values of the mixing parameter P.

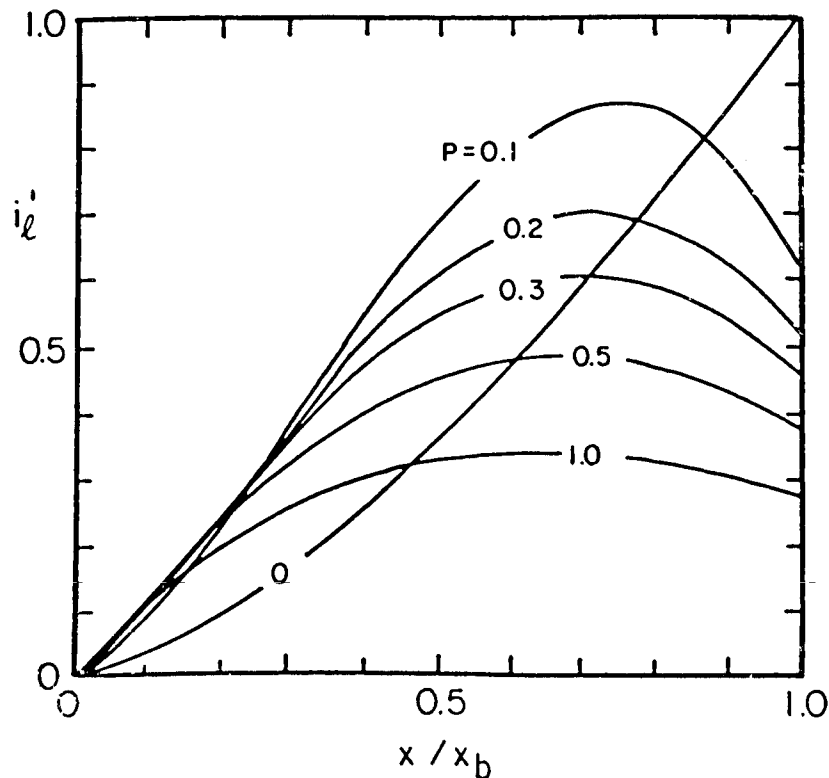


Figure 9-9: Dimensionless longshore transport across the surf zone for a planar beach assuming linear wave decay from the break-point to the still water line. Evaluated for various values of the longshore current mixing parameter P (indicated for each curve).

Although the Longuet-Higgins solution predicts longshore current seaward of the breakpoint (for  $P \neq 0$ ), the preferred longshore transport model does not predict longshore transport seaward of the breakpoint since it was assumed that no wave energy dissipation occurs seaward of the break point.

Finally, in suggesting the form of the concave-up equilibrium beach profile  $h = Ax^{2/3}$ , Dean (1977) argued that the rate of wave energy dissipation per unit surf volume is uniform across a beach which is in equilibrium (assuming that the stability characteristics of the sediment are uniform across shore). If this is the case, then for a beach in equilibrium the preferred distributed longshore transport model, Eq. (8.21), becomes

$$i_l = k_3 D^* V_l \left( \frac{dh}{dx} \right)^{1/2} \quad (9.34)$$

where  $D^*$  is the equilibrium rate of wave energy dissipation per unit volume for a sediment of given stability characteristics. For  $H = \kappa h$  across the surf zone, Dean showed that

$$D^* = \frac{5}{24} \rho g^{3/2} \kappa^2 A^{3/2} \quad (9.35)$$

where  $A$  is the sediment-related parameter in the  $h = Ax^{2/3}$  equilibrium profile.

## CHAPTER 10

### SUMMARY AND CONCLUSIONS

The primary focus of this study was an investigation of the distribution of longshore sediment transport across the surf zone as determined from the short-term impoundment of sediment against a shore-perpendicular barrier in both field and laboratory environments. Methodologies were developed to remove tidal and cross-shore effects from the impoundment (survey) data of the experiments, and to assess the effectiveness of the barriers as impoundment agents. From the experimental data, several generalizations were made concerning the relative significance of the longshore transport in the swash, surf, and offshore regions of the surf zone, as well as the shape of the longshore transport distribution and its relationship to surf and beach parameters. In addition, insight was gained to the effect of offshore smearing of the impoundment fillet caused by the presence of the groyne as caused principally for the longer-term impoundment intervals. Some observations were also made of the relationship (or lack thereof) of local downdrift beach profile changes relative to the local updrift impoundment of sediment against the groyne. The normalized distributions of the longshore transport developed from the experimental data were compared to several existing and alternate predictive models. A new, simple engineering model was proposed which appears to fairly accurately and consistently describe the normalized longshore transport

distribution landward of the wave breakpoint. Some theoretical arguments based primarily upon non-linear wave theory were advanced in support of the model and the experimental findings. The proposed distributed longshore transport model was evaluated for an equilibrium beach profile shape which exhibits a non-singular (finite-sloped) foreshore. For the evaluation, expressions were developed for the wave induced set-up and longshore current across the profile. In general, the experimental findings of this study qualitatively support the observations and conclusions of previous investigations of the total longshore transport. The experimental findings represent a significant contribution to the existing data base of the distribution of longshore sediment transport across shore, and in general, support these previous data. However, the findings differ from the commonly held belief that the longshore sediment transport is most significant across the middle and outer portions of the surf zone.

The results of the field work indicate that the rapid deployment of a groyne and the subsequent intensive survey effort necessary for a short-term impoundment study are practicable in relatively low-energy open-coast field environments; however, the field tasks demand considerable effort and dedication. Pyramid-shaped sand bag units were found to be ideal for rapid, effective groyne construction. Each unit consists of three self-closing sand bag tubes sewn together in a triad with the top bag overlapping the bottom two such that the groyne is constructed in a brick-laying fashion. In order to minimize "spurious" swash-related impoundment during groyne construction, deployment of the groyne should commence at the berm at the end of high tide, and proceed down the beach with the falling tide. The post-deployment survey loops

should be planned such that the profiles nearest the groyne are initially surveyed just after the wave breakpoint moves landward of the end of the groyne on the rising tide, and the final survey of these profiles should occur just before the breakpoint moves seaward of the end of the groyne on the subsequent falling tide. For any impoundment interval, the elapsed time between surveys should be relatively uniform for each profile. It is recommended that profiles be spaced logarithmically updrift and away from the groyne to a minimum distance of two groyne lengths along the beach.

From the field results, it appears that the groynes led to very "noisy" impoundment data for depth contours blocked by the groyne for less than half the time between profile survey loops, or for a time-weighted effective barrier relief at a given contour of less than 10 to 20 cm (or about 20% to 30% of the significant breaking wave height). However, there appears to be a limit to the desired maximum elevation of the groyne. From the laboratory experiments, it was found that a low-profile groyne was best suited for short-term sediment impoundment studies. Specifically, the best trade-off between barrier by-passing and severe barrier-related rip generation and wave reflection was found with a groyne for which the crest was just at or below the upper envelope of the swash and waves across the foreshore and inner surf zone, just at or below the mean water level across the mid-surf zone, and about half the local wave height above the bed across the outer surf zone. For this study, the laboratory groynes were tapered to zero-relief at about two to three surf zone widths from the shoreline.

For longer period impoundment intervals, it was found from the laboratory data that the groynes, or barriers, smear the longshore

transport impoundment fillet primarily towards the offshore direction. From the data, it is difficult to suggest specific guidelines for the appropriate impoundment duration of an experiment. The smearing is a result of (i) a rip directed offshore at the groyne caused by diversion of the longshore current, (ii) local wave steepening at the groyne caused by the rip, and (iii) the action of local cross-shore processes at the groyne which act to re-equilibrate the beach profile immediately updrift of the groyne due to the near-groyne surplus of sand associated with longshore impoundment. The former two processes are minimized for lower-profile groynes. The effect of the latter is best minimized through the execution of shorter-term impoundment studies. Onshore smearing of the impoundment fillet can occur due to berm-building associated with the steeper slopes (and therefore greater runup) and the surplus of sand updrift of the groyne due to longshore impoundment. Onshore smearing was observed only for low steepness waves with low-phase swash.

From both the field and laboratory data, it was found that local profile changes immediately downdrift of the groyne are poor and/or inconsistent indicators of local profile changes updrift of the groyne. Additionally, it was found that the updrift extent of the impoundment fillet in each experiment was about one surf zone width updrift of the groyne.

Two techniques designed to remove the effect of tidal fluctuations from the survey data were introduced: "simple" and "matrix" tidal deconvolution. The former simply describes the depth at a given reference elevation as the tidally-averaged value calculated over the interval for which the given elevation was wetted. The latter assumes

that the rate of profile change is uniquely determined for each water depth, such that the measured profile change at a given reference elevation is determined by the local rate of profile change associated with those depth contours which occupied the given elevation as the tide fluctuated between profile surveys. As such, calculation of the gradient in transport rate, or the so-called "total transport function," is determined from a set of linear equations which are solvable by linear algebra using matrix manipulation. It was found that the matrix technique is generally more powerful as it distinguishes the gradient of the transport rate at individual depths, while the simple technique inherently smooths profile change data over depth. However, the matrix technique was found to be very sensitive to survey errors reflected in the measured profile change data used to develop the transport gradient at each depth. To account for this, the linear equations central to the technique were overconstrained, solved by the method of least-squares, and the results were subsequently smoothed over depth. The appropriate degree of over-constraint was found to be a function of the tidal excursion (during the interval between surveys) relative to the vertical extent of reference elevation over which survey data were available. A laboratory investigation did not definitely confirm the effectiveness of either tidal deconvolution technique. Specifically, a directional wave event was established in the laboratory basin and impoundment experiments were executed in both the presence and absence of tidal fluctuations. The longshore transport distribution developed from the data of the former tests (using tidal deconvolution) were only generally similar to the results of the latter tests. This was probably because the tidal deconvolution techniques assume that the local transport gradient is a

function only of depth, but the final results of the study indicate that the local longshore transport rate is strongly related to local bed slope and depth. The field experiment site was relatively planar and so the effect of bed slope on the results of the tidal deconvolution was probably not as severe as for the laboratory experiments, for which the profiles exhibited very non-uniform local bed slope.

The presence of tide in short-term impoundment experiments has potentially beneficial and detrimental effects. Regarding the former, effective execution of the field experiments can be made possible through coordination of the groyne deployment and survey sequence with the tide. Additionally, it is possible that smearing is not as severe for experiments executed with tide because the fluctuating mean water level distributes the longshore impoundment more evenly across the beach such that groyne-local cross-shore processes (which are difficult to identify from the data) do not significantly smear the impoundment in an attempt to "re-equilibrate" the near-groyne beach profiles. However, the presence of tide requires the use of tidal deconvolution, the effectiveness of which has not yet been proven.

Several techniques were introduced to identify the cross-shore transport contributions to the surveyed impoundment data. These techniques were based upon the assumption that the profile change along a depth contour or offshore location consists of a longshore contribution which is modeled by a function which decreases exponentially updrift and away from the groyne, and a cross-shore contribution assumed to be uniform along the contour or offshore location and which is modeled by a constant. The combined exponential-plus-constant function is fit to the profile change data along a contour or offshore location

in order to identify the value of the constant which corresponds to the cross-shore contribution. Alternately (yet consistent with the above-described approach) profile changes far updrift of the groyne are assumed to represent solely cross-shore transport signals. Once identified, the cross-shore component of the profile change for each depth contour or offshore location is removed from the survey data such that, presumably, only the longshore transport signal remains.

The most complete field data set of this study indicates that 16% to 22% of the total longshore transport occurs seaward of the breakpoint; the results of each of the laboratory data sets indicate that 7% to 9% occurs seaward of the breakpoint. In general, however, this agrees with previous investigations, for which it has been reported that 10% to 30% of the total longshore transport occurs seaward of the breakpoint. The two "best" field data sets of this study indicate that 16% to 25% of the longshore transport occurs in the swash zone. All of the field data sets suggest that, at the least, longshore transport in the swash zone is significant. Each of the field experiments was conducted on relatively similar beach profiles and for similar (spilling and/or plunging) surf conditions. The laboratory data sets similarly indicate that longshore transport in the swash zone is significant, and that the relative contribution of the swash varies with the profile and/or surf condition. From the laboratory data, the swash zone contribution comprised 2% of the total longshore transport for the spilling series, 29% for the spilling/plunging series, 34% for the plunging series, 45% for the plunging/collapsing series, and 60% for the collapsing series. It is believed that the swash zone contribution for the spilling case was under-estimated.

As is reflected by the existing data and observations of previous investigators, the longshore transport distribution profile across the surf zone was found to vary significantly. From the results of this study, it can be said that the distribution is generally bimodal with one peak just landward of the breakpoint ( $x/x_b \approx 0.8$ ) and the other peak near or at the shoreline. However, the significance of each peak differs with the profile and/or surf conditions; that is, the near-breakpoint peak dominates for spilling conditions, both peaks are of relatively equal significance for plunging conditions, and the near-shoreline peak dominates for collapsing conditions. (Alternately, for the latter case, it might be said that the two distribution peaks become one and the same since the breakpoint approaches the shoreline for collapsing wave conditions.)

Previous investigators have found that the total longshore transport increases with increasing surf similarity parameter (for a given level of longshore wave energy flux or radiation stress), which in turn indicates that the total longshore transport increases as the surf tends from spilling to collapsing conditions. Since the latter is characterized by a surf zone concentrated near the shoreline and in the swash zone, the near-shoreline and swash zone longshore transport must be significant such that the total longshore transport for these conditions exceeds that of a non-collapsing condition. Hence, it is not surprising that near-shoreline and swash zone contributions to the longshore transport were found to be very significant.

It was argued that the longshore transport is enhanced near the shoreline due to onshore convection of the longshore current by wave mass transport which in turn leads to enhanced longshore stress near the

shoreline. Additionally, near-shoreline longshore current appears to be advected into the swash zone by the uprush of water particles from the shore-break to the foreshore. Both ideas were substantiated by observation and limited data. The former idea was presented through the use of non-linear wave theory and warrants further investigation.

From non-linear wave theory, it was also found that the contribution to the longshore stress from non-linear considerations of wave orbital motion is not typically significant compared to the contribution from longshore current. Additionally, non-linear (stream function) evaluation of the longshore wave energy flux and/or radiation stress indicates that the total longshore transport should be less than that calculated by linear-theory for decreasing values of wave steepness; however, this disagrees with previously reported results from laboratory investigations of the total longshore transport.

The longshore transport distribution profiles were observed to be correlated with the local longshore current, bed slope, and gradient of the wave height, and inversely correlated with the local water depth. Because the field and laboratory beach profiles were fairly well equilibrated with the wave conditions before each impoundment interval began, the existence, if any, of a correlation between local longshore and local cross-shore processes was not addressed in this study. The approach of the laboratory portion of this study was structured to investigate the longshore transport distribution profile associated with various surf conditions. Accordingly, the results were presented as a function of breaker type, and as described, the longshore transport distribution profiles were found to differ for various breaker type or surf conditions. However, it is probably more appropriate to say that

the longshore transport distribution is a function of the beach profile, especially as the local bed slope and reciprocal water depth were found to be particularly well correlated with the local longshore transport. This agrees with the majority of the existing data. It is the beach profile, after all, which partly determines the character of the surf zone, including the per-volume dissipation of breaking wave energy across shore and the longshore current profile. Of course, at the same time, it may not necessarily be wrong to describe the longshore transport distribution as a function of the surf condition, because the surf condition plays a central role in determining the beach profile in the first place. Additionally, the relative significance of the longshore transport in the swash zone may be said to be reasonably well correlated with the surf conditions. Swash zone longshore transport was found to be very significant for collapsing conditions--for which the swash is low-phase and well organized--while swash zone longshore transport was found to be small for spilling conditions. The swash associated with spilling conditions is high-phase and poorly organized; that is, the swash is over-saturated and prone to run-outs along the beach. These run-outs, associated with the return flow of the "excess" of water pumped onto the foreshore by the high-phase swash, interrupt the longshore drift along the shoreline and/or lead to a disorganized flow field along the foreshore which may not be conducive to effective sediment transport.

The normalized longshore transport distributions developed from the best-conditioned and/or most complete laboratory and field data sets were compared against the results of the Bagnold model, a generic form of the stress model, and 5 alternate models. The predictions of one of

the proposed alternate models agrees fairly well and consistently with the normalized distributions of longshore transport across shore found from the laboratory data, and to some extent, the field data. The model describes the local longshore sediment transport as a function of the local longshore current, bed slope, and dissipation of wave energy per unit volume. Specifically, the preferred model is of the form

$$i_{\ell} = k_3 \frac{1}{h} \frac{\partial}{\partial x} (E C_g) V_{\ell} \left[ \frac{dh}{dx} \right]^r \quad (10.1)$$

where  $k_3$  is a constant with dimensions of time, and where the value of  $r$  is best described between 0 and 0.5, where  $r=0.5$  is most preferred. Agreement between the values of the constant  $k_3$  determined for the laboratory experiments was reasonably good (i.e., a normalized standard deviation of about 30%). The normalized longshore transport distribution profiles developed from the data were well represented by the evaluation of Eq. (10.1) where the local water depth  $h$  was taken as the sum of the local wave height  $H$  and the total water depth  $d$ , where  $d$  included an estimate of the local set-up. That is,

$$h = H + d \quad (10.2)$$

and the local wave group celerity was taken as

$$C_g = \sqrt{g(H+d)} \quad (10.3)$$

Evaluation of Eq. (10.1) using Eqs. (10.2) and (10.3) enables estimation of the local longshore transport across the shoreline and the swash zone, where the local wave height  $H$  in the swash zone is taken as the maximum instantaneous local water depth observed at each (local) point

across the swash zone. The model described by Eq. (10.1) does not predict transport seaward of the breaker line if no wave energy dissipation is assumed seaward of the breakpoint. Knowledge of the beach profile and the wave height and longshore current distribution across the profile are required for practical application of the model.

In describing the longshore transport distribution, many previous investigators and practicing engineers have assumed a longshore current profile which is based upon the classical expression for a planar beach given by Longuet-Higgins (1970). This model suggests maximum longshore current in the seaward half of the surf zone where the longshore current decreases to zero at the shoreline. Primarily because of the common use of the planar beach expression, the maximum longshore transport has been assumed to occur in the seaward half of the surf zone while longshore transport at the shoreline and in the swash zone has been neglected. The existing data and the data from this study suggest that neither of these assumptions or beliefs is generally appropriate. Natural beaches are infrequently planar; accordingly, expressions for the longshore current (which include the swash zone) developed for non-planar beaches should be used where appropriate to evaluate the longshore transport distribution across shore. An expression for the longshore current across a monotonic beach profile characterized by a planar foreshore matched to an equilibrium concave-up profile shape was developed in this study. The longshore current expression matches the (Lagrangian) measured longshore current distribution in the laboratory experiments fairly well--except that the measured distribution is displaced landward of the predicted distribution by about  $x/x_b = 0.2$ . Use of this predictive longshore current expression suggests that the longshore

transport is maximum near the shoreline. However, the longshore transport evaluation was based upon a spilling breaker assumption, and features such as bars and terraces were not considered in the evaluation.

In closing, it is suggested that short-term impoundment techniques, using a low-profile groyne which allows passage of at least most of the wave envelope across the mid- and outer-surf zone, is a reasonable approach for the measurement of the distribution of longshore transport. The longshore transport distribution profile is determined primarily by the beach profile, which determines and/or is determined by the surf conditions. The local longshore transport across the surf zone is most significant in areas of large-value wave energy dissipation per unit volume, strong longshore current, and steep bed slope. These conditions often typify the swash zone, which can exhibit significant levels of longshore sediment transport. A model based upon these three parameters was proposed and is best evaluated across the surf zone--including the swash zone--for the actual beach profile shape of interest.

APPENDIX A  
CONSTRUCTION OF PYRAMID-STYLE  
SAND BAG UNITS

Figure A-1 illustrates the technique developed for the construction of individual sand bags and pyramid-style sand bag units used in the field impoundment experiments. Pyramid-style units consist of three bags: (1) downdrift-side bottom, (2) updrift-side bottom, and (3) overhanging top. The top bag should be of 30% smaller diameter than the bottom bags. All three are of identical length. Details of the construction process follow.

Step 1. Cut the tube section of the bag from filter cloth material; approximate sheet size is  $L+2S$  by  $\pi D+F+2S$ , where  $L$  = desired bag length,  $D$  = desired tube diameter,  $F$  = flap width, and  $S$  = seam allowance. Flap width should generally be about one-fifth of the bag circumference.

Step 2. Fold B-B' at A-A'.

Step 3. Fold C-C' over B-B' to make the flap. Position one end of a rope tie within fold B-B' for a downdrift-side bottom bag or within fold C-C' for an updrift-side bottom bag. No rope tie is needed at this step for a top bag. Stitch along B-B'. Stitch C-C' to the upper section of the sheet formed by A-B-B'-A'. The end of rope ties which are to be stitched into a seam should be frayed in order to facilitate stitching.

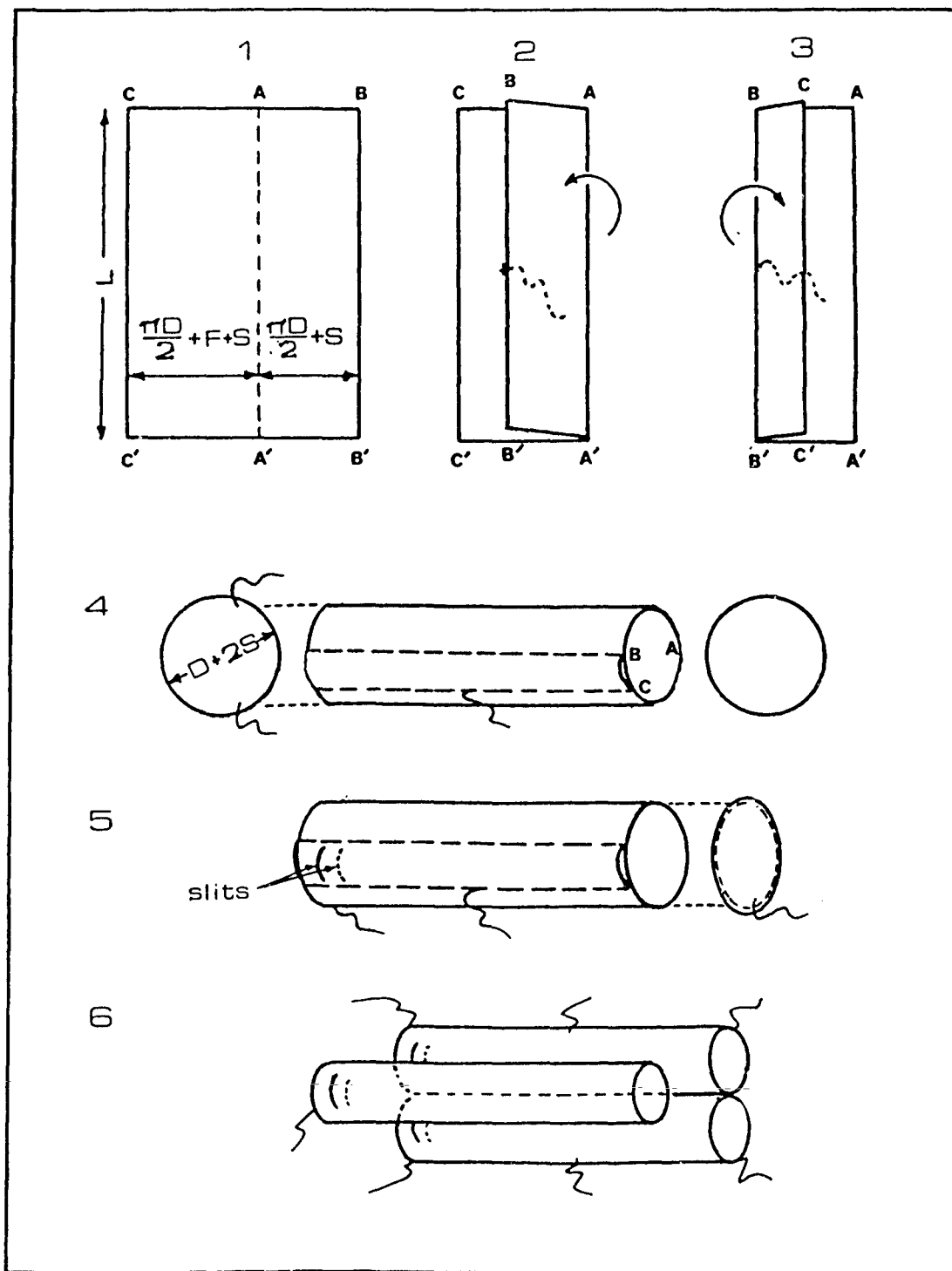


Figure A-1: Construction detail for an individual sand bag unit for use in the pyramid-style groyne.

Step 4. Cut out two circular end-pieces of diameter  $D+2S$ . Stitch one end-piece onto the landward end of the bag. Include a rope tie in the seam--with the free end inside the tube--corresponding in location to the rope tie sewn into the side of the bag in the previous step. For the top bags, the end-piece rope ties should be positioned on the under-side of the bag; that is, opposite the flap.

Step 5. Turn assembly inside-out. Stitch on remaining (seaward) end-piece including one rope tie in the seam as described in Step 4, but with the free end outside the bag. Slit across the outside and inside of the flap at the landward end of the bag as shown in the figure.

Step 6. After constructing the three component bags of the pyramid, stitch the two bottom bags together by gathering material along their sides to make a seam. Stitch the top onto the bottom bags (in a similar manner) such that the landward end of the top bag overhangs the bottom bags by one-third of the bag length. Material from the flap sections should not be used to make the seams between bags.

Comments. The rope ties are used to secure the bags between two shore-perpendicular ropes--stretched across the beach through the surf zone--during the filling operation. The rope ties should be cut or removed after each unit is filled in order to facilitate groyne removal. Sand bag units filled on the foreshore should be placed upon large filter-cloth sheets which extend to the water line in order to minimize scour and bag-jetting into the bed during the filling operation.

APPENDIX B

EVALUATION OF ELEMENTS  
IN THE TIDAL DECONVOLUTION  
MATRIX, A

For the purpose of tidal deconvolution (as described in Chapter 4, Section 5), the beach is considered as N horizontal layers of vertical dimension  $\Delta z_o$ . The center of each layer corresponds to an NGVD elevation  $z_{o_n}$ . The total transport function  $\Lambda(z)$  is discretized for evaluation at M depth contours. Each of the M depth contours has thickness  $\Delta z$ , with the center described by depth  $z_m$ .

Since the transport function  $\Lambda_m$  is defined in the center of each depth contour layer (i.e., at  $z=z_m$ ), the elapsed-time elements  $a_{n,m}$  can be approximated as follows,

$$a_{n,m} = \left\{ 1 - \frac{1}{\Delta z} \left| (z_{o_n} - \bar{\eta}(t)) - z_m \right| \right\} \delta t \quad (B.1)$$

$$a_{n,m\pm 1} = \frac{1}{\Delta z} \left| (z_{o_n} - \bar{\eta}(t)) - z_m \right| \delta t \quad (B.2)$$

for  $\left| (z_{o_n} - \bar{\eta}(t)) - z_m \right| < \Delta z/2$ , and  $a_{n,m} = 0$ , otherwise.

In Eq. (B.2), the index increment (positive sign) is taken if  $z_{o_n} - \bar{\eta}(t) < z_m$ ; the index decrement (negative sign) is taken if  $z_{o_n} - \bar{\eta}(t) > z_m$ . The value  $\delta t$  is the elapsed time between sampled tide values. The tide value  $\bar{\eta}(t)$  is appropriately taken as the average

value of the tide during the interval  $\delta t$ . Equations (B.1) and (B.2) assign 100% weighting of the elapsed time  $\delta t$  to a depth contour layer  $z_m$  if the center of this layer corresponds exactly to the middle of a beach lamina  $z_{o_n}$ . If the center of a beach lamina  $z_{o_n}$  corresponds to, say, the upper surface of depth contour  $z_{m+1}$  and the lower surface of  $z_m$ , then  $a_{n,m}$  and  $a_{n,m+1}$  are each assigned a proportionate weighting of the elapsed time interval  $\delta t$  (50% of  $\delta t$  in this case). This linear apportionment within the A matrix helps to lessen the severity of discontinuities between layers in a discretized model. (Note in Eq. (B.2) that if  $z_{o_n} - \bar{\eta}(t) < z_m$  and  $m=M$ , or if  $z_{o_n} - \bar{\eta}(t) > z_m$  and  $m=1$ , then 100% weighting of  $\delta t$  is assigned to  $a_{n,m}$ .)

## APPENDIX C

### LEAST-SQUARES SOLUTION OF THE OVER-CONSTRAINED TIDAL DECONVOLUTION TECHNIQUE

A unique solution of Eq. (4.13) in the text for the total transport function  $\Lambda(z)$  is not straight-forward if the system is over-constrained (i.e., if there exists more NGVD elevations  $z_{o_n}$ , for which profile-change data are specified than depth contours  $z_m$ ). For the over-constrained case,  $N > M$ , Eq. (4.13) may be solved using a least-squares technique as described below.

Consider a beach profile change  $\tilde{\Delta x}_n$  at NGVD elevation  $z_{o_n}$ , where

$$\tilde{\Delta x}_n(z_{o_n}) = \sum_m^M a_{n,m} \cdot \Lambda_m(z_m) \quad (C.1)$$

as per Eq. (4.11) in the text. It is desired to minimize the error  $\epsilon$  between the calculated profile change,  $\tilde{\Delta x}_n(z_{o_n})$ , and the measured profile change,  $\Delta x_n(z_{o_n})$ , where

$$\epsilon = \sum_n^N (\tilde{\Delta x}_n - \Delta x_n)^2 \quad (C.2)$$

Incorporating Eq. (C.1),

$$\epsilon = \sum_n^N \left( \sum_m^M a_{n,m} \Lambda_m - \Delta x_n \right)^2 \quad (C.3)$$

The error  $\epsilon$  will be minimized with respect to the total transport function  $\Lambda_m(z_m)$  at any particular depth contour  $m=k$ ,

$$\frac{\partial}{\partial \Lambda_k} \sum_n^N \left( \sum_m^M a_{n,m} \Lambda_m - \Delta x_n \right)^2 = 0 \quad (C.4)$$

which simplifies to

$$\sum_m^M \Lambda_m \sum_n^N a_{n,m} \cdot a_{n,k} = \sum_n^N a_{n,k} \cdot \Delta x_n \quad (C.5)$$

Equation (C.5) represents the  $k$ 'th equation in a total of  $M$  equations, where  $k$  is the index of the particular transport value  $\Lambda_m (= \Lambda_k)$ , for which the error is to be minimized. Equation (C.5) is evaluated for  $k = 1, 2, \dots, M$ . Rewriting Eq. (C.5),

$$\sum_m^M b_{k,m} \cdot \Lambda_m = s_k \quad (C.6)$$

where

$$b_{k,m} = \sum_n^N a_{n,m} \cdot a_{n,k} \quad (C.7)$$

and

$$s_k = \sum_n^N a_{n,k} \cdot \Delta x_n \quad (C.8)$$

Then a solution for  $\overline{\Lambda(z)}$  is found by

$$\overline{\Lambda(z)} = B^{-1} \overline{s} \quad (C.9)$$

If  $M=N$ , then Eq. (C.9) reduces to the original solution expressed by Eq. (4.14) in the text.

## APPENDIX D

### LEAST-SQUARES FIT TO THE TOTAL TRANSPORT FUNCTION ALONG A DEPTH CONTOUR

As described by Eq. (4.24) in the text, the total transport function  $\Lambda(z)$  is fit to an exponential function which describes the longshore component and a constant which describes the cross-shore component. For a given depth contour  $z=-h$ ,

$$\Lambda = Ae^{-B|y|} + C \quad (D.1)$$

The error  $\epsilon$  between the tidally deconvolved values of  $\Lambda$  and Eq. (D.1) is defined as

$$\epsilon = \sum_i^I (Ae^{-B|y_i|} + C - \Lambda_i)^2 \quad (D.2)$$

One attempts to minimize the error  $\epsilon$  with respect to the unknown coefficients  $A$ ,  $B$ , and  $C$  using the  $I$  values of  $\Lambda$  known along  $y$ . That is,

$$\frac{\partial \epsilon}{\partial A} = 2\{A \sum e^{-2B|y|} + C \sum e^{-B|y|} - \sum \Lambda e^{-B|y|}\} = 0 \quad (D.3)$$

$$\frac{\partial \epsilon}{\partial B} = 2\{A \sum y e^{-2B|y|} + C \sum y e^{-B|y|} - \sum \Lambda y e^{-B|y|}\} = 0 \quad (D.4)$$

$$\frac{\partial \epsilon}{\partial C} = 2\{A \sum e^{-B|y|} + IC - \sum \Lambda\} = 0 \quad (D.5)$$

where the index  $i$  has been dropped for brevity. For notation purposes, express

$$G = e^{-B|y|} \quad (D.6a)$$

$$H = e^{-2B|y|} \quad (D.6b)$$

Using Eqs. (D.6a) and (D.6b), and substituting Eq. (D.5) into (D.3), one finds

$$A = \frac{\sum \Lambda G - \frac{1}{I} \sum \Lambda \sum G}{\sum H - \frac{1}{I} (\sum G)^2} \quad (D.7)$$

Substituting Eq. (D.5) into (D.4) yields

$$A = \frac{\sum y \Lambda G - \frac{1}{I} \sum \Lambda \sum y G}{\sum y H - \frac{1}{I} \sum G \sum y G} \quad (D.8)$$

Equations (D.7) and (D.8) represent a coupled pair which describe the unknown  $A$  in terms of the unknown  $B$  and the known values  $\Lambda(y)$ . Equations (D.7) and (D.8) were solved by selecting values of  $B$  by numerical trial and error in order that the two equations converged upon a single value of  $A$ . Hence, both the values of  $B$  and  $A$  were found, and the value of  $C$  was subsequently found through Eqs. (D.3), (D.4), and/or (D.5).

## APPENDIX E

### ESTABLISHING BED COORDINATES FROM LABORATORY PROFILER DEVICE

As described in Chapter 6, Section 3, the laboratory profiler apparatus provided voltage drop signals corresponding to (1) the horizontal distance which the cart's tracking wheel rolled along the top rails, and (2) the angle which the profiler arm made with the cart horizontal as the arm's profiling wheel touched the bed. The reduction of these voltage signals to beach profile (bed) coordinates is described below and by Figure E-1. The circuit diagram of the profiling system is illustrated in Figure E-2.

The maximum range of motion (plus a 5% allowance) was established for the horizontal tracking wheel as  $\Delta x$  and for the profiler arm as  $\Delta\theta$ . For these maximum mechanical swings, the maximum voltage swing for the corresponding potentiometers was set to  $\pm\Delta V$  (through use of the system's two-sided zero-offset and amplification capabilities). In practice,  $\Delta V=5$  volts, such that the 11-bit A/D converter resolved 4.883 mV. The voltage levels corresponding to a reference horizontal location along the rails,  $X_0$ , and a reference profiler arm angle below cart horizontal,  $\theta_0$ , were established for each profile run as  $V_{x0}$  and  $V_{\theta_0}$ , respectively. The position,  $x_w$ , of the tracking wheel along the rails, referenced to  $X_0$ , is therefore given by

$$x_w = (V_x - V_{x0}) \frac{\Delta x}{\Delta V} + X_0 \quad (\text{E.1})$$

The angle  $\theta$  between the profiler arm and the cart horizontal is given by

$$\theta = (v_{\theta} - v_{\theta_0}) \frac{\Delta\theta}{\Delta V} + \theta_0 \quad (\text{E.2})$$

where  $V_x$  and  $V_{\theta}$  indicate the voltage drop signals from the horizontal tracking and profiler arm potentiometers, respectively.

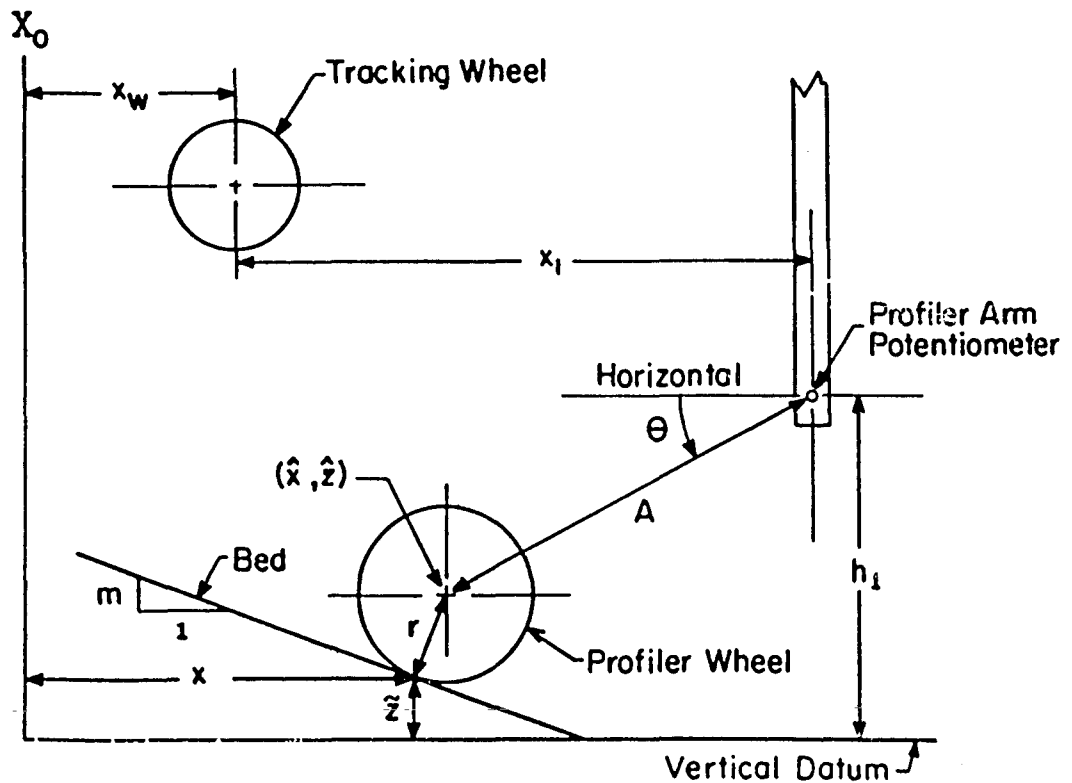


Figure E-1: Illustrative sketch of profiler apparatus geometry.

As shown in Figure E-1, the tracking wheel was located a distance  $x_1$  landward of the profiler arm potentiometer. The profiler arm was of length  $A$  and the center of the profiler arm potentiometer was at elevation  $h_1$  (with respect to a vertical datum). The coordinates of the

center of the profiler wheel upon the bed are therefore given by  $(\hat{x}, \hat{z})$ , where

$$\begin{aligned}\hat{x} &= x_w + x_1 - A \cos \theta \\ \hat{z} &= h_1 - A \sin \theta\end{aligned}\tag{E.3}$$

(It is assumed here that the x-axis is positive seaward and the profiler arm angle is positive counter-clockwise.)

The coordinates of the bed upon which the profiler wheel rests are given by  $(x, z)$ , where

$$\begin{aligned}x &= \hat{x} - \frac{m r}{\sqrt{1 + m^2}} \\ z &= \hat{z} - \frac{r}{\sqrt{1 + m^2}} - h\end{aligned}\tag{E.4}$$

where  $m$  is the local bed slope at  $(x, \tilde{z})$ ,  $r$  is the profiler wheel radius, and  $h$  is the still (or reference) water level. In practice, the local bed slope  $m$  was evaluated as the average slope between the wheel coordinates of the previous, present, and next points along the profile (i.e.,  $(\hat{x}_{i-1}, \hat{z}_{i-1})$ ,  $(\hat{x}_i, \hat{z}_i)$ , and  $(\hat{x}_{i+1}, \hat{z}_{i+1})$ ). Accordingly, all of the profiler wheel coordinates,  $(\hat{x}, \hat{z})$ , were calculated along a profile before the corresponding bed coordinates,  $(x, z)$ , were calculated. Since both the still (or reference) water level  $h$  and the profiler arm reference elevation  $h_1$  were measured with respect to the same datum (i.e., the basin floor), Eq. (E.4) yields the bed elevation  $z$  with respect to the still (or reference) water level.

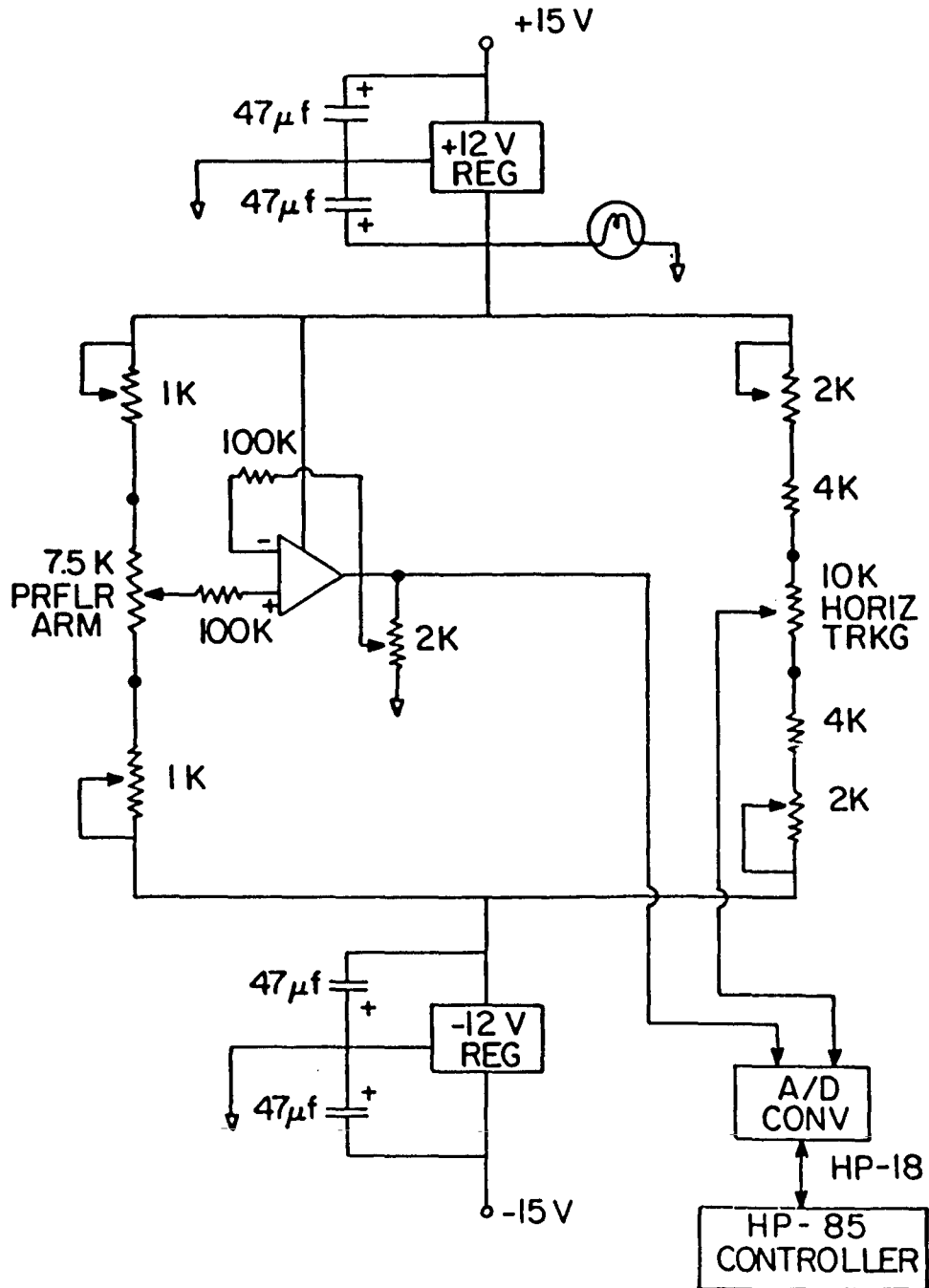


Figure E-2: Circuit diagram of profiler.

## APPENDIX F

### SWASH ON A PLANAR BEACH

This appendix presents a brief discussion of the governing equations of motion, and some considerations thereof, for three-dimensional swash motion on a planar beach. Consider a planar foreshore inclined at angle  $\theta$  to the horizontal, as shown in Figure F-1. The coordinate axis  $\zeta$  is oriented upslope with origin at the still water line. With respect to the usual offshore-directed horizontal axis  $x$ ,

$$\zeta = -x \sec\theta \quad (\text{F.1})$$

where the foreshore slope is described by  $m_f = \tan\theta$ . Assuming that a free water surface gradient  $dh/d\zeta$  exists up and down the slope, but that no gradients exist alongshore, the equations of motion for the swash in the upslope and alongshore directions, respectively, are

$$\zeta: \frac{du}{dt} = -g \left( \frac{dh}{d\zeta} + m_f \right) - f_\zeta \quad (\text{F.2})$$

$$y: \frac{dv}{dt} = -f_y \quad (\text{F.3})$$

where  $h$  is the water depth measured perpendicular to the slope,  $u$  and  $v$  represent the swash particle velocities up and along the slope, respectively, and  $f_\zeta$  and  $f_y$  represent frictional terms. One might proceed

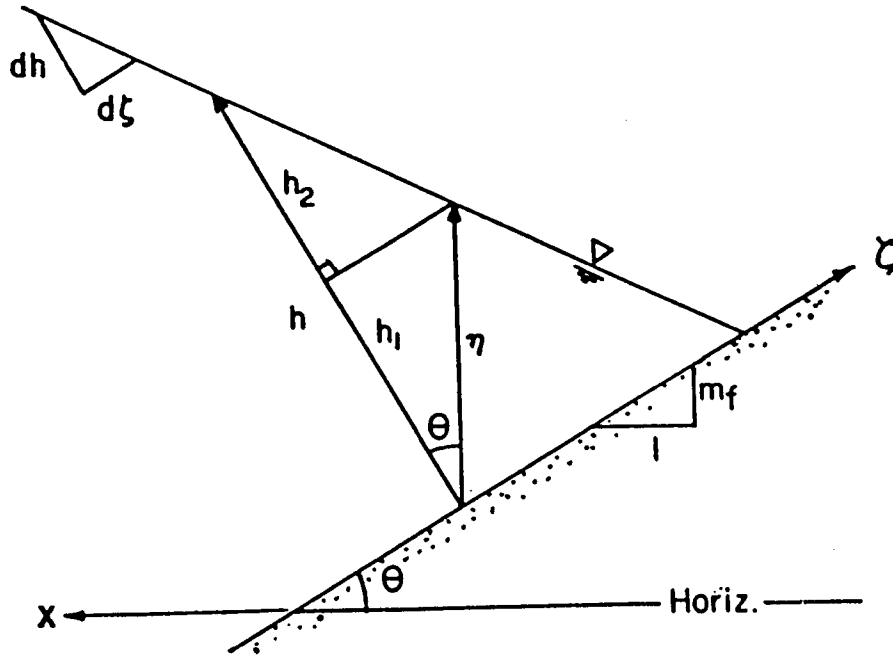


Figure F-1: Geometry of swash upon an inclined plane.

towards solution by assuming that the frictional terms may be expressed in a linearized fashion i.e.,

$$\begin{aligned} f_{\zeta} &= \beta u \\ f_y &= \beta v \end{aligned} \quad (\text{F.4})$$

where

$$\beta = \frac{f|u|}{h} \quad (\text{F.5})$$

and where  $f$  is a coefficient of friction, and  $|u|$  and  $h$  are selected as representative (constant) values. Assuming small angles of bore incidence and neglecting set-up, it is convenient to allow  $|u|=u_0$ ,

$h=H_{bs}$ , and reasonable to assume  $u_o = \sqrt{gH_{bs}}$ , where  $H_{bs}$  is the height of the incident bore at the shoreline, and  $u_o$  is the initial particle velocity upon uprush. Accordingly,

$$\beta = \frac{gf}{u_o} \quad (F.6)$$

Some form of the free surface slope,  $dh/d\zeta$ , must be assumed as a function of time and perhaps distance upslope,  $\zeta$ . An assumed variation of surface slope with upslope distance complicates solution of the problem but simultaneously introduces a water surface curvature which in turn leads to the prediction of a non-uniform instantaneous velocity field. An assumption of planar instantaneous surface slope leads to the prediction of a uniform instantaneous velocity field. Kemp and Plinston (1974) suggested that the former is more realistic for higher phase difference swash while the latter is more realistic for lower phase difference (surging) swash.

With an assumed form of  $dh/d\zeta$  and the linearized friction terms, the equations of motion are solved for the velocity field,  $u$  and  $v$ , subject to the initial conditions

$$\begin{aligned} u(t=0) &= u_o \\ v(t=0) &= V_{\ell s} + u_o \sin \alpha_s \end{aligned} \quad (F.7)$$

For an instantaneous planar swash surface (i.e.,  $dh/d\zeta=f(t)$ ), the location of the shoreward-most edge of the swash up the beach is given by

$$x_s(t) = \int_0^t u \, dt \quad (F.8)$$

The instantaneous local swash depth  $h$ , measured perpendicular to the beachface at any upslope location  $\zeta$ , is

$$h(\zeta, t) = (x - x_s) \frac{dh}{dt} \quad (\text{F.9})$$

Combining the following geometric relations evident from Figure F-1,

$$h = h_1 + h_2 \quad (\text{F.10a})$$

$$h_1 = \eta \cos\theta \quad (\text{F.10b})$$

$$h_2 = -\eta \sin\theta \frac{dh}{d\zeta} \quad (\text{F.10c})$$

such that

$$h = \eta \left( \cos\theta - \sin\theta \frac{dh}{d\zeta} \right) \quad (\text{F.11})$$

the instantaneous local swash depth  $\eta$ , measured vertically from the beachface, is

$$\eta(\zeta, t) = \frac{h(\zeta, t)}{\cos\theta - \sin\theta \frac{dh}{d\zeta}} \quad (\text{F.12})$$

For typically small beachface slopes, such that  $\cos\theta \approx 1$  and  $\sin\theta \approx \tan\theta \approx m_f$ , Eq. (F.12) may be written

$$\eta(\zeta, t) \approx \frac{(x - x_s) \frac{dh}{d\zeta}}{1 - m_f \frac{dh}{d\zeta}} \quad (\text{F.13})$$

This author investigated solutions of the swash equations, (F.2) and (F.3), for the swash surface slope given by

$$(i): \quad \frac{dh}{d\zeta}(t) = A_1 e^{-\mu t} \quad (F.14a)$$

$$(ii): \quad \frac{dh}{d\zeta}(t) = \frac{A_1}{\mu t} \quad (F.14b)$$

where  $\mu$  and  $A_1$  are constants to be determined. The former expression yields closed-form explicit solutions for the velocity field, swash trajectory and depth; but because the surface slope is finite at  $t=0$  (i.e., the arrival of the bore), it is not possible to demand  $\eta(0,0)=H_{bs}$  without requiring that  $\mu < 0$ . (This can be easily shown by using l'Hospital's rule to evaluate  $\lim_{t \rightarrow 0} \eta(0,t) = H_{bs}$ .) From Eq. (F.14a), the condition  $\mu < 0$  implies that the slope of the swash surface relative to the foreshore increases with time, when in fact, it is generally observed to decrease with time as the swash progresses up the beachface. The latter expression, Eq. (F.14b), satisfactorily implies infinite water surface slope at the arrival of the bore but leads to a non-closed-form solution for  $u(t)$ . Further study will hopefully illuminate more satisfactory candidate expressions and solutions for the swash equations presented.

## REFERENCES

- Abdelrahman, S. M., "Longshore Sand Transport Distribution Across the Surf Zone due to Random Waves," Thesis, Naval Postgraduate School, Monterey, CA; June, 1983.
- Ackers, P., and W. R. White, "Sediment Transport: New Approach and Analysis," J. Hydraulics Div., ASCE, Vol. 99, HY 11, pp. 2041-2060; November, 1973.
- Bagnold, R. A. "Beach and Nearshore Processes Part I: Mechanics of Marine Sedimentation," in The Sea: Ideas and Observations, Vol. 3, M.N. Hill, ed., Interscience, New York pp. 507-528; 1963.
- Bailard, J. A., "A Simplified Model for Longshore Sediment Transport," Proc., 19th Int. Conf. on Coastal Eng., ASCE, pp. 1454-1470; 1984.
- Bailard, J. A. and D. L. Inman, "A Reexamination of Bagnold's Granular-Fluid Model and Bed Load Transport Equation," J. Geophysical Res., Vol. 84, No. C12, pp. 7827-7833; 1979.
- Bailard, J. A. and D. L. Inman, "An Energetics Bedload Model for a Plane Sloping Beach: Local Transport," J. Geophysical Res., Vol. 86, pp. 2035-2043; 1981.
- Bajournas, L., "Littoral Transport and Energy Relationships," Proc., 12th Int. Conf. on Coastal Eng., ASCE, pp. 787-798; 1970.
- Bakker, W. T., "Littoral Drift in the Surf Zone," Lecture, held at the Hydraulics Research Station, Wallingford, England, Ref. 94.56-B3-L4, Univ. of Fla. Coastal Engineering Archives, Gainesville, FL 32611; December 15, 1970.
- Battjes, J. A., "Set-up Due to Irregular Waves," Proc., 13th Int. Conf. on Coastal Eng., ASCE, pp. 1993-2004; 1972.
- Battjes, J. A., "Surf Similarity," Proc., 14th Int. Conf. on Coastal Eng., ASCE, pp. 466-480; 1974.
- Battjes, J. A. and M. Stive, "Calibration and Verification of a Dissipation Model for Random Breaking Waves," Proc., 19th Int. Conf. on Coastal Eng., ASCE, pp. 649-660; 1985.
- Beach Erosion Board, "Interim Report," U.S. Army Corps of Engineers, Washington, D.C.; 1933.

- Berek, E. P. and R. G. Dean, "Field Investigation of Longshore Transport Distribution," Proc., 18th Int. Conf. on Coastal Eng., ASCE, pp. 1620-1639; 1982.
- Bijker, E. W., "Longshore Transport Computations," J. Waterways, Harbors, and Coastal Eng. Div., ASCE, WW4; November, 1971.
- Birkemeier, W. A., A. E. DeWall, C. S. Gorbics, and H. C. Miller, "A Users Guide to CERC's Field Research Facility," U.S. Army Corps of Engineers, Coastal Engineering Research Center, Misc. Report No. 81-7, Vicksburg, MS; October, 1981.
- Bodge, K. R., and R. G. Dean, "Short-Term Impoundment of Longshore Sediment Transport in the Field," Final Report, Submitted to U.S. Army Corps of Engineers, Waterways Experiment Station, Coastal Engineering Research Center, Vicksburg, MS, 39180, 52 pp; June 15, 1985.
- Bowen, A. J., D. L. Inman, and V. P. Simmons, "Wave Set-Down and Set-Up," J. Geophysical Res., Vol. 73, No. 8, pp. 2569-2577; 1968.
- Brown, C. B., "Sediment Transportation," in Engineering Hydraulics, H. Rouse, ed., John Wiley and Sons, N. Y., 1039 pp.; 1950.
- Bruno, R. O., R. G. Dean, and C. G. Gable, "Longshore Transport Evaluations at a Detached Breakwater," Proc., 17th Int. Conf. on Coastal Eng., ASCE, pp. 1453-1475; 1980.
- Bruno, R. O., and C. G. Gable, "Longshore Transport at a Total Littoral Barrier," Proc., 15th Int. Conf. on Coastal Eng., ASCE, pp. 1203-1222; 1976.
- Bruun, P., "Coast Erosion and Development of Beach Profiles," Beach Erosion Board, Tech. Memo. No. 44, Washington, D.C.; 1954.
- Bruun, P., "Quantitative Field Research on Littoral Drift Using Tracers," Proc., 22nd Int. Congress on Navigation, P.I.A.N.C., 155 rue de la Loi, Brussels; 1969.
- Caldwell, J., "Wave Action and Sand Movement near Anaheim Bay, California," U.S. Army Corps of Engineers, Beach Erosion Board, Tech. Mem. No. 68, Washington, D.C.; 1956.
- Castanho, J., "Influence of Grain Size on Littoral Drift," Proc., 12th Int. Conf. on Coastal Eng., ASCE, pp. 891-898; 1970.
- CERC-Coastal Engineering Research Center, "Shore Protection, Planning and Design," U.S. Army Corps of Engineers, Tech. Report No. 4, 3rd Edition, Vicksburg, MS; 1966.
- CERC-Coastal Engineering Research Center, Shore Protection Manual, 4th Ed., U.S. Army Corps of Engineers, Waterways Experiment Station, Coastal Engineering Research Center, Vicksburg, MS; 1984.

- Das, M. M., "Longshore Sediment Transport Rates: A Compilation of Data," U.S. Army Corps of Engineers, Coastal Engineering Research Center, Misc. Paper No. 1-71, Vicksburg, MS; September 1971.
- Dean, R. G., "Heuristic Model of Sand Transport in the Surf Zone," Conference on Engineering Dynamics in the Surf Zone, Sydney, Australia; 1973.
- Dean, R. G., "Evaluation and Development of Water Wave Theories for Engineering Application," Vols. 1 and 2, Special Report No. 1, U.S. Army Corps of Engineers, Coastal Engineering Research Center, Vicksburg, MS; 1974.
- Dean, R. G., "Equilibrium Beach Profiles: U.S. Atlantic and Gulf Coasts," Ocean Engineering Report No. 12, Dept. of Civil Engineering, Univ. of Delaware, Newark, DE, 45 pp; January 1977.
- Dean, R. G., "Review of Sediment Transport Relationships and the Data Base," Proc., Workshop on Coastal Sediment Transport, Dept. of Civil Engineering and Sea Grant College Program, Univ. of Delaware, Newark, DE; December, 1978.
- Dean, R. G., E. P. Berek, C. G. Gable, and R. J. Seymour, "Longshore Transport Determined by an Efficient Trap," Proc., 18th Int. Conf. on Coastal Eng., ASCE, pp. 954-968; 1982.
- Dean, R. G. and R. A. Dalrymple, Water Wave Mechanics for Engineers and Scientists, Prentice-Hall Inc., Englewood Cliffs, N.J.; 1984.
- Delft (Hydraulics Laboratory), "The Influence of Groins on the Coast," Report No. M918, Delft, Netherlands; 1976.
- Downing, J. P., "Suspended Sand Transport on a Dissipative Beach," Proc., 19th Int. Conf. on Coastal Eng., ASCE, pp. 1765-1781; 1984.
- Einstein, H. A. "A Basic Description of Sediment Transport on Beaches," in Waves on Beaches, R. E. Meyer, ed., Academic Press, N.Y.; 1972.
- Fairchild, J. C., "Laboratory Tests of Longshore Transport," Proc., 12th Int. Conf. on Coastal Eng., ASCE, pp. 867-889; 1970.
- Freeman, J. C. and B. LeMehaute, "Wave Breakers on a Beach and Surges on a Dry Bed," J. Hydraulics Div., ASCE, Vol. 90, HY2, pp. 187-215; March, 1964.
- Fulford, E. T., "Distribution of Longshore Sediment Transport Across the Surf Zone," Master's Thesis, Dept. of Civil Engineering, Univ. of Delaware, Newark, DE; 1982.
- Galvin, C. J., "Breaker Type Classification on Three Laboratory Beaches," J. Geophysical Res., Vol. 73, No. 12, p. 3651-3659; 1968.

- Greer, M. N., and O. S. Madsen, "Longshore Sediment Transport Data: A Review," Proc., 16th Int. Conf. on Coastal Eng., ASCE, pp. 1563-1576; 1978.
- Hallermeier, R. J., "Uses for a Calculated Limit Depth to Beach Erosion," Proc., 16th Int. Conf. on Coastal Eng., ASCE, pp. 1493-1512; 1978.
- Hallermeier, R. J., "Bedload and Wave Thrust Computations of Alongshore Sand Transport," J. Geophysical Res., Vol. 87, No. C8, pp. 5741-51; July, 1982.
- Hughes, S. A., "Movable-Bed Modeling Law for Coastal Dune Erosion," J. Waterway, Port, Coastal and Ocean Eng., ASCE, Vol. 109, WW2, pp. 164-179; May, 1983.
- Ingle, J. O., The Movement of Beach Sand, Elsevier Pub. Co., Amsterdam; 1966.
- Inman, D. L., "Status of Surf Zone Sediment Transport Relations," Proc., Workshop on Coastal Sediment Transport, Dept. of Civil Engineering and Sea Grant College Program, Univ. of Delaware, Newark, DE; December, 1978.
- Inman, D. L., and R. A. Bagnold, "Beach and Nearshore Processes Part II: Littoral Processes," in The Sea: Ideas and Observations, Vol. 3, M. N. Hill, ed., Interscience, N.Y., pp. 529-553; 1963.
- Inman, D. L., J. A. Zampol, T. E. White, D. M. Harris, B. W. Waldorf, and K. A. Kastens, "Field Measurements of Sand Motion in the Surf Zone," Proc., 17th Int. Conf. on Coastal Eng., ASCE, pp. 1215-1234; 1980.
- Johnson, J. W., "Sand Transport by Littoral Currents," Inst. of Engineering Research, Wave Research Laboratory, Univ. of California at Berkeley, T. R. Series 3, Issue 338; 1952.
- Kamphius, J. W., and J. S. Readshaw, "A Model Study of Alongshore Sediment Transport Rate," Proc., 16th Int. Conf. on Coastal Eng., ASCE, pp. 1656-1674; 1978.
- Kamphius, J. W. and O. Sayao, "Model Tests on Littoral Sand Transport Rate," Proc., 18th Int. Conf. on Coastal Eng., ASCE, pp. 1305-1325; 1982.
- Keller, H. B., D. A. Levine, and G. B. Whitman, "Motion of a Bore over a Sloping Beach," J. Fluid Mechanics, No. 7, pp. 302-316; 1960.
- Kemp, P. H. and D. T. Plinston, "Internal Velocities in the Uprush and Backwash Zone," Proc., 14th Int. Conf. on Coastal Eng., ASCE, pp. 575-585; 1974.
- King, C. A. M., Beaches and Coasts, St. Martin's Press, New York, pp. 263-294; 1972

- Knoth, J.S. and D. Nummedal, "Longshore Sediment Transport Studies using Fluorescent Tracers," Proc., Coastal Zone '78, ASCE, pp. 2319-2331; 1978.
- Komar, P. D., "The Mechanics of Sand Transport on Beaches," J. Geophysical Res., Vol. 76, No. 3, pp. 713-721; 1971.
- Komar, P. D., "Longshore Currents and Sand Transport on Beaches," Proc., Civil Eng. in the Oceans/III, ASCE, Vol. 1, pp. 333-354; June, 1975.
- Komar, P. D., "Beach Sand Transport: Distribution and Total Drift," J. Waterway, Port, Coastal and Ocean Eng, ASCE, Vol. 103, WW2, pp. 225-239; May, 1977.
- Komar, P. D., and D. L. Inman, "Longshore Sand Transport on Beaches," J. Geophysical Res., Vol. 75, No. 30, pp. 5914-5927; October, 1970.
- Kraus, N. C., M. Isobe, H. Igarashi, T. Sasaki, and K. Horikawa, "Field Experiments on Longshore Sand Transport in the Surf Zone," Proc., 18th Int. Conf. on Coastal Eng., ASCE, pp. 969-988; 1982.
- Kraus, N. C. and L. Nakashima, "Field Method for Rapidly Determining the Dry Weight of Wet Sand Samples," J. Sed. Petrology (in review); 1986.
- Krumbein, W. C., "Shore Currents and Sand Movement on a Model Beach," U.S. Army Corps of Engineers, Beach Erosion Board, Tech. Mem. No. 7, Washington, D.C.; September, 1944.
- Liu, P., and R. A. Dalrymple, "Bottom Frictional Stresses and Longshore Currents Due to Waves with Large Angles of Incidence," J. Marine Research, Vol. 36, No. 2, pp. 357-375; 1978.
- Longuet-Higgins, M. S., "Longshore Currents Generated by Obliquely Incident Sea Waves, 1 and 2," J. Geophysical Res., Vol. 75, No. 33, pp. 6778-6801; November, 1970.
- Longuet-Higgins, M. S., "Recent Progress in the Study of Longshore Currents," in Waves on Beaches, R. E. Meyer, ed., Academic Press, New York, pp. 203-248; 1972.
- Madsen, O. S., "An Analytical Model of Longshore Sediment Transport," Proc., Workshop on Coastal Sediment Transport, Dept. of Civil Engineering and Sea Grant College Program, Univ. of Delaware, Newark, DE; December, 1978.
- Madsen, O. S., and W. D. Grant, "Quantitative Description of Sediment Transport by Waves," Proc., 15th Int. Conf. on Coastal Eng., ASCE, pp. 1093-1112; 1976.
- Mason, C., N. Kraus, and R. Holman, "The Fall 1985 Nearshore Processes Experiment, Duck-85," Proc. 44th Meeting of the Coastal Engineering Research Board, U.S. Army Corps of Eng., San Francisco, CA; November, 1985.

- McDougal, W. G. and R. T. Hudspeth, "Wave Induced Setup/Setdown and Longshore Current; Non-Planar Beaches: Sediment Transport," OCEANS, IEEE, pp. 834-846; September, 1981.
- Meyer, R. E. and A. D. Taylor, "Run-up on Beaches," in Waves on Beaches, R. E. Meyer, ed., Academic Press, New York, pp. 357-411; 1972.
- Mizuguchi, M., "Swash on a Natural Beach," Proc., 19th Int. Conf. on Coastal Eng., ASCE, pp. 678-695; 1984.
- Moore, B. D., "Beach Profile Evolution in Response to Changes in Water Level and Wave Height," Master's Thesis, Dept. of Civil Engineering, Univ. of Delaware, Newark, DE; 1982.
- Moore, G. W. and J. Y. Cole, "Coastal Processes in the Vicinity of Cape Thompson, Alaska," U.S.G.S. Trace Elements Investigations Report 753, U. S. Geological Survey; 1960.
- Ozhan, E., "Laboratory Study of Breaker Type Effect on Longshore Sand Transport," in Proc., Euromech 156: Mechanics of Sediment Transport, Istanbul, July, 1982, B. M. Sumer and A. Muler, ed., A. A. Balkema Publishers, Rotterdam; 1982.
- Savage, R. P., "Laboratory Study of the Effect of Groins on the Rate of Littoral Transport: Equipment Development and Initial Tests," U.S. Army Corps of Engineers, Beach Erosion Board, Tech. Mem. No. 114, Washington, D.C.; June, 1959.
- Savage, R. P., "Laboratory Determination of Littoral Transport Rates," J. Waterways and Harbors Div., ASCE, Vol. 88 No. WW2, pp. 69-92; May, 1962.
- Saville, T., "Model Study of Sand Transport Along an Infinitely Long, Straight Beach," Trans., American Geophysical Union, Vol. 31, No. 4, pp. 555-65; August, 1950.
- Sawaragi, T., and I. Deguchi, "Distribution of Sand Transport Rate Across a Surf Zone," Proc., 16th Int. Conf. on Coastal Eng., ASCE, pp. 1596-1613; 1978.
- Sayao, O., and J. W. Kamphius, "Littoral Sand Transport: Review of the State of the Art," Report No. 78, Dept. of Civil Eng., Queen's Univ., Kingston, Canada; January, 1983.
- Shay, E. A. and J. W. Johnson, "Model Studies on the Movement of Sand Transported by Wave Action Along a Straight Beach," Issue 7, Series 14, Inst. of Engineering Research, Univ. of California, Berkeley, CA; 1951.
- Shen, M. C. and R. E. Meyer, "Climb of a Bore on a Beach, Part 3: Run-up," J. Fluid Mechanics, Vol. 16, pp. 113-125; May, 1963.

- Sternberg, R. W., N. C. Shi, and J. P. Downing, "Field Investigations of Suspended Sediment Transport in the Nearshore Zone," Proc., 19th Int. Conf. on Coastal Eng., ASCE, pp. 1782-1798; 1984.
- Sunamura, T., and N. C. Kraus, "Prediction of Average Mixing Depth of Sediment in the Surf Zone," J. Marine Geology, Vol. 62, pp. 1-12; 1985.
- Svendsen, I. A., "Wave Heights and Set-Up in a Surf Zone," J. Coastal Engineering, Vol. 8, pp. 303-329; 1984.
- Swart, D. H., "Predictive Equations Regarding Coastal Transports," Proc., 15th Int. Conf. on Coastal Eng., ASCE, pp. 1113-1132; 1976.
- Swart, D. H., and C. A. Fleming, "Longshore Water and Sediment Transport," Proc., 17th Int. Conf. on Coastal Eng., ASCE, pp. 1275-1294; 1980.
- Thornton, E. B., "A Field Investigation of Sand Transport in the Surf Zone," Proc., 11th Int. Conf. on Coastal Eng., ASCE, pp. 335-351; 1968.
- Thornton, E. B., "Distribution of Sediment Transport Across the Surf Zone," Proc., 13th Int. Conf. on Coastal Eng., ASCE, pp. 1049-1068; 1972.
- Tsuchiya, Y., "The Rate of Longshore Sediment Transport and Beach Erosion Control," Proc., 18th Int. Conf. on Coastal Eng., ASCE, pp. 1326-1334; 1982.
- van de Graaff, J., and J. van Overeem, "Evaluation of Sediment Transport Formulae in Coastal Engineering Practice," J. Coastal Engineering, Vol. 3, pp. 1-32; 1979.
- van Hijum, E., "Equilibrium Profiles and Longshore Transport of Coarse Material Under Oblique Wave Attack," Proc., 15th Int. Conf. on Coastal Eng., ASCE, pp. 1258-1277; 1976.
- Vitale, P., "Movable-Bed Laboratory Experiments Comparing Radiation Stress and Energy Flux Factor as Predictors of Longshore Transport Rate," U.S. Army Corps of Engineers, Coastal Engineering Research Center, Misc. Report No. 81-4, Vicksburg, MS; April, 1981.
- Waddell, E., "A Field Investigation of Swash Characteristics," Coastal Engineering in Japan, Vol. 16, pp. 61-71; 1973.
- Walton, T. L., and T. Y. Chiu, "Littoral Sand Transport on Beaches," Technical Report TR-041, Dept. of Coastal and Oceanographic Engineering, Univ. of Florida, Gainesville, FL; 1979.
- Wang, H. and W. C. Yang, "A Similarity Model in the Surf Zone," Proc., 17th Int. Conf. on Coastal Eng., ASCE, pp. 529-547; 1980.

- Watts, G. M., "A Study of Sand Movement at South Lake Worth Inlet, Florida," U.S. Army Corps of Engineers, Beach Erosion Board, Tech. Mem. No. 42, Washington, D.C.; 1953.
- Weggel, J. R., "Maximum Breaker Height," J. Waterways and Harbors Div., ASCE, Vol. 98, WW4, pp. 529-548; November, 1972.
- Weishar, L. L., and R. J. Byrne, "Field Study of Breaking Wave Characteristics," Proc., 16th Int. Conf. on Coastal Eng., ASCE, pp. 487-506; 1978.
- Zenkovitch, V. P., "Fluorescent Substances as Tracers for Studying the Movement of Sand on the Sea Bed; Experiments Conducted in the U.S.S.R.," Dock and Harbor Authority, Vol. 40, pp. 280-83; 1960.